Institut für Verbrennungskraftmaschinen und Thermodynamik
Univ.-Prof. Dipl.-Ing. Dr.techn. Helmut Eichlseder

# CFD-based Optimization Strategies for the Development Process of Turbocharged Direct Injection SI-Engines

## Dissertation

eingereicht am

Institut für Verbrennungskraftmaschinen und Thermodynamik

der Technischen Universität Graz

Verfasser

Dipl.-Ing. Matthias Karch

Betreuer

Univ.-Prof. Dipl.-Ing. Dr.techn. Helmut Eichlseder

Graz 2010

# Vorwort

Die vorliegende Arbeit entstand während meiner Tätigkeit als Doktorand in der Abteilung "Entwicklung Thermodynamik" der BMW Group in München.

An erster Stelle gilt mein Dank Herrn Univ.-Prof. Dipl.-Ing. Dr.techn. Helmut Eichlseder für die Anregungen und die unkomplizierte Betreuung dieser Arbeit.

Mein herzlicher Dank richtet sich an Dr.-Ing. habil. Fabian Duddeck für sein Interesse an meiner Arbeit, die zahlreichen Treffen und die Übernahme des Korreferats.

Besonders danke ich Herrn Dr.-Ing. Bodo Durst, Leiter der Gruppe "Simulation Verbrennung", für die Ermöglichung der Arbeit und die große fachliche und persönliche Unterstützung beim Durchführen der Arbeit.

Mein ganz besonderer Dank gilt dem Betreuer der Arbeit seitens BMW, Herrn Dr.-Ing. Joachim Ebner, der in zahlreichen und ausgedehnten Diskussionen sehr zum Gelingen der Arbeit beigetragen hat. Daneben möchte ich mich für die hilfreichen Korrekturvorschläge während meiner Zeit bei BMW und danach bedanken.

Bei allen Kollegen der Gruppe bedanke ich mich für die stets große Hilfsbereitschaft und die sehr kompetenten Anregungen zur Arbeit. Insbesondere die außerordentlich angenehme Arbeitsatmosphäre sei erwähnt, zu der vor allem auch die lebhaften Unterhaltungen während der Mittagspause und die gemeinsamen privaten Aktivitäten beigetragen haben. Weiterhin möchte ich den Herren Dipl.-Ing. Markus Full und Dipl.-Ing. Karim Elwan danken, die mir durch Ihre Diplomarbeiten sehr bei der Erstellung der Dissertation geholfen haben.

Nicht zuletzt danke ich meiner Frau Brigitta für die verständnisvolle Unterstützung während und vor allem am Ende der Arbeit, ohne die das Fertigstellen dieser Dissertation nur schwer möglich gewesen wäre.

Beilngries, im Februar 2010            Matthias Karch

# Contents

# List of Figures

# List of Tables

# Symbols and Indices

**Latin Symbols - General**

| | | |
|---|---|---|
| $A$ | $mm^2$ | Cross section area |
| $c$ | $m/s$ | Velocity |
| $c_f$ | – | Flow coefficient |
| $\bar{c}_f$ | – | Weighted flow coefficient |
| $c_{f(piston)}$ | – | Flow coefficient based on piston area |
| $I, I_{xx}$ | $kgm^2$ | Moment of inertia |
| $L$ | $Nms$ | Angular momentum |
| $l_F$ | $m$ | Laminar flame thickness |
| $l_t$ | $m$ | Turbulent length scale |
| $M$ | $Nms$ | Momentum |
| $m$ | $kg$ | Mass |
| $\dot{m}_i$ | $kg/s$ | Mass flow rate in area element $A_i$ |
| $\dot{m}_{theo}, \dot{m}_{actual}$ | $kg/s$ | Ideal and actual mass flow rate |
| $n$ | $rev/min$ | Engine speed |
| $p_A, p_B$ | $N/m^2$ | Stagnation point pressure upstream, static pressure downstream |
| $p_{boost}$ | $bar$ | Boost pressure |
| $r$ | $m$ | Radius |
| $r_i$ | $m$ | Distance to tumble axis of element area $A_i$ |
| $SR$ | – | Swirl ratio |
| $SW_{VOL}$ | – | Volume swirl number |
| $s_L$ | $m/s$ | Laminar flame velocity |
| $s_T$ | $m/s$ | Turbulent flame velocity |
| $TR$ | – | Tumble ratio |
| $TU_{AVG}$ | – | Average tumble number |
| $TU_{VOL}$ | – | Volume tumble number |
| $\overline{TU}_{VOL}$ | – | Weighted volume tumble number |
| $t$ | $s$ | Time |
| $t_i$ | – | Relative valve opening duration at valve lift $i$ |
| $\dot{V}$ | $m^3/s$ | Volumetric flow |
| $V_h$ | $m^3$ | Displacement |
| $v'$ | $m/s$ | Turbulent intensity |
| $v_i, w_i$ | $m/s$ | $y$- and $z$-velocity component at area element $A_i$ |
| $w_{c_f}$ | – | Weighting factor for $c_f$ |

| | | |
|---|---|---|
| $x_{cent}, y_{cent}, z_{cent}$ | $m$ | $x$-, $y$- and $z$-coordinate of tumble center |
| $x_i, y_i, z_i$ | $m$ | Distance to tumble center |

## Latin Symbols - Fluid Dynamics

| | | |
|---|---|---|
| $a_1$ | $-$ | Model constant of the SST turbulence model |
| $C$ | $-$ | Log-layer constant |
| $C_{1\varepsilon}, C_{2\varepsilon}, C_\mu$ | $-$ | Model constants of the $k$-$\varepsilon$ turbulence model |
| $CD_{k\omega}$ | $-$ | Limiter function in the SST turbulence model |
| $c_p$ | $J/(kgK)$ | Specific heat capacity at constant pressure |
| $F_1, F_2$ | $-$ | Blending functions of the SST turbulence model |
| $f$ | $-$ | Flow quantity |
| $f_j$ | $N/kg$ | Volume force in direction $j$ |
| $h$ | $J/kg$ | Specific enthalpy |
| $k$ | $m^2/s^2$ | Turbulent kinetic energy based on the Reynolds-decomposition, $\frac{1}{2}\overline{u_i' u_j'}$ |
| $l_t$ | $m$ | Turbulent length scale |
| $Pr$ | $-$ | Prandtl number |
| $Pr_{eff}$ | $-$ | Effective Prandtl number |
| $Pr_t$ | $-$ | Turbulent Prandtl number |
| $p$ | $Pa$ | Static pressure |
| $P_k$ | $kg/(s^3m)$ | Shear production of turbulence |
| $\dot{Q}$ | $J/(m^3s)$ | Heat source term |
| $q_j$ | $J/(m^2s)$ | Heat flux |
| $R_0$ | $J/(moleK)$ | Universal gas constant, $R_0 = 8314.5$ J/(mole K) |
| $Re$ | $-$ | Reynolds number |
| $S$ | $1/s$ | Rate-of-strain invariant, $(2S_{ij}S_{ij})^{1/2}$ |
| $T$ | $K$ | Temperature |
| $T_0$ | $K$ | Reference temperature, $T_0 = 298.15$ K |
| $t$ | $s$ | Time |
| $u$ | $m/s$ | Velocity component in direction $x$ |
| $u_i$ | $m/s$ | $i$-component of velocity |
| $u_\tau$ | $m/s$ | Friction velocity |
| $u_+$ | $m/s$ | Normalized velocity |
| $v$ | $m/s$ | Velocity component in direction $y$ |
| $W$ | $kg/mole$ | Molecular weight |
| $w$ | $m/s$ | Velocity component in direction $z$ |
| $\mathbf{x}$ | $m, m, m$ | Cartesian coordinate vector |
| $x_i$ | $m$ | $i$-component of the Cartesian coordinate vector |
| $Y_{lim}^+$ | $-$ | Limiting factor of the wall-function method |

| | | |
|---|---|---|
| $y$ | $m$ | Wall distance in the SST turbulence model |
| $y_+$ | $-$ | Normalized wall unit |

**Latin Symbols - Optimization**

| | | |
|---|---|---|
| $a_i$ | $-$ | Individual |
| $D_i$ | $-$ | Diversity |
| $F_i$ | $-$ | Fitness value |
| $f_m(.)$ | $-$ | Objective function |
| $g_j(.)$ | $-$ | Equality constraint function |
| $\mathbf{H}$ | $-$ | Hessian matrix |
| $h$ | $-$ | Finite difference |
| $h_k(.)$ | $-$ | Inequality constraint function |
| $I$ | $-$ | Space of individuals |
| $k$ | $-$ | Number of regression variables |
| $L(.)$ | $-$ | Least square function |
| $m_\Theta$ | $-$ | Mutation operator |
| $N(0,1)$ | $-$ | Normally distributed random variable with expectation zero and standard deviation one |
| $n$ | $-$ | Number of sampling points |
| $P$ | $-$ | Population |
| $p$ | $-$ | Number of regression coefficients |
| $p_m$ | $-$ | Mutation rate |
| $Q$ | $-$ | Additional set of individuals |
| $R^2$ | $-$ | Coefficient of determination |
| $R^2_{adj}$ | $-$ | Adjusted coefficient of determination |
| $r_\Theta$ | $-$ | Recombination operator |
| $r_{xy}$ | $-$ | Linear correlation coefficient |
| $S$ | $-$ | Search direction for steepest descent method |
| $S_i$ | $-$ | Strength |
| $s_{\Theta_s}$ | $-$ | Selection operator |
| $s_{(\mu+\lambda)}$ | $-$ | $(\mu+\lambda)$-selection |
| $s_{(\mu,\lambda)}$ | $-$ | $(\mu,\lambda)$-selection |
| $t$ | $-$ | Generation counter |
| $\vec{x}$ | $-$ | Set of optimization variables |
| $x_i$ | $-$ | $i$-component of optimization variable set $\vec{x}$ |
| $x_j$ | $-$ | Regressor variable |
| $y$ | $-$ | Output parameter |
| $\hat{y}$ | $-$ | Meta-model |

## Greek Symbols - General

| | | |
|---|---|---|
| $\varepsilon$ | – | Compression ratio |
| $\eta_V$ | – | Volumetric efficiency |
| $\kappa$ | – | Isentropic coefficient |
| $\omega$ | $1/s$ | Angular velocity |
| $\omega_0$ | $1/s$ | Crankshaft angular velocity |
| $\rho$ | $kg/m^3$ | Density |
| $\rho_n$ | $kg/m^3$ | Normal density |

## Greek Symbols - Fluid Dynamics

| | | |
|---|---|---|
| $\alpha, \alpha_1, \alpha_2$ | – | Model constants of the SST turbulence model |
| $\beta, \beta_1, \beta_2, \beta'$ | – | Model constants of the SST turbulence model |
| $\delta_{ij}$ | – | Kronecker delta |
| $\varepsilon$ | $m^2/s^3$ | Turbulent dissipation rate |
| $\kappa$ | – | von Karman constant |
| $\lambda$ | $N/m^2$ | Heat diffusion coefficient |
| $\mu$ | $kg/(ms)$ | Dynamic viscosity |
| $\mu_{eff}$ | $kg/(ms)$ | Effective viscosity |
| $\mu_t$ | $kg/(ms)$ | Turbulent viscosity |
| $\nu$ | $m^2/s$ | Kinematic viscosity, $\nu = \mu/\rho$ |
| $\nu_t$ | $m^2/s$ | Kinematic turbulent viscosity |
| $\omega$ | $1/s$ | Eddy frequency, $\omega = \varepsilon/k$ |
| $\rho$ | $kg/m^3$ | Density |
| $\sigma_\varepsilon, \sigma_k$ | – | Model constants of the $k$-$\varepsilon$ turbulence model |
| $\sigma_k, \sigma_{k1}, \sigma_{k2}$ | – | Model constants of the SST turbulence model |
| $\sigma_\omega, \sigma_{\omega1}, \sigma_{\omega2}$ | – | Model constants of the SST turbulence model |
| $\tau_{ij}$ | $N/m^2$ | Viscous tensor |
| $\tau_w$ | $N/m^2$ | Wall shear stress |
| $\vartheta_t$ | $m/s$ | Turbulent velocity scale |
| $\zeta, \zeta_1, \zeta_2$ | – | Model constants of the SST turbulence model |

## Greek Symbols - Optimization

| | | |
|---|---|---|
| $\alpha$ | – | Step size for steepest descent method |
| $\beta_j$ | – | Regression coefficient |
| $\delta$ | – | Finite difference |
| $\varepsilon$ | – | Approximation error |
| $\iota(.)$ | – | Termination criterion |
| $\lambda$ | – | Number of offspring individuals |
| $\mu$ | – | Number of parent individuals |

| | | |
|---|---|---|
| $\nabla$ | – | Gradient |
| $\Omega$ | – | Set of genetic operators |
| $\omega_{\Theta_i}$ | – | Genetic operator |
| $\Phi(.)$ | – | Fitness function |
| $\Psi(.)$ | – | Generation transition function |
| $\sigma$ | – | Standard deviation |
| $\tau_0$ | – | Learning rate at self-adaption mechanism |

## Subscripts

| | |
|---|---|
| $a$ | Axial component |
| $E$ | Quantities at the inlet |
| $u$ | Quantities of the unburned mixture |
| $t$ | Tangential component |
| $x, y, z$ | Quantities in $x$-, $y$- and $z$-direction |
| $0$ | Reference values |

## Superscripts

| | |
|---|---|
| $^-$ | Mean value |
| $'$ | Fluctuating component |
| $L$ | Lower bound |
| $U$ | Upper bound |

## Abbreviations - General

| | |
|---|---|
| *CAD* | Computer aided design |
| *CAE* | Computer aided engineering |
| *CFD* | Computational fluid dynamics |
| *DGV* | Doppler Global Velocimetry |
| *DoE* | Design of Experiment |
| *EA* | Evolutionary Algorithm |
| *EP* | Evolutionary Programming |
| *ES* | Evolutionary Strategy |
| *FB* | Flow box |
| *GA* | Genetic Algorithm |
| *LDV* | Laser Doppler velocimetry |
| *LHS* | Latin hypercube sampling |
| *MOO* | Multi-objective optimization |
| *NSGA* | Non-dominated Sorting Genetic Algorithm |
| *PIV* | Particle image velocimetry |
| *RANS* | Reynolds-averaged Navier-Stokes |
| *rpm* | Revolutions per minute |
| *RS* | Response surface |
| *RSM* | Response surface methodology |
| *RSME* | Root square mean error |
| *SA* | Simulated Annealing |
| *SOO* | Single-objective optimization |
| *SPEA* | Strength Pareto Evolutionary Algorithm |
| *SST* | Shear stress transport |
| *TKE* | Turbulent kinetic energy |

## Abbreviations - Internal Combustion Engines[1]

| | |
|---|---|
| *BDC* | Bottom dead center |
| *BMEP* | Brake mean effective pressure |
| *CA* | Crank angle |
| *CD* | Combustion duration |
| *CO* | Carbon monoxide emissions |
| *DI* | Direct injection |
| *DISI* | Direct injecting spark-ignition |
| *CoV* | Coefficient of variation |
| *EGR* | Exhaust gas recirculation |

| | |
|---|---|
| *EV* | Exhaust valve angle |
| *HC* | Hydrocarbon emissions |
| *IC* | Internal combustion |
| *IMEP* | Indicated mean effective pressure |
| *ISCO* | Indicated specific carbon monoxide emissions |
| *ISFC* | Indicated specific fuel consumption |
| *IV* | Intake valve angle |
| *IVC* | Intake valve closing |
| *LET* | Low end torque |
| *MFB* | Mass fraction burned |
| *MPI* | Multi-point injection |
| *NA* | Naturally aspirated |
| *PFI* | Port fuel injection |
| *PMEP* | Pumping mean effective pressure |
| *SI* | Spark-ignition |
| *SOI* | Start of injection |
| *TC* | Turbocharged |
| *TDC* | Top dead center |
| *VSR* | Valve seat ring |
| *VVT* | Fully variable valve drive |
| *WOT* | Wide open throttle |

---

[1]Explanations and definitions can be found in Taylor (1985a,b)

# 1 Introduction

In the development process of internal combustion (IC) engines, the apparent conflict between reducing fuel consumption and exhaust emissions on the one hand and enhancing performance on the other hand arises. In particular the reduction of fuel consumption is currently in the main focus due to the worldwide $CO_2$ discussion. In order to solve this conflict, downsizing is a very promising approach, which denotes the replacement of large displacement engines by engines with reduced displacement Golloch (2005). Fuel saving potential then results from a shifting of the operational range towards higher loads with accordingly better efficiency (Koenigstein et al. (2008)) and reduced frictional losses. To eliminate the disadvantage in performance arising from reduced displacement, supercharging by means of a turbocharger is commonly applied.

Downsizing using turbocharging of course is not a completely new approach. Nevertheless, it definitely gained in significance with the introduction of direct injection (DI). While for diesel engines this combustion concept is already state-of-the-art for several years, for spark-ignition (SI) engines it has been introduced recently, while it can be expected to become the dominating combustion system in the near future. In the past turbocharged (TC) SI-engines based on port fuel injection (PFI) had to deal with the problem of enlarged fuel consumption at high loads. As a consequence of intensified knocking tendency the compression ratio has to be decreased and significant mixture enrichment is required at high loads. Apart from knocking, mixture enrichment is additionally applied to lower exhaust gas temperatures, which is clearly limited due to the turbocharger. As a result, the engine's overall efficiency particularly at full load operation was rather poor. For direct injecting spark-ignition (DISI) engines these problems can be clearly mitigated due to the cooling effect resulting from fuel vaporization inside the combustion chamber (Lecointe and Monnier (2003)). Thus, a high compression ratio can be retained and the demand for fuel enrichment at full load operation reduced. As a result, significant fuel reductions can be realized by downsizing SI-engines using turbocharging and direct injection (Korte et al. (2008) and Blaxill et al. (2008)).

However, in order to exploit the full potential delivered by this combustion system, the following problems have to be addressed. Concerning fuel direct injection, mixture preparation is clearly more demanding, as the available time is reduced, in particular at high engine loads and speeds. The further decrease in fuel consumption at full load operation by reducing the engine's knock tendency is another important issue (Sorger et al. (2008)), which requires fast burning rates. In order to operate the engine close to the knock limit a robust combustion process is desired. The optimization of the in-cylinder flow, which is mainly influenced by the intake ports, combustion chamber and piston design, is an adequate measure to solve these challenges and is accordingly a crucial part within the engine development process of SI-engines.

## 1.1 Automatic Optimization in Engine Development

Concerning naturally aspirated (NA) SI-engines the focus is commonly on the flow rate characteristics exclusively in order to maximize the engine's performance. In the context of

turbocharged SI-engines however charge motion is another important objective when optimizing the in-cylinder flow, which significantly rises the problem's complexity (**Fig. 1.1**). Currently the optimization of the in-cylinder flow is performed manually and sequentially, which results in a trial-and-error procedure. Nevertheless, in the past different approaches for the efficient optimization of the flow-guiding devices were proposed. Tuertscher (1991) introduced a CAD-based method for developing intake ports, which allowed for fast parameter variation within the design process. Measurements by means of a steady flow test rig were applied for assessing the characteristics of the design proposals. As an outlook the implementation of 3D-CFD simulations for design evaluation were mentioned, which at that time failed due to the limited computing power and accordingly coarse mesh resolution.
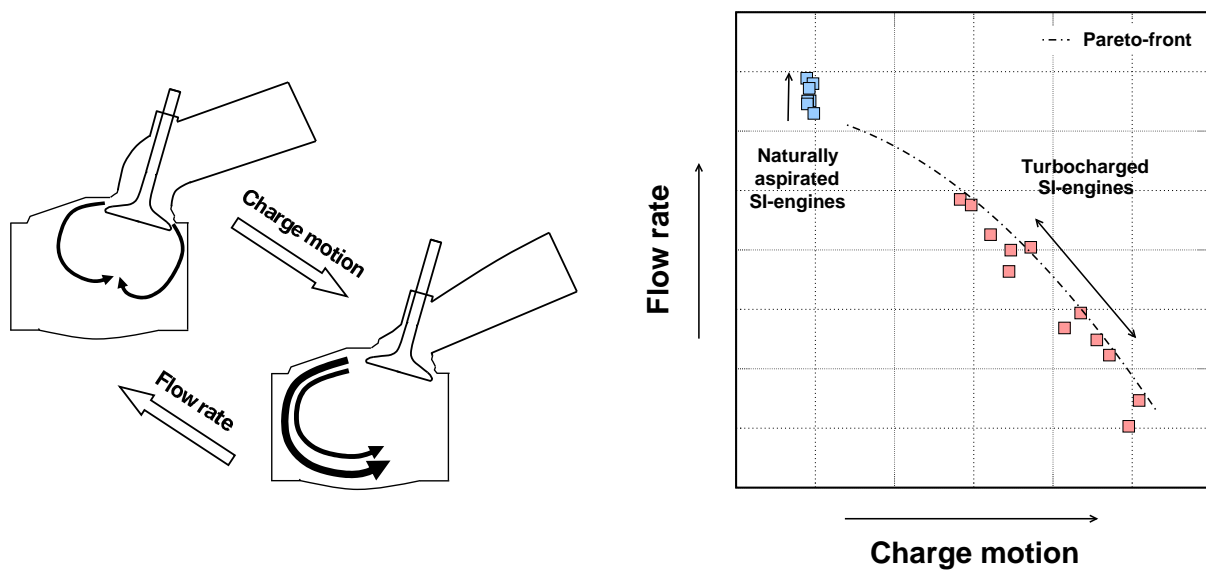


**Fig. 1.1:** Objectives concerning an intake port optimization for SI-engines.

An intake port developing process including computational fluid dynamics (CFD) methods was presented by Tremel (1997). As CFD-simulations alone were found to be insufficient for analyzing, experimental methods were applied simultaneously during this process. In order to analyze and validate the port characteristics flow rate and charge motion, steady state as well as transient calculation and measuring approaches were used. As a consequence of this extensive evaluation process the number of iterations was clearly limited.

However, in the last years CFD has been established more and more as an efficient and reliable tool, which successively substitutes time- and cost-intensive measurements. An important step therefore was the introduction of automated mesh generation, which significantly reduced the effort for performing CFD simulations (Wieser et al. (1998)). By this, fully automated design optimization based on CFD methods has been enabled.

A closed-loop optimization process concerning an intake port is described in Makk (1998), where the increase of flow rate was the optimization target calculated by means of a steady state flow analysis. In order to reduce the computational effort, combustion chamber and cylinder were neglected and for the intake port geometry a coarse, unstructured mesh was applied (Makk et al. (1999)). The parametric intake port itself was quite detailed containing

23 CAD-parameters. To handle this variety of parameters an Evolutionary Algorithm (EA) was used. As a result, the feasibility of automated design optimization was revealed. However, due to the simplifications the numerical accuracy was rather poor. Furthermore, the computation cycle times were still hardly acceptable (Makk et al. (1999)).

A more detailed optimization process, where combustion chamber and cylinder were included, was used by Affes et al. (1998) in order to optimize the shape of intake ports and chambers. A gradient-based optimization approach was selected, which restricted the number of design parameters with respect to reasonable computational costs. Thus, only four parameters were chosen for this study. As optimization targets discharge coefficient and angular momentum flux were defined, which resulted in a multi-objective problem. Thus, for an intake port of a two-valve IC engine a strict trade-off between both targets was revealed.

Haslinger and Steinhagen (2005) described a shape optimization for a filling port of a six-cylinder NA engine with port fuel injection. The maximization of the inlet mass flow at steady state boundary conditions was defined as unique objective. The intake port geometry was represented by a parametric CAD-model containing 8 variable parameters. In a first step, a Genetic Algorithm (GA) was used for the optimization, where a total of 175 designs were evaluated. As a result, an increase in mass flow by approx. 3% was achieved. In a second step the results gained by the GA were applied to calculate a meta-model (Response Surface). Based on this model another GA optimization was carried out, while no further improvement was realized.

A very extensive intake port optimization for a naturally aspirated (NA) SI-engine with direct injection was performed by Roettger et al. (2005). Based on a CAD-model with 8 parameters, 950 designs were analyzed in terms of flow coefficient and tumble by means of a steady flow simulation at maximum valve lift. Apart from the intake port, the detailed numerical model included the intake manifold and the combustion chamber. For the optimization a Genetic Algorithm was applied, where both objectives were combined to a single term by means of weighting factors. As a result, a global optimum for a pre-defined relation between flow coefficient and tumble number was found (Roettger et al. (2004)). Based on this optimization process Abad Lozano et al. (2007) investigated an intake port geometry for a turbocharged diesel engine, where the flow coefficient was regarded in combination with the swirl number. In addition, a swirl intake port optimization was performed with the aim of reducing exhaust emissions and specific fuel consumption. For this purpose a design of experiment (DoE) method was used to perform a sensitivity analysis, which revealed the important relations between design parameters and optimization targets.

The optimization of a tumble port of a turbocharged eight-cylinder with direct injection is studied in Loy (2005). As the basic contour of this series production port was already defined within the development process, the main focus was on the design parameters of the milling cutter applied for the final machining operation. In addition, the intake port angle was varied. By applying a multi-objective GA, the contradictory character between the two objectives, the mass flow and the tumble number, was revealed. Apart from this optimization a simple approach for a robustness analysis was given, where tolerances resulting from the production process were

simulated by means of DoE. Due to the limited computational power only 10 variations were investigated. However, the general influence of production tolerances has been identified.

Adomeit et al. (2006) introduced an optimization process for the intake and exhaust ports for both diesel and SI-engines. Concerning the intake port adequate flexibility was offered by a CAD-model with about 20 parameters. The feasibility of the automated process was demonstrated by means of an intake port optimization, where three design parameters were varied. Evolutionary Algorithms were implemented for resolving the multi-objective problem between flow coefficient and tumble number. The optimization progress was illustrated in comparison to the boundary curve defined by the corresponding values of state-of-the-art series production engines.

## 1.2 Aims and Objectives

The approaches mentioned so far are mainly stand-alone solutions, which are dedicated to a single specific problem respectively. Due to the partly very limited computational power rather simple calculation methods, less detailed parametric models or insufficient numbers of design evaluations were applied. In addition, existing multi-objective problems were often simplified to single objective ones by means of pre-defined weighting factors.

The present work focuses on implementing a flexible, automatic CFD-based process for the multi-objective optimization of the intake port and the combustion chamber, which satisfies the requirements of a series development process. For this purpose the following tasks have to be solved:

- Definition of the requirements concerning the in-cylinder flow for a turbocharged combustion process with direct fuel injection.

- Development of fully parametric CAD-models for the intake port and the combustion chamber, which are flexible and detailed enough to cover the whole range of feasible designs respectively. Furthermore, for the intake port the model setup has to be defined such that an automatic robustness evaluation can be performed.

- Implementation of CFD-based analysis methods, which allow for the adequate assessment of the particular cylinder head designs concerning the in-cylinder flow characteristics. This requires efficient CFD methods as well as automatic mesh generation and post processing.

- Combination of the new defined CAE-based development process with suitable methods for optimization and robustness analysis in order to enable a fully automatic process.

- Application and validation of the CFD-based optimization process by means of different optimization problems for the intake port and the combustion chamber.

The basic physical principals of CFD are described in Chapter 2, where the general as well as the time-averaged governing equations are introduced. For turbulent flows two different turbulence models and their corresponding near-wall treatment are described in detail.

In Chapter 3 efficient optimization methods are presented, where special emphasis is put on global approaches that can handle real multi-objective problems. Furthermore, the basics concerning sensitivity analysis are explained, which is used for analyzing the influence of the CAD parameters.

The requirements of a turbocharged SI-engine concerning flow characteristics and charge motion are investigated in Chapter 4 by means of a cylinder head variation. Subsequently, well-known characteristical numbers are given for these measures, by means of which the proper assessment of different design concepts is enabled. Finally, CFD-based evaluation methods of different complexity are described.

In Chapter 5 the modular concept of the optimization process is specified. The specific modules CAD model, mesh generation and CFD evaluation are described in more detail.

Chapter 6 is dedicated to several optimization problems concerning the intake port and the combustion chamber. In a first step a sensitivity analysis is performed in order to investigate the influences of the CAD-parameters on the resulting in-cylinder flow. Based on these results, a strategy for optimizing the intake port layout is analyzed applying different optimization methods. The feasibility of this strategy is illustrated by means of a global intake port optimization and a specific optimization of a tumble port of a series production engine. For validating the optimization results detailed CFD-simulations are included. In addition, an optimization strategy for a combustion chamber is discussed. A global optimization as well as a detailed problem of a cylinder head with masking are considered and validated by detailed CFD-methods and engine tests respectively.

A robustness analysis for the intake port is introduced in Chapter 7, where generic as well as real process tolerances are regarded. This analysis is applied to a series production port and an optimized design of this port. For both ports the influence of parameter variations on the in-cylinder flow are quantified and suitable measures for evaluating the robustness of an intake port design are derived.

# 2 Physics of Fluid Dynamics

Computational Fluid Dynamics (CFD) is today an inherent part of the powertrain design process, especially in the early stage before hardware for the testing of the engine is available. In this Chapter the general equations of fluid dynamics are presented. As the Reynolds averaged equations are applied, turbulence models are required. Therefore, two well-known models from the literature (e.g. Wilcox (2006), Pope (2000)), the $k$-$\varepsilon$ and the SST model, and their specific near-wall treatments are introduced briefly.

## 2.1 Governing Equations

The governing equations expressed by the equation of mass, momentum and energy conservation are introduced as implemented by ANSYS (2006).

**Continuity Equation:**

$$\frac{\partial \rho}{\partial t} + \frac{\partial}{\partial x_i}(\rho u_i) \;=\; 0 \qquad with \quad i = 1, 2, 3 \quad . \tag{2.1}$$

$\rho$ denotes the density, $u_i$ the velocity components, $t$ the time and $x_i$ the cartesian coordinates, respectively. The continuity equation or equation of mass conservation includes the rate of change in time of the density $\partial \rho / \partial t$ and the convective term, which describes the net flow of mass out of the domain (Versteeg and Malalasekera (1995)).

**Momentum Equation:**

$$\frac{\partial \left( \rho u_j \right)}{\partial t} + \frac{\partial}{\partial x_i}\left( \rho u_i u_j \right) \;=\; -\frac{\partial p}{\partial x_j} + \frac{\partial \tau_{ij}}{\partial x_i} + \rho f_j \qquad with \quad i \neq j = 1, 2, 3 \quad . \tag{2.2}$$

The momentum equation (or Navier-Stokes equation), based on Newton's second law, states that the rate of change of momentum of a fluid particle equals the sum of the forces on the particle. The terms on the right-hand side describe the surface and body forces experienced by the fluid, where $f_j$ denotes the volume forces (e.g. gravity or Coriolis force) acting in direction $j$. Volume forces can be neglected in most CFD-applications. Surface forces are pressure forces and viscous forces denoted by $\tau$. For a Newtonian fluid the stress tensor $\tau_{ij}$ is:

$$\tau_{ij} \;=\; \mu \left( \frac{\partial u_i}{\partial x_j} + \frac{\partial u_j}{\partial x_i} - \frac{2}{3}\frac{\partial u_k}{\partial x_k} \delta_{ij} \right) \quad , \tag{2.3}$$

where $\mu$ denotes the locally constant dynamic viscosity of the fluid and $\delta_{ij}$ the Kronecker symbol.

**Conservation of Energy:**

$$\frac{\partial (\rho\, h)}{\partial t} + \frac{\partial}{\partial x_i}(\rho\, u_i\, h) \;=\; \frac{\partial p}{\partial t} + u_i\frac{\partial p}{\partial x_i} - \frac{\partial q_i}{\partial x_i} + \tau_{ij}\frac{\partial u_i}{\partial x_j} + \dot{Q} \quad . \tag{2.4}$$

The energy equation is derived from the first law of thermodynamics. The rate of change of energy is equal to the rate of heat addition and the work done on a fluid element. The conservation equation is given for the specific enthalpy $h$ as:

$$h \;=\; h_0 + \int_{T_0}^{T} c_p\, dT \qquad with \quad c_p = f(T) \quad , \tag{2.5}$$

where $h_0$ denotes the enthalpy at reference temperature $T_0$ and $c_p$ the heat capacity for an Ideal Gas at constant pressure. The heat flux due to conduction can be computed using Fourier's law:

$$q_i \;=\; -\lambda\frac{\partial T}{\partial x_i} \quad , \tag{2.6}$$

where $\lambda$ denotes the thermal conductivity. Introducing the Prandtl number with

$$Pr \;=\; \frac{\mu c_p}{\lambda} \quad , \tag{2.7}$$

which compares molecular momentum and heat transfer, the heat flux can be written as:

$$q_i \;=\; -\frac{\mu}{Pr}\frac{\partial h}{\partial x_i} \quad . \tag{2.8}$$

The source term $\dot{Q}$ denotes the heat addition due to chemical reactions and radiation. If one is interested in the small Mach number limit only the convective change of pressure does not need to be considered as the pressure can be assumed as constant Pope (2000).

**Equation of State:**

$$\rho \;=\; \frac{W\, p}{R_0\, T} \quad , \tag{2.9}$$

where $W$ denotes the molecular weight of the gas and $R_0$ the universal gas constant. The Ideal Gas equation of state is additionally applied to close the set of governing equations by linking pressure, density and temperature.

## 2.2    Turbulence Modeling

Flows in the laminar regime are described completely by the equations given in Section 2.1. For simple cases, analytical solutions can be found (Versteeg and Malalasekera (1995)). However, most flows in engineering applications like in-cylinder flows or the mixing phenomena of fuel and air in internal combustion engines are highly turbulent. According to Pope (2000) the direct approach of solving the time-dependent Navier-Stokes equations, called direct numerical simulation (DNS), is impossible for turbulent flows of practical interest.

In order to solve the equations with reasonable computational effort the flow quantities are splitted into a mean value $\bar{f}$ and a fluctuation component $f'$:

$$f = \bar{f} + f' \quad . \tag{2.10}$$

This leads to the following equations in analogy to the governing equations in Chapter 2.1:

**Continuity Equation:**

$$\frac{\partial \rho}{\partial t} + \frac{\partial}{\partial x_i}(\rho \overline{u_i}) = 0 \quad . \tag{2.11}$$

**Momentum Equation:**

$$\frac{\partial \left( \rho \overline{u_j} \right)}{\partial t} + \frac{\partial}{\partial x_i}\left( \rho \overline{u_i u_j} \right) = -\frac{\partial \overline{p}}{\partial x_j} + \frac{\partial \overline{\tau_{ij}}}{\partial x_i} - \frac{\partial}{\partial x_i}\left( \rho \overline{u_i' u_j'} \right) + \rho \overline{f_j} \quad . \tag{2.12}$$

**Conservation of Energy:**

$$\frac{\partial \left( \rho \overline{h} \right)}{\partial t} + \frac{\partial}{\partial x_i}\left( \rho \overline{u_i h} \right) = \frac{\partial \overline{p}}{\partial t} + \overline{u_i}\frac{\partial \overline{p}}{\partial x_i} - \frac{\partial \overline{q_i}}{\partial x_i} + \overline{\tau_{ij}}\frac{\partial \overline{u_i}}{\partial x_j} - \frac{\partial}{\partial x_i}\left( \rho \overline{u_i' h'} \right) + \overline{\dot{Q}} \quad . \tag{2.13}$$

The equation set (2.12) is called the Reynolds-averaged Navier-Stokes (RANS) equations or Reynolds equations, containing the three components of the momentum equation in $x$, $y$ and $z$-direction. These time-averaged equations show an extra term $(\overline{u_i' u_j'})$, which can be interpreted as additional stresses, referred to as the Reynolds stresses. These stresses appear as unknowns leading to the so called closure problem as there are more unknowns than equations.

The scalar fluxes of the energy equation (2.13) play an analogous role to that of the Reynolds equations (Pope (2000)). Via the eddy-viscosity hypothesis of Boussinesq (1877), the Reynolds shear stress tensor can be simplified. This model suggests, that turbulence consists of small eddies which are continuously forming and dissipating, and in which the Reynolds stresses are assumed to be proportional to the mean velocity gradients:

$$-\rho \overline{u'_i u'_j} = \mu_t \left( \frac{\partial u_i}{\partial x_j} + \frac{\partial u_j}{\partial x_i} \right) - \frac{2}{3} \delta_{ij} \left( \rho k + \mu_t \frac{\partial u_k}{\partial x_k} \right) \quad , \tag{2.14}$$

where the turbulent kinetic energy $k$ is defined as:

$$k = \frac{1}{2} \overline{u'_i u'_i} = \frac{1}{2} \left( \overline{u'^2} + \overline{v'^2} + \overline{w'^2} \right) \quad . \tag{2.15}$$

The Reynolds heat flux density vector is modeled in the same way:

$$-\rho \, \overline{u'_i h'} = \frac{\mu_t}{Pr_t} \frac{\partial h}{\partial x_i} \quad , \tag{2.16}$$

whereas $Pr_t$ is the turbulent Prandtl number and $\mu_t$ the turbulent viscosity. With these simplifications the viscous and turbulent terms can be summarized and the following variables can be defined:

$$\mu_{eff} = \mu + \mu_t \tag{2.17}$$

$$\frac{\mu_{eff}}{Pr_{eff}} = \frac{\mu}{Pr} + \frac{\mu_t}{Pr_t} \quad . \tag{2.18}$$

The turbulent or eddy viscosity $\mu_t$ and the turbulent Prandtl number $Pr_t$ are unknown and have to be determined by simplified assumptions. The turbulent Prandtl number for gas flows can be found in Patankar (1980) with $Pr_t = 0.9$. The turbulent viscosity $\mu_t$ is a function of the flow and not a material property like the molecular viscosity $\mu$. Turbulence models are applied to provide the turbulent viscosity and thus close the Reynolds equations (2.12).

Several approaches for turbulence models are known from the literature which mainly differ in terms of accuracy, modeling complexity and computational effort (Pope (2000), Wilcox (1988)). Concerning automatic optimization, where many designs need to be assessed, the conflict between computational effort and robustness on the one hand and accuracy on the other hand arises. In this work so-called two-equation models, more precisely the $k$-$\varepsilon$ model and the shear-stress transport (SST) model, are used as these models have been found to be stable and numerically robust. Furthermore they were found to offer a good compromise between numerical effort and accuracy of prediction (ANSYS (2006)). The description of both turbulence models is in the focus of the next sections.

## 2.2.1   The $k$-$\epsilon$ Model

The standard $k$-$\varepsilon$ model from Launder and Spalding (1974) is the most widely used and validated turbulence model. It consists of two transport equations, one for the turbulent kinetic energy $k$ and one for the rate of viscous dissipation $\varepsilon$. In contrast to more complex turbulence models only the large energetic eddies are regarded. Their turbulent kinetic energy $k$ is transferred to successively smaller and smaller eddies, until the energy is dissipated by viscous action. The model transport equations for $k$ and $\varepsilon$ are:

**Turbulent Kinetic Energy:**

$$\frac{\partial (\rho k)}{\partial t} + \frac{\partial}{\partial x_i} \left( \rho u_i k \right) \quad = \quad \frac{\partial}{\partial x_i} \left( \mu + \frac{\mu_t}{\sigma_k} \right) \frac{\partial k}{\partial x_i} + P_k - \rho \varepsilon \tag{2.19}$$

**Turbulence Dissipation Rate:**

$$\frac{\partial (\rho \varepsilon)}{\partial t} + \frac{\partial}{\partial x_i} \left( \rho u_i \varepsilon \right) \quad = \quad \frac{\partial}{\partial x_i} \left( \mu + \frac{\mu_t}{\sigma_\varepsilon} \right) \frac{\partial \varepsilon}{\partial x_i} + \frac{\varepsilon}{k} \left( C_{1\varepsilon} P_k - \rho\, C_{2\varepsilon}\, \varepsilon \right) \tag{2.20}$$

$$with \quad P_k \quad = \quad \mu_t \left( \frac{\partial u_i}{\partial x_j} + \frac{\partial u_j}{\partial x_i} \right) \frac{\partial u_i}{\partial x_j} - \frac{2}{3} \frac{\partial u_i}{\partial x_i} \left( 3\mu_t \frac{\partial u_i}{\partial x_i} + \rho k \right) \quad , \tag{2.21}$$

where $P_k$ is the turbulent production. The model constants $\sigma_k$, $\sigma_\varepsilon$, $C_{1\varepsilon}$ and $C_{2\varepsilon}$ are derived by comparison with experimental observations (Pope (2000)). Standard values are listed in **Table 2.1**.

In order to determine an appropriate specification of the turbulent viscosity, the turbulent velocity scale $\vartheta_t$ and the turbulent length scale $l_t$ are estimated from properties of the turbulence field, the turbulent kinetic energy $k$ and its dissipation rate $\varepsilon$:

$$\vartheta_t \sim k^{1/2} \qquad\qquad l_t \sim \frac{k^{3/2}}{\varepsilon} \quad . \tag{2.22}$$

The $k$-$\varepsilon$ model assumes that the turbulence viscosity $\mu_t$ is linked to the turbulence kinetic energy and dissipation via the following relation:

$$\mu_t \quad = \quad C_\mu \rho \frac{k^2}{\varepsilon} \quad , \tag{2.23}$$

where $C_\mu$ is a dimensionless constant (**Table 2.1**).

| $C_\mu$ | $\sigma_k$ | $\sigma_\varepsilon$ | $C_{1\varepsilon}$ | $C_{2\varepsilon}$ |
|---------|-----------|----------------------|--------------------|--------------------|
| 0.09    | 1.00      | 1.30                 | 1.44               | 1.92               |

**Table 2.1:** Constants of the $k$-$\varepsilon$ turbulence model (Wilcox (2006)).

## 2.2.2   The SST Model

The shear-stress transport (SST) model was developed by Menter (1994). It combines the $k$-$\varepsilon$ model with the $k$-$\omega$ model from Wilcox (1988).

The standard $k$-$\varepsilon$ model is insensitive to adverse pressure gradients in boundary-layers. It clearly overpredicts the shear-stress and the turbulent length scale in the near wall region, which leads to a significant delay in flow separation. Another problem is the numerical stiffness in the viscous sublayer. Since $\varepsilon$ does not automatically tend to zero at boundaries with no-slip condition, complex non-linear damping functions are required.

The $k$-$\omega$ model performs much better under adverse pressure-gradients. In contrast to the $k$-$\varepsilon$ model there is no need for damping functions in the viscous sublayer leading to high numerical robustness. However, the results are very sensitive to the values of $\omega$, which is the turbulent frequency, in the freestream (Wilcox (2006)).

The SST model is equivalent to the standard $k$-$\omega$ model within the boundary layer and gradually changes to the standard $k$-$\varepsilon$ model in the outer region using a blending function ($F_1$). In order to perform the blending of the two models with one set of equations, the $k$-$\varepsilon$ model has been transferred into a $k$-$\omega$ formulation with a transport equation for $\omega$ using the simple relation $\omega = \varepsilon/k$ (e.g. ANSYS (2006)). Besides differences in modeling constants, the transport equations for the turbulent kinetic energy in both the $k$-$\omega$ and the $k$-$\varepsilon$ model are equivalent.

**Turbulent Kinetic Energy:**

$$\frac{\partial(\rho k)}{\partial t} + \frac{\partial}{\partial x_i}(\rho u_i k) = \tilde{P}_k + \frac{\partial}{\partial x_i}\left(\mu + \frac{\mu_t}{\sigma_k}\right)\frac{\partial k}{\partial x_i} - \beta'\rho k \omega \tag{2.24}$$

$$\text{with} \quad \tilde{P}_k = \min\left(P_k, 10\cdot\rho\beta'k\omega\right) \quad, \tag{2.25}$$

where the volumetric generation rate $P_k$ is calculated as in the $k$-$\varepsilon$ model (Equation 2.21).

**Turbulent Frequency:**

$$\frac{\partial(\rho\omega)}{\partial t} + \frac{\partial}{\partial x_i}(\rho u_i \omega) = \alpha\frac{\omega}{k}\tilde{P}_k + \frac{\partial}{\partial x_i}\left(\mu + \frac{\mu_t}{\sigma_\omega}\right)\frac{\partial\omega}{\partial x_i} - \beta\rho\omega^2$$

$$+ 2(1-F_1)\rho\frac{1}{\sigma_{\omega 2}\omega}\frac{\partial k}{\partial x_i}\frac{\partial\omega}{\partial x_i} \quad. \tag{2.26}$$

To switch between the two turbulence models of the SST model, a blending function $F_1$ is used. Its formulation is based on the distance to the nearest surface and on the flow variables (Menter (1994)).

$$F_1 = \tanh(arg_1{}^4) \tag{2.27}$$

$$with \quad arg_1 = min\left[max\left(\frac{\sqrt{k}}{\beta'\omega y}, \frac{500\nu}{y^2\,\omega}\right), \frac{4\rho k}{CD_{k\omega}\,\sigma_{\omega 2}\,y^2}\right] \tag{2.28}$$

$$and \quad CD_{k\omega} = max\left(2\rho\frac{1}{\sigma_{\omega 2}\omega}\frac{\partial k}{\partial x_i}\frac{\partial \omega}{\partial x_i}, 1.0\times 10^{-10}\right) \quad, \tag{2.29}$$

where $y$ is the distance to the nearest wall and $\nu$ represents the kinematic viscosity. $F_1$ is close to one in the boundary layer to preserve the desirable features of the $k$-$\omega$ model and goes to zero at the edge of the boundary layer to take advantage of the freestream independence of the $k$-$\varepsilon$ model. The model constants are blended as well according to $\zeta = \zeta_1 F_1 + \zeta_2(1-F_1)$. The index 1 is used for the set of constants for the $k$-$\omega$ model and the index 2 for the set for the $k$-$\varepsilon$ model. The complete set of modeling constants of the SST model is given in **Table 2.2**.

| $\beta'$ | $\alpha_1$ | $\beta_1$ | $\sigma_{k1}$ | $\sigma_{\omega 1}$ | $\alpha_2$ | $\beta_2$ | $\sigma_{k2}$ | $\sigma_{\omega 2}$ |
|------|------|-------|------|------|------|--------|------|-------|
| 0.09 | 5/9 | 0.075 | 2.00 | 2.00 | 0.44 | 0.0828 | 1.00 | 1.168 |

**Table 2.2:** Constants of the SST turbulence model (Menter (1994)).

The formulation of the turbulent viscosity is modified in order to apply *Bradshaw's assumption*:

$$\nu_t = \frac{\mu_t}{\rho} = \frac{a_1 k}{max(a_1\omega, SF_2)} \tag{2.30}$$

$$with \quad S = \sqrt{2S_{ij}S_{ij}}, \quad S_{ij} = \frac{1}{2}\left(\frac{\partial u_i}{\partial x_j}+\frac{\partial u_j}{\partial x_i}\right) \quad, \tag{2.31}$$

where $S$ is the mean rate of strain invariant and $a_1$ is a constant of proportionality. It states that the shear-stress is proportional to the turbulent kinetic energy $k$, which is only valid in the boundary layer. Therefore a second blending function $F_2$ similar to the first one is used, which is set to one in the boundary layer:

$$F_2 = \tanh(arg_2{}^2) \tag{2.32}$$

$$with \quad arg_2 = max\left(\frac{2\sqrt{k}}{\beta'\omega y}, \frac{500\nu}{y^2\,\omega}\right) \quad. \tag{2.33}$$

## 2.3  Near-Wall Treatment

Simulating the internal flows in IC-engines the domain is bounded by solid surfaces like the cylinder wall or the piston, where no-slip conditions are applied. This means that both the tangential and the normal velocity components vanish at the wall. Far away from the wall there are free turbulent flows, modeled by the formulations mentioned above. The treatment of the near-wall region between is considerably different and is described in this section.

The near-wall region can be subdivided into two layers, the so-called viscous sublayer, where the flow is almost laminar-like, and the logarithmic layer, where turbulence dominates the mixing process. Between the viscous sublayer and the logarithmic layer is the so-called buffer layer defined. The formulation and numerical treatment of the equations in regions near to solid walls is an important issue, as the near wall treatment determines the accuracy of the wall shear stress and has an important influence on the development of boundary layers including the onset of separation. To model the flow near to a no-slip wall, typically two different approaches are used (Vieser et al. (2002)):

- the wall-function method and

- the low-Reynolds-number method.

In the wall-function approach, empirical formulae are applied for the sublayer region affected by viscosity that assume the mean flow velocity to be dependent on the distance from the wall, fluid density $\rho$, viscosity $\mu$ and the wall shear stress $\tau_w$. The logarithmic relation for the near wall velocity is given by:

$$u^+ \;=\; \frac{1}{\kappa} ln(y^+) + C \qquad with \quad y^+ = \frac{\rho \Delta y u_\tau}{\mu} \quad . \tag{2.34}$$

$u^+$ is the near wall velocity, $u_\tau = (\tau_w/\rho)^{1/2}$ is the friction velocity, $\Delta y$ is the distance from the wall and $y^+$ is the dimensionless distance from the wall. $\kappa$ denotes the von Karman constant and $C$ is a log-layer constant depending on the wall roughness. According to e.g. Versteeg and Malalasekera (1995) the application of this relation is restricted to values of $y^+$ between 30 and 300, which has to be considered for the near-wall grid resolution. In order to overcome this limitation, scalable wall functions are implemented for the $k$-$\varepsilon$ model in ANSYS CFX, where:

$$\tilde{y}^+ \;=\; max(y^+, Y^+_{lim}) \quad . \tag{2.35}$$

The limiting value of $Y_{lim}^+$ = 11.06 marks the intersection between the logarithmic and the linear profile (ANSYS (2006)). Thus, all mesh points are forced to lie outside the viscous sublayer.

For the $k$-$\omega$ based SST model, an automatic near-wall treatment is available including a low-Reynolds-number method where, in contrast to the wall-function method, the details of the boundary layer profile in the viscous sublayer are resolved. As a consequence the low-Re approach requires a very fine mesh in the near-wall zone. In order to avoid numerical instabilities and to lower the stringent requirements concerning the near-wall grid resolution, this approach shifts gradually between a viscous sublayer formulation and wall functions, based on the grid density.

# 3   Optimization Fundamentals

Finding optimal and robust solutions is a central issue when developing new products. Numerous optimization algorithms and methods have been developed according to the assigned task of optimization. In this Chapter an outline of optimization methods is given. In the framework of this thesis Evolutionary Algorithms (EAs), response surface methodology (RSM) and Design of Experiment (DoE) based methods are applied as optimization methods and are therefore explained in more detail. The basics concerning the sensitivity analysis are presented in the last part of this Chapter.

In a general form an optimization problem can be defined as:

$$minimize \; (f(\vec{x})) \quad , \tag{3.1}$$

where $f$ is the objective function and $\vec{x}$ denotes the set of optimization or design variables $x_i$. Usually the objective function is subjected to constraints, separating the feasible and infeasible region. These constraints are defined as equality and inequality constraints:

$$g_j(\vec{x}) = 0 \qquad j = 1, 2, \dots, J \quad , \tag{3.2}$$
$$h_k(\vec{x}) \leq 0 \qquad k = 1, 2, \dots, K \quad , \tag{3.3}$$

where $J$ and $K$ denote the number of equality and inequality constraints. Furthermore, the design space is limited by the upper and lower bounds, $x_i^{(U)}$ and $x_i^{(L)}$:

$$x_i^{(L)} \leq x_i \leq x_i^{(U)} \qquad i = 1, 2, \dots, n \quad , \tag{3.4}$$

where $n$ is the number of optimization variables. Hence, the purpose of solving an optimization problem is to find a set of design parameters $\vec{x}$ such that the objective function $f$ is minimized or maximized (according to $minimize \; (f(\vec{x})) = -maximize \; (-f(\vec{x}))$), while complying with all existing restrictions and limitations. In addition, it is normally intended to avoid local minima and to search for the global optimum. This is a rather complex task as there is no explicit criterion for an global optimum (Bäck (1996)). Thus, in the literature many algorithms have been proposed and discussed in detail to tackle the problem of pre-mature termination of the optimization in a local extremum (Deb (1995)).

## Multi-Objective Optimization

However, most real-world optimization problems involve more than one objective function, which have to be minimized or maximized simultaneously. Problems of this type are called multi-objective optimization (MOO) problems and can be defined analog to Equation 3.1 as:

$$minimize\ (f_m(\vec{x})) \qquad m = 1, 2, \ldots, M \quad , \tag{3.5}$$

where $M$ is the number of different objective functions. MOO problems are significantly different from single-objective (SOO) problems. Most often these multiple objectives are in conflict with each other, leading to the need to obtain a set of optimal solutions instead of one single optimum. In consequence, there is no best solution but different good compromises, as none of these solutions can be said to be better than the other. To find these different solutions, the principle of dominance can be applied, which compares all solutions to each other (Deb et al. (2000)). Non-dominated solutions are all of the same quality for an optimization. The set of non-dominated solutions is called Pareto-front (**Fig. 3.1**). The quality of a solution belonging to the Pareto-front (or Pareto-optimal set) can be improved with respect to a single criterion only by becoming worse with respect to at least one other criterion.
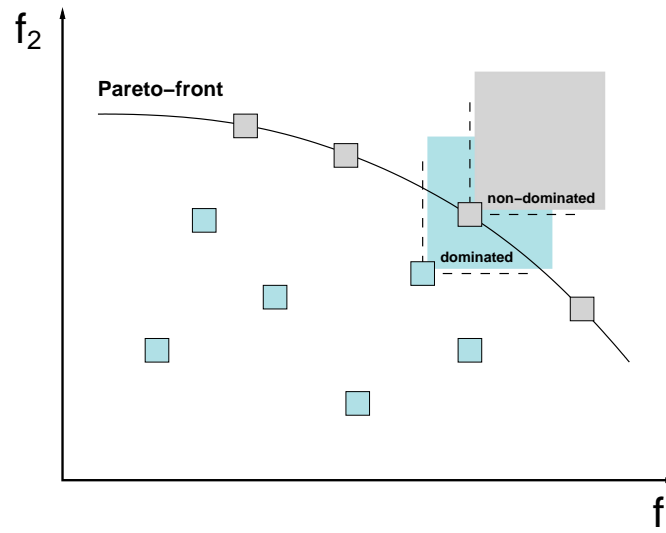


**Fig. 3.1:** Pareto-front of a maximizing problem gained by the principle of dominance.

Due to this fact there are two important goals in a multi-objective optimization (Deb (2001)):

1. to find a set of solutions as close as possible to the Pareto-front (convergence),

2. to find a set of solutions as diverse as possible (diversity).

As all solutions are equivalent concerning the quality, higher-level information is required to make a decision on the final solution (Deb (2001)), which usually leads to a compromise.

The simplest way to solve a multi-objective optimization problem is to scalarize it to a single-objective problem. This method is known as weighted sum method (Ehrgott (2005)). By pre-multiplying each objective with a weighting factor and summing the weighted objectives, a single-objective is obtained. However, the result is one Pareto-optimal solution only instead of the entire Pareto-front. In order to get the Pareto-front the optimization has to be performed

several times, while the particular weighting factors are varied. To determine appropriate factors is another difficulty of this method.

Therefore, optimization algorithms were developed (e.g. Schaffer (1984), Goldberg (1989)), which can deal with more than one objective. A general overview of optimization algorithms is given in the following section.

## 3.1   Overview of Optimization Methods

The large number of optimization methods makes it difficult to classify them adequately.
**Fig. 3.2** shows a very general overview where the main distinction is made between deterministic and stochastic methods (Dynardo (2008)). Deterministic methods apply well-defined operators, e.g. gradients derived from an objective function, in order to determine an appropriate search direction, while stochastic methods choose this direction by implying randomization.

Optimization Methods

Deterministic                                          Stochastic
Approach                                               Approach

*Gradient based*

*Quasi-Newton/*

*Newton methods*

*...*

Simulated                                          Evolutionary
Annealing                                          Algorithms

Evolutionary        Genetic        Evolutionary
Strategies        Algorithms      Programming
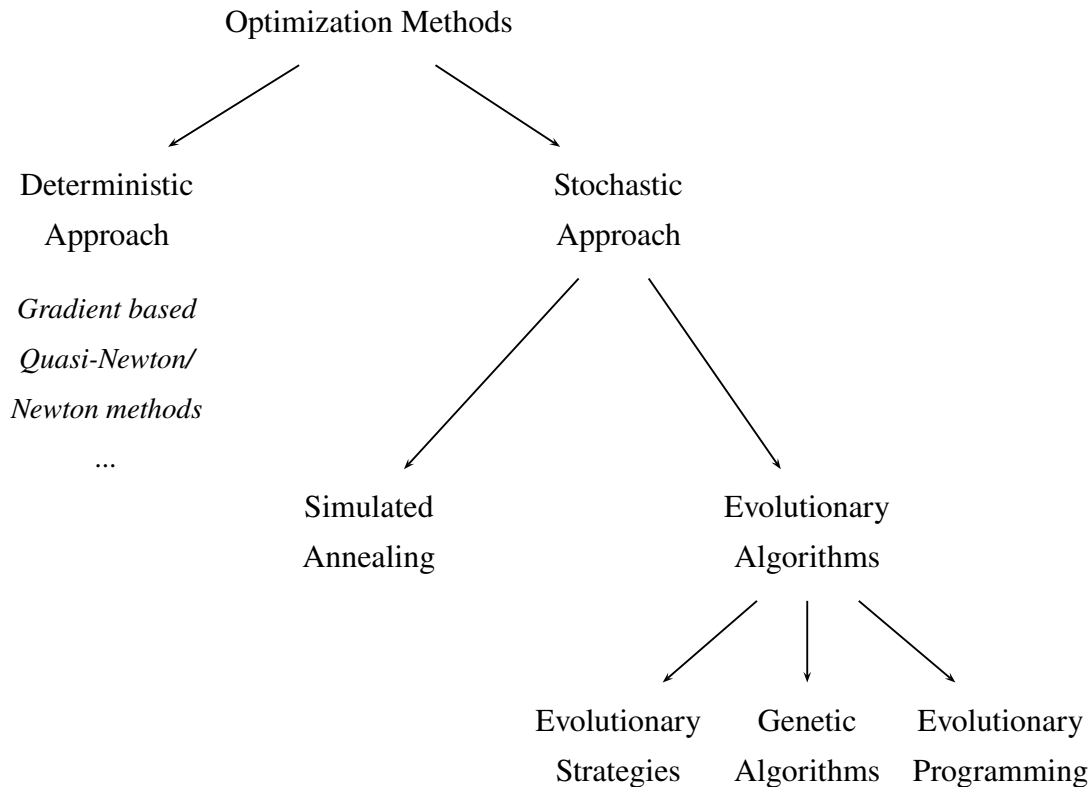
**Fig. 3.2:** Overview of deterministic and stochastic optimization methods.

### 3.1.1   Deterministic Methods

Deterministic methods can be classified into direct methods and gradient-based methods (Deb (1995)). While direct methods only evaluate the objective function itself, gradient-based methods involve first- and eventually second-order derivatives of the objective function to determine search direction and step size. Well-known gradient-based methods are the method of steepest descent, Newton- or Quasi-Newton methods. For example, to find the minimum of a function by using the method of steepest descent, steps proportional to the negative of the gradient of the function at the current point are taken according to:

$$\vec{S} = -\nabla f(\vec{x}) \quad , \tag{3.6}$$

where $S$ denotes the search direction. Depending on whether the gradient is obtained using analytical or differential gradients one differentiates between direct and indirect gradient-based methods. In order to use analytical gradients, the objective function has to be a mathematical term. Regarding numerical simulations (e.g. CFD) the objective function cannot be given analytically. Thus, the gradients normally have to be calculated using finite differences (Equation 3.7). A new approach is currently developed where the gradients are obtained by adjoint methods (Othmer (2006)).

$$\nabla f(\vec{x}) = \frac{f(\vec{x}+\vec{h}) - f(\vec{x})}{\vec{h}} \quad . \tag{3.7}$$

The new optimization vector $\vec{x}$ is obtained by:

$$\vec{x}_{k+1} = \vec{x}_k + \alpha \cdot \vec{S} \quad , \tag{3.8}$$

where $\alpha$ denotes the step size and $S$ the search direction. This procedure is repeated until the optimum is reached.

This approach is improved by using Newton methods as they additionally use the second derivative to obtain the search direction thus, depending on the specific problem, promising much faster convergence (Dynardo (2008)). The objective function $f$ is approximated by a second order Taylor series:

$$f(\vec{x}_{k+1}) \;=\; f(\vec{x}_k) + \nabla f(\vec{x}_k) \cdot \delta\vec{x} + \frac{1}{2}\delta\vec{x} \cdot H(\vec{x}_k) \cdot \delta\vec{x} \quad , \tag{3.9}$$

with

$$\delta\vec{x} = \vec{x}_{k+1} - \vec{x}_k = \alpha \cdot \vec{S} \quad and \quad H = \nabla^2 f(\vec{x}_k) \quad , \tag{3.10}$$

where $H$ denotes the Hessian matrix.

The search direction $S$ for the Newton method is:

$$\vec{S} = -[H(\vec{x}_k)]^{-1} \cdot \nabla f(\vec{x}_k) \quad . \tag{3.11}$$

According to Equations 3.9 and 3.11 the objective function is supposed to be twice-differentiable and the Hessian matrix has to be invertible. Due to this conditions the Newton method tend to be unstable and the solution may diverge. Furthermore, finding the inverse of the Hessian matrix may be an expensive operation that has to be performed for each iteration. Alternatively, Quasi Newton methods avoid all these problems by approximating the inverse Hessian matrix using

only first derivatives of two consecutive iterations. Very popular methods are Broyden-Fletcher-Goldfarb-Shanno (BFGS) and Davidon-Fletcher-Powell (DFP) (Thum (2007)).

However, all these deterministic methods do not meet the requirements for global multi-objective optimization problems. On the one hand the optimization may end up in a local optimum depending on the starting point and the objective function. On the other hand they can only deal with one single-objective function simultaneously. Furthermore, with a rising number of optimization variables the calculation of the gradients by finite differences becomes very expensive in the case of numeric simulations like CFD.

### 3.1.2  Stochastic Methods

In contrast to deterministic methods, stochastic methods do not use gradient information to obtain a particular search direction. Randomization is used to generate new possible designs and to avoid the convergence towards a local optimum. Furthermore, most of the stochastic methods deal with several designs simultaneously, which are combined to populations, instead of single designs. As a result, regarding CFD problems, the particular designs of a population can be calculated in parallel, which is an important advantage in terms of developing times. Typical stochastic methods are Simulated Annealing (SA) and Evolutionary Algorithms (EAs). Particularly Evolutionary Algorithms gained in importance in the last years due to their robustness (no derivatives needed), performance and universal applicability (Hammel and Bäck (1998)) concerning complex and time-consuming multi-objective and multi-disciplinary optimization problems (e.g. Duddeck (2008)). Precisely these properties qualify EAs for the integration into the engine development process where typically a large number of design parameters and objectives occur (Clement et al. (2004), Vajna et al. (2005)).

EAs are stochastic search methods based on a model of natural, biological evolution using the operators of mutation, recombination and selection (Bäck (1996)). Accordingly, in the context of EAs the particular designs are called individuals and a set of individuals is denoted as population. Starting from an initial set of individuals (parents) a new generation of individuals (offspring) is created by means of recombination and/or mutation. Due to the population-approach EAs are suitable for multi-objective optimization problems, as they can find and maintain multiple solutions in one single optimization run, which is a unique feature for evolutionary optimization techniques (Deb (2001)). Subsequently the best individuals are selected to serve as new parents. These randomly created designs are step by step guided towards the region of optimal solutions by means of selection. Therefore, EAs are also called "guided random"-methods.

The three different main stream algorithms concerning EAs are Evolutionary Strategies (Rechenberg (1973) and Schwefel (1981)), Evolutionary Programming (Fogel et al. (1966)) and Genetic Algorithms (Holland (1975) and Goldberg (1989)). All these methods are based on the evolutionary concept mentioned before. However, they differ in terms of initialization, fitness evaluation, mutation, recombination and selection (Bäck (1996)).

For the optimization problems discussed in the present work, commercial optimization tools containing an Evolutionary Algorithm and a Genetic Algorithm are used. The optimization tools applied are Optimus V5.2 from NOESIS (Noesis (2006)) and optiSLang V3.0 from DYNARDO (Dynardo (2008)), as they offer well established and tested Evolutionary Algorithms and enable the automation of the simulation process. In the subsequent section the general components of Evolutionary Algorithms are introduced and the applied algorithms are discussed in more detail.

## 3.2   Evolutionary Algorithms

As proposed by Bäck (1996) an Evolutionary Algorithm can be defined as:

$$EA = (I, \Phi, \Omega, \Psi, s, \iota, \mu, \lambda) \quad . \tag{3.12}$$

In the following a short description of this mathematical notation is given, while the most important components will be explained in more detail later.

- $I$ is the space all individuals (designs) $\vec{a}_i$ are in, called design space.

- $\Phi$ denotes a fitness function assigning real values to all individuals, which represents the quality of the particular individuals. Concerning an intake port problem this may be e.g. flow rate quality or tumble level. Based on these values all individuals (solutions) can be sorted and finally the most suitable can be selected.

- $\Omega$ is a set of probabilistic genetic operators $\omega_{\Theta_i}$, namely mutation $m_{\Theta_m}$ and/or recombination $r_{\Theta_r}$. These are applied to manipulate existing individuals and thus generate new individuals for the evolutionary search process. These operators are always probabilistic, which characterizes EAs as stochastic approaches in contrast to the deterministic methods mentioned above.

- $s$ denotes the selection operator, which is applied to select the most suitable parent individuals $\mu$ from the set of offspring individuals $\lambda$ in the case of $(\lambda, \mu)$ and offspring and parents in the case of $(\lambda+\mu)$, changing the number of individuals from $\lambda$ or $\lambda + \mu$ to $\mu$. Thus, the number of parents $\mu$, which is a crucial parameter for EAs, is kept to the desired number. The selection operator $s$ may be probabilistic or completely deterministic.

- $\iota$ is the termination criterion for the EA, which can be a maximum run time, a maximum number of individuals/generations or a measure for the relative improvement of the best objective function.

- $\Psi$ is the transition function, which symbolizes the complete transformation of a population $P_i$ into a subsequent one $P_{i+1}$ performed by applying genetic operators $\omega_{\Theta_i}$ and selection $s$.

A general outline of an Evolutionary Algorithm is illustrated in **Fig. 3.3**. Here, $t$ denotes the generation counter. Accordingly $P(t)$ is the population at generation $t$, containing the individuals $\vec{a}_i \in I$. The parent population size is given by $\mu$. $Q$ denotes an additional set of individuals (e.g. the parent population itself) that may be taken into account by selection.



**initialize** $P(0)) := \{\vec{a}_1(0), \dots, \vec{a}_\mu(0)\}$ *in* $I^\mu$

**evaluate** $P(0) : \{\Phi(\vec{a}_1(0)), \dots, \Phi(\vec{a}_\mu(0))\}$

**recombine**:
$P'(t) := r_{\Theta_r}(P(t))$

**select**:
$P(t+1) := s_{\Theta_s}(P''(t) \cup Q)$

**while** $(\iota(P(t)) \neq$ **true**$)$ **do**
$t = t+1$

**mutate**:
$P''(t) := m_{\Theta_m}(P'(t))$

**evaluate**:
$P''(t) : \{\Phi(\vec{a}''_1(t)), \dots, \Phi(\vec{a}''_\lambda(t))\}$
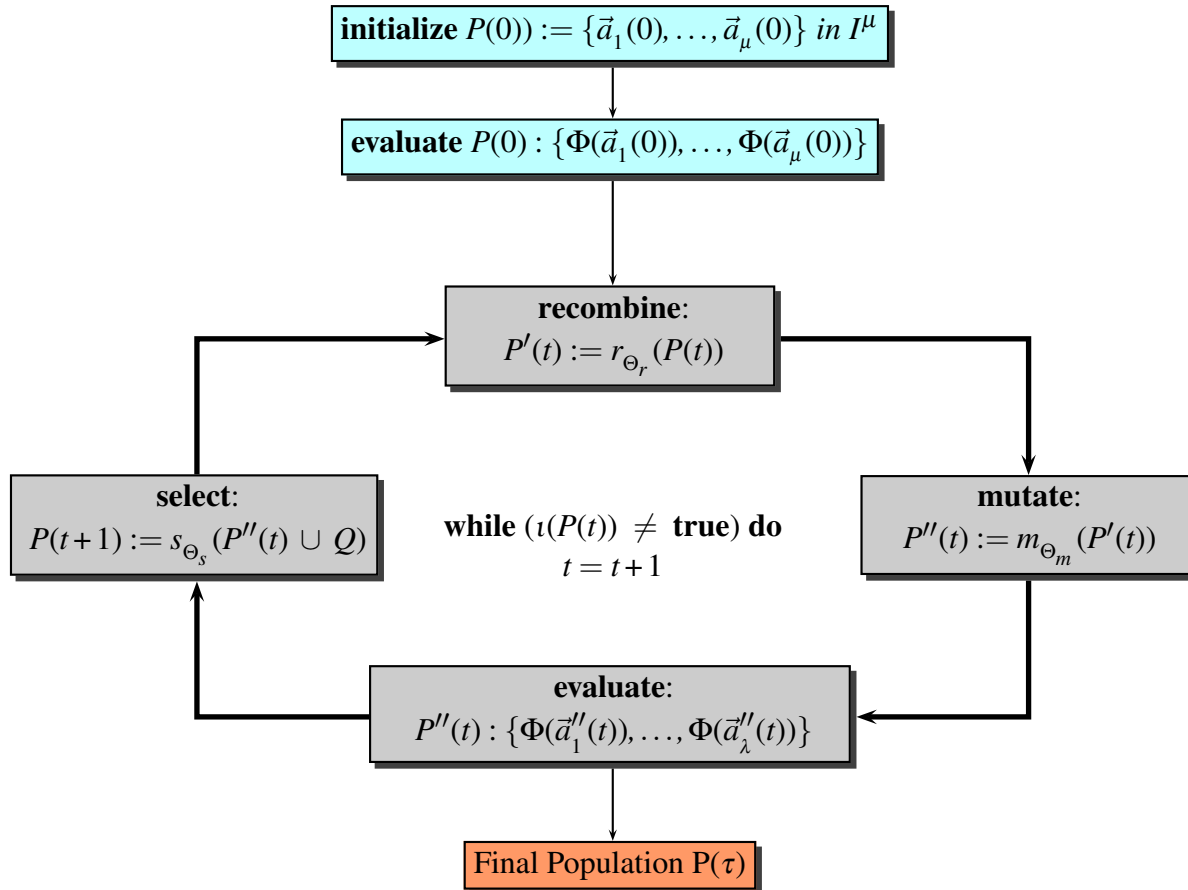
Final Population P($\tau$)

**Fig. 3.3:** General flowchart of an Evolutionary Algorithm (based on Bäck (1996)).

**Initialization**

The initialization of the start population $P(0)$ is the first step using an Evolutionary Algorithm and is usually performed randomly. The original implementation of Schwefel (1981) intended to derive the initial population from one single initial starting point by means of mutation. A suitable point may be the design, which should be optimized. By adapting the mutation parameters the initial spreading can be very local or rather global. Another possibility for creating the initial population is using DoE sampling methods, which are introduced in Section 3.3. By this, the whole design space is expected to be explored uniformly, thus building the basis for a broad spread among the final solutions.

**Evaluation**

The next step is to evaluate the particular individuals of the initial population. Concerning CFD-optimization the evaluation of the objective functions $f_m$ is supposed to be the most time-consuming step, as for each design a CFD simulation has to be performed. Based on the objective functions a fitness value is assigned to the particular designs.

Subsequently the loop of recombination, mutation, evaluation and selection is passed through for each particular generation $t$ until the termination criterion $\iota$ is reached.

**Mutation**

Regarding Evolutionary Strategies mutation is the main operator for creating new individuals, which distinguishes ESs from GAs and EP (Bäck (1996)). Mutation describes the process of varying several design parameters of an individual in order to generate a new offspring. According to observations from nature it is essential that smaller mutations occur more often than larger ones. Schwefel (1981) originally defined the mutation mechanism using normally distributed variables having an expectation value of zero and a given standard deviation $\sigma$, which is identical for all design variables. Therefore, the notation $N(0, \sigma)$ is used. Applying mutation with a specific probability (or mutation rate) $p_m$ to the design variables $x_i$ of an individual a new set of design variables $\vec{x}'$ is obtained:

$$\vec{x}' = \vec{x} + N(0, \sigma) \quad . \tag{3.13}$$

Hence, the standard deviation $\sigma$ determines the size of the mutation steps for all design parameters. The mutation rate $p_m$ and the course of the standard deviation $\sigma$ are often specified a priori. Typically, the standard deviation is decreased during the optimization run as the individuals are expected to get closer to the optimum region, requiring smaller step-sizes.

Of course, it is difficult to define appropriate values for $\sigma$ a priori without knowing the later optimization progress. A more sophisticated approach is to adapt $\sigma$ automatically according to the actual local topology of the objective function (Bäck (2006)):

$$\begin{aligned}
\vec{a} &= ((x_1, \ldots, x_n), \sigma) \\
\vec{\sigma}' &= \sigma \cdot \exp(\tau_0 \cdot N(0, 1)) \\
x_i' &= x_i + \sigma' \cdot N_i(0, 1) \\
\vec{a}' &= ((x_1', \ldots, x_n'), \sigma') \quad ,
\end{aligned} \tag{3.14}$$

where $\tau_0$ denotes the learning rate and $\sigma'$ is the adapted standard deviation. Thus, optimization not only takes place on design parameters, but also on strategy parameters like $\sigma$. This mechanism is known as self-adaption. According to Bäck (1996) a further improvement of this mechanism can be achieved by the application of particular standard deviations $\sigma_i$ for each design parameter $x_i$ .

**Recombination**

Apart from mutation EAs use recombination as operator. Similar to mutation a variety of different mechanisms are normally used. The general idea of recombination is to produce new offspring by copying and recombining information from different parent individuals. Recombination is intended to create individuals which benefit from advantageous segments of their parents. Thus, introducing recombination can lead to remarkable acceleration of the search process. While recombination is of less importance for Evolutionary Strategies it is the most important search operator for Genetic Algorithms (Bäck (1996)), where it is denoted as crossover. Crossover is often realized on a binary coding although real number crossovers are as well established.

The principle of crossover is schematically shown in **Fig. 3.4** on the basis of multipoint crossover. The operator randomly selects multiple points for crossover and divides the parent set of design variables (called chromosomes in GAs) into sections. The genes of the parents are exchanged at every second section. The traditional crossover introduced by Holland (1975) only contained a single crossover point called one-point crossover.
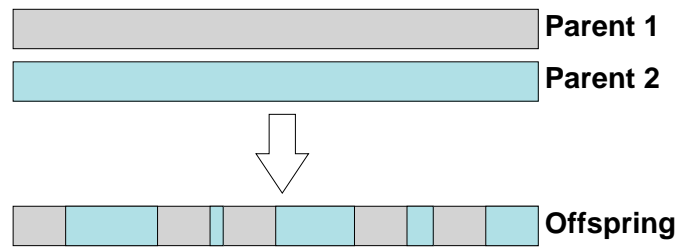


**Fig. 3.4:** Principle of multipoint crossover.

**Selection**

As mentioned before the selection operator may be probabilistic or deterministic. Concerning Evolutionary Strategies the selection operators are completely deterministic. Two different mechanisms exist differing in terms of basic method and numbers of parent ($\mu$) and offspring ($\lambda$) individuals respectively. In the case of ($\mu+\lambda$)-selection the $\mu$ best individuals are selected out of the union of parents $\mu$ and offspring $\lambda$ to form the next parent generation:

$$s_{(\mu+\lambda)} : I^{\mu+\lambda} \rightarrow I^{\mu} \quad . \tag{3.15}$$

As good solutions are strictly preserved, loss of optimality is not accepted and a monotonous behavior of improvement is guaranteed. However, the ($\mu+\lambda$)-selection may stagnate in a local optimum. Furthermore, it hinders the self-adaption mechanism (Bäck (1996)). To prevent this disadvantages, the ($\mu,\lambda$)-selection chooses the $\mu$ best individuals out of the offspring only:

$$s_{(\mu,\lambda)} : I^{\lambda} \rightarrow I^{\mu} \quad . \tag{3.16}$$

Thus, good solutions can be forgotten in principle which allows for leaving local optima. Of course, worsening can not be excluded.

In contrast, selection operators for Genetic Algorithms are based on probabilistic survival rules. Common methods are "roulette wheel" or "tournament selection" (Deb (2001)). Roulette wheel selection is based on the roulette wheel mechanism. Every individual of the population is represented by a division of a roulette wheel, where the division size is defined in proportion to the fitness of the particular individual. The wheel is spun and the solution indicated by the pointer is selected. This process is repeated until the desired number of individuals is obtained.

In the case of tournament selection for each tournament a specified number (tournament size) of individuals is randomly chosen out of the selection pool ($\mu$ or $\mu+\lambda$) and the fittest design is selected to survive. As for roulette wheel selection, the tournament is repeated until the desired number of parent individuals is reached.

**Fitness evaluation**

As mentioned in Section 3.1 the goal of a multi-objective optimization is to find a Pareto-optimal set, which is as diverse as possible. To comply with this requirement every individual is assigned a fitness value, by means of which a ranking is performed. This ranking is important, if there are more optimal solutions than parents actually needed. Using this ranking, the fittest solutions can be identified and selected.

Usually, the fitness value $F_i$ is splitted into the strength $S_i$ and a measure for the diversity $D_i$. The strength $S_i$ is proportional to the number of solutions a individual dominates or is dominated by, respectively. Concerning diversity several approaches exist. In general the goal is to estimate the density of solutions surrounding a design. One possibility is to calculate the average distance of two points on either side of the particular solution point along each of the objectives. Deb et al. (2000) denotes this quantity as crowding distance. In **Fig. 3.5**, the crowding distance is
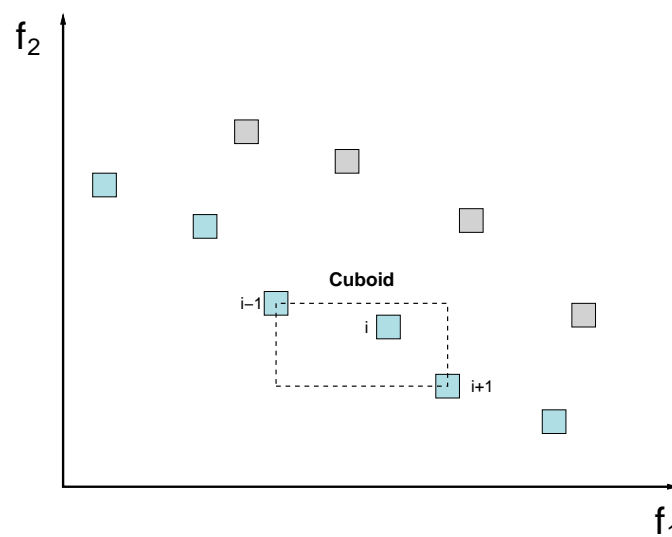


**Fig. 3.5:** Crowding distance calculation for a maximizing problem based on Deb et al. (2000) .

illustrated as the average side-length of the cuboid (shown as dashed box). A large crowding distance indicates a low density of solution points around the particular individuum $i$ and thus a high degree of diversity. Finally, a solution is of high quality (or fitness) if it dominates several other solutions and has a large distance to its surrounding neighbors.

### 3.2.1  Evolutionary Strategy

The ClearVu Global Optimizer for Optimus (NuTech (2005)) from NuTech Solutions is selected as representative of an Evolutionary Strategy. This algorithm is based on the explicit diversity-preserving mechanism of the Non-Dominated Sorting Genetic Algorithm II (NSGA-II) from Deb et al. (2000). Furthermore, a self-adaption mechanism is applied to enable automatic adaption of the search parameters and thus ensure an efficient optimization process.

In order to adapt the algorithm to a specific optimization problem several parameters are provided (**Table 3.1**). The initialization is performed either by distributing the individuals uniformly in the design space (problem initialization=0) or by deriving a population starting from one particular design (problem initialization=1). In the case of a single starting point the offspring of the initial generation are created by applying mutation with a predefined initial standard deviation, which can be varied in the range of 0 (small distribution) to 3 (wide distribution). Concerning the number of offspring, Bäck (1996) recommends a ratio of $\mu/\lambda \approx 1/7$ as optimal for the acceleration effect of self-adaption. Furthermore, $\mu$ should be chosen clearly larger than one.

| *Parameter* | *Value* |
|---|---|
| Number of parents $\mu$ | $1 \dots 3$ |
| Number of offspring $\lambda$ | $7 \dots 20$ |
| Number of evaluations | $10 \dots 12 * \lambda$ |
| Initial search distribution | 0 / 1 / 2 / 3 |
| Problem initialization | 0 / 1 |
| Include reference point | 0 / 1 |
| Selection mechanism | $(\mu,\lambda)$, $(\mu+\lambda)$ |

**Table 3.1:** Settings for the NuTech CVE-algorithm in Optimus (NuTech (2005)).

Subsequently, the fittest $\mu$ individuals are selected as parents for the next generation, where the fitness is evaluated as suggested for the NSGA-II. At first a non-dominated sorting is applied for classification. According to their level of non-domination all solutions are distributed to different fronts. If an individuum is not dominated by any other it is classified into level 1, if it is dominated by one it is classified into level 2, and so on. The best non-dominated fronts are gradually selected as parents. If the number of solutions of a front exceeds the number of required parents, a criterion for preserving diversity is applied. Therefore, the crowding distance is calculated analogously to **Fig. 3.5**. Solutions with a large crowding distance are then preferred

as parents. Thus, the selection of parent individuals is deterministic. Concerning the selection operator, both $(\mu+\lambda)$- as well as $(\mu,\lambda)$-strategy are available.

For the following generations new offspring are created from the parent population exclusively by mutation. In order to define appropriate mutation parameters self-adaption is included. Thus, standard deviation and mutation rate are adapted for every optimization variable separately.

Finally, the termination criterion for the optimization run is a selected number of individuals.

### 3.2.2   Genetic Algorithm

The Genetic Algorithm applied for this thesis is the Strength Pareto Evolutionary Algorithm 2 (SPEA2) from Zitzler et al. (2001) implemented in optiSLang. This algorithm is characterized by a specialized method to preserve diversity and the use of an external population $\bar{P}$ serving as pool to select the parents for reproduction from.

In contrast to the ClearVu Global Optimizer above, the algorithm starts with a user-defined or a randomly created population $P_0$, typically using a DoE sampling method (Section 3.3). All individuals of $P_0$ are copied to the empty external archive $\bar{P}_0$. In the following, new individuals are created by applying mutation and recombination. The implemented mutation mechanism does not use a self-adaption mechanism. Instead, the parameters for mutation rate and standard deviation are defined at the beginning of the optimization run. The default values suggested in Dynardo (2008) are listed in **Table 3.2**. Mutation rate is set to 0.1, denoting a mutation probability of 10 %. Standard deviation decreases from 0.1 at the beginning to 0.01 at the end of the optimization run thus leading to a iterative refinement of the step-size, which assumes that the optimization converges towards the Pareto-front at the end. In terms of recombination so called simulated binary crossover is implemented. A detailed description of this method can be found in Deb and Agrawal (1994).

| *Parameter* | *Value* |
|---|---|
| Population / archive size | 20 |
| Number of parents | 10 |
| Number of generations | $\geq 10$ |
| Tournament size | 2 |
| k-th neighbor | 2 |
| Crossover probability | 0.50 |
| Mutation rate | 0.10 |
| Standard deviation | 0.10 (start) ... 0.010 (end) |
| Selection mechanism | $(\mu+\lambda)$ |

**Table 3.2:** Settings for the Pareto-algorithm in optiSLang (Dynardo (2008)).

For every new generation, newly found non-dominated solutions are compared with the members of the external population $\bar{P}$. According to their fitness value the best individuals enter the external population by removing worse samples. Criteria for the strength and the diversity are used to assign a fitness value. Strength is measured according to the number of dominated individuals. In order to preserve diversity, solutions in less crowded regions are preferred. Therefore, the distance of an individual to its $k$-th nearest neighbor serves as an estimator of density. Accordingly, large distances to the $k$-th neighbor lead to higher fitness.

The parents for the next generation are selected out of the external population $\bar{P}$ by means of tournament selection. This mechanism of creating new individuals is repeated until the desired number of generations is reached.

## 3.3 Design of Experiment

Design of Experiment (DoE) is a method to generate an appropriate set of sampling points within a given design space. According to Dynardo (2008) DoE methods can be divided into systematic and stochastic schemes, depending on whether the sampling points are distributed systematically or random-based. **Fig. 3.6** shows an example for each scheme, respectively.



**(a)** Full factorial design   **(b)** Latin hypercube sampling
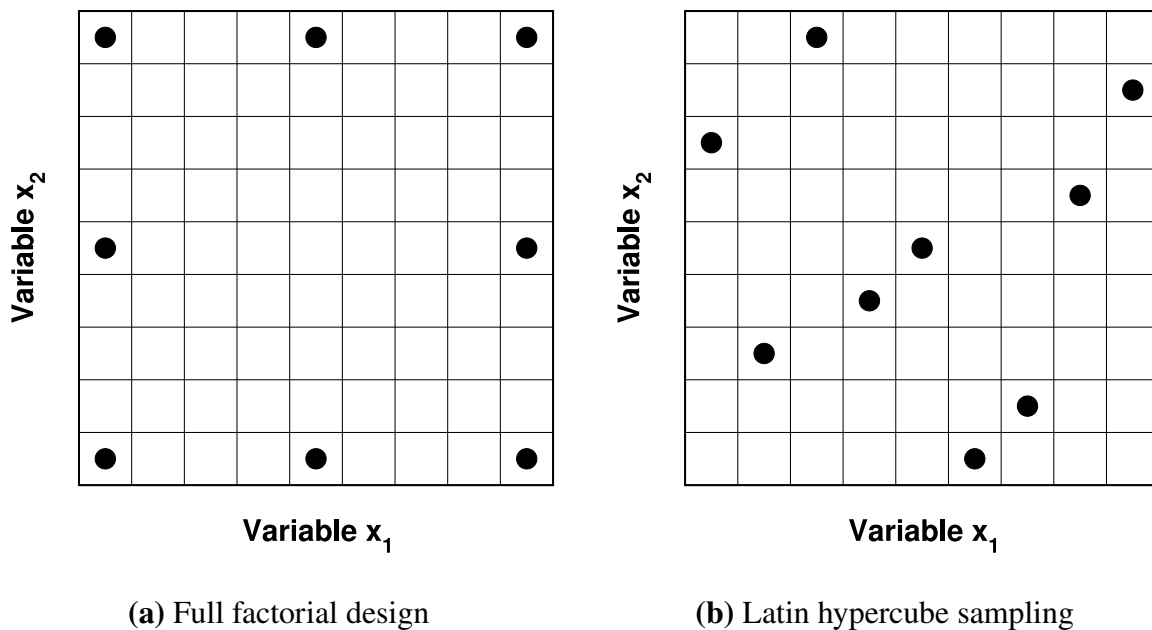
**Fig. 3.6:** Full factorial design (a) and latin hypercube sampling (b).

Full factorial design is a classical systematic method (**Fig. 3.6(a)**). For each design variable $x_i$ ($i = 1 \ldots n$) $m$ sample points are created, thus producing $n^m$ points. Usually $m=2$ or $m=3$ is implemented, where $m=2$ includes the maximum and minimum value of $x_i$ and $m=3$ additionally the average. Obviously, this method is strictly limited to problems with a low number of design variables as the number of sampling points increases rapidly according to $n^m$.

Concerning stochastic sampling schemes, Monte Carlo and latin hypercube sampling (LHS) are well-established methods implemented in various engineering tools. Primarily LHS is applied as it is qualified to reduce the number of sampling points significantly (Bucher (2005)). Using latin hypercube sampling the design space is subdivided into $N$ classes of the same probability, where $N$ denotes the number of desired sampling points. Thus, $N^n$ hypercubes are created. Subsequently, one representative value is randomly assigned to each class (**Fig. 3.6(b)**).

DoE methods are used for a variety of applications, e.g. for Evolutionary Algorithms to create the initial population or for Response Surface approximations to deliver a set of supporting points. Moreover, plain DoE methods may be used for the task of optimization as well. However, as they do not apply any mechanism to guide the search process their efficiency is quite poor leading to a high number of evaluations.

## 3.4   Response Surface Methodology

Concerning engineering applications computational times are usually very high. Especially in the context of CFD-optimization it is a crucial aspect. Therefore, one is interested in substituting the simulation procedure by meta-models, which approximate the physical behavior of a system. The relationship between the input parameters $x_i$ and the output parameter $y$ may be approximated by a mathematical expression $f$:

$$y = f(x_1, x_2, \ldots, x_k) + \varepsilon = \hat{y} + \varepsilon \quad , \tag{3.17}$$

where $\varepsilon$ denotes the approximation error and $\hat{y}$ the meta-model. The great benefit is that $f$ can be evaluated easily and fast compared to the simulation. To create the mathematical model, a suitable set of sampling points obtained from a DoE evaluation is used. The number of necessary supporting points depends on the number of input parameters and the mathematical model type.

In practice, polynomial functions are most widely used for setting up a meta-model. This models are known as response surface models. In order to obtain the response surface the technique of regression analysis is often applied. First order and second order models are commonly used in response surface methodology (RSM). In general, the first-order model is (Myers and Montgomery (2002))

$$\hat{y} = \beta_0 + \beta_1 x_1 + \beta_2 x_2 + \ldots + \beta_k x_k \tag{3.18}$$

and the second-order model is

$$\hat{y} = \beta_0 + \sum_{j=1}^{k} \beta_j x_j + \sum_{j=1}^{k} \beta_{jj} x_j^2 + \sum_{i<j=2}^{k} \beta_{ij} x_i x_j \quad , \tag{3.19}$$

where $x_j$ denotes the regressor variables and $\beta_j$ the regression coefficients. To estimate the regression coefficients (called model fitting) the method of least squares is typically used, which minimizes the sum of the squares of the errors, $\varepsilon_i$. Concerning a linear regression model the least square function is:

$$L = \sum_{i=1}^{n} \varepsilon_i^2 = \sum_{i=1}^{n} \left( y_i - \beta_0 - \sum_{j=1}^{k} \beta_j x_{ij} \right)^2 \quad . \tag{3.20}$$

This function has to be minimized with respect to $\beta_0, \beta_1, \ldots, \beta_k$. Hence, the value of $L$ is a measure for the model quality. Dividing by the number of sampling points $n$ this leads to the root mean squared error RMSE:

$$RMSE = \sqrt{\frac{1}{n} \sum_{i=1}^{n} (y_i - \hat{y}_i)^2} \quad . \tag{3.21}$$

Apart from this the coefficient of determination $R^2$ and the adjusted $R_{adj}^2$ coefficient are used for model assessment. $R^2$ is defined as:

$$R^2 = \frac{\sum_{i=1}^{n} (\hat{y}_i - \bar{y})^2}{\sum_{i=1}^{n} (y_i - \bar{y})^2} \quad , \tag{3.22}$$

where $\bar{y}$ is the mean value of the output parameters $y_i$. $R^2$ is a measure for the variance of the meta-model responses, depending on the regressor variables. The coefficient of determination represents the percentage of the data that is closest to the regression model best fit (Dynardo (2008). It ranges between 0 and 1. However, adding a variable to the model always increases $R^2$, even though the variable is not significant. Thus, a large value of $R^2$ does not necessarily imply that the regression model is a good one.

To overcome this problem $R_{adj}^2$ is a suitable measure:

$$R_{adj}^2 = 1 - \frac{n-1}{n-p} (1 - R^2) \quad , \tag{3.23}$$

with $p$ being the number of regression coefficients. A great difference between $R^2$ and $R_{adj}^2$ indicates that non significant terms have been included in the model (Myers and Montgomery (2002)). One should definitely avoid this, as the number of sampling points $n$ increases with the number of regression variables $k$. For a full model based on a polynomial function the number of required samplings accounts to:

$$n = \prod_{i=1}^{m} \frac{k+i}{i} \quad, \tag{3.24}$$

where $m$ denotes the degree of the polynomial function.

Using meta-models for optimization purposes the crucial factor besides the required number of sampling points is the model's prediction quality. A large number of samples will lead to a high quality of the response surface, but increases the computational effort. In order to solve this conflict, Blumhardt (2001) suggested to calculate the response surface stepwise on the basis of regression analysis. Thus, terms with little influence are neglected decreasing the required number of samples. During the calculation of the model the representation quality is controlled by so called cross-validation. One part (e.g. 80%) of the DoE samples is used to generate the response surface, while the other part is used to validate the accuracy of forecast. This cross-validation is performed five times in each case. Finally, the best performing model is selected.

Apart from response surface methodology there are further approaches for developing meta-models like Support Vector Machines, Neural Networks, Kriging or decision trees. These techniques are taken into account by ClearVu Meta-Modeling from NuTech Solutions, where tenfold cross-validation and several criteria are implemented to assess the model's prediction quality (Ganser et al. (2007)).

## 3.5 Sensitivity Analysis

Apart from using DoE methods for optimization, primarily in combination with response surface methodology, they can be used for the purpose of analyzing parameter sensitivity. By means of a sensitivity analysis relevant correlations between the input and output variables are identified, thus establishing better understanding for the optimization problem. Furthermore, by neglecting non-relevant parameters the complexity of an optimization problem can be reduced.

For the analysis of correlation various statistical measures exist. Most commonly linear and quadratic correlations are regarded, represented by the linear and quadratic correlation coefficients, respectively. The linear correlation coefficient $r_{xy}$ is defined as (Bartsch (1999))

$$r_{xy} = \frac{\sum_{i=1}^{n} (x_i - \bar{x})(y_i - \bar{y})}{\sqrt{\sum_{i=1}^{n} (x_i - \bar{x})^2 \sum_{i=1}^{n} (y_i - \bar{y})^2}} \quad. \tag{3.25}$$

This correlation coefficient measures the strength (or exactness) of a linear relationship as well as the direction. It ranges between $-1 \leq r_{xy} \leq 1$. For a positive coefficient the values

of $y_i$ increase with increasing $x_i$ and vice versa, while for a negative value $y_i$ decreases with increasing $x_i$.

In order to obtain the quadratic coefficients, a quadratic relation between the input parameters $x_i$ and the output parameters $y_j$ is assumed (Dynardo (2008)). A quadratic regression model in analogy to Equation 3.19 is applied:

$$\hat{y}_j = \beta_0 + \sum_{i=1}^{k} \beta_i x_i + \sum_{i=1}^{k} \beta_{ii} x_i^2 = f(x_i) \quad , \tag{3.26}$$

where $\hat{y}_j$ is a function of $x_i$. Hence, the correlation coefficient between the fitted value $\hat{y}_j$ and the corresponding actual value $y_j$ can be calculated analogously to Equation 3.25:

$$r_{xy} = \frac{\sum\limits_{i=1}^{n} (\hat{y}_j - \bar{y})(y_j - \bar{y})}{\sqrt{\sum\limits_{i=1}^{n} (\hat{y}_j - \bar{y})^2 \sum\limits_{i=1}^{n} (y_j - \bar{y})^2}} \quad , \tag{3.27}$$

where a strong linear correlation, indicated by a high value of $r_{xy}$, confirms the assumption of a quadratic relation. The value for the quadratic correlation coefficient ranges between $0 \leq r_{xy} \leq 1$.

As a rule of thumb, an absolute correlation value greater than 0.7 indicates a strong correlation, whereas a value lower than 0.3 indicates a weak or negligible correlation (Dynardo (2008)). However, applying this rule it is important to consider the significance of the correlation coefficient (statistical significance). This means to assess whether the observed correlation represents the real physical behavior or results from mere coincidence (Lowry (2010)). The probability that the correlation results from mere coincidence can be determined by means of a null hypothesis. For a significant correlation coefficient this probability should typically fall below 5%. Especially for problems with high computational-effort like CFD-Optimization statistical significance is a critical issue, as only a very limited number of samplings can be examined.

Another important statistical measure concerning correlation coefficients is the confidence interval. It denotes the range in which the true correlation value is expected to be enclosed with a certain probability, commonly 95%. A definition for the confidence interval can be found in Bucher (2009).

In addition to the linear and quadratic correlation coefficient the coefficient of determination $R^2$ (Equation 3.22) is often used as it is an indicator for the exactness of the linear or quadratic regression model.

# 4 In-Cylinder Flow in IC-Engines

The gas motion within the cylinder (charge motion) is one of the major factors that controls the combustion process in internal combustion engines, both for compression ignition (CI) engines and spark ignited (SI) engines (Heywood (1988)). Consequently, the layout of the in-cylinder charge motion is an essential part in the framework of the engine development process and has to be adapted to the particular combustion system, respectively. In the first part of this chapter the characterization as well as the influence of charge motion on mixture preparation, combustion and cylinder filling are discussed. The second part describes CFD based methods for the analysis of the in-cylinder flow, ranging from simplified steady state approaches up to transient simulations of the charge cycle.

## 4.1 In-Cylinder Flow Patterns

Nowadays multi-valve technology is clearly state of the art, thus providing substantial potential for the in-cylinder flow design. During the intake phase the in-cylinder flow is mainly influenced by the intake ports, the combustion chamber design and valve timing. Later on, during the compression stroke it is affected by the combustion chamber and the piston design. Hence, special attention has to be given to the design of the cylinder head and the piston.

The vortices generated by the incoming air flow have dimensions of the order of the cylinder diameter (bore). According to their rotational axis they can be divided into two fundamental types, swirl and tumble. Swirl is the rotation around the cylinder axis, generally the z-axis, while tumble is the rotational motion perpendicular to the cylinder axis, accordingly the x- and y-axis (**Fig. 4.1**). This strict differentiation is rather theoretical as for the real air flow inside a
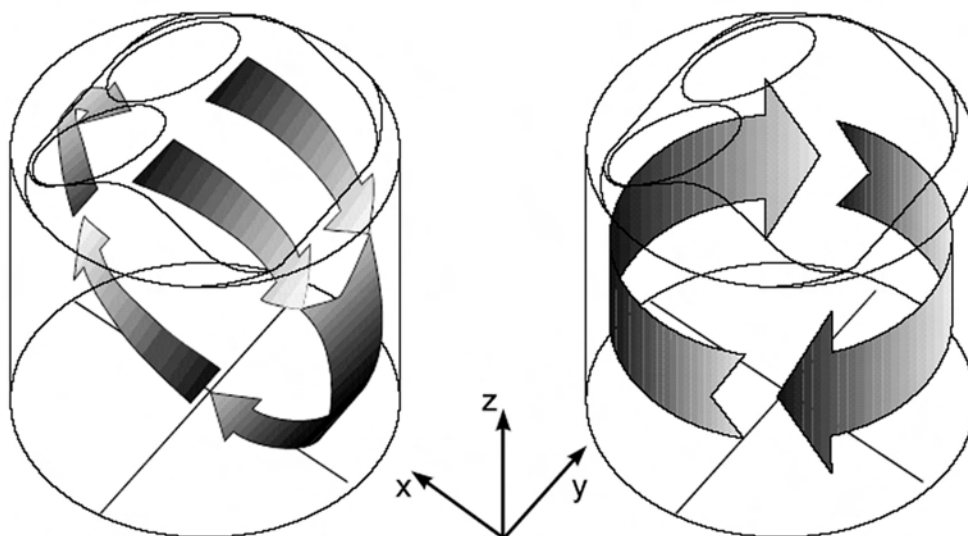


**Fig. 4.1:** Tumble and swirl flow patterns (Arcoumanis (1988)).

combustion engine tumble and swirl patterns often occur simultaneously. Nevertheless, modern combustion systems are usually based on one dominating flow pattern.

For direct injection diesel engines commonly swirl flow structures are applied to assure rapid fuel air mixing (Mollenhauer and Tschöke (2007)). The generation of swirl is mainly obtained by the intake port geometry. Helical ports are used to introduce a pre-swirl to the flow, while excentric positioned directed ports induce a rotational motion inside the cylinder. Another method for multi-valve engines is port or valve deactivation, where one of the intake ports or intake valves respectively is closed resulting in a swirl motion of the air inside the cylinder. Using a variable valve lift system swirl can be induced by means of different lifts, where one valve remains almost closed. This technique is known as phasing (Eichlseder et al. (2007)). In general, unlike tumble the induced swirl motion remains until the end of compression.

Tumble flow structures in contrast are the dominant flow pattern concerning SI-engines. Likewise swirl the in-cylinder tumble motion is primarily generated by the intake ports. By means of the intake port design an unequal distribution of the inlet air flow over the valve head is obtained. A large amount is guided over the front part of the intake valve thus directing the air flow towards the combustion chamber dome and the cylinder liner resulting in the vortex generation. This effect is intended also by active tumble systems, where a switchable port flap closes the lower half of the intake port in order to force the air along the upper part of the intake port. Another tumble generating method particularly applied for variable valve lift systems is valve masking (Eichlseder et al. (2007)), where the backside of the intake valve is covered and the air guided over the front part.

According to Wurms (1994) the initial tumble formation can be divided into three different phases (**Fig. 4.2**). For small valve lifts the flow is distributed more or less equally over the
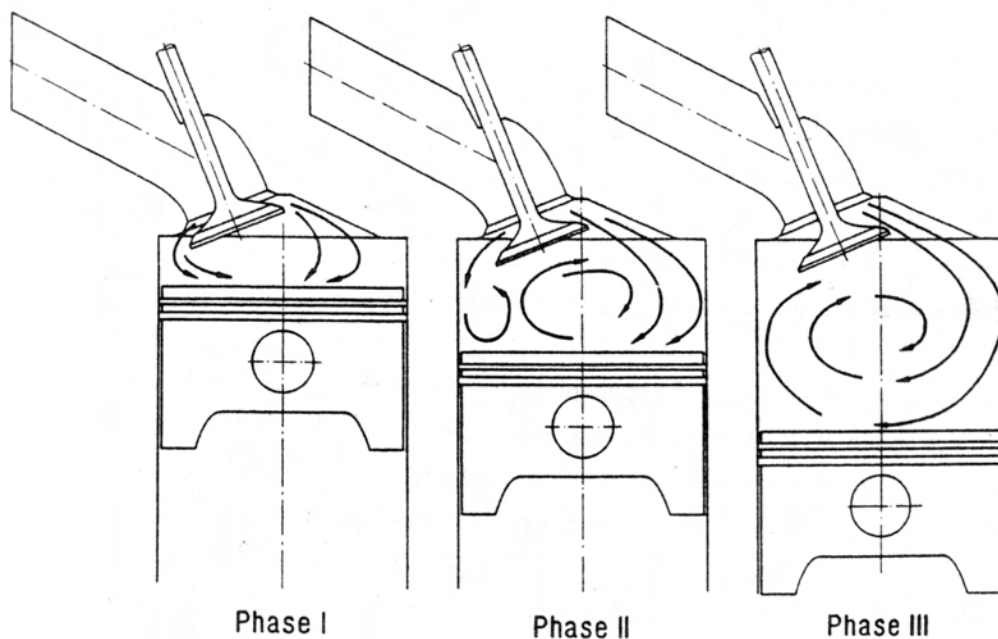


**Fig. 4.2:** Formation of tumble flow (Wurms (1994)).

intake valve (phase I). With rising valve lifts the air flow tends towards the front part of the valve gap due to inertia (phase II). Inside the cylinder it is redirected to the cylinder head by means of the cylinder liner and the piston. Finally, for large valve lifts flow separation occurs in the valve seat area forcing almost the total air over the top of the intake valves and through the front part of the valve gap (phase III). During this process the weak vortex at the beginning of induction is amplified by the piston motion until bottom dead center (BDC). The high mass flow rate in the region of maximum valve lift leads to a maximum of the tumble motion, before it decreases by closing the intake valves (**Fig. 4.3**). However, during compression the tumble motion is further intensified by the upward motion of the piston. Due to the conservation of angular momentum the rotating velocity increases as the specific volume and thus the lever arm is reduced. At the end of compression the further decreasing cylinder volume leads to the tumble decay into smaller and even smaller vortices. Thus, the tumble is dissipated as the turbulent kinetic energy is raised - according to the Kolmogorov energy cascade (Kolmogorov (1941)). The magnitude of the tumble motion and the intensification of turbulence is mainly controlled by the intake port and combustion chamber geometry. The persistence of the tumble vortex and the decay into turbulent kinetic energy strongly depends on the geometry of the piston and the combustion chamber dome (Das and Dent (1995)).
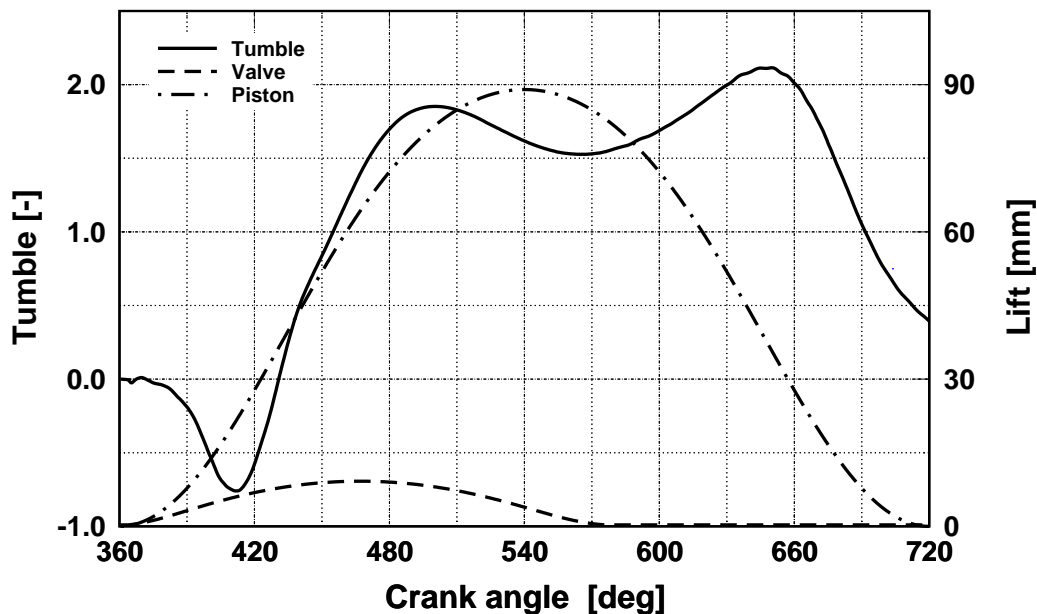


**Fig. 4.3:** Predicted tumble development during intake and compression stroke for the eight-cylinder SI-engine '8CBasis' (**Table A.1 (p.139)**) at 6000 rpm.

## 4.1.1   Mixture Preparation

As in any case of combustion the existence of an ignitable mixture of air and fuel is required, where good homogenization is essential for a complete combustion with low emissions. For direct injecting SI-engines the mixture preparation takes place inside the cylinder, which means having less time for the charge preparation compared to port injection engines, where mixture

preparation already starts inside the intake ports. In addition, fuel-spray atomization by means of high velocities and high turbulence intensity at the intake valves, which significantly impacts mixture homogenization at PFI (Lenz (1990)), misses for direct fuel injection. Hence, mixture preparation is a critical point for DISI-engines, especially for high loads and speeds (Gold et al. (2001)). Beneath optimized injection parameters like injection timing and pressure, charge motion is a another suitable measure to improve fuel evaporation and homogenization. The raised fluid velocities and the highly 3-dimensional flow structures accelerate the mixing process and the charge is more uniformly distributed inside the cylinder. Moreover, charge motion leads to increased turbulence during the intake stroke due to drag forces between inlet jet, cylinder charge and fuel spray resulting from higher relative velocities. This turbulence enhances fuel evaporation within the cylinder as mass- and heat transfer rise due to smaller droplets with accordingly larger surface (Lauer (2007)).

In addition, charge motion is applied for critical operating points such as cold start or idling (Lenz (1990)), where emissions and cycle-to-cycle variations are of special interest. Lee et al. (2000) show significant improvements of the cold start performance in terms of the accumulated hydrocarbons by means of a tumble system due to better fuel vaporization and fuel-air mixing. According to Fischer (2004) cycle-to-cycle variations resulting from cyclic fluctuations of the air-fuel distribution can be decreased by adapting the in-cylinder flow. Nevertheless, unsuitable in-cylinder flow patterns can also lead to inhomogeneous mixture or unrequested stratification (Section 6.3.2).

## 4.1.2   Combustion Process

Besides mixture preparation charge motion highly affects the combustion process. Combustion in homogeneous charge SI-engines is initiated as the mixture is ignited by a spark forming a laminar kernel at first. This kernel develops into a turbulent flame, which grows nearly spherical until it reaches the combustion chamber walls (Peters (2000)).

In a laminar premixed homogeneous air-fuel mixture the flame front propagation depends on various parameters such as fuel and oxidizer composition, fresh gas temperature and pressure, respectively. Accordingly, the propagation speed $s_L$ is called laminar burning velocity. According to Göttgens et al. (1992) the thickness of the laminar flame $l_F$ can be determined by:

$$l_F = \frac{(\lambda/c_p)_0}{(\rho s_L)_u} \quad , \tag{4.1}$$

where $\lambda$ is the heat conductivity and $c_p$ the heat capacity at the inner layer temperature $T_0$, while $\rho$ is the density and $s_L$ the laminar burning velocity defined in the unburned mixture.

In a turbulent homogeneous air-fuel mixture the flame propagation is influenced by the interaction of turbulence with the flame front. This interaction can be described by the relations of $l_t/l_F$ and $v'/s_L$, where $l_t$ denotes the turbulent length scale and $v'$ the turbulent intensity related to the square root of the turbulent kinetic energy. According to Peters (2000) the turbulent burning velocity $s_T$ can be expressed by means of this relation:

$$\frac{s_T}{s_L} = 1 - \alpha\frac{l_t}{l_F} + \sqrt{\left(\alpha\frac{l_t}{l_F}\right)^2 + 4\alpha\frac{v'l_t}{s_L l_F}} \qquad \alpha = 0.195 \quad . \tag{4.2}$$

**Fig. 4.4** shows the correlation between the ratio of the turbulent flame velocity to the laminar flame velocity and the turbulence intensity on the basis of a six-cylinder turbocharged SI-engine. The turbulent flame velocity rises with higher speeds, as the turbulence intensity varies almost proportionally to the engine speed (**Fig. 4.4(a)**). Higher turbulence intensities expressed by turbulent kinetic energy lead to a wrinkling of the flame front thus increasing its surface. As a result faster propagation of the flame front is achieved as a larger amount of mixture is captured. However, the gradient of the turbulent burning velocity decreases with increasing turbulence intensity (**Fig. 4.4(b)**). Hence, the acceleration of the flame front due to increasing turbulence intensity is reduced and the burning duration does not scale inversely proportional with the engine speed (Linse et al. (2009)).



**(a)** Turbulence intensity                    **(b)** Burning speed
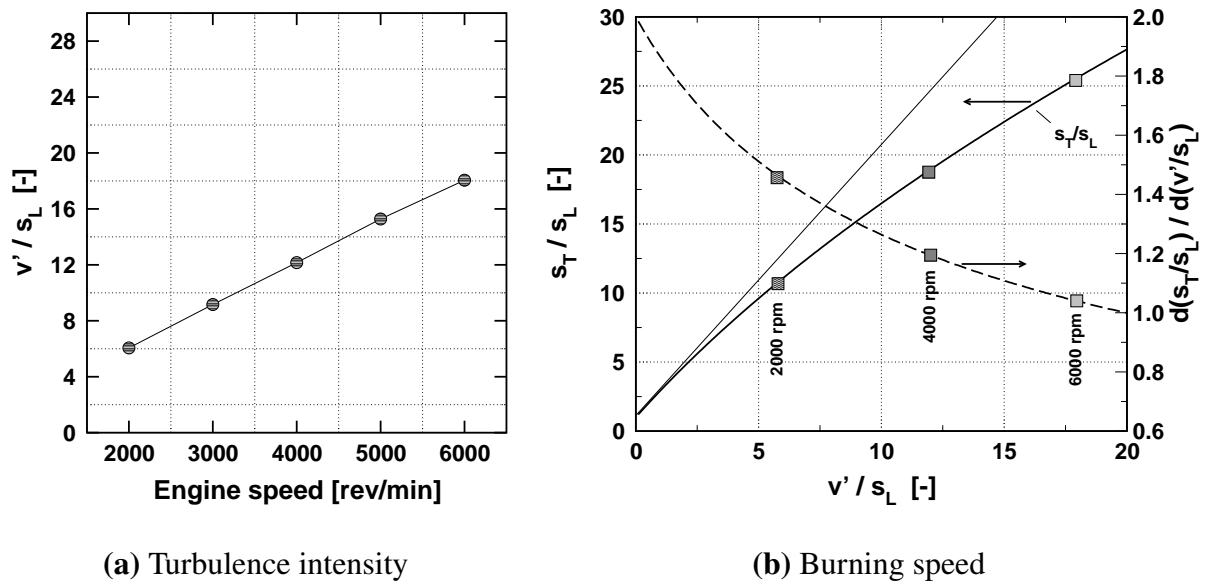
**Fig. 4.4:** Variation of the characteristic velocity scales of turbulence and flame (a) and variation of burning speed with turbulence intensity (b) for a speed variation at BMEP=10 bar (Linse et al. (2009)).

In order to induce turbulence, both swirl and tumble are suitable measures. Swirling flows lead to a quick growth of the flame kernel at the beginning of combustion shortly after ignition and by that accelerate the combustion (Van Basshuysen (2002)). In the case of tumble the decay of the large scale vortices into small scale turbulence leads to faster flame propagation. As a result engine efficiency improves as the combustion process comes up to the constant volume cycle.

Fast flame propagation also reduces the knocking tendency as the time for pre-reactions is shortened (Taylor (1985b)). Thus, spark advance can be reduced leading to higher efficiency. Moreover, reduced cycle-to-cycle variations resulting from better homogenization allow for

operating the engine close to the knocking limit at high loads. Especially for state-of-the-art turbocharged DISI-engines this is a crucial factor as one aims for high loads at low engine speeds (LET), which is very critical in terms of knocking.

Concerning the part load range, lean combustion and exhaust gas recirculation (EGR) are well-known measures to reduce fuel consumption. Particularly EGR is a suitable measure for homogeneous stoichiometric SI-engines, as a conventional three-way catalyst can be applied for exhaust-gas aftertreatment. However, as the combustion duration significantly rises with increased air-fuel ratio and EGR-ratio, respectively leading to increased cycle-to-cycle variations and HC-emissions the variation range is limited. Charge motion can expand this range by accelerating the combustion process (Quissek (1984) and Lauer (2007)) and reducing ignition delay (Kiefer et al. (2004)), thus improving engine stability.

### 4.1.3 Cylinder Filling

Apart from mixture preparation and combustion the in-cylinder flow affects the cylinder filling, which is mainly responsible for the attainable power output. The quality of the cylinder filling or rather the quality of the gas exchange process can be evaluated by means of the volumetric efficiency $\eta_V$ (Pischinger et al. (2002)):

$$\eta_V = \frac{m_{actual}}{m_{theo}} \quad with \quad m_{theo} = \rho_E V_h, \tag{4.3}$$

where $m_{actual}$ denotes the total mass of charge actually being pumped during a combustion cycle and $m_{theo}$ the complete filling of the displacement $V_h$ based on the conditions at the inlet ($\rho_E$, $T_E$). It is well known that enhanced charge motion often leads to a worsening of the volumetric efficiency. As mentioned in Section 4.1 the air flow is guided by the intake port design in order to induce swirl or tumble motion. In the case of a tumble port the air should ideally pass through the upper part of the valve seat, exclusively. Accordingly, only a part of the intake port cross section is used as a flow passage. The effective cross section is therefore smaller than the geometric, which is actually defined by the valve seat diameter. As a result reduced filling of the cylinder capacity appears. Moreover, the increased vorticity of the fluid motion leads to a pressure drop inside the cylinder with negative effects on the volumetric efficiency as the cylinder filling results from the pressure difference between the intake port and the cylinder (Heywood (1988)). This reveals the strict conflict of high charge motion and high cylinder filling.

## 4.2    Requirements for Turbocharged DISI-Engines

In order to quantify the influence of the in-cylinder flow on the aspects mentioned before (mixture preparation, combustion process and cylinder filling), two different intake port geometries are analyzed on an engine test bench, where the testing program is focused on the part load, low end torque and rated power operating range. Subsequently, the main targets for the purpose of an intake port optimization can be derived. The results presented in this section are based on tests carried out within the PhD thesis of Helmetsberger (2009).

| Number of cylinders | 6 | - |
|---|---|---|
| Displacement | 2874 | ccm |
| Bore | 82.5 | mm |
| Stroke | 89.6 | mm |
| Number of valves | 4 | - |
| Compression ratio $\varepsilon$ | 10.5 | - |
| Camshaft spread intake | 50 - 120 | deg |
| Camshaft spread outlet | 60 - 115 | deg |

**Table 4.1:** Technical data of the test engine with turbocharging, direct injection and VVT.

Both intake port geometries are designed as tumble ports. As shown in **Fig. 4.5**, they vary in terms of flow rate and tumble ratio (def. in Section 4.3), realized by different milling cutter types but using the same cylinder head. Thus, the cylinder head - cylinder liner assembly as well as the surface quality of the ports are identical. The main engine data are listed in **Table 4.1**.
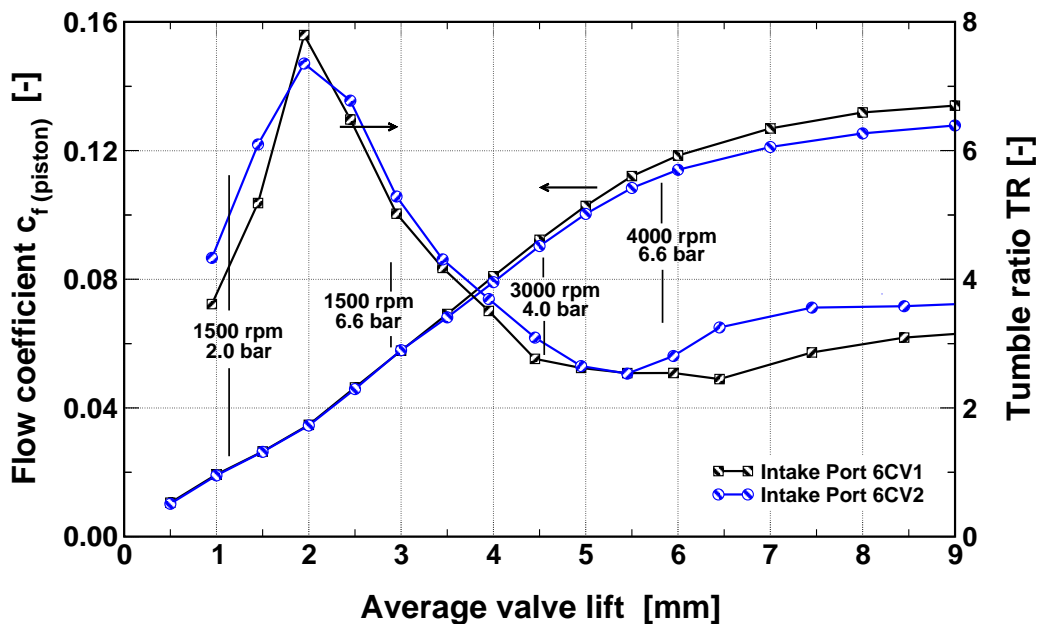


**Fig. 4.5:** Flow coefficient and tumble ratio of intake port '6CV1' and '6CV2' vs. valve lift.

The six-cylinder in-line SI-engine is based on a combustion system with homogeneous direct injection and turbocharging. The solenoid-type multi-hole injector is placed centrally within the cylinder head. The spark-plug is therefore slightly inclined towards the outlet side. Additionally, the four-valve cylinder head contains a fully variable valve drive (VVT) described in Unger et al. (2008).

## Part Load

Concerning the part-load range of conventional SI-engines, one has to focus mainly on fuel consumption, as there is still a great deficiency towards modern turbocharged Diesel engines. Downsizing by means of turbocharging is currently one of the most-promising approach to reduce fuel consumption gained by shifting the engines' operating range towards more efficient map areas (Golloch (2005)). Applying variable valve actuation, fuel consumption can be reduced further, as early intake valve closing can be realized at part load thus reducing throttling losses. Furthermore, variable valve actuation allows for different lifts among the intake valves, in the following denoted as phasing, thus enhancing charge motion through an additional swirling component, which leads to faster combustion and subsequently increased EGR compatibility (Kiefer et al. (2004)). As a result, engine efficiency can be further improved (Bunsen. et al. (2007)).

**Fig. 4.5** shows the maximum average valve lift for different operating points. The average valve lift is considered as the lift is different for the particular intake valve by applying phasing. It is noticeable that both ports perform similar for small valve lifts in terms of flow coefficient and tumble ratio. There is hardly any influence of the intake port design. In contrast, the combustion chamber design, the intake valve contour and the valve seat area, which are identical for both variants, are clearly dominating. Due to valve masking, the tumble ratios are very high for small valve lifts. For valve lifts over five to six millimeters differences between both variants can be determined, as the intake port geometry gains in importance. Intake port '6CV1' is then characterized by a higher flow coefficient, while intake port '6CV2' reaches a higher tumble level. Accordingly, identical engine performance is to be expected for low loads and speeds due to small valve lifts, while from rising valve lifts (above five to six millimeters), required for rising loads and speeds, different engine behavior can be estimated.

**Fig. 4.6** illustrates the part load performance of both intake ports concerning indicated specific fuel consumption (ISFC) and pumping mean effective pressure (PMEP). Engine parameters such as spark timing, injection timing or valve overlapping are adjusted for minimum ISFC, respectively. As expected similar ISFC values are measured for the lower load and speed range. However, a slight increase of approximately two percent is determined for the intake port variant '6CV2' at 4000 rpm and 6.6 bar. Increased pumping losses due to a lower flow rate coefficient in comparison to variant '6CV1' result in lower efficiency. The slightly enhanced charge motion has no measurable influence in contrast. Hence, when optimizing the intake port for part load operation with small valve lifts one mainly has to focus on the flow rate characteristics.
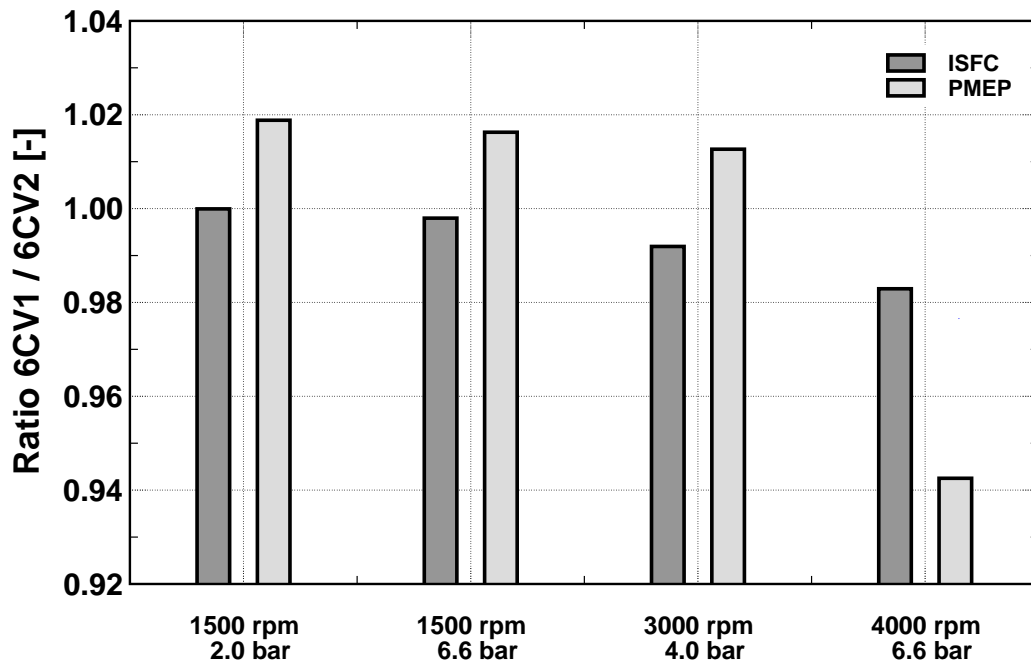
**Fig. 4.6:** Ratio between intake port '6CV1' and '6CV2' concerning ISFC and PMEP for different part load operating points.

## Low End Torque

A crucial operating range concerning turbocharged SI-engines is the low end torque (LET) range, which denotes the torque output at low engine speeds. In general, supercharged SI-engines heavily tend to knocking combustion due to the high pressure and temperature levels. However, the LET range is limited by knocking in particular as the turbulence level is significantly lower compared to high engine speeds due to the turbulence intensity scaling with mean piston speed. Therefore, conventional turbocharged SI-engines require significant mixture enrichment in order to lower combustion temperatures and thus reduce knocking tendency. Of course, this leads to an extensive increase in fuel consumption. Direct injection can diminish this problem, as a cooling effect derived from fuel vaporization inside the cylinder occurs. Enhanced charge motion is expected to reduce the problem of knocking further as mentioned in Section 4.1.2.

**Fig. 4.7** shows the potential in terms of low end torque for both port designs in the range between 1000 and 2000 rpm. Significant influences concerning ISFC, 50% mass fraction burned (MFB50) and combustion duration (CD) can be observed. Enhanced charge motion realized by intake port '6CV2' can reduce fuel consumption by 2-6%. Faster combustion resulting from increased tumble motion increases the combustion efficiency. Furthermore, the knocking tendency is reduced as the time for pre-reactions is shortened. Thus, the center of heat release (MFB50) can be realized more suitable leading to further increased efficiency. These accelerating influence of charge motion can be observed over the entire low end torque range, while it is obviously very strong at high loads for engine speeds above 1500 rpm, where the combustion process is significantly faster compared to intake port '6CV1'.
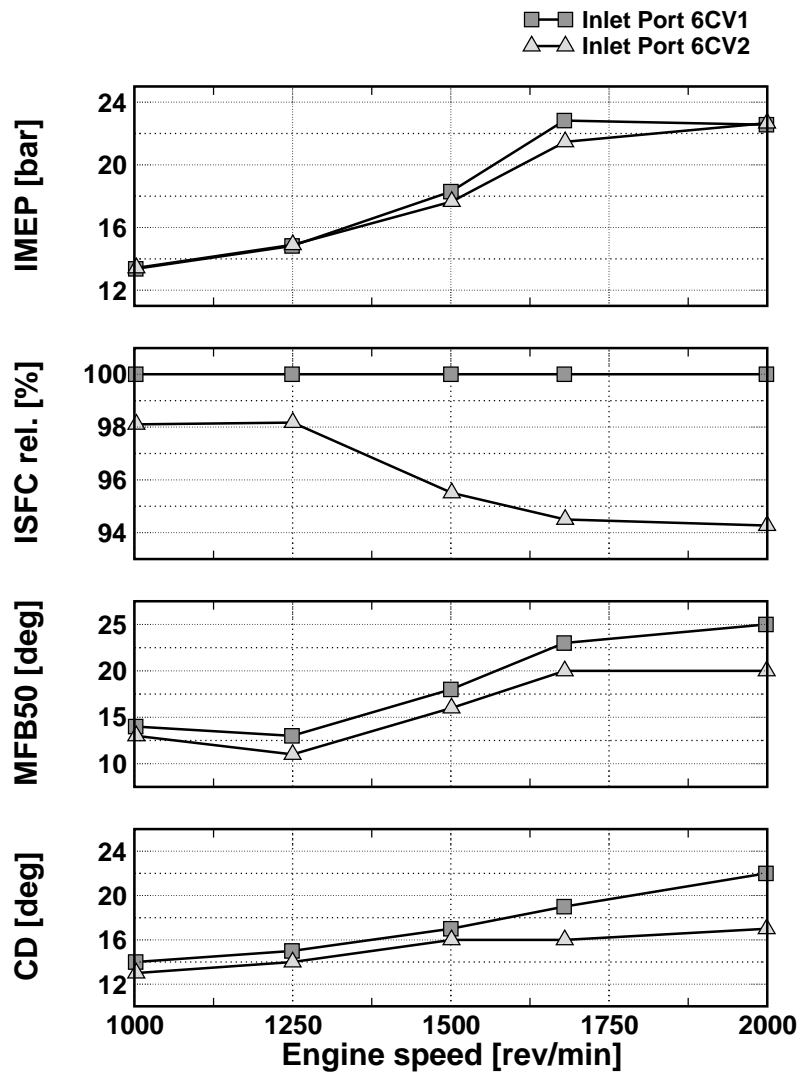
**Fig. 4.7:** Comparison of LET-potential and combustion characteristics for the intake ports
'6CV1' and '6CV2'.

However, faster combustion also leads to lower exhaust-gas temperatures and consequently
exhaust-gas enthalpy as the end of combustion is earlier (**Fig. 4.8**). As a consequence the
reachable boost pressure provided by the turbocharger is reduced for the intake port '6CV2'.
Below 1250 rpm this disadvantage is more than compensated by superior combustion efficiency
resulting from the enhanced tumble level. The same IMEP can be realized, while fuel
consumption is even reduced for the intake port '6CV2'. Between 1250 and 2000 rpm port
'6CV2' does not come up to the peak IMEP value of port '6CV1', in spite of superior efficiency.
The lack of boost pressure amounts up to 150 mbar at 1680 rpm. Of course, by shifting the
combustion towards later the enthalpy can be increased, but the increased boost pressure can
not compensate the resulting drop in efficiency. Only from 2000 rpm the exhaust-gas enthalpy
of port '6CV2' is high enough to achieve the same IMEP value, as the low end torque curve is
restricted. Thus, the targeted LET is reached at a higher engine speed. Obviously, intake port
'6CV1' could realize even higher torque output. Apart from an advantage in boost pressure this
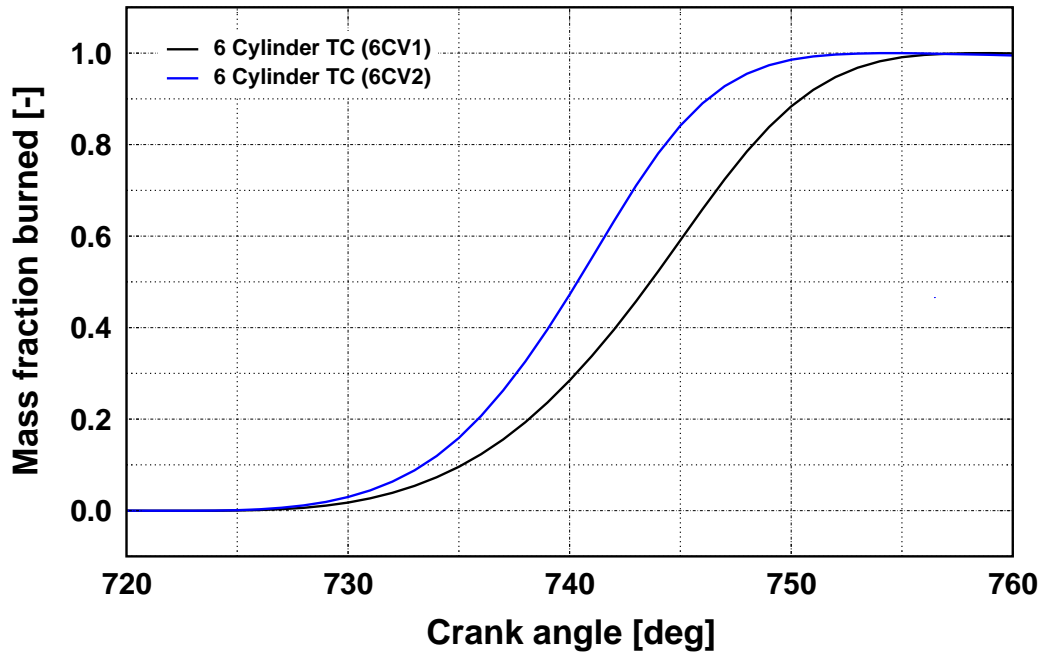
**Fig. 4.8:** Heat release at 1680 rpm and WOT for intake port '6CV1' and '6CV2'.

intake port shows a higher volumetric efficiency $\eta_V$ due to the higher flow coefficient (**Fig. 4.9**). It is noticeable, that this difference in $\eta_V$ exists over the entire speed range, as one would assume less influence of the poorer flow characteristics at lower speeds. Hence, the cylinder filling is continuously inferior, which further intensifies the disadvantage in terms of available boost pressure and thus reachable LET output.

Summing up, concerning the LET range enhanced charge motion allows for respectable reductions in fuel consumption. In contrast, less exhaust enthalpy due to faster combustion and poorer flow characteristics reduce the cylinder filling and thus the maximum IMEP. Increased combustion efficiency resulting from enhanced charge motion partly compensates
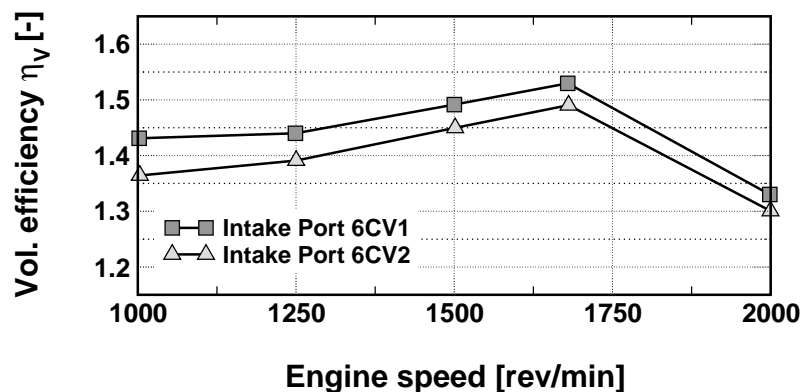


**Fig. 4.9:** Volumetric efficiency of intake port '6CV1' and '6CV2' for a speed variation between 1000 and 2000 rpm at WOT.

this disadvantages. Hence, an obvious conflict of goals exists between charge motion and flow rate regarding the LET range leading to a multi-objective optimization problem.

## Rated Power

Originally turbocharging was used to increase the cylinder filling and thus increase the power output of IC-engines (Pischinger et al. (2002)), as rated power is an important benchmark data for engine developers. **Fig. 4.10** shows the comparison of both intake ports at rated speed (5800 rpm). It presents ISFC, MFB50, combustion duration and required boost pressure for different engine loads. Likewise LET, fuel consumption can be reduced by means of intake port '6CV2'. However, this reduction only amounts to about 1% and is based on different reasons compared to the low end torque range.
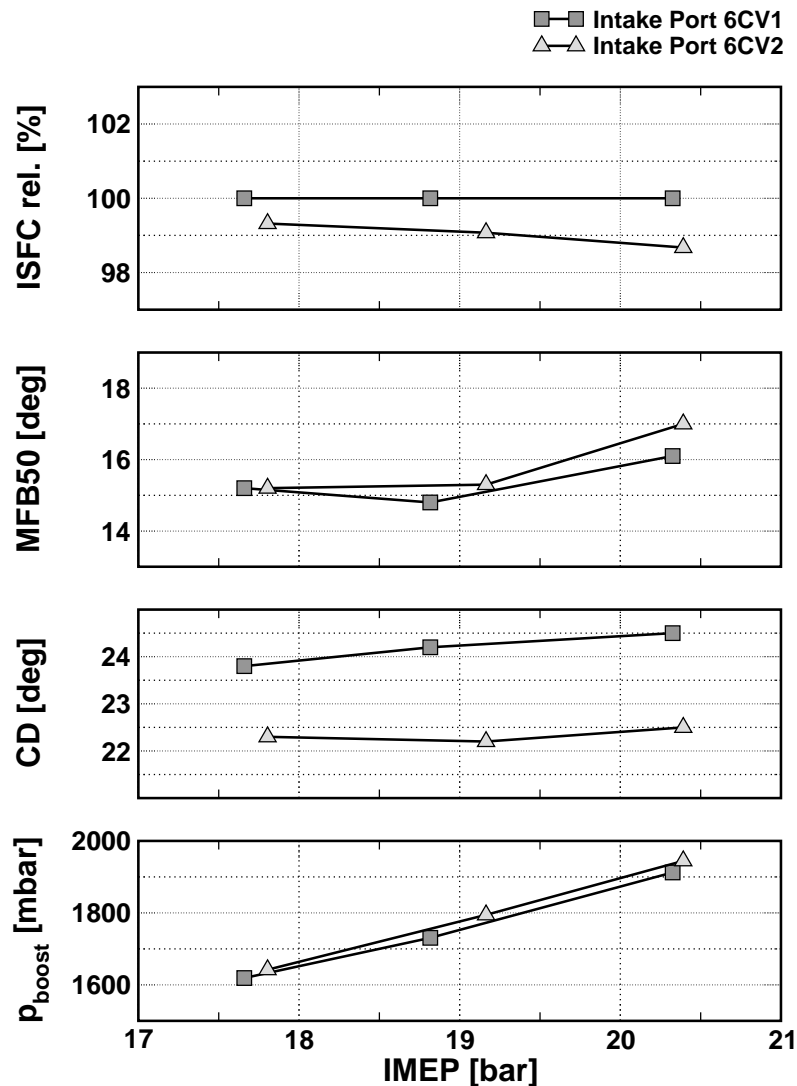


**Fig. 4.10:** Comparison of ISFC, combustion characteristics and boost pressure of intake port '6CV1' and '6CV2' for a variation of load at 5800 rpm.

The knocking tendency for higher engine speeds is reduced in general as these correlate with rising turbulence intensities. Accordingly, the center of heat release at rated speed is definitely closer to the optimal position compared to lower engine speeds. The further increase of turbulence gained by intake port '6CV2' obviously does not impact the center of heat release in addition. This can be explained by **Fig. 4.4(b)**, which shows that the acceleration effect caused by turbulence is reduced at higher turbulence levels. Thus, the MFB50 values are almost identical for both port designs. Nevertheless, spark advance and combustion duration are still reduced in contrast to intake port '6CV1' (**Fig. 4.11**). Furthermore, slightly less mixture enrichment is required for design '6CV2', altogether leading to higher efficiency. Due to higher pumping losses and lower $\eta_V$ resulting from worse flow rate characteristics the required boost pressure is elevated for intake port '6CV2'. A difference of 35 to 50 mbar between both intake ports has to be compensated in order to achieve the same IMEP. Concerning rated speed these elevated boost pressures can be delivered by the turbocharger. Therefore the exhaust-gas temperatures are on the same level for both ports and reach the maximum tolerable temperature regarding the turbine. Altogether, a small reduction in fuel consumption can be gained from enhanced charge motion.
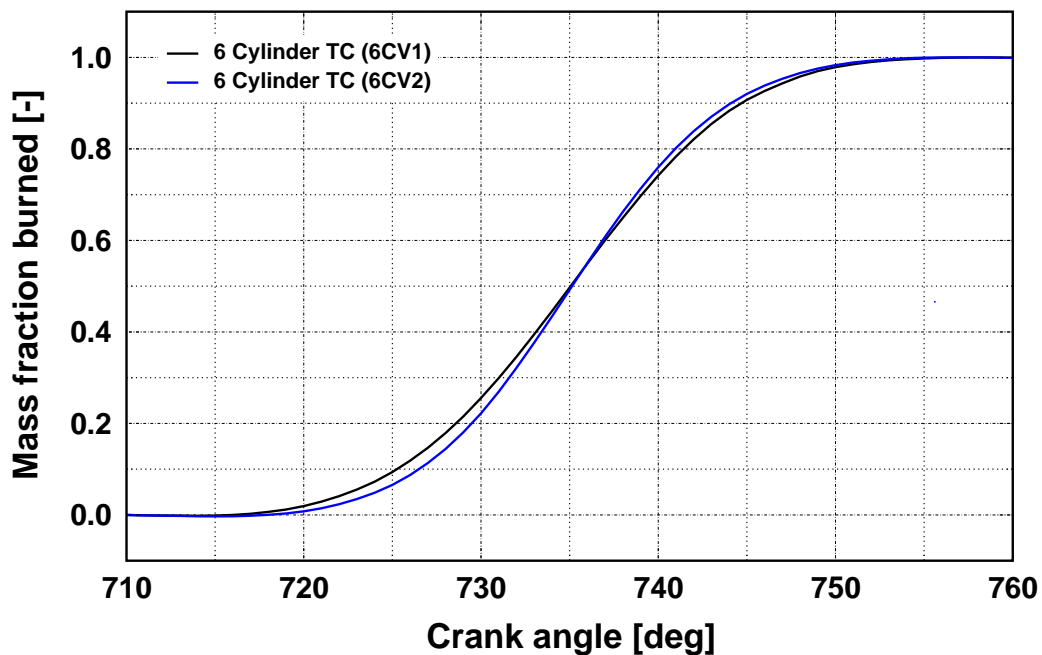


**Fig. 4.11:** Heat release of intake port '6CV1' and '6CV2' at 5800 rpm and 17.8 bar IMEP.

Summing up the testing results, different aspects according to the particular operating range of the engine are of importance. Concerning part load operation and using a variable valve lift device the focus is clearly on the flow rate characteristics. In terms of low end torque a conflict of objectives arises as higher charge motion provides significant potential for efficiency improvement, but partly lowers the reachable IMEP as the exhaust enthalpy decreases. Reduced flow rate capacity amplifies this trade-off further. A compromise between flow rate for high LET and charge motion in terms of fuel consumption must be found. Concerning rated power, both charge motion and flow rate are of interest again. Enhanced charge motion can reduce fuel

consumption, while less cylinder filling resulting from worse flow rate characteristics can be compensated by slightly increased boost pressure, provided that this additional boost potential is available. Altogether, it becomes obvious that multiple objectives need to be included simultaneously for an optimization of the in-cylinder flow regarding the entire operating range. For automatic optimization approaches it is essential to express this multiple objectives as concrete numerical values, which are introduced in the following section.

## 4.3   Flow Characteristics

As mentioned in Section 4.1 the in-cylinder flow is highly 3-dimensional and unsteady. Although flow-field measurements for motored engines with optical methods inside the cylinder are available as standardized methods (Seidel and Steuker (2008)), it is still complex and time-consuming to characterize the flow patterns of different cylinder head assemblies adequately. For this purpose steady flow testing has become widely accepted in the combustion systems development process. Several measurement techniques have been suggested in order to quantify the flow characteristics in terms of flow rate and charge motion.

### Flow Coefficient

The flow rate characteristics of the intake port and combustion chamber design significantly influence cylinder filling and gas exchange losses of an IC-engine and thus its performance and fuel consumption. In order to assess these characteristics usually the flow coefficient $c_f$ is used, which is defined as the ratio of the measured mass flow rate to the theoretically calculated flow rate:

$$c_f = \frac{\dot{m}_{real}}{\dot{m}_{theo}} \quad . \tag{4.4}$$

The real mass flow $\dot{m}_{real}$ is determined for different valve lifts by means of a steady flow test rig (**Fig. 4.12**), where a constant pressure difference $p_A$-$p_B$ or pressure ratio $p_A/p_B$, respectively is regulated in order to suck or blow the air through the cylinder head. The real mass flow can be measured by a rotary gas meter, mass air flow meter or a standard orifice. The difference to the
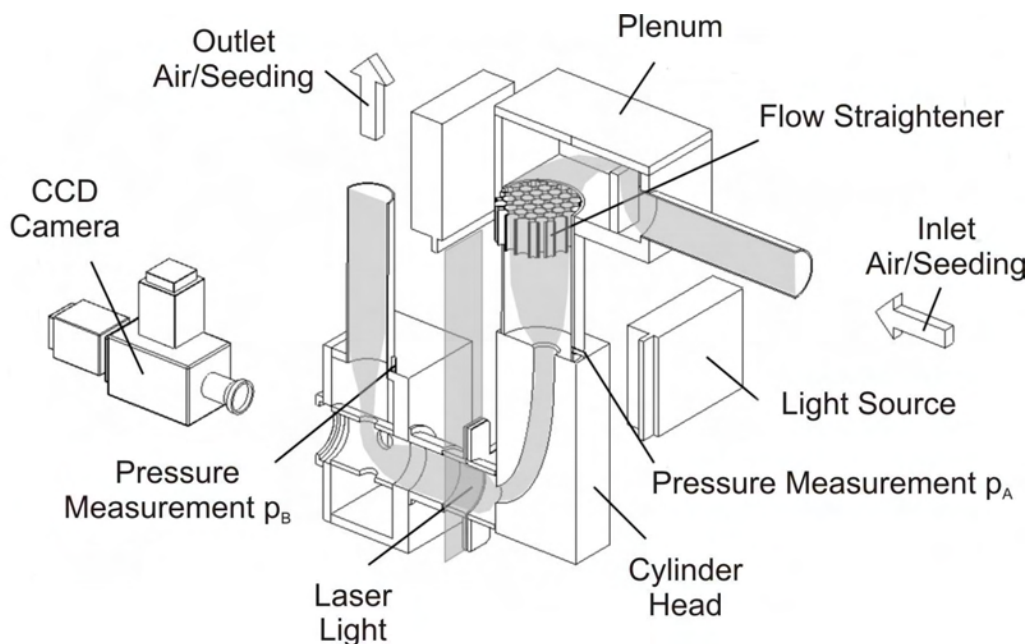


**Fig. 4.12:** Setup of steady flow test rig for optical DGV measurements (Dingel et al. (2003)).

theoretical mass flow rate results from flow losses. For naturally aspirated engines these losses
limit the maximum power output. Concerning turbocharged engines increased boost pressure is
required in order to achieve equal performance. The corresponding theoretical mass flow $\dot{m}_{theo}$
is based on a steady adiabatic reversible (isentropic) flow of an ideal gas through a reference
flow area:

$$\dot{m}_{theo} = A_{ref} \frac{p_A}{\sqrt{RT_A}} \sqrt{\frac{2\kappa}{\kappa - 1} \left[ \left( \frac{p_B}{p_A} \right)^{\frac{2}{\kappa}} - \left( \frac{p_B}{p_A} \right)^{\frac{\kappa+1}{\kappa}} \right]} \quad , \tag{4.5}$$

where $p_A$ and $T_A$ are the stagnation pressure and the stagnation temperature in the intake system,
$p_B$ is the static pressure inside the cylinder and $\kappa$ is the isentropic exponent. For the reference
flow area $A_{ref}$ several different definitions can be found in the literature. A very detailed
overview is given by Frank (1985). Most commonly the valve inner seat diameter is applied
to determine $A_{ref}$. In order to compare different cylinder heads or engines the cylinder-bore
diameter is a suitable parameter as well.

## Swirl Ratio and Tumble Ratio

Apart from the flow characteristics charge motion is of great importance as it significantly
influences the mixture preparation and the subsequent combustion as mentioned in the previous
sections. However, evaluating the in-cylinder charge motion is far more difficult than assessing
the flow rate characteristics (Hongming (2001)). Therefore, numerous methods were proposed
based on steady flow testings analogue to the flow coefficient before, which can mainly be
distinguished by two different types, integral and differential methods.

Integral methods characterize the in-cylinder flow by non-dimensional numbers without
resolving the flow pattern in particular. The probably best known integral method for swirl
flows was proposed by Thien (1965). Using a paddle wheel anemometer that is aligned with
the cylinder axis, the swirl strength can be quantified by measuring the angular velocity of the
paddle wheel. Analog to this method the company FEV uses a paddle ring, which is aligned
perpendicular to the cylinder axis (**Fig. 4.13(a)**). Closing the cylinder by means of a dummy
piston and sucking the air laterally at the level of the rotation axis, tumble flow patterns like in an
engine can be simulated and evaluated. Accordingly the angular velocity is used to quantify the
tumble strength. Tippelmann (1997) proposed an axially mounted spherical honeycomb, which
is deflected according to the torque imposed upon it by the in-cylinder flow (**Fig. 4.13(b)**). This
method is a very sophisticated one as it allows for measuring all three components (swirl, x-
and y-tumble) of the in-cylinder flow simultaneously.

In general, integral methods are extensively used in the engine development process as they
allow for cost-effective and fast measuring of the in-cylinder flow characteristics. Even for
monitoring cylinder heads at machining lines this measuring devices are applied. However,
all these methods significantly impact the in-cylinder flow as an additional device is placed
within the cylinder and by this modify the actual flow structure. Furthermore, only non-
dimensional swirl or tumble numbers can be derived, without resolving the actual structure
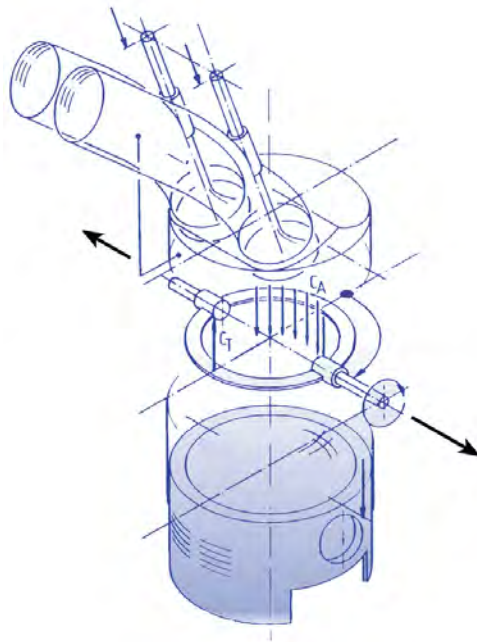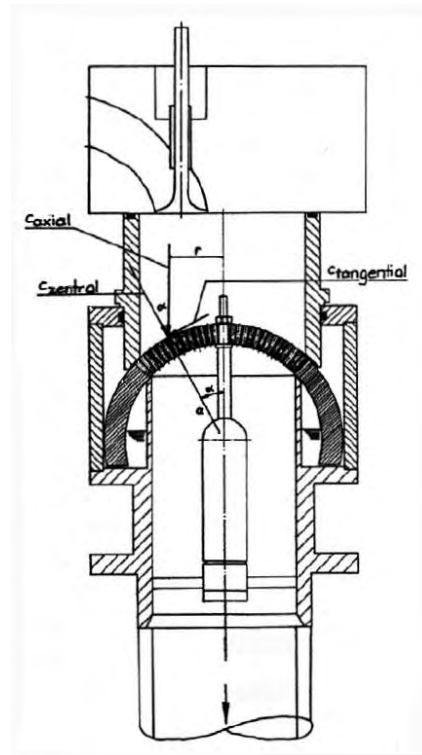
**(a)** FEV (FEV (2000))          **(b)** Tippelmann (Tippelmann (1997))

**Fig. 4.13:** Principle of the tumble measuring methods from FEV (a) and Tippelmann (b).

of the in-cylinder flow. More detailed information of the in-cylinder flow structure must be assessed when optimizing the mixture and the combustion process in IC-engines. The major restriction using integral methods can be addressed to the fact that identical non-dimensional numbers can be obtained for engine designs with different flow structures (Glanz (2000)), thus leading to different engine behavior.

Therefore differential methods are applied, which analyze the in in-cylinder flow by means of non-intrusive optical methods. Commonly used techniques are laser Doppler velocimetry (LDV) applied by Glanz (2000), particle image velocimetry (PIV) used by Bensler et al. (2002) and Doppler Global Velocimetry (DGV) proposed by Dingel et al. (2003). The experimental setup of DGV is illustrated in **Fig. 4.12**. The laser-optical measurement technique is based on the Doppler effect. Using the DGV method the time-averaged three-dimensional velocity field within the cylinder is measured, which can be used for the validation of CFD-simulations.

Once having measured the in-cylinder flow, either by integral or differential methods, the charge motion has to be quantified by means of non-dimensional numbers. Definitions widely used for this purpose are swirl and tumble ratios, respectively. In the case of swirl pattern a vortex can be detected even under steady flow test conditions. By assuming a solid body rotating flow of the size of the cylinder bore (represented by the paddle wheel) the swirl ratio is defined as the ratio between the tangential velocity $c_t$ and the axial velocity $c_a$:

$$SR = \frac{c_t}{c_a} \quad with \quad c_t = \omega r \quad and \quad c_a = \frac{\dot{V}}{A} \quad , \tag{4.6}$$

where $\omega$ denotes the angular velocity, $r$ the cylinder radius, $\dot{V}$ the volumetric flow and $A$ the corresponding area. Concerning the FEV technique for tumble structures an analog tumble ratio can be derived.

Applying the steady flow measurements mentioned before for tumble inducing systems, a rotating flow as for the real engine does not occur. Nevertheless, the unequal distribution of the air flow over the intake valve, responsible for the tumble initialization (Section 4.1), can be evaluated. Based on the solid body rotating flow assumption the conservation of the angular momentum can be written as:

$$\Delta \vec{L} = \int \vec{M} dt = I \int d\vec{\omega} \quad with \quad I = \frac{mr^2}{2} \quad , \tag{4.7}$$

where $L$ is the angular momentum, $M$ the momentum, $I$ the moment of inertia and $m$ the mass. For steady flow conditions Equation 4.7 delivers:

$$\omega = 2\frac{Mt}{mr^2} \quad . \tag{4.8}$$

The tumble ratio can finally be derived analogously to Equation 4.6:

$$TR = 2\frac{M \cdot t \cdot r \cdot A}{m \cdot r^2 \cdot \dot{V}} = 2\pi \frac{r \cdot M}{\rho \cdot \dot{V}^2} \quad . \tag{4.9}$$

Applying Tippelmann's honeycomb device, the momentum $M$ can be measured directly. Concerning optical methods this momentum has to be derived by means of the measured velocity field. The momentum in $x$-direction is calculated for a specific area element $A_i$ according to:

$$\Delta M_{x,i} = w_i \cdot r_i \cdot |\Delta \dot{m}_i| \quad , \tag{4.10}$$

where $w_i$ is the axial velocity component, $r_i$ the particular lever arm and $\dot{m}_i$ the particular mass flow. The resulting overall momentum is subsequently determined for a plane perpendicular to the cylinder axis by:

$$M_x = \sum_i \Delta M_{x,i} \quad . \tag{4.11}$$

The horizontal plane, located half of the bore below the cylinder head gasket, has been found to be suitable as the in-cylinder vortex is assumed to be of the size of the bore (Glanz (2000)). Dingel et al. (2003) suggested to include further planes below and above this plane in order to calculate a volume tumble number $TU_{VOL}$. For non-symmetric engine designs both tumble components $M_x$ and $M_y$ are regarded:

$$TU_{VOL} = \frac{\sum\limits_{j=1}^{n} TU_j}{n} \quad with \quad TU_j = \frac{r\sqrt{M_x^2 + M_y^2}}{\rho_n \, \dot{V}^2} \quad , \tag{4.12}$$

where $n$ is the number of planes. The volumetric swirl number is defined accordingly as:

$$SW_{VOL} = \frac{\sum\limits_{j=1}^{n} SW_j}{n} \quad with \quad SW_j = \frac{r \, M_z}{\rho_n \, \dot{V}^2} \quad . \tag{4.13}$$

Apart from these non-dimensional numbers for swirl and tumble further definitions have been suggested based on the paddle wheel anemometry or the measuring of the angular momentum, which can be found in Frank (1985).

Regarding the engine development process CFD-simulations are intensively applied for the purpose of designing the in-cylinder flow. The validation of these simulations is mainly performed by means of integral methods such as the paddle wheel or the Tippelmann honeycomb, as optical methods are not available during the complete process. Optical methods are more likely used for adjusting the particular simulation methods at the beginning. Therefore the problem arises, that the simulations need to include the measuring devices of integral methods, which is very complex. However, according to Dingel et al. (2002) very promising agreement between results from a Tippelmann test rig and results derived from optical DGV-measurements can be achieved.

In order to evaluate the comparability between the Tippelmann honeycomb, used within this work, and the DGV technology, three different types of intake ports, a filling port ('FB01'), a low tumble port ('FB03') and a tumble port ('FB05'), are analyzed. In order to calculate the volume tumble $TU_{VOL}$ for the DGV measurement 5 evaluation planes are used, located at half of the bore and 5 and 10 mm above and below, respectively. **Fig. 4.14** shows the particular tumble number over valve lift for this analysis. For small valve lifts the correlation is rather poor. The momentum of the air flow is low due to small mass flow rates at low valve lifts. Therefore the influence of the honeycomb device cannot be neglected leading to a significant impact on the in-cylinder flow. For valve lifts greater than 4 mm both methods show good accordance concerning the tumble characteristic, though the absolute values differ. However, translating the particular Tippelmann results to the DGV-results at a specific valve lift (here 8 mm) such that both $TR$ and $TU_{VOL}$ become equal, very good agreement in general is achieved for high valve lifts (**Fig. 4.15**). Altogether, both methods lead to similar results in terms of tumble characteristics, while the absolute tumble number may differ.
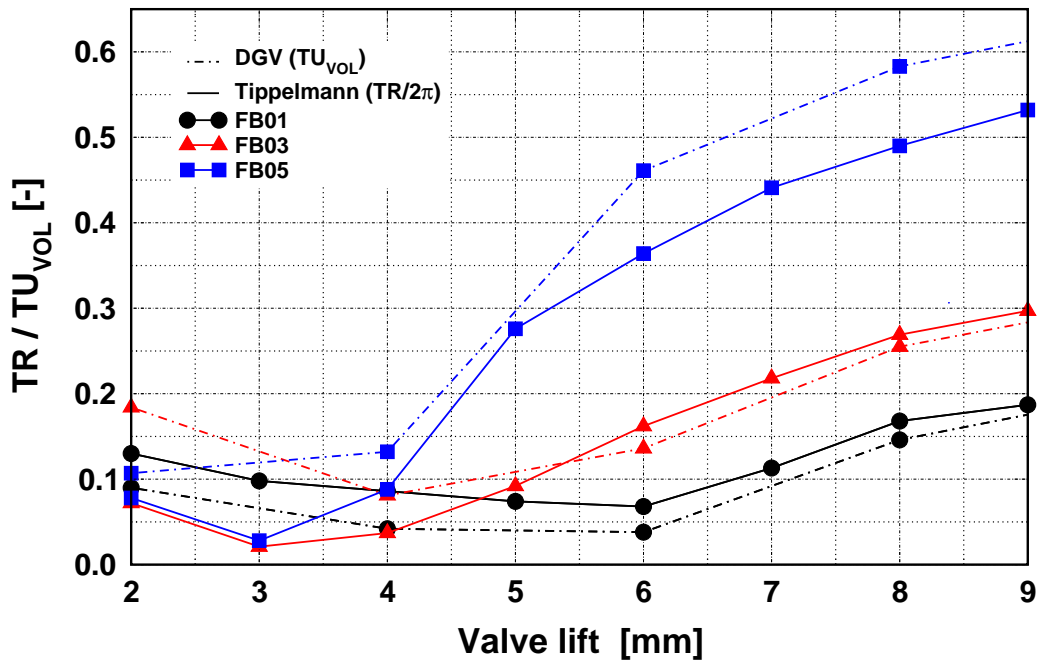
**Fig. 4.14:** Comparison of Tippelmann (*TR*) and DGV (*TU_{VOL}*) tumble numbers for a filling, a medium tumble and a high tumble port.
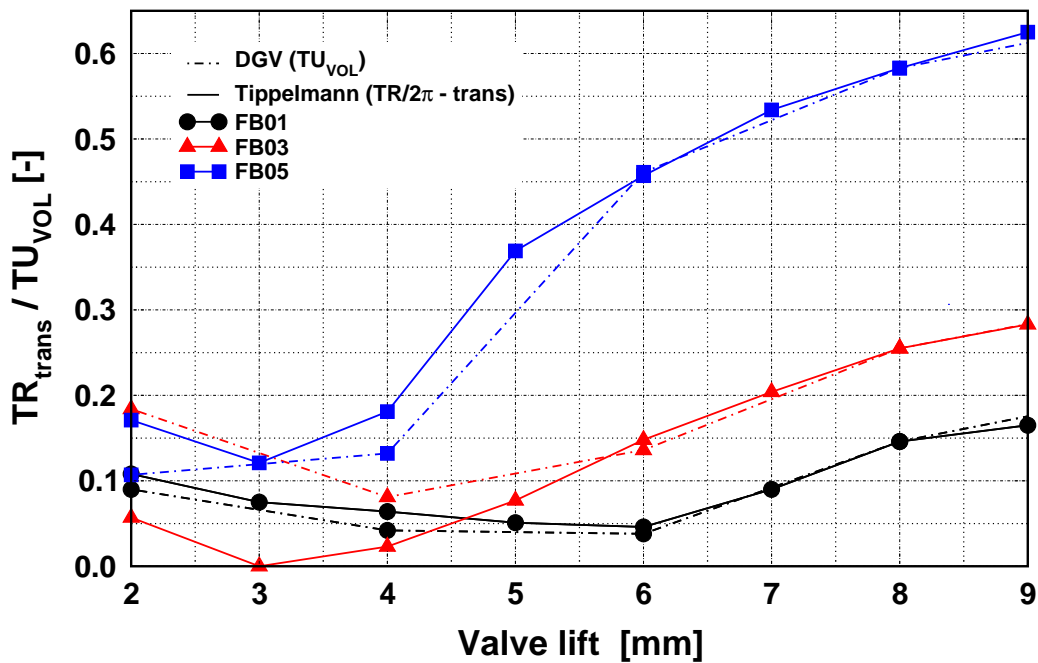


**Fig. 4.15:** Comparison of translated Tippelmann (*TR*) and DGV (*TU_{VOL}*) tumble numbers for a filling, a medium tumble and a high tumble port.

## 4.4 CFD Analysis Methods

The in-cylinder flow in IC-engines, characterized by flow rate and charge motion, significantly influences the engine performance. As shown in Section 4.2 both flow rate and charge motion have to be regarded simultaneously. Therefore, great emphasis is placed on the flow-guiding parts such as intake ports, combustion chamber and valve seat region. The design of these devices by means of CFD-simulations is state-of-the-art, while measurements either optical or integral rather serve for validating the simulation results. Therefore, several CFD analysis methods exist, which mainly differ concerning the level of detail and computational effort.

### 4.4.1 Steady Flow Analysis

The most common experimental method to analyze the flow characteristics of a cylinder head is the steady flow test rig as explained in Section 4.3. The steady flow analysis is defined in analogy to this experiment using CFD. Accordingly, a constant pressure difference (100 mbar) is applied between the inlet flange of the cylinder-head and the cylinder outlet, while the intake valves are fixed at specific valve lifts. The flow coefficient (Equation 4.4), tumble and swirl number (Equation 4.12 and 4.13) can be derived for a particular valve lift, respectively. In order to calculate the volumetric swirl and tumble numbers five evaluation planes are included. **Fig. 4.16** shows the computational domain containing these planes, which is defined similar to the steady flow test rig illustrated in (**Fig. 4.12**). For simplification only the intake ports, the combustion chamber layout and the cylinder liner are considered. The cylinder length amounts
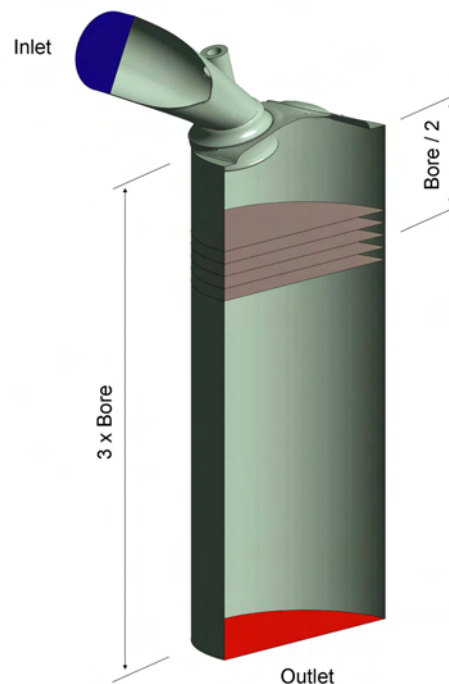


**Fig. 4.16:** Computational domain for the steady flow analysis.

to three times the bore diameter in order to avoid an impact of the outlet boundary on the flow upstream.

**Fig. 4.17** shows different series production and prototype ports of naturally aspirated (NA) and turbocharged (TC) engines in terms of flow coefficient $c_{f(Piston)}$ and tumble number $TU_{VOL}$ at 10 mm valve lift. The technical data of the corresponding engines are listed in **Table A.1 (p.139)**. Two groups of intake ports can be distinguished, filling ports in the upper left and tumble ports in the lower right. It is noticeable, that a well-defined correlation between flow rate and tumble exists, as the flow coefficient decreases for rising tumble numbers. The steady flow analysis regarding a single valve lift is an efficient method to characterize different intake ports and evaluate these relations.
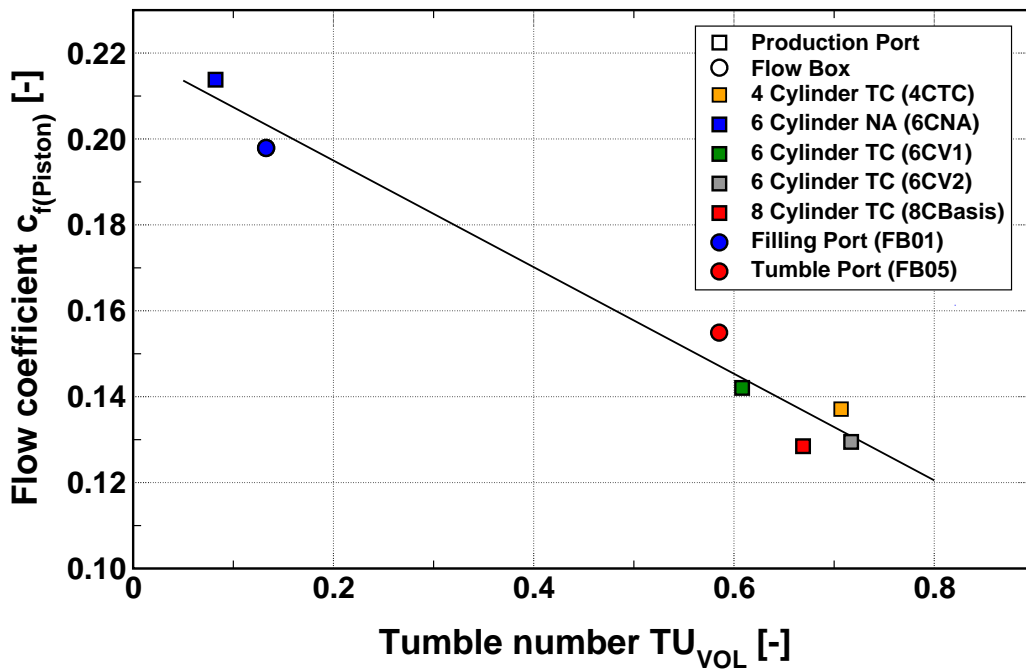


**Fig. 4.17:** Flow coefficient $c_{f(Piston)}$ and tumble number $TU_{VOL}$ of different series production and prototype ports (flow boxes) predicted by the steady flow analysis at 10 mm valve lift.

Apart from a single lift only several valve positions can be considered by means of the steady flow analysis in order to evaluate the entire valve lift range. However, for reducing the number of calculations and simplifying the simulation process a different analysis setup is defined. Starting from a small valve lift of 1 mm the valve is linearly opened during the simulation until the maximum lift of 10 mm is reached. Thus, the flow characteristics are resolved very detailed over the entire valve lift range by means of a single simulation run. Compared to a steady flow analysis at a single lift the computational effort is of course significantly higher. In addition, this simulation is a transient one as the valve is moved during the simulation, which increases the calculation time further. However, in order to realize a quasi-static flow similar to the steady flow test rig, the intake valve is translated very slowly.

**Fig. 4.18** shows the results concerning flow coefficient gained by the steady flow analysis for the intake port study of Section 4.2. The simulation reveals the differences between both intake
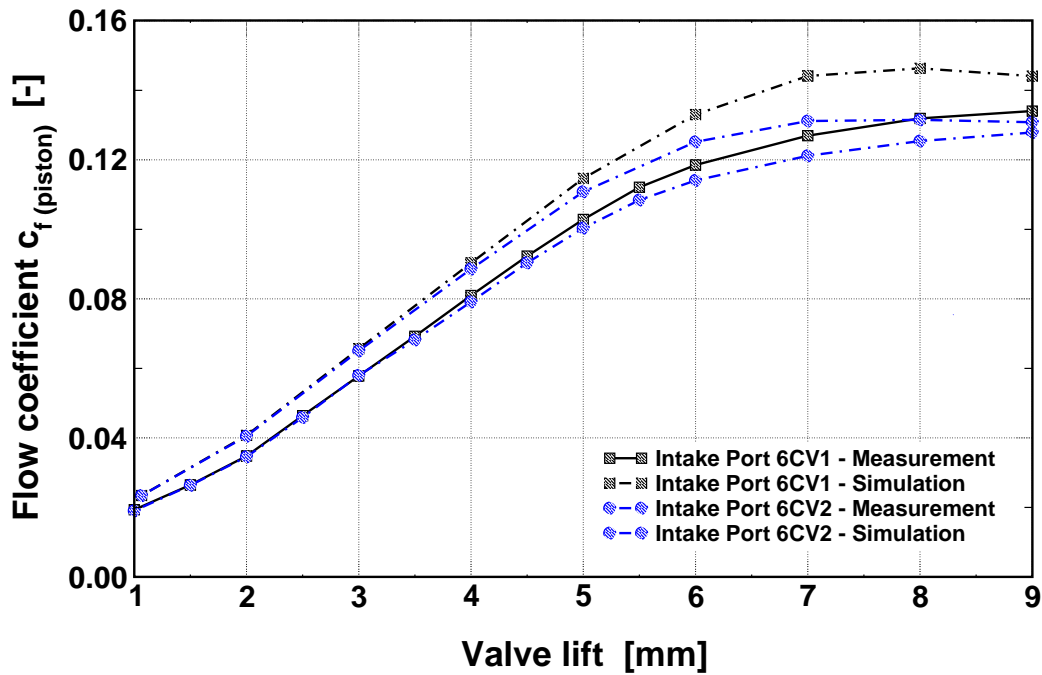
**Fig. 4.18:** Measured and simulated flow coefficient $c_{f(Piston)}$ for the intake ports '6CV1' and '6CV2'.

ports analog to the test rig measurements. Both ports show equal values for $c_{f(Piston)}$ for valve lifts up to 3 to 4 mm, before they spread as the port '6CV1' is characterized by a higher flow coefficient compared to port '6CV2'. The absolute flow rate level is overestimated by the
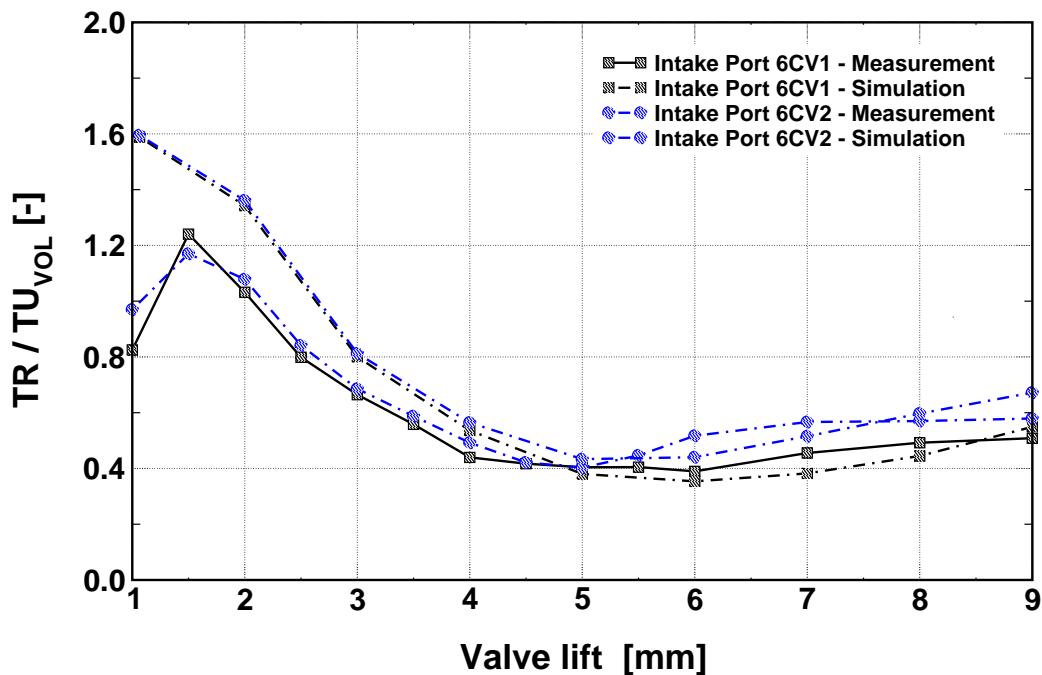


**Fig. 4.19:** Measured and simulated tumble number $TU_{VOL}$ for the intake ports '6CV1' and '6CV2'.

simulation. One reason is, that solid walls are regarded as smooth thus neglecting influences due to wall roughness. Sensitivity to mesh resolution and numerical parameters can be regarded as further reasons. The tumble ratios are shown in **Fig. 4.19**, where satisfying accordance between simulation and measurement is achieved. Both simulation and experiment affirm higher tumble ratios for intake port '6CV2' compared to port '6CV1' for valve lifts over 5 mm.

Altogether, the steady flow analysis is able to adequately represent the in-cylinder flow under stationary conditions. Based on non-dimensional numbers this method is an efficient tool for assessing different cylinder head designs within the in-cylinder flow development. The possibility to validate the simulation results by means of experimental results from a steady flow test rig is another great benefit.

## 4.4.2 Dynamic Analysis

The steady flow analysis has been proved to be a suitable method for the purpose of assessing different cylinder-head designs. However, they cannot reproduce the real in-cylinder flow in IC-engines and its influence on mixture preparation and combustion as several simplifications are assumed. Due to applying constant pressure ratio and simplified valve lifting, but particularly due to neglecting the piston movement the resulting air-flow is clearly different. Therefore, CFD methods have to be applied, where real piston geometry and movement, real valve lift curve as well as realistic boundary conditions over the entire combustion cycle are regarded. Thus, cylinder filling and charge motion of the real engine can be analyzed. However, as the in-cylinder flow pattern has to be evaluated before any measurement data from engine testing is available, it is difficult to define suitable boundary conditions. The 1D gas exchange simulation may deliver these in the future. The lack of measurement data is also a problem in terms of model validation for the injection and combustion process. Furthermore, the computational effort of such a detailed simulation is still enormous, which significantly limits the number of evaluable designs.

In order to overcome these problems, a simplified simulation method, in the following denoted as dynamic analysis, has been defined. **Fig. 4.20** shows the computational domain considered



**Fig. 4.20:** Computational domain for the dynamic analysis of an intake port.

for the dynamic analysis. This method is based on rated speed conditions (6000 rpm WOT) due to several reasons. As there is, in contrast to the LET range, commonly minimal valve overlapping, expansion stroke and intake stroke can be regarded more or less separately. For the dynamic analysis only the intake phase followed by the compression stroke have to be considered, where the intake valve is assumed to open at top dead center (**Fig. 4.3**). Due to the reasons mentioned before, injection and combustion are neglected. Additionally, the amount of residual gas is rather small and is accordingly neglected. Pure air is considered instead. A constant total pressure of 1 bar is defined at the inlet flange, which means that dynamic effects within the intake manifold are not regarded and the pistons sucks the air under ambient conditions. This is not a serious drawback concerning turbocharged SI-engines as dynamic effects are intended to be eliminated anyway. The additional boost effect gained from intake manifold dynamic increases the cylinder filling but also the cylinder temperature, which results in increased knocking tendency. Therefore, in the case of supercharged IC-engines, it is more advantageous to avoid these effects and elevate the boost pressure as the air is subsequently cooled by means of the charge-air cooler thus entering the cylinder at a lower temperature level. In total, by means of the dynamic analysis the influence of the in-cylinder flow on cylinder filling and charge motion can be evaluated under engine-like boundary conditions (Linse (2006)).

Similar to the steady flow considerations before, characteristic numbers can be defined. In order to assess the quality of the intake process, the cylinder mass after intake valve closing or the volumetric efficiency (Equation 4.3) are used. **Fig. 4.21** shows the cylinder mass for an eight-cylinder and a six-cylinder turbocharged SI-engine, where the eight-cylinder results are scaled by the displacement ratio. According to the results of the steady flow analysis (**Fig. 4.17**),
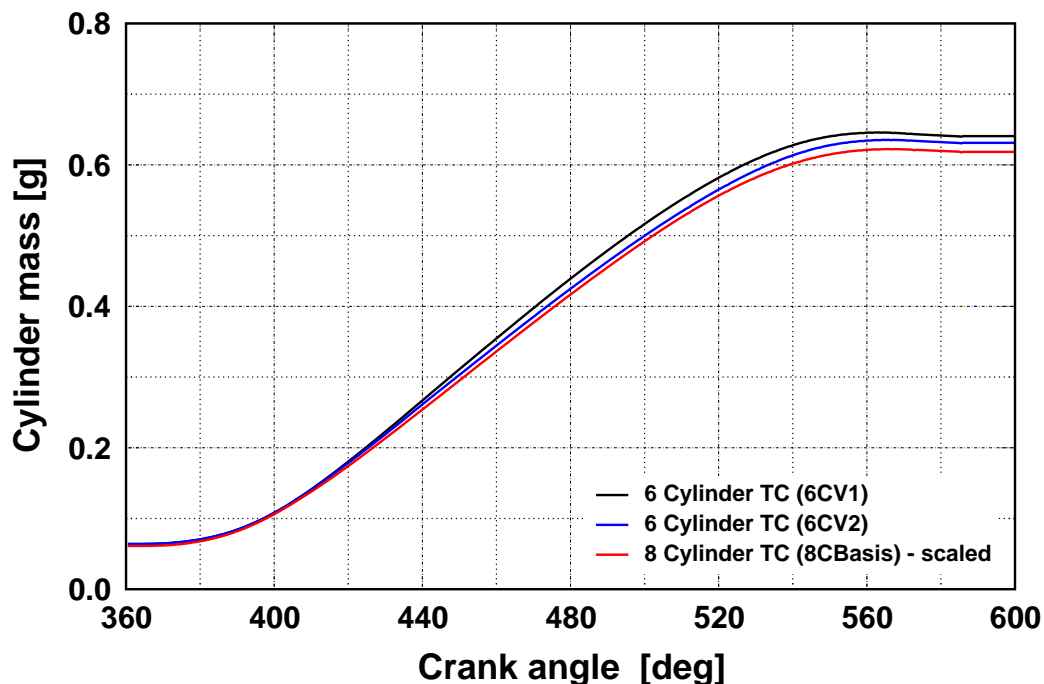


**Fig. 4.21:** Cylinder mass vs. crank angle for the eight-cylinder '8CBasis' and the six-cylinder engine designs '6CV1' and '6CV2'.

variant '6CV1' achieves a higher cylinder filling compared to '6CV2', which correlates well with experimental data from the engine test bench, while the eight-cylinder shows the lowest specific cylinder mass.

Likewise steady flow analysis charge motion is expressed by swirl and tumble ratios, while the definition is clearly different as the piston leads to real tumble motion inside the cylinder. According to Haworth et al. (1990) these ratios can be defined by the angular momentum of the actual air motion divided by the product of the crankshaft angular velocity and the moment of inertia of the air volume as a solid body. Hence, the tumble ratio in x-direction $TR_x$ is:

$$TR_x = \frac{\int_{Cyl} (L_{x,i}) \, dm}{\int_{Cyl} (I_{xx,i}) \, dm \cdot \omega_0} \quad , \tag{4.14}$$

$$with \quad L_{x,i} = (y_i - y_{cent}) \cdot w_i - (z_i - z_{cent}) \cdot v_i \quad ,$$

$$and \quad I_{xx,i} = (y_i - y_{cent})^2 + (z_i - z_{cent})^2 \quad ,$$

where $L_{x,i}$ denotes the angular momentum per unit mass and $I_{xx,i}$ the moment of inertia. Angular momentum and moment of inertia are determined around a moving center, the instantaneous center of cylinder volume expressed by $x_{cent}$, $y_{cent}$ and $z_{cent}$. Accordingly, $x_{cent}$ and $y_{cent}$ amount to zero, $z_{cent}$ is half the current stroke plus half the squish gap. The tumble ratio $TR_y$ and the swirl ratio $SR$ are defined in analogy to Equation 4.14. These ratios are normalized with the aid of the crankshaft angular velocity $\omega_0$, which is defined as:

$$\omega_0 = \frac{2\pi n}{60} \quad , \tag{4.15}$$

where $n$ is the engine speed. **Fig. 4.22** shows the tumble ratios $TR_x$ for the analyzed engines. For all engines the tumble ratios show a steep increase during the intake phase, which is further intensified during the compression stroke until a maximum is reached at about 70 degrees before top dead center. Subsequently, the characteristical tumble breakdown can be observed. The six-cylinder engine '6CV2' shows the highest tumble, followed by the '8CBasis' and the '6CV2' designs, analogously to the steady flow results. The tumble ratio in y-direction $TR_y$ as well as the swirl ratio SR remain almost zero as expected for symmetric four-valve engines.

**Fig. 4.23** shows the curves of the turbulent kinetic energy (TKE) for the analyzed engines. All curves show a steep increase at the beginning of the intake stroke, resulting from shear flows between the incoming air jet and the cylinder charge. With the intake valve closing all setups show a similar TKE dissipation, until it rises again at the end of compression when the tumble motion is destroyed. The level of turbulent kinetic energy correlates with the particular tumble strength before tumble decay. Hence, the TKE values of '6CV2' exceed both the eight-cylinder and the '6CV1' variant at spark timing, which is approximately around 10 degrees before TDC. Together with a higher tumble ratio, this explains the faster burn rates observed in Section 4.2.
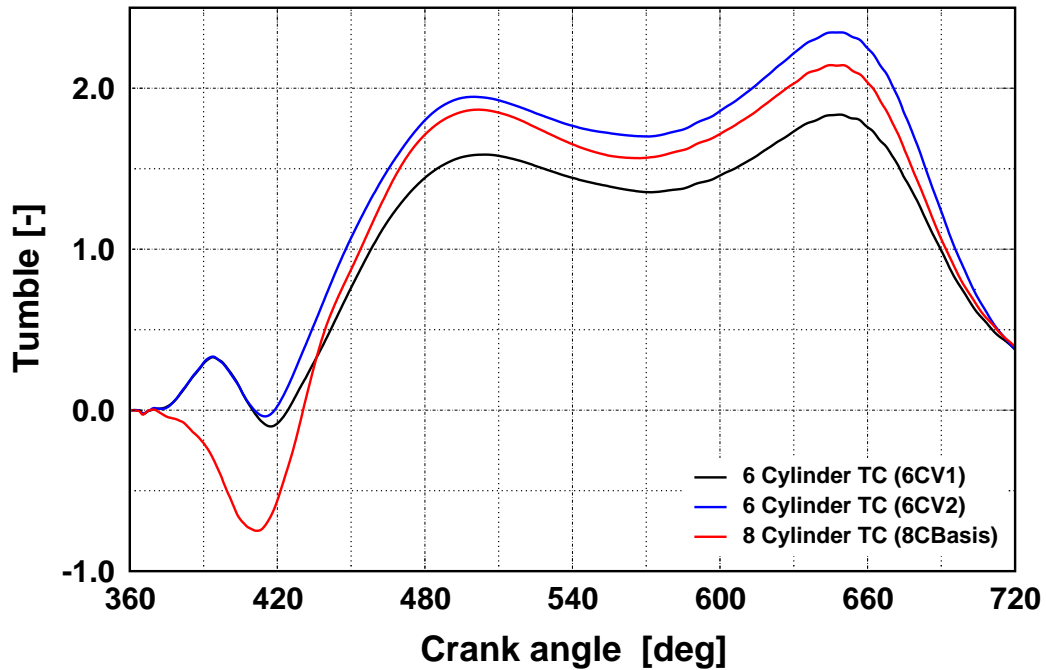
**Fig. 4.22:** Tumble vs. crank angle for the eight-cylinder '8CBasis' and the six-cylinder engine designs '6CV1' and '6CV2'.

In contrast to steady flow simulations the validation of these results by measurements is exceedingly difficult. Hascher et al. (1997, 2000) measured the in-cylinder flow of a V8 four-valve engine by means of a 3D LDV system during the intake and compression stroke from 600
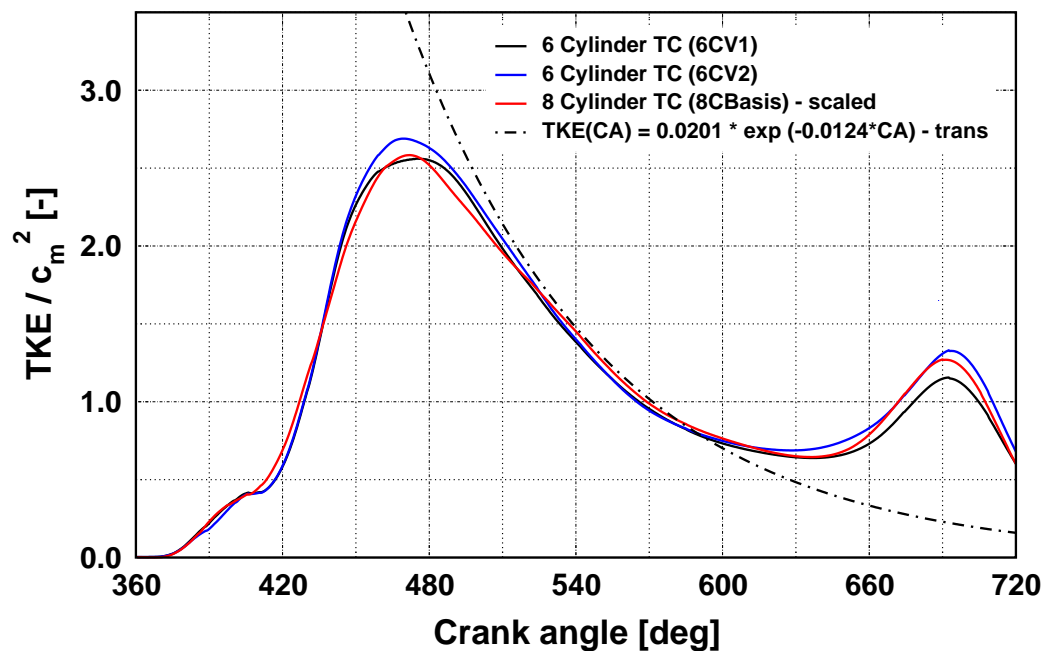


**Fig. 4.23:** Scaled turbulent kinetic energy (TKE) for the eight-cylinder '8CBasis' and the six-cylinder engine variants '6CV1' and '6CV2' throughout piston speed, compared with a fitted TKE-curve from Hascher et al. (2000) based on experimental data.

to 1500 rpm. Based on this study the turbulent kinetic energy and the in-cylinder charge motion expressed by tumble and swirl ratios were derived. The research engine setup is very close to the before mentioned V8 engine, while the engine speed is significantly lower. However, according to Hascher et al. (2000) the investigated in-cylinder flow appears to be less affected by speed variations. Thus, the results of both engines are comparable. In terms of tumble ratio the simulated curve compares well with the measured one. Even the absolute level is very similar, as the tumble ratio is normalized by the engine speed. Concerning TKE, Hascher et al. (1997) refer that, after a short period of increase in the beginning of the intake stroke, the TKE decreases over the remaining measured crank angle range. This decay during the intake stroke and beyond BDC can be fitted with an exponential function (Hascher et al. (2000)), which leads to a very good comparability with the scaled simulated curve of both the V8 as well as the six-cylinder engine (**Fig. 4.23**). The steep increase of TKE at the beginning of the intake phase can be observed for all simulated setups as well. The course of TKE for late CAs is not investigated as the entire cylinder volume is not accessible.

Altogether, the dynamic analysis enables the evaluation of the cylinder filling during the intake stroke as well as the tumble initialization, amplification and dissipation into turbulent kinetic energy at the end of compression. The results obtained from this simulation correspond well with the results from the intake port study in Section 4.2. Thus, the influence of the particular intake port on the combustion process can be adequately estimated, as the in-cylinder charge motion is reproduced realistically. The computational effort in contrast is significantly reduced compared to a simulation of the complete combustion cycle. In general, it is noticeable that steady flow and dynamic analysis appear to exhibit similar characteristics for the investigated engine setups concerning charge motion and cylinder filling, respectively.

# 5 CFD-based Optimization Process

Reducing development costs and times while increasing product quality is one of the major challenges within the engine development process. The layout of the in-cylinder charge motion is an essential part of this process as mentioned in Chapter 4. By means of CFD approaches a significant increase in efficiency can be achieved, as fast design evaluation is enabled and the number of expensive test parts can be reduced. However, the particular evaluations are commonly performed manually and sequentially, which still result in a time-consuming process. Furthermore, there is no guarantee for the optimality of the final design. In order to ensure optimal design quality, the combination of CFD and optimization methods is a very promising approach. Suitable optimization methods are introduced in Chapter 3. In order to achieve an efficient usage of computational power and to reduce the development time further, a fully automated simulation-based optimization process has been developed. The general setup of the optimization process applied in the present work as well as the particular components are described in this Chapter.

## 5.1 CFD Optimization

From the literature mainly three different optimization strategies are known in combination with CFD: topology optimization, adjoint methods and parameter optimization. Topology optimization is widely used in the context of finite element methods, where weight reduction is in the focus gained by removing iteratively areas from the given design space, that do not influence the part's strength. Moos et al. (2004) applied this method for CFD applications, where he optimized an air manifold in terms of pressure drop by avoiding areas of flow separation. These areas are step by step removed as the computational cells are filled with 'numerical sand' according to the local level of pressure drop (Klimetzek et al. (2006)). Thus, the flow searches the most efficient way in the predefined space by itself. The great benefit of this method is, that only a few CFD simulations are required, which leads to a very efficient optimization approach. Furthermore, no design parameters have to be defined, thus reducing the complexity of the optimization problem. However, for each optimization target an indicator is required. In the case of mass flow, this can be local pressure drop; concerning charge motion an adequate indicator lacks. Hence, for the multi-objective optimization problem of the intake port geometry topology optimization is not applicable.

Kaminski et al. (2005) proposed an optimization approach based on the sensitivities of the objective function. These sensitivities indicate how to change the geometry in order to increase e.g. mass flow. The modification of the geometry is performed by transforming the particular nodes of the surface mesh according to the sensitivities by means of mesh morphing. Hence, the sensitivities have to be calculated at these nodes. Using gradient-based algorithms these sensitivities are usually derived by finite differences (Equation 3.7) leading to extensive computational effort, as for $n$ design variables, which are the mesh nodes in this case, at least $n+1$ calculations are required. The surface mesh of the intake port for example typically

contains several 1000 nodes. Using adjoint methods in contrast all sensitivities are obtained by a single CFD solver call independent of the number of design variables (Othmer and Grahs (2005)). Thus, a similar reduction of pressure drop compared to a topology optimization could be realized, while the calculation time is further reduced. However, the implementation of the adjoint approach into general-purpose CFD solvers is still in its infancy (Othmer et al. (2007), FlowHead (2009)). Accordingly, this method is of rather experimental stage and not yet suitable for the application within a series development process.

The major drawback however both approaches have to deal with is the reintegration of the final optimized design into the CAD-based development process, as in the case of topology optimization the result is a stepped surface shape existing of the mesh elements and in the case of adjoint methods a simple surface mesh. Precisely this fact accounts for the parametric optimization, as this method is based on the parametric geometry description by means of CAD models. Thus, the final design can be used within the development process without modifications. For this type of optimization the CAD parameters are the design variables. The actual optimization is performed by varying these parameters and evaluating the resulting designs by means of CFD simulations, while the optimization algorithm is thought to find optimal parameter combinations. Hence, the achievable improvement strongly depends on the choice of the geometrical parameters. The setup of the parametric CAD models accordingly is a crucial task. Another advantage in contrast to the approaches mentioned above is that the actual physics are not taken into account. Therefore, so-called 'black box' optimizers like Evolutionary Algorithms can be applied, which only require input and output data without knowing the physical relations between both leading to a robust and all-purpose optimization strategy (Othmer and Grahs (2005)). Altogether, parametric optimization is currently the most suitable approach for the integration of optimization methods into the series development process and is therefore applied for the optimization process introduced in the following.

## 5.2   Optimization Process Setup

**Fig. 5.1** shows the automatic optimization process. The setup is completely modularized consisting of a CAD, a meshing and a 3D-CFD module. Thus, the individual components like the parametric CAD model or the CFD analysis method can easily be replaced and adapted to specific problems. This loop is finally closed by means of dedicated optimization programs to perform a fully automatic optimization. Flexibility and automation together with robustness and efficiency are the major requirements for the implementation of optimization tools into the powertrain development process.
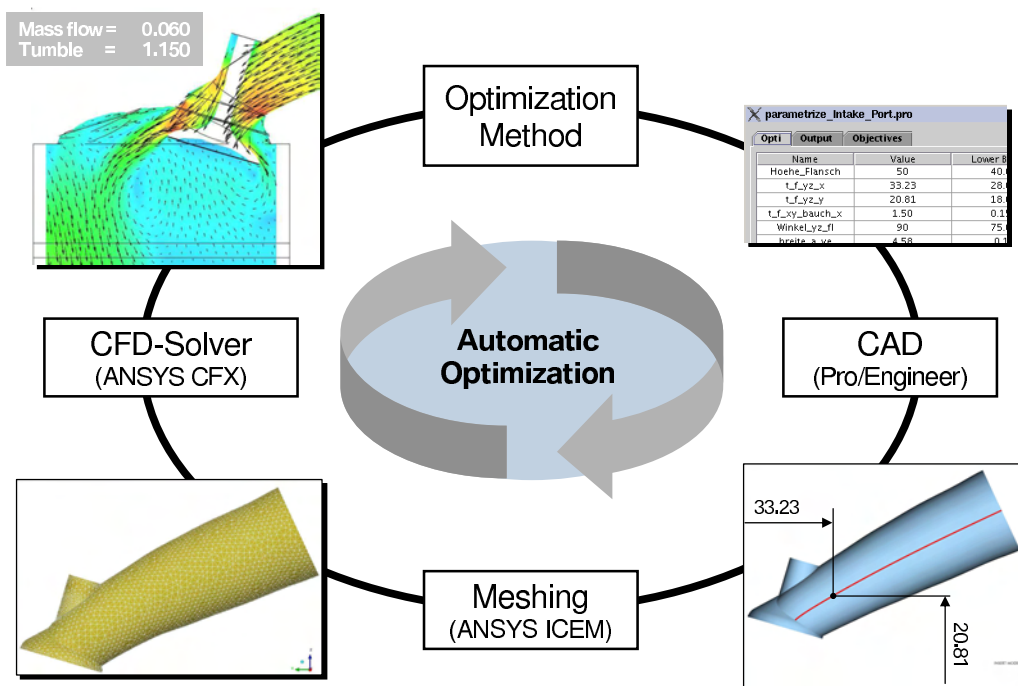


**Fig. 5.1:** Overview on the automatic CFD-based optimization process.

The flowchart of the CFD-based evaluation process is shown in **Fig. 5.2**. In general, this process is a stand-alone process and can be applied also manually without the use of an optimization algorithm. It is based on parametric CAD models designed in Pro/ENGINEER, that deliver appropriate designs according to the design parameters of the input file (trail-file). For an automatic optimization, the design parameters are modified by the optimization program. However, the trail-file can be edited manually by the user as well. ANSYS ICEM CFD is applied for the subsequent mesh generation according to the corresponding meshing restrictions and parameters defined in the replay-file. During the pre-processing the CFD definition-file is created by assigning boundary conditions to the mesh-file. ANSYS CFX is used for the analysis of the design variants by means of CFD methods. In a final step, the particular objectives of the optimization are derived from the result-file and written into an ASCII file, which is read by the optimization program in order to assess the quality of the actual design proposal. For ensuring a stable evaluation process, automatic monitoring is permanently applied. Therefore,

| INPUT-Files | | Module | | OUTPUT-Files |
|---|---|---|---|---|
| trail-file (*.txt) | → | CAD Module | → | geometry-file (*.tin) |
| replay-file (*.rpl) | → | Meshing Module | → | mesh-file (*.msh) |
| CCL-file (*.ccl) | → | CFD Pre Module | → | definition-file (*.def) |
| | | CFD Solver Module | → | result-file (*.res) |
| session-file (*.cse)<br>state-file (*.cst) | → | CFD Post Module | → | objective-file (*.txt) |
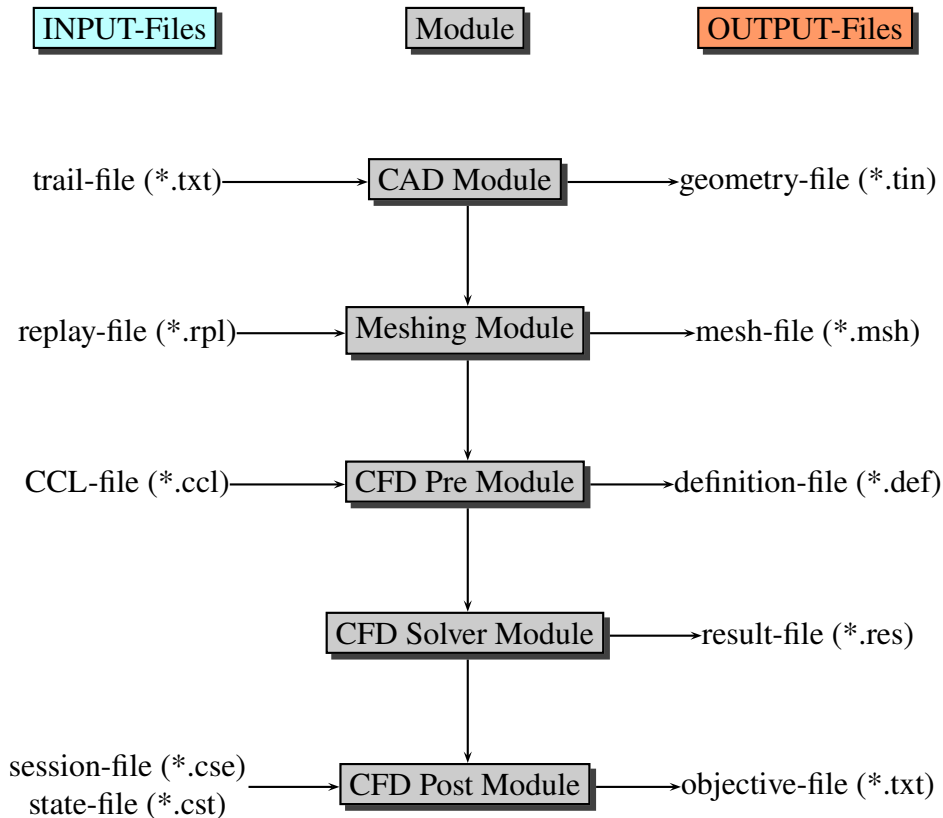
**Fig. 5.2:** Flowchart of the CFD-based evaluation process.

the feasibility of the geometry, the mesh quality and the simulation progress are checked. In the following, the individual components of the optimization process are described in more detail.

## 5.2.1 Parametric CAD Models

As mentioned in Chapter 4 the in-cylinder flow is mainly influenced by the intake ports and the combustion chamber. For the purpose of optimization parametric CAD models are created for both devices using the CAD tool Pro/ENGINEER.

**Intake Port Model**

The setup of the intake port model is shown in **Fig. 5.3**. It is designed according to the real manufacturing process, which is divided into a casting process and a machining operation. By this, it allows for a robustness evaluation of the manufacturing process by simulating a possible displacement of the raw part during the casting process relative to the subsequent machining operation. The CAD raw part represents the sand core of the casting process. It is based on the contour of the tumble port '8CBasis' applied for the series eight-cylinder turbocharged DISI-engine. In order to cover the whole range between tumble ports and filling ports by means

Raw part

Milling cutter
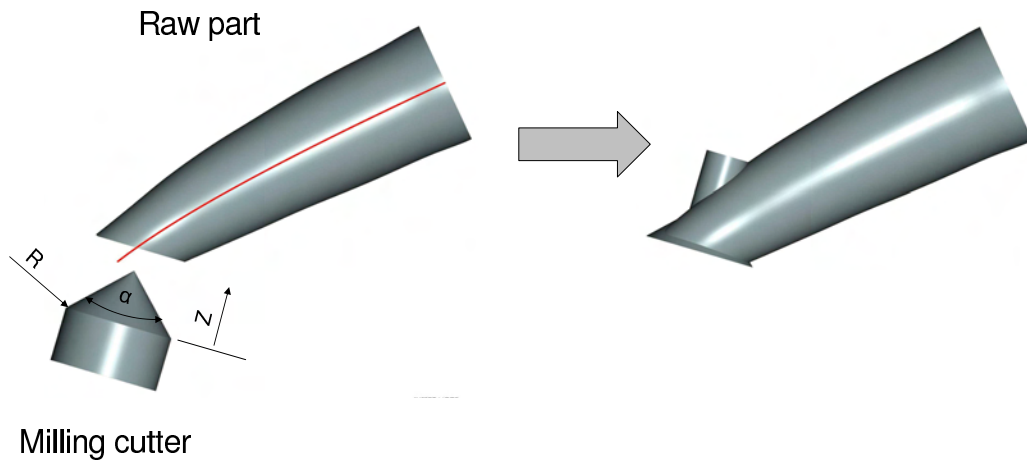
**Fig. 5.3:** General setup of the parametric intake port model based on the tumble port '8CBasis'.

of one CAD model, several parameters are added, while a well-known filling port design is used for the model adjustment. As shown in **Fig. 5.4** the parametric CAD model is based on a main construction line. In the vertical plane it is controlled by the x- and y-coordinate and the position of the intake flange defined by *Flange height* and *Flange angle*. The parameters *Sb_basis*, *Sb01*, ... , *Sb04* enable a s-bend-like or a rather straight course of the port within the horizontal plane. Along the construction line a total of ten cross-sectional planes, CS1 to CS10,
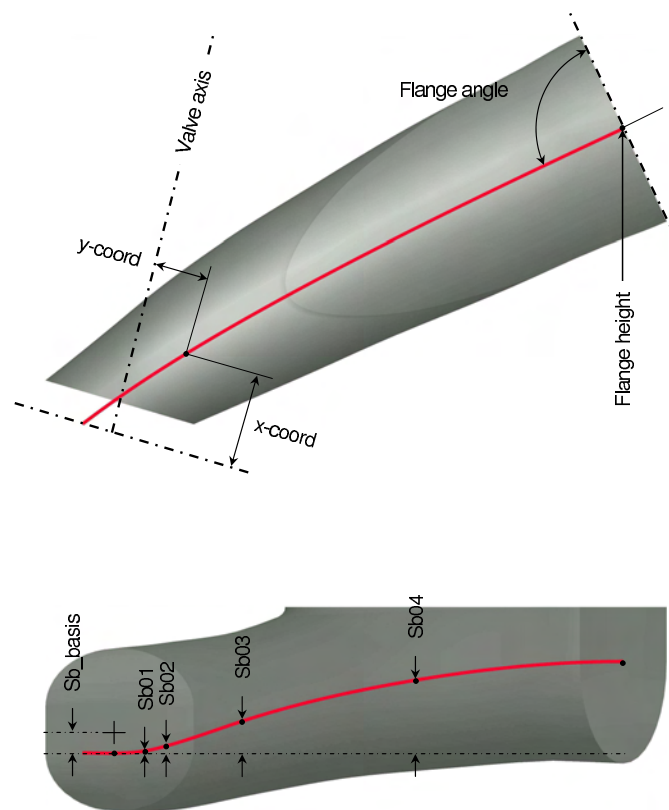


**Fig. 5.4:** Lateral and top view of the parametric intake port model containing the main construction line (red line).

are defined (**Fig. 5.5**). Additionally, the cross section at the line's beginning (CSB) and at its end (CSE) can be adapted. For each plane the cross section profile and area can be set individually by various parameters. These are the upper and lower radius $R_u$ and $R_l$, the upper and lower height $H_u$ and $H_l$ and the width $W$. For simplification only the half of the symmetric port model is shown in the Figures above. The upper cross sectional planes are therefore trimmed until the port is divided.
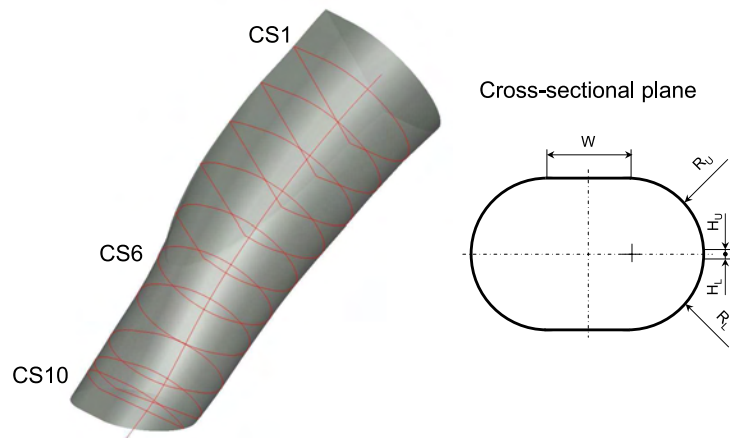


**Fig. 5.5:** Arrangement and definition of the cross sections along the intake port's centerline.

The machining operation is represented by a milling cutter. This cutter ensures the correct arrangement of the valve seat ring. In the case of a tumble port it further creates a characteristical edge at the port's backside in order to enforce flow separation, which is essential for the tumble formation. Concerning filling ports the machining operation is intended to improve the surface quality and to limit the tolerances resulting from the casting process. The milling cutter model is driven by three parameters: angle $\alpha$, radius $R$ and depth of cut $Z$ (**Fig. 5.3**). Altogether, 23 parameters are required for the proper representation of both filling and tumble port designs and the complete intermediate region between.

**Combustion Chamber Model**

In analogy to the intake port model, a parametric combustion chamber model has been developed. It is based on the four-valve cylinder head of the series four-cylinder engine '4CTC'. The real combustion chamber design is quite complex as it contains several machinings and roundings. Therefore, the original parametric CAD model is slightly simplified in order to guarantee adequate flexibility and reliable regeneration for the whole set of possible parameter combinations. Furthermore, as the engine design is symmetric only a half model is applied.

**Fig. 5.6** shows the side and the top view of the parametric combustion chamber model. The basic design is defined by the arrangement of the intake valves (IV) and exhaust valves (EV), characterized by the particular valve angle, valve depth and valve distance. The valve depth (*EV-/IV-depth*) is defined as the distance between the cylinder axis and the penetration point of the particular valve axis through a plane parallel to the cylinder head gasket. The distance
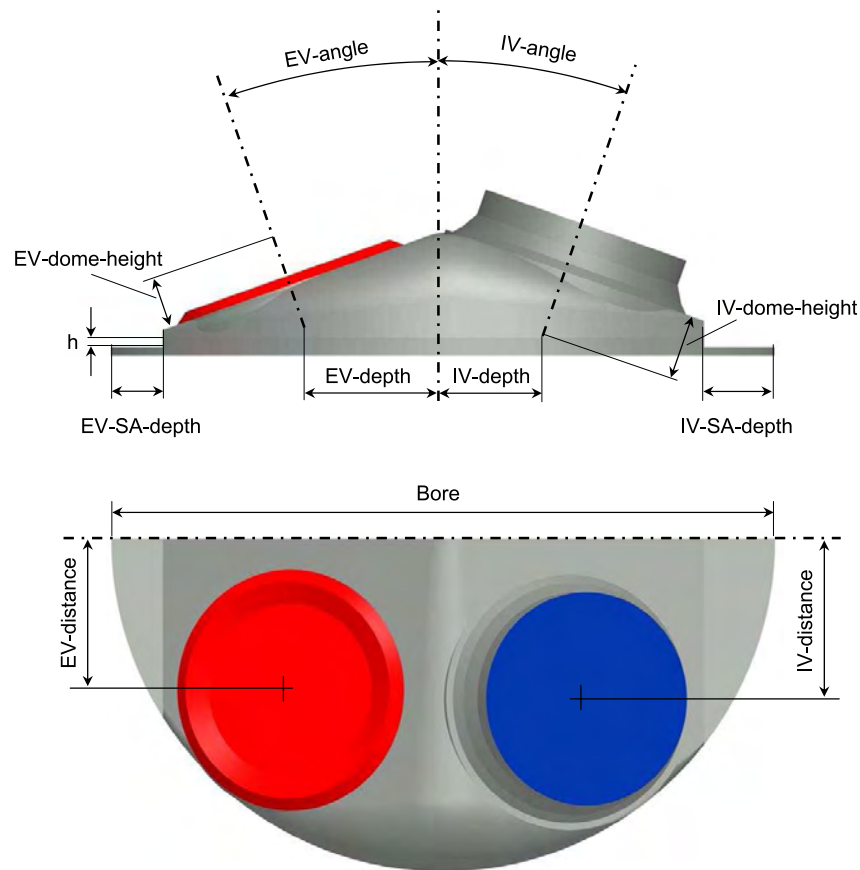
**Fig. 5.6:** Lateral and top view of the parametric combustion chamber model.

between both planes is driven by the height parameter *h*. The valve distance (*EV-/IV-distance*) is the distance between the valve axis and the symmetry plane. Valve depths and distances are limited such, that the particular gaps between the valves do not fall below a certain minimum, which is required due to thermal or structural stresses, and do not outreach the cylinder bore (Full (2007)). In this context the central arrangement of the spark plug device is regarded as well. The injector is located laterally between the intake ports. For simplification the roundings of the combustion chamber are either static or adjusted by relations according to the valve angle combination. The squish areas on both sides can be adapted by a single parameter respectively, the length in y-direction (*EV-/IV-SA-depth*). The dome height at the intake and exhaust side is adjusted by the particular valve seat ring (VSR) locations, *IV-dome-height* and *EV-dome-height*. The valve seat ring geometry itself and the intake valve are completely parametrized as well shown in **Fig. 5.7**. The changeable parameters are the height and the main angle of the intake VSR, *IV-VSR-height* and *IV-VSR-angle*, the *valve-stem-diameter* and the radius between valve stem and valve head, denoted as *valve-stem-radius*.

By varying the model parameters the engine's compression ratio $\varepsilon$ inevitably changes. Concerning the evaluation by means of steady flow simulations this fact can be neglected. However, for the assessment of turbulent kinetic energy or tumble motion by means of the dynamic analysis, the correct compression ratio has to be adjusted. Therefore, the combustion chamber volume is

**(a)** Valve seat ring                    **(b)** Intake valve
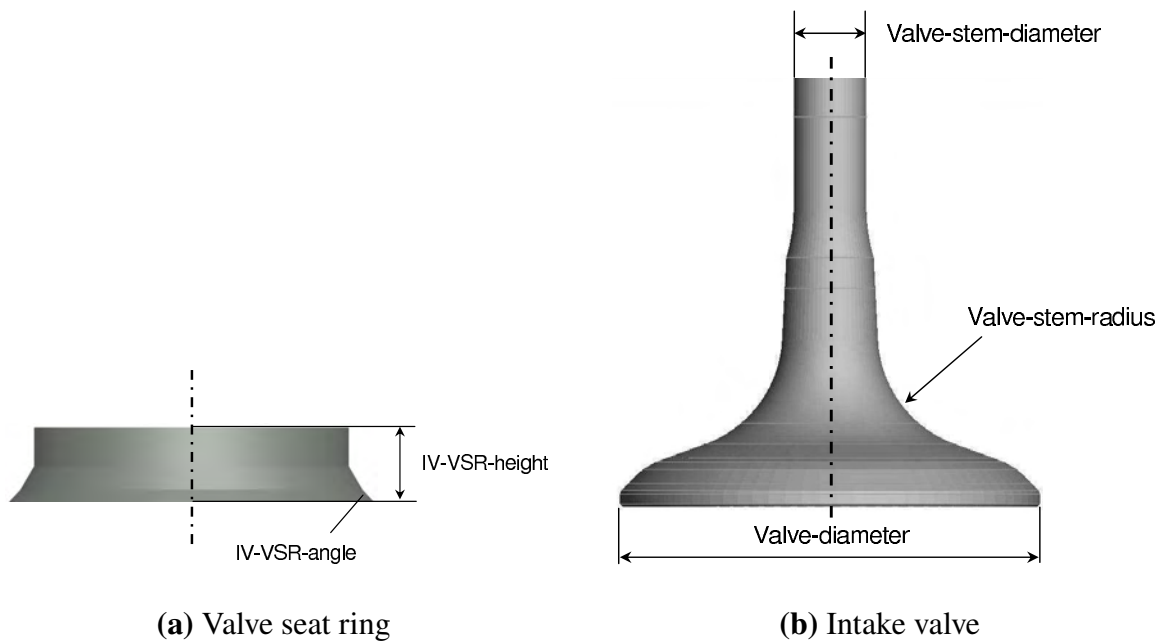
**Fig. 5.7:** Parametric CAD models for the valve seat ring (a) and the intake valve (b).

adapted by a height parameter $h$ between the chamber and the cylinder (**Fig. 5.6**). This parameter is chosen as small changes already lead to fast increase or decrease of the resulting volume due the large base area of the combustion chamber, while the general design of the combustion chamber is not affected. Altogether, about 15 individual parameters are investigated concerning the combustion chamber model.

## 5.2.2   Meshing Strategy

The different designs of the particular parametric CAD model are delivered in the TETIN format containing the geometry information in terms of surfaces, lines and points. The subsequent process of grid generation is performed automatically using tetrahedral elements. In order to account for boundary layers near the walls five prismatic layers are applied at solid walls. Tetrahedral based meshes are used, because hexahedral meshes do not offer the flexibility required for automatic mesh generation in the view of varying topologies during the optimization process. Tetrahedral elements in contrast offer suitable representation and resolution even for small design changes during a detailed local optimization.

As in any case of numerical simulation the mesh topology influences the simulation results as long as the grid resolution does not reach a grid independent solution. However, due to the size of the computational domain and with respect to reasonable calculation times the grid resolution is restricted. Thus, concerning optimization, where most often rather small improvements have to be assessed, it is very important to ensure similar mesh topology and quality for all designs. Otherwise, it can not be guaranteed that an improvement is gained by the particular geometry adaption and not by a different mesh topology. Therefore, new grids are created only for the

changing parts like different intake ports in the case of a port optimization, while the other parts like the combustion chamber and the cylinder region are created a priori and kept fixed. For the varying mesh parts similar quality is achieved by using the same set of meshing parameters during the entire optimization process. The changing part and fixed part meshes are merged afterwards by means of pre-defined interfaces, which enable direct grid connection for all mesh parts, thus avoiding interpolation errors. **Fig. 5.8** e.g. shows the interface (blue part) between port and combustion chamber for an intake port optimization. The prismatic layers along solid walls are created at last in order to keep these direct interfaces. As a result of this specific meshing process the mesh influence is minimized and it is ensured that it is similar for all investigated designs.
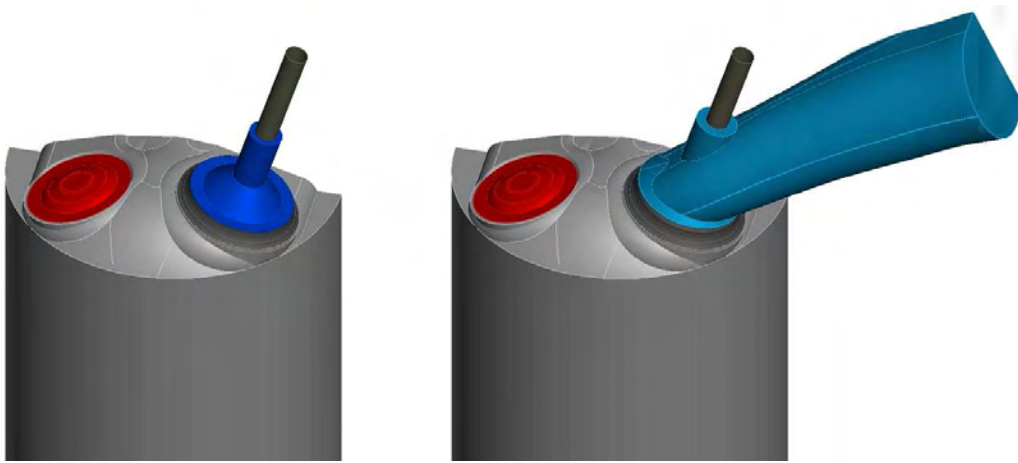


**Fig. 5.8:** Setup of the automatic meshing process for the intake port optimization.

Apart from simulation results, the mesh configuration also influences the calculation time according to the number of nodes and due to different convergence behavior. In the view of optimization, calculation times are of special interest. In order to quantify these influences, different meshing parameters are investigated. The main focus here lies on tumble inducing ports; hence this investigation is based on the tumble port 'FB05' introduced in Section 4.3. This port is very well analyzed by means of optical methods (**Fig. 4.14**) providing detailed information concerning characteristic numbers and the velocity field within the cylinder. Therefore, a detailed study concerning different grid types and resolutions applying the steady state analysis is performed shown in **Table 5.1**.

The standard mesh, which has been established within the series development process, is an unstructured mesh consisting of tetrahedral elements and prismatic layers at the wall. In order to reduce the number of nodes, a structured mesh is used within the cylinder for the variant 'Extrusion CYL', while the standard mesh is retained for the rest of the computational domain (**Fig. 5.9**). This structured mesh is derived by extruding the grid nodes lying in an interface below the cylinder head gasket along the cylinder axis. Thus, the unstructured standard tetrahedral-prismatic mesh inside the cylinder is replaced by a structured prismatic-hexahedral with a reduced number of nodes. For the 'Extrusion CYL fine' variant the average height of the prisms is reduced from h=1.8mm to h=0.9 for a better resolution of the cylinder. For the

| Type | Num. of Nodes | Description Mesh Type |
|------|---------------|----------------------|
| Standard mesh | 728 048 | Tetrahedral / Prismatic |
| Extrusion CYL | 608 762 | Mesh extrusion in Cylinder (h=1.8 mm) |
| Extrusion CYL fine | 780 098 | Mesh extrusion in Cylinder (h=0.9 mm) |
| Extrusion CYL / VS fine | 668 169 | Valve Seat fine |
| Standard mesh + Inlet | 828 408 | Inlet device rounded |
| Extrusion CYL + Inlet | 704 631 | Inlet device rounded |

**Table 5.1:** Overview on the investigated mesh types and parameters.

'Extrusion CYL / VS fine' variant the resolution of the valve seat region is refined, as this region is expected to be crucial for the typical flow separation concerning tumble ports. Finally, an additional inlet pipe with a rounded chamfer at the intake flange is arranged for both standard and extrusion mesh. This inlet pipe is commonly used for DGV-measurements, where it is placed between the flow straightener and the cylinder head (**Fig. 4.12**).

**Table 5.2** shows the measurement and the simulation results such as flow coefficient and tumble number. Additionally, the number of iterations and the CPU time of the CFD simulations are
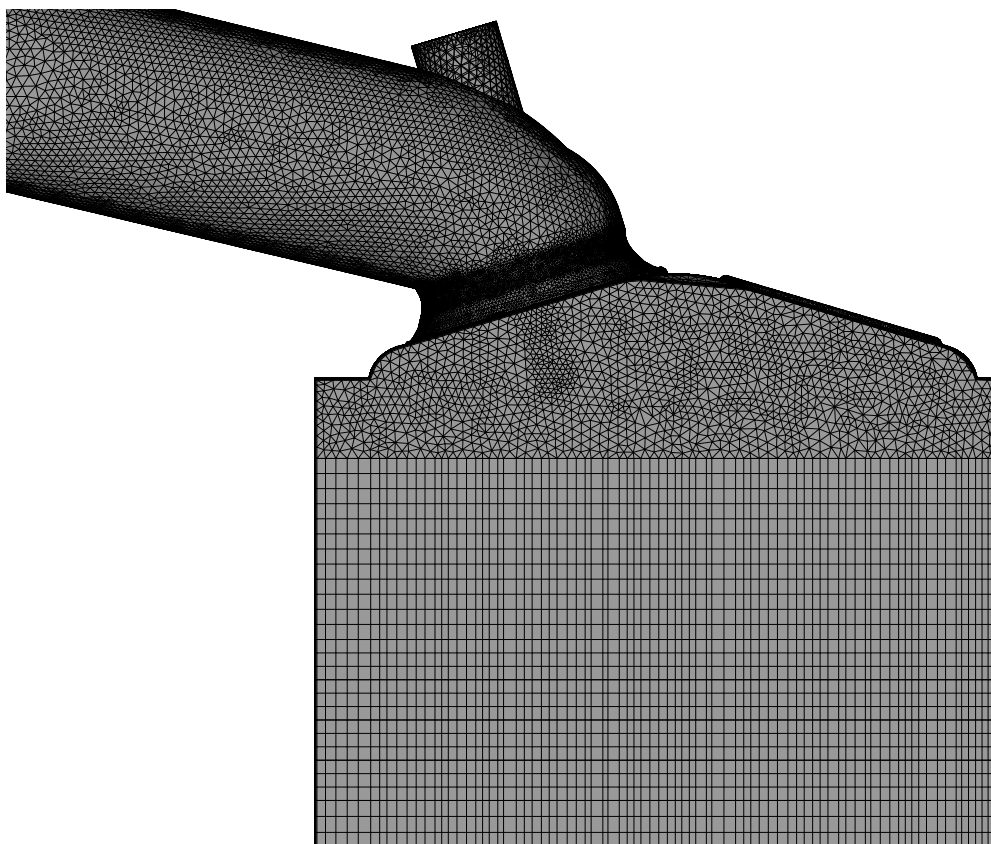


**Fig. 5.9:** Mesh type 'Extrusion CYL' containing an unstructured mesh for the intake port and the combustion chamber and a structured mesh for the cylinder.

listed. For this preliminary study the $k$-$\varepsilon$ turbulence model and the Upwind advection scheme are applied. The number of iterations is limited to maximum 300.

| Mesh type | $c_{f(piston)}$ ($\Delta$ *meas.*) | $TU_{VOL}$ ($\Delta$ *meas.*) | Iterations | CPU Time |
|---|---|---|---|---|
| Measurement | 0.145 | 0.640 | - | - |
| Standard mesh | 0.156 (7.6%) | 0.657 (2.7%) | 247 | 2h 15min |
| Extrusion CYL | 0.156 (7,6%) | 0.671 (4.8%) | 191 | 1h 23min |
| Extrusion CYL fine | 0.156 (7.6%) | 0.677 (5.8%) | 176 | 1h 41min |
| Extrusion CYL / VS fine | 0.156 (7.6%) | 0.675 (5.5%) | 195 | 1h 39min |
| Standard mesh + Inlet | 0.147 (1.4%) | 0.659 (3.0%) | 300 | 3h 11min |
| Extrusion CYL + Inlet | 0.147 (1.4%) | 0.676 (5.6%) | 118 | 1h 3min |

**Table 5.2:** Influence of grid type and resolution on the simulation results for $c_f$ and $TU_{VOL}$ using the steady state analysis based on the inlet port 'FB05'.

Good agreement between simulation and experiment concerning $TU_{VOL}$ ($\Delta$ 2.7%) is achieved for the standard mesh, while it is worse for the flow coefficient $c_f$ ($\Delta$ 7.6%). Using a structured mesh inside the cylinder, the flow rate difference remains while the tumble results worsen. The unstructured mesh seems to be more suitable for the non-directed tumble vortex. However, the CPU time is almost reduced by half as intended by using a structured mesh. Very promising results for $c_f$ ($\Delta$ 1.4%) are gained by regarding the inlet pipe of the DGV-setup (**Fig. 4.12**). Due to the inlet pipe the boundary layer is represented more realistically as it already starts at the rounded chamfer and is therefore almost fully developed at the beginning of the intake port. Without this pipe the boundary layer develops later inside the port resulting in lower flow losses and thus higher $c_f$. The general flow pattern in contrast is not influenced by the inlet pipe. For the specific mesh types similar results for $TU_{VOL}$ are delivered independent of the inlet pipe. Actually, the inlet pipe device is neglected for the purpose of simplification and saving of CPU time by reducing the computational domain. But for the extrusion mesh the computational effort is even reduced with the inlet pipe although the number of nodes is increased, which results from better convergence behavior. Accordingly, this type of mesh can be interesting for very extensive optimization problems or fast optimization with less demand of accuracy. In contrast, very good results for both objective values are gained by means of the standard mesh with inlet pipe, with a deviation of 1.4% for $c_f$ and 3.0% for $TU_{VOL}$. However, the computational effort is significantly enlarged, which is a critical factor concerning optimization.

For the present optimization process the adequate prediction of $TU_{VOL}$ is essential as the main focus is on tumble inducing ports. For this reason the basic standard mesh without inlet pipe is applied, as it shows the best accordance between simulation and experiment concerning $TU_{VOL}$. Reasonable computational effort is another fact which accounts for this mesh type.

In general, the results in **Table 5.2** show, that the influence of the mesh topology on the flow coefficient $c_f$ is negligible. It is solely determined by the fact if the inlet pipe is regarded or not. In contrast, the tumble number $TU_{VOL}$ is obviously influenced by the mesh topology,

while an unstructured mesh is found to be most suitable. The deviation between simulation and measurement varies between 3% and 6%, which is however acceptable.

### 5.2.3   3D-CFD Simulation

In Section 4.4 methods for the analysis of the in-cylinder flow using 3D-CFD tools are presented. These methods mainly differ in terms of level of detail and computational effort. Concerning optimization many designs need to be assessed, particularly in an early development stage, where the degree of freedom is relatively high. Accordingly, the calculation time of a single CFD evaluation is of special interest. **Table 5.3** contains a short overview of the different analysis methods and on the particular computational effort. Obviously, only the steady flow analysis at a specific valve lift is suitable regarding the computational costs. Using this method, more than 10 times the designs compared to the steady flow or the dynamic analysis can be evaluated in the same time. The specific valve lift(s) included for evaluation have to be defined for the specific optimization problem respectively. Concerning intake ports, typically

| Parameter | Steady Flow Analysis | | Dynamic Analysis |
|---|---|---|---|
| Simulation type | Steady state | Transient | Transient |
| Time-step | - | 3.375e-4 s | 1.3889e-5 s (0.5 deg CA) |
| Advection scheme | Upwind | | High Resolution |
| Turbulence model | $k$-$\varepsilon$ | | $k$-$\varepsilon$ |
| Boundary conditions | | | |
|   Inlet | Type: Inlet | | Type: Opening |
|  | Total pressure: 1 bar | | Total pressure: 1 bar |
|  | Static temperature: 293 K | | Static temperature: 293 K |
|   Outlet | Type: Opening | | - |
|  | Static pressure: 0.9 bar | | - |
|  | Static temperature: 293 K | | - |
|   Wall | Type: Wall | | Type: Wall |
|  | No-slip / smooth wall | | No-slip / smooth wall |
|  | Static temperature: 293 K | | Static temperature: 293 K |
| Valve lift range | Single lift(s) | 1 - 10 mm | Valve lifting curve |
| Computat. effort* | 2 h | 24 h | 36 h |

*6 CPUs, Half model

**Table 5.3:** Overview of the numerical setup of steady flow and dynamic analysis and the computational effort based on tumble port '8CBasis'.

the maximum valve lift is considered, as the most significant differences appear at this region (**Fig. 4.5**). Accordingly, the different design proposals during an optimization are evaluated by means of characteristic numbers for the flow rate and the charge motion, e.g. the flow coefficient $c_f$ and the tumble number $TU_{VOL}$, at maximum valve lift.

# 6 Application and Validation of Optimization Strategies

The aim of the present work is the development of an automatic optimization approach for the design of flow-guiding devices like the intake ports and the combustion chamber. In Chapter 5 a CFD-based optimization process is introduced. The application and validation of this process is presented in the following. In the first part the general influence of the particular CAD-parameters on the optimization objectives is investigated. Subsequently, an optimization strategy concerning the intake port design is introduced and applied for a global as well as for a local problem. This strategy is then validated by means of more detailed simulation methods. In the last section a corresponding approach for the combustion chamber is proposed and analyzed by means of a general optimization and a detailed optimization of a masking edge.

## 6.1 Influence of CAD-Parameters on Flow Rate and Charge Motion

Before performing a comprehensive optimization process, it is important to establish a general understanding for the influences of the CAD-parameters on the objectives like flow rate and charge motion, which have been identified as important measures by means of the intake port study in Section 4.2. For this purpose a sensitivity analysis, introduced in Section 3.5, is performed for both the intake port and the combustion chamber model respectively. As a result, the most important CAD-parameters are identified and the particular CAD-models can thus be simplified by removing less important parameters. For the engine development process, general guidelines concerning the engine design can be derived. Furthermore, by means of a sensitivity analysis possible conflicts between different objectives can be revealed.

### 6.1.1 Intake Port Geometry

As mentioned in Section 5.2.1 the parametric intake port model is designed to cover the whole range from filling ports, commonly applied for naturally aspirated SI-engines, to tumble ports, favorably used for turbocharged SI-engines. For this reason the CAD-model is rather complex containing more than 20 parameters. According to Dynardo (2008) the number of sampling points required for a stable sensitivity analysis correlates with the number of parameters, which rapidly rises the calculation effort for such a detailed model. Thus, for the purpose of gaining a general understanding, at first a less detailed model containing 8 parameters is applied. For the selection of the optimization parameters experiences gained from former projects are used (Loy (2005), Haslinger and Steinhagen (2005)). The varying parameters are given in **Table 6.1**, all other parameters are defined according to the tumble port '8CBasis', on which the parametric model is based on.

By default, the cross section area along the main construction line is defined by the particular parameters for width and radius. In order to reduce the number of parameters and modify the

| Parameter | Lower limit | Upper limit |
|---|---|---|
| *y*-coord | 15.0 mm | 17.95 mm |
| Cross section factor | 0.40 | 0.95 |
| Cross section width | 0.5 mm | 5.0 mm |
| Flange height | 52.0 mm | 56.0 mm |
| Flange angle | 75.0 deg | 95.0 deg |
| Milling cutter angle | 10.0 deg | 45.0 deg |
| Milling cutter depth | 0.0 mm | 7.0 mm |
| Milling cutter radius | 0.1 mm | 25.0 mm |

**Table 6.1:** CAD-parameters of the simplified intake port model used for the DoE.

cross section area by a single value, the parameter *cross section factor* is introduced. It drives the cross section area relative to the plane *CS6* (**Fig. 5.5**). A value of 1 denotes, that the cross section area from *CS6* on stays constant along the construction line, while a value of 0.5 linearly decreases the area from *CS6* on to the half until the last cross section (here the valve seat ring). The cross sectional width is also exclusively defined at the plane *CS6* and kept constant for the remaining planes *CS7* to *CSE*. The upper part of the intake port's cross section (*CS1* to *CS5*) is not modified at all.

Based on the combustion chamber of the eight-cylinder SI-engine, a total of 479 intake port variations are defined by means of a Latin-Hypercube-DoE. From these, 268 designs are feasible and can be evaluated, while the remaining 211 designs are infeasible or failed. Concerning the intake port the classification into feasible, infeasible and failed designs can be described as:

- **Feasible design**: The intake port design is accurately regenerated by the CAD program, evaluated by means of 3D-CFD and is producible.

- **Infeasible design**: The intake port design is accurately regenerated by the CAD program but is not producible, which occurs when the raw part exceeds the milling cutter leading to a freestanding valve seat ring.

- **Failed design**: The intake port design cannot be assessed accurately as a module within the optimization loop fails. In the majority of cases the regeneration by the CAD program fails, while mesh generation and CFD-analysis are found to be very stable.

**Fig. 6.1** shows the feasible designs in terms of flow coefficient $c_f$, for which the inner seat diameter is taken as reference, and the volumetrically averaged tumble number $TU_{VOL}$ gained by means of a steady flow analysis at 10 mm valve lift. Additionally the series filling port '6CNA' (blue square) and the tumble port '8CBasis' (red square) are regarded as reference ports. Obviously, the parametric intake port model is able to cover the entire range of common port types. Concerning filling ports, characterized by high $c_f$ values, the simplified model performs very well. Some ports even exceed the six-cylinder port concerning $c_f$. However, one has to
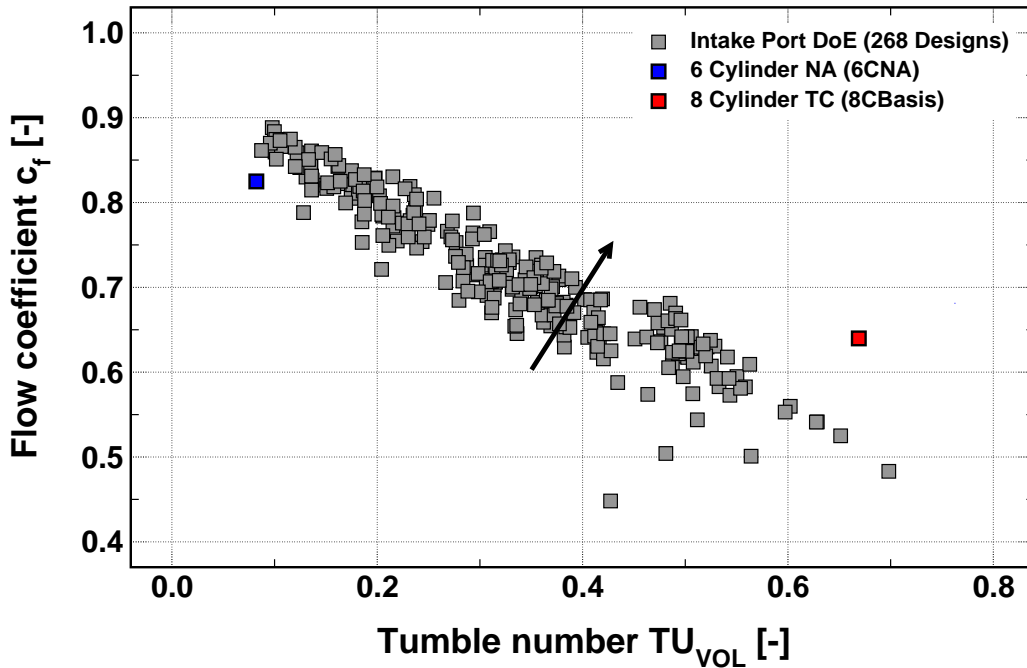
**Fig. 6.1:** Flow coefficient $c_f$ vs. tumble number $TU_{VOL}$ for the intake port DoE.

consider that this port is evaluated on the basis of a different combustion chamber with different cylinder bore and inner valve seat diameter and therefore hardly comparable. Concerning the high tumble region in contrast, no design comes up to the series tumble port. Furthermore, the density of designs decreases significantly at this region. Nevertheless, by means of this rather simple model the strict conflict between mass flow and charge motion is illustrated, resulting in a multi-objective optimization problem.

Based on these DoE-results a sensitivity analysis is performed using the statistical measures introduced in Section 3.5. **Fig. 6.2** shows the linear correlation $r_{xy}$ of the particular CAD-parameters to both objectives, flow coefficient and tumble number. As depicted in Section 3.5, a value larger than 0.7 indicates a strong correlation and a value below 0.3 no correlation (Dynardo (2008)). However, as only 268 designs are evaluated it is important to regard the statistical significance. Based on this sampling size the probability that the correlation results from mere coincidence is only $1e^{-5}\%$ for $r_{xy} = 0.7$ and $5e^{-5}\%$ for $r_{xy} = 0.3$ (see Lowry (2010)). Thus, the correlation coefficients can be regarded as significant.

Concerning $c_f$, the cross section area, represented by the *cross section factor*, is the dominating parameter. For a high value of $c_f$ an almost constant progression of the cross section area along the port is essential. Another important parameter is the *y-coord*. With increasing values the lower part of the intake port more and more runs parallel to the valve axis. This is illustrated by means of the radial mass flow distribution through the valve gap comparing a filling port, characterized by a large *y-coord*, and a tumble port with accordingly small *y-coord* (**Fig. 6.3**). Applying the filling port, the fluid flow is guided more uniformly over the valve head, which increases the flow rate compared to the tumble port. A likewise effect is gained by a large *milling cutter radius* and *milling cutter depth* concerning the machining operation.

**(a)** Flow coefficient $c_f$            **(b)** Tumble number $TU_{VOL}$
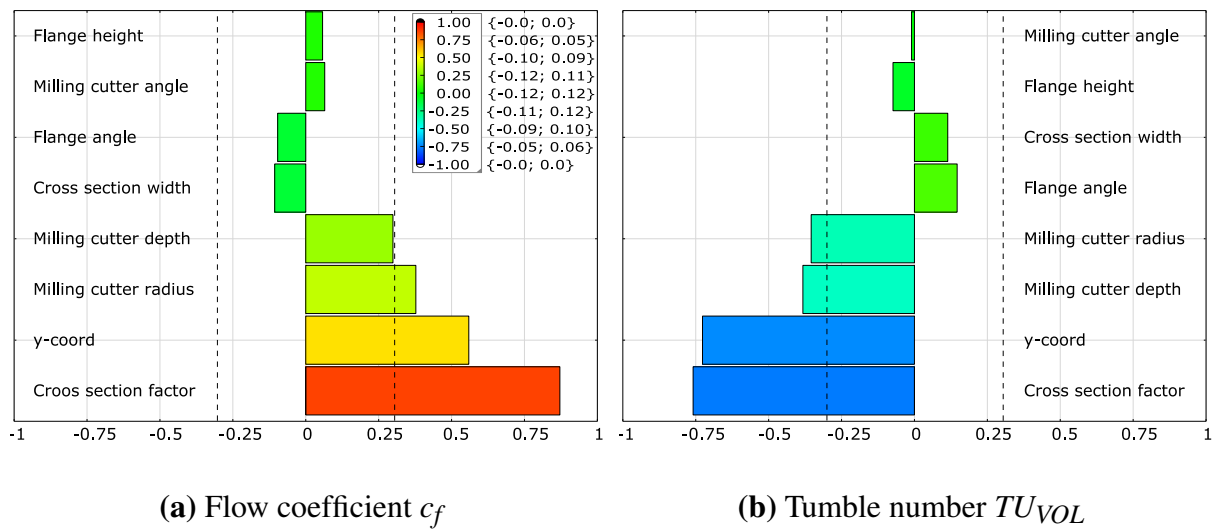
**Fig. 6.2:** Linear correlations and confidence interval gained from the sensitivity analysis for the intake port model estimated by 268 samplings.

In terms of tumble the same parameters as for $c_f$ are important, however their influence is directly opposed, which leads to the conflict between flow rate and charge motion. For high values of $TU_{VOL}$ both *cross sectional factor* and *y-coord* tend to small values, indicated by a strong negative correlation. With decreasing *y-coord* values the fluid flow meets the valve stem under a significant off-axis angle. As a result, the air flow is mainly guided over the front part of the valve head as depicted in **Fig. 6.3** for the tumble port, thus leading to a non-uniform flow into the combustion chamber and finally to a high $TU_{VOL}$. This effect is enforced by a well-defined edge at the port's backside, which leads to a well-defined flow separation. Both *milling cutter depth* and *milling cutter radius* directly influence this edge. In order to increase $TU_{VOL}$, small
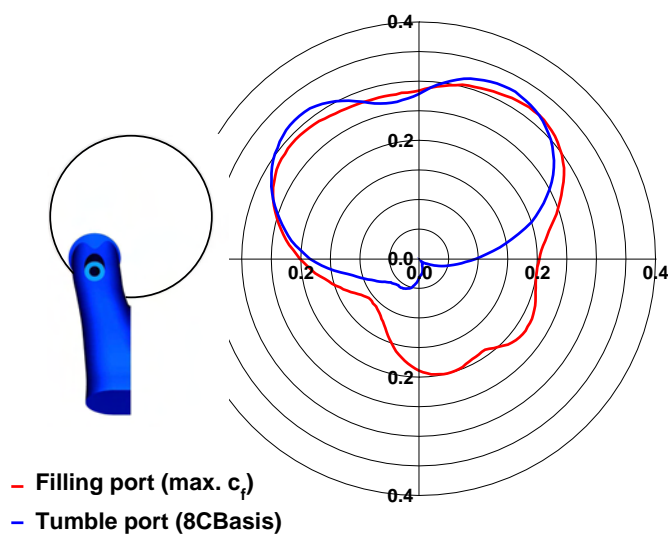


**Fig. 6.3:** Radial mass flow distribution through the intake valve gap for the filling port with max. $c_f$ and the tumble port '8CBasis'.

values are required for both parameters. All other parameters do not have a strong influence on the objectives and may be neglected. Thus, an intake port model containing 4 CAD-parameters is suitable to represent both filling and tumble ports.

**Fig. 6.4** shows a vertical cut through the valve plane for the optimal filling port and the basic tumble port '8CBasis' with their corresponding flow patterns. By means of these ports, the specific relations between CAD-parameters and resulting in-cylinder flow, identified by the sensitivity analysis, can be illustrated. In general, this analysis revealed, that the influence of the raw part design (*cross sectional factor*, *y-coord*) is significantly more important compared to the milling cutter (*milling cutter depth*, *milling cutter radius*). Accordingly, the design of the raw part, which has to be defined in an early stage of the development process, is a crucial task. A later adaption of the tumble or flow rate characteristic by a modified machining operation is limited and less efficient. In the case of the intake port '8CBasis', a further increasing of the tumble number could only be realized by a modified design of the raw part as the parameters of the milling cutter are already set for maximum tumble.
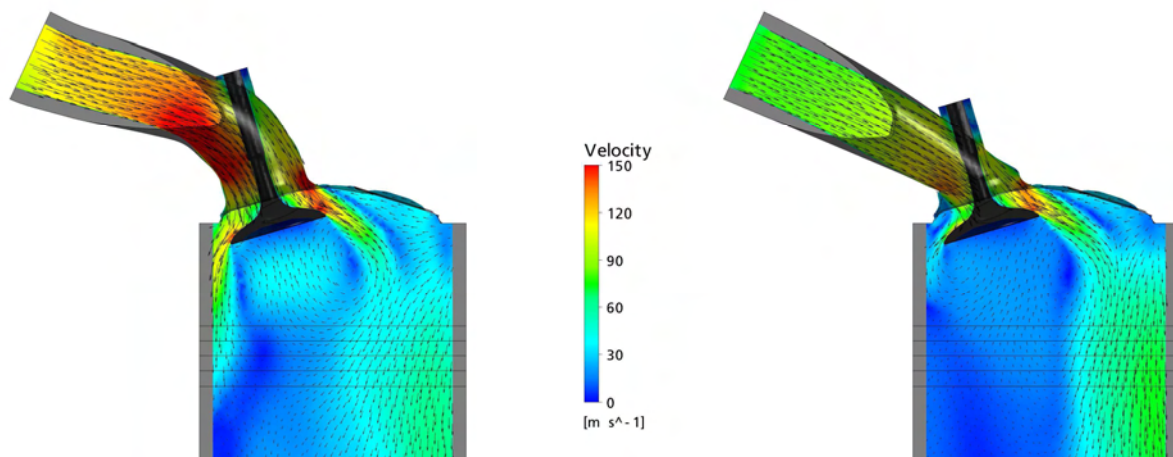


**Fig. 6.4:** Flow pattern of a filling (left hand side) and a tumble port (right hand side).

Apart from the relations mentioned above, the sensitivity analysis can also explain the low density of designs at high tumble numbers (**Fig. 6.1**). The reason for this is the high number of infeasible and failed designs particularly in this region.

As depicted by the sensitivity analysis in **Fig. 6.2**, a negative correlation between *y-coord* and $TU_{VOL}$ exists. Accordingly, for higher tumble numbers *y-coord* has to decrease. However the cross section area has then to decrease as well, as otherwise the raw part exceeds the milling cutter and the design becomes infeasible as described before. As the CAD-parameters are distributed statistically by means of the DoE, the probability for infeasible designs is significantly higher in the range of low *y-coord* values (**Fig. 6.5**), which are characteristically for tumble ports. A restriction of the *cross sectional factor* according to the value of *y-coord* could prevent this problem. However, to define this relation adequately without restricting the model's flexibility too much is very difficult, as the feasible variation range of a parameter depends on the current values of the remaining parameters respectively. Instead, infeasible designs
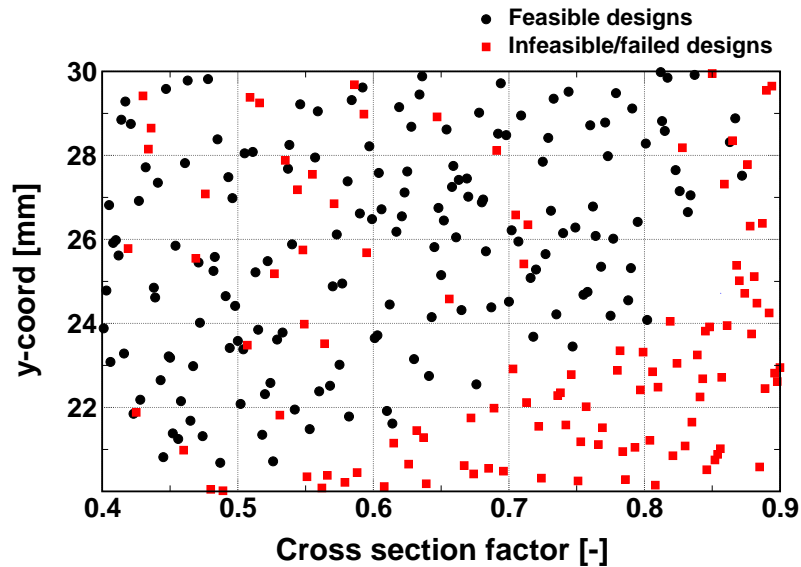
**Fig. 6.5:** *y-coord* vs. *cross section factor* for feasible and infeasible/failed intake port designs.

are identified by evaluating the actual area of the valve seat machining, which for infeasible designs exceeds the nominal size, and rejected from the optimization process. For the real manufacturing process this is a problem as well, as casting tolerances can lead to rejections due to freestanding valve seat rings. Altogether, from a total of 479 samplings, 268 (56%) designs are evaluated, while 211 (44%) designs are infeasible or failed.

## 6.1.2  Combustion Chamber Geometry

As for the intake port, a sensitivity analysis based on a DoE is performed for the combustion chamber geometry in order to evaluate the influence of its CAD-parameters on the objectives mass flow and tumble. Unlike the intake port, where geometry variations lead to a general improvement or worsening over the entire valve lift range, most combustion chamber parameters do not have a well-defined influence on the particular objectives (Elwan (2008)). In fact, geometry variations show e.g. worsening effects at low lifts combined with enhancements at high lifts and vice versa. This phenomena is illustrated in **Fig. 6.6** exemplarily for the parameter *IV-SA-depth*, which denotes the depth of the squish area on the intake side (**Fig. 5.6**). Due to this fact, the combustion chamber influence on the in-cylinder flow behavior cannot be assessed by means of one single lift only. Instead, the entire valve lift range or several representative valve lifts have to be investigated by means of the steady flow analysis. For this investigation two particular valve lifts are regarded, the maximum valve lift (9 mm) and a medium valve lift (6 mm), which significantly increases the computational effort compared to the intake port DoE before. Due to this the number of design variations for this DoE is reduced to 300 designs leading to similar overall computing time as for the intake port investigation.

**Fig. 6.7** shows the results of a parameter variation for the combustion chamber model, while the basic intake port '4CTC' has been retained unchanged. The varying CAD-parameters for this problem are listed in **Table 6.2**. From 300 proposed designs, 184 (61%) designs are found to be
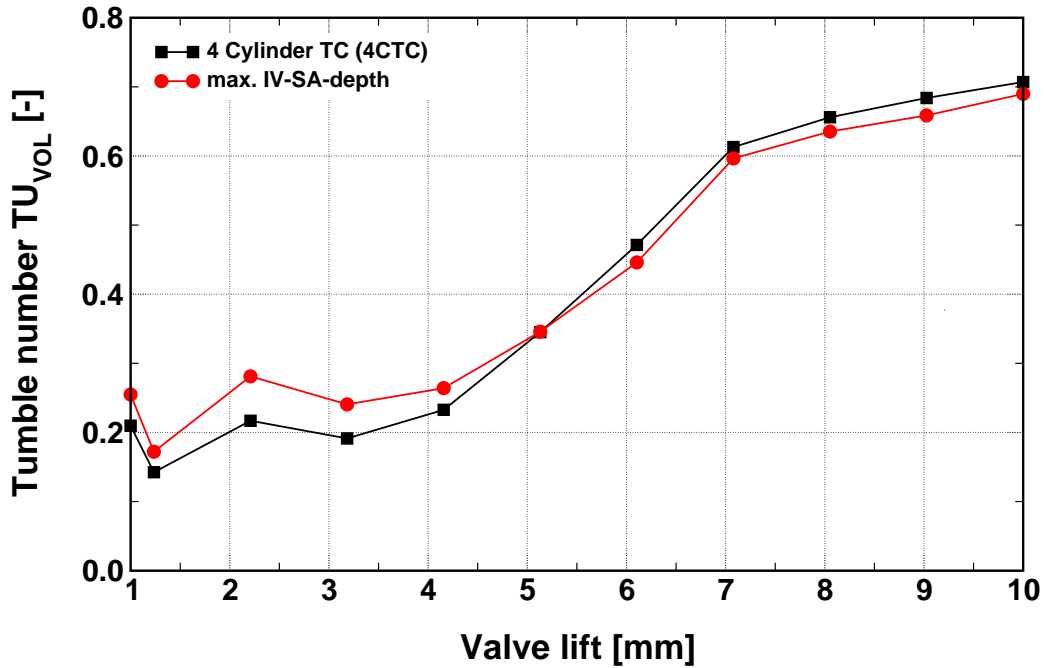
**Fig. 6.6:** Influence of combustion chamber parameter *IV-SA-depth* (squish area depth) on tumble number $TU_{VOL}$.

feasible, while the remaining 116 designs are infeasible or failed. For the combustion chamber investigation the classification of feasible, infeasible and failed designs is defined as:

- **Feasible design**: The combustion chamber design is accurately regenerated by the CAD program, evaluated by means of 3D-CFD and is producible.

- **Infeasible design**: The combustion chamber design is accurately regenerated by the CAD program but is not producible or applicable. This occurs for example when the distance between the particular valves is too small in the view of mechanical or thermal stresses or the valves outreach the cylinder bore. For this purpose constraints based on minimum distances are introduced as described in Section 5.2.1, which have to be fulfilled for feasible designs.

- **Failed design**: The combustion chamber design cannot be assessed accurately as a module within the optimization loop fails. As for the intake port in the majority of cases the regeneration by the CAD program fails due to extreme parameter combinations like very different valve angles on the intake and exhaust side. Mesh generation and CFD-analysis in contrast are again found to be very stable.

The feasible designs are evaluated at both valve lifts by means of the steady flow analysis. Although less design variations are evaluated for the combustion chamber DoE (184 compared to 268 for the intake port DoE), the level of statistical significance still is high. For a correlation coefficient of e.g. $r_{xy} = 0.7$ the probability that the correlation results from mere coincidence is below $1e^{-5}\%$, for $r_{xy} = 0.3$ still below $1.75e^{-3}\%$ (see Lowry (2010)).
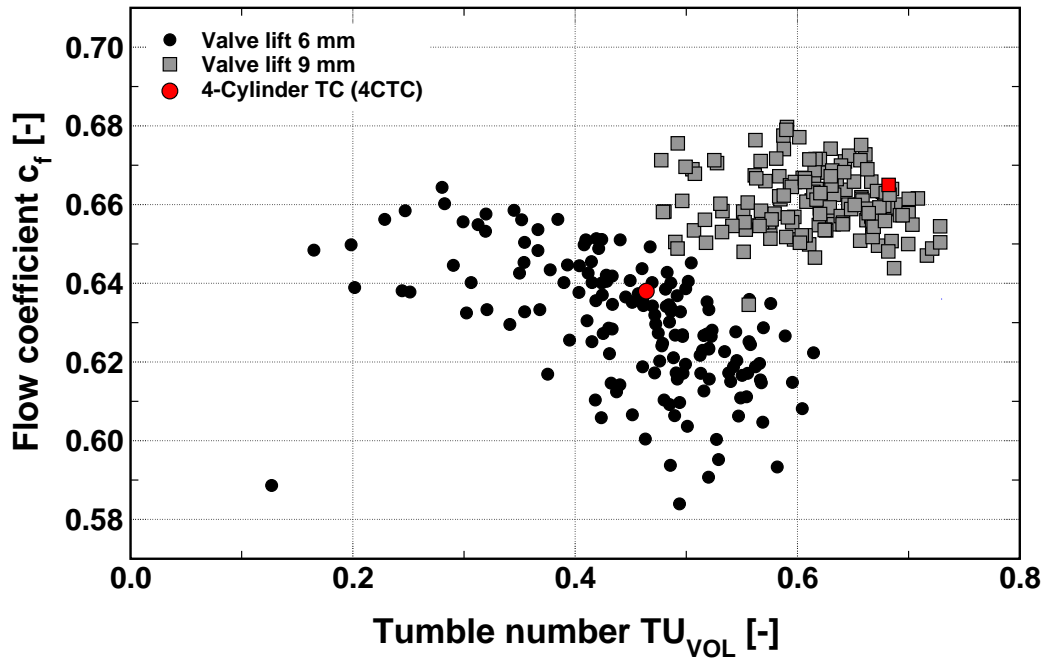
**Fig. 6.7:** Flow coefficient $c_f$ vs. tumble number $TU_{VOL}$ for the combustion chamber DoE.

The results in **Fig. 6.7** confirm significant influence of the combustion chamber geometry, primarily on the tumble number. For a valve lift of 6 mm the tumble variations are almost on the same level as for the intake port investigation before. **Fig. 6.7** also shows, that the variations at 9 mm are smaller than at 6 mm. Obviously, the influence of the combustion chamber decreases with rising valve lifts, as the influence of the intake port gains in significance. These results clarify that different parts of the cylinder head are of interest when optimizing the in-cylinder flow of SI-engines with fully variable valve drive. According to the intake port comparison in

| Parameter | Lower limit | Upper limit |
|---|---|---|
| IV-distance | 16.35 mm | 18.50 mm |
| IV-depth | 10.5 mm | 14.0 mm |
| IV-angle | 15.0 deg | 25.0 deg |
| IV-dome-height | 6.5 mm | 8.5 mm |
| IV-SA-depth | 6.0 mm | 12.0 mm |
| EV-angle | 15.0 deg | 25.0 deg |
| EV-dome-height | 6.0 mm | 7.5 mm |
| IV-VSR-angle | 45.0 deg | 55.0 deg |
| IV-VSR-height | 4.4 mm | 6.5 mm |
| Valve-stem-radius | 4.0 mm | 10.0 mm |
| Valve-stem-diameter | 2.485 mm | 3.150 mm |

**Table 6.2:** CAD-parameters of the combustion chamber model used for the DoE.

Section 4.2, at part load with VVT operation, the focus is on the flow characteristics at small valve lifts, which are mainly dominated by the combustion chamber and the valve seat ring design. The intake port geometry has to be investigated primarily at full load conditions due its dominating influence at large valve lifts. Likewise for the intake port, a clear trade-off between $c_f$ and $TU_{VOL}$ appears, which is however less strict indicated by a rather narrow spread of the designs.

**Fig. 6.8** illustrates the results for the linear correlation $r_{xy}$ gained from a sensitivity analysis at 6 mm valve lift. This analysis reveals that the height of the valve seat ring (*IV-VSR-height*) is the only parameter with a well-defined influence at this valve position. However, the influence on both objectives is contrary leading to a conflict of objectives. A higher seat ring leads to an increase of $c_f$, as less flow separation occurs and the air flow is distributed more evenly over the valve orifice (Elwan (2008)). A shortened valve seat in contrast significantly enhances the tumble number, as the point of flow separation comes closer to the intake valve, which prevents a reattachment of the flow. Furthermore, the transition from the port to the chamber is more suitable for the tumble formation, as the step between the VSR and the combustion chamber roof on the exhaust side is smaller. As a result, the flow of the inlet jet along the chamber roof is supported, thus resulting in enhanced tumble motion.



**(a)** Flow coefficient $c_f$                                **(b)** Tumble number $TU_{VOL}$
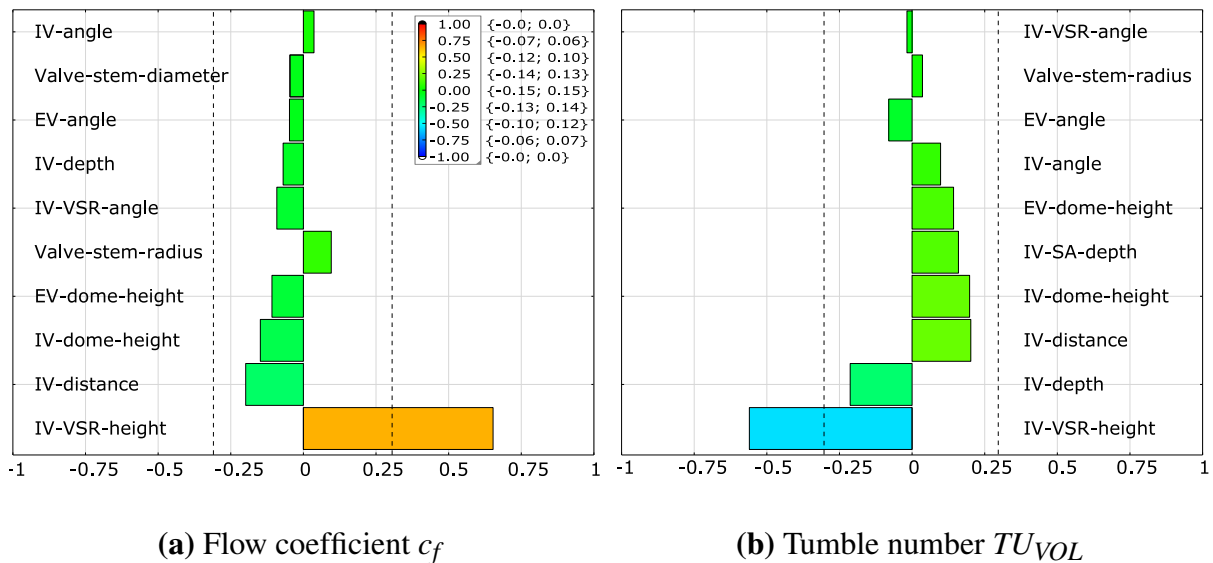
**Fig. 6.8:** Linear correlations and confidence interval gained from the sensitivity analysis for the combustion chamber model at 6 mm lift estimated by 184 samplings.

The results of the sensitivity analysis at 9 mm valve lift are given in **Fig. 6.9**. In terms of mass flow a single parameter is dominating, the squish area at the intake side (*IV-SA-depth*). The enlargement of this area has a similar effect as a masking of the intake valves, as the combustion chamber wall comes very close to the valves. Usually, masking is applied to increase the tumble at low valve lifts, which simultaneously decreases the flow coefficient $c_f$. At high lifts valve masking shows a slightly enlarged $c_f$, as the air flow of both ports is separated by the masking edge and their influence on each other thus reduced. Furthermore, the vortex formation in the

**(a)** Flow coefficient $c_f$        **(b)** Tumble number $TU_{VOL}$
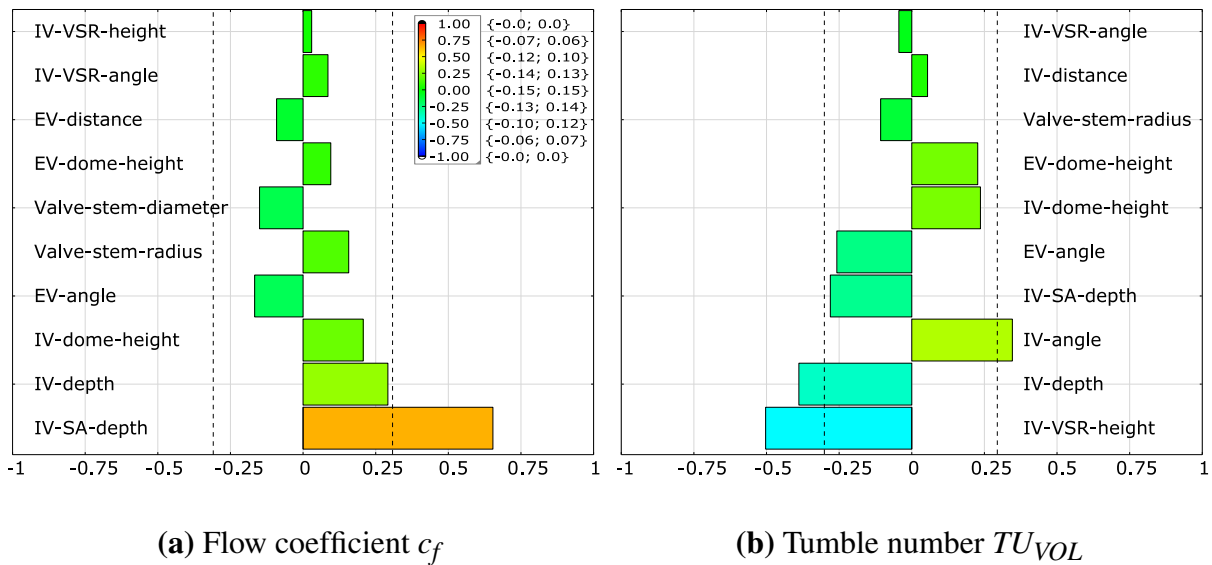
**Fig. 6.9:** Linear correlations and confidence interval gained from the sensitivity analysis for the combustion chamber model at 9 mm lift estimated by 184 samplings.

region of separation is prevented by means of masking (Elwan (2008)). Concerning tumble the influence of the seat ring height (*IV-VSR-height*) on the in-cylinder flow again is the dominating parameter as for the 6 mm lift case. Additionally, the distance of intake valve to the cylinder axis *IV-depth* and the intake valve angle (*IV-angle*) gain in significance. By decreasing *IV-depth*, which denotes that the intake valves are moved towards the cylinder axis, a higher value for $TU_{VOL}$ is gained. The reason for this is that the air flow tends to guide towards the exhaust side, which leads to an enlarged lever arm with respect to the referenced tumble axis. The same effect is obtained by increasing the intake valve angle *IV-angle*.

## 6.1.3 Conclusions

Concerning the intake port a strict conflict between both objectives $c_f$ and $TU_{VOL}$ is revealed by means of the DoE and sensitivity analysis. As a consequence, a multi-objective optimization has to be performed requiring suitable optimization algorithms, which are able to deal with such problems. The intake port model is furthermore found to be suitable for a global optimization, as it is able to cover continuously the whole range of port designs from filling to tumble ports. Thus, a single CAD-model is sufficient. However, in order to achieve promising results, particularly for the tumble port region, a more detailed model has to be applied instead of the simplified one. In addition the number of infeasible and failed designs must be reduced in this region. According to the sensitivity analysis the main focus concerning the intake port optimization has to be put on the design of the raw part, due to its major influence on the in-cylinder flow. Nevertheless, raw part and machining operation have to be investigated simultaneously, as both have to be co-ordinated.

For the combustion chamber a conflict of objectives is observed as well. However, this conflict is less strict. For a global assessment of a combustion chamber design the evaluation at a single valve lift only is not sufficient. Thus, for an overall optimization of the system several lifts have to be regarded, while with rising valve lifts the influence of the chamber shape obviously decreases and the influence of the intake port increases. Nevertheless, the influence of the chamber roof is partly in the range of the intake port geometry.

In general, by means of a sensitivity analysis the dominating CAD-parameters can be identified, while for both parametric models only a few are of major interest. Thus, for an optimization the number of design parameters can be reduced leading to less computational effort. Furthermore, proper guidelines for the design of the cylinder head components can be derived. The results also clarify that different parts are of interest for an optimization of the in-cylinder flow according to the particular operating point. While the focus is on the combustion chamber shape for part load conditions with small valve lifts (VVT), it shifts to the intake port design with rising valve lifts. For the purpose of pure optimization however a DoE-approach is not efficient.

## 6.2 Optimization Strategy for an Intake Port Geometry

In this section, an optimization strategy for an intake port geometry is investigated, where the characterization of the particular port designs is based on a single valve lift evaluation using the steady flow analysis at a single lift. Therefore, the maximum lift is regarded as it is assumed to be representative for the entire lift range. Apart from design evaluation, suitable optimization methods are required for the actual search towards optimal solutions. As observed by means of the sensitivity analysis, regarding the intake port optimization, a multi-objective problem arises due to the conflict of objectives between $c_f$ and $TU_{VOL}$. For this purpose, Evolutionary Algorithms (EAs) are suitable optimization methods, as they can deal with multiple objectives simultaneously due to their population approach (Deb (2001)). Thus, in the following different EAs are investigated, both for solving the optimization problem directly and in combination with a Response Surface Method (RSM), where a surrogate model is built which is intended to represent the physics of the real problem by means of analytical expressions. For the investigation and validation of the single lift based strategy, a global optimization problem as well as a very detailed optimization problem of an existing series port are discussed.

### 6.2.1 Response Surface Methods

Apart from a sensitivity analysis the DoE results can be applied for meta modeling techniques like Response Surface Methods (RSM). As mentioned in Section 3.4 meta models are applied for the purpose of optimization, as they can reduce the computational effort significantly (Myers and Montgomery (2002)). The results derived by a DoE serve as input for the calculation of the meta model, which is intended to represent the physical relations of the optimization problem by means of mathematical terms. During the final optimization the mathematical meta model is evaluated instead of performing further time consuming CFD simulations. For the optimization process this implies, that the CFD-module is replaced by the evaluation of the RSM. However, it is required that the model can represent the physics of the problem adequately. To set up the mathematical formulation of the Response Surfaces an in-house Matlab-based tool is used (Blumhardt (2001)), which calculates the RS stepwise on the basis of regression analysis. During the calculation, the prediction quality is evaluated and optimized by cross validation as introduced in Section 3.4. During the evaluation process, reduced quadratic models are found to perform best for both $c_f$ and $TU_{VOL}$. Finally, the regression coefficients of these models are determined on the basis of all DoE designs. For both objectives good values for $R^2_{adj}$ are achieved, as for $c_f$ it amounts to 0.989 and for $TU_{VOL}$ to 0.961 (see Equation 3.23).

**Fig. 6.10** shows the results gained by the optimization evaluating the RS models for $c_f$ and $TU_{VOL}$ (blue points). For the optimization process the ClearVu Global Optimizer in Optimus V5.2 is applied, which is suitable due to its multi-objective approach. Compared to the DoE results significant improvements are gained towards high $TU_{VOL}$, while for high values of $c_f$ both DoE and RSM deliver results of equal quality. In general, the strict conflict between mass flow and charge motion again is revealed, while the Pareto-front predicted by the meta model seems to be almost linear. Of course, the subsequent validation of these approximated results
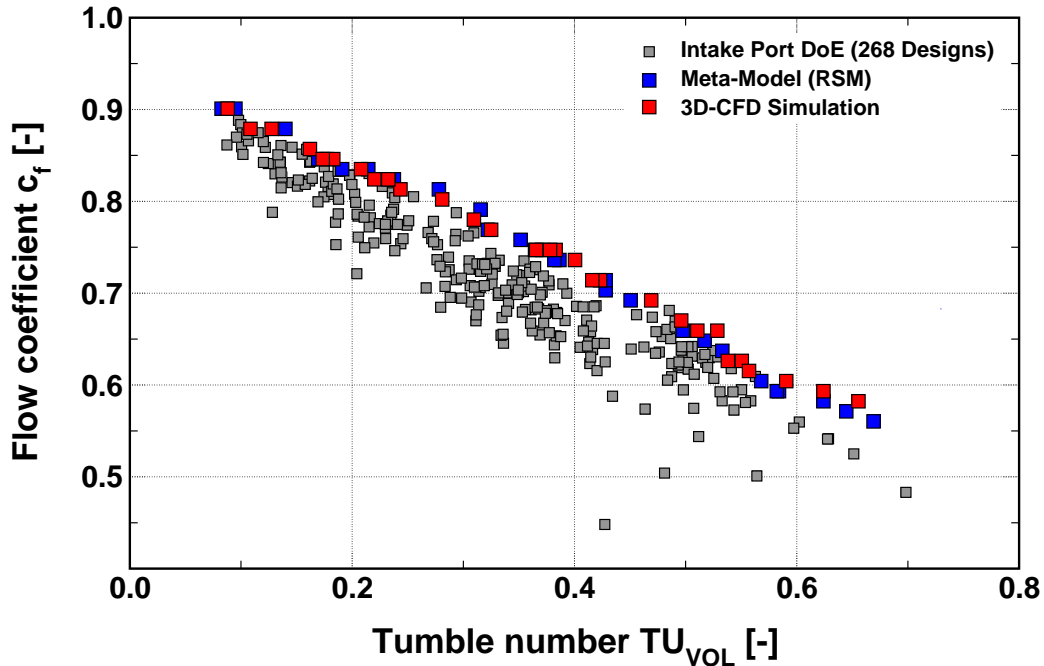
**Fig. 6.10:** Flow coefficient $c_f$ vs. tumble number $TU_{VOL}$ for the intake port RSM optimization.

is an essential step. For this, the suggested optimal designs are evaluated by means of 3D-CFD simulations (red points) according to the DoE results before. As expected due to $R^2_{adj}$ the flow coefficient is predicted very well. The average error of the considered Pareto-designs amounts to 1.1%, while the maximum error observed stays below 3.5%. Concerning tumble, the average error rises to 4.3%, which is still acceptable. However, in the area of high tumble ports, where only a few reference designs are available for the setup of the model, the variance increases significantly. Absolute errors of more than 15% occur, which is definitely too much for a reliable optimization. In order to improve the accuracy of forecast in this range, additional CFD simulations can be included, which further rises the computational effort.

As mentioned above further RSM approaches are assessed besides the finally applied reduced quadratic model. For this purpose, a fully quadratic and a fully cubic model are calculated and analyzed by means of 38 validation designs. These designs are selected from the Pareto-front as one is mainly interested in Pareto-optimal designs in the view of optimization. In **Fig. 6.11** the results of all RS-models are compared with the corresponding CFD-simulations. For a perfect agreement between approximation and calculation all values would be on a diagonal. The offset to this diagonal is an indicator for the model's prediction quality: large distances correspond to bad model performance. In order to set up a fully quadratic model with 8 design parameters at least 45 samplings are required, for a fully cubic model at least 165 (see Equation 3.24). For the reduced quadratic models for $c_f$ and $TU_{VOL}$ a total of 19 samplings is sufficient. Concerning $c_f$ very promising performance is observed for all approaches, while the reduced model performs best. The average error for the quadratic model amounts to 1.2%, for the cubic to 1.7%. In terms of $TU_{VOL}$ the prediction quality is worse in general. However, the reduced quadratic model delivers significant improvements concerning the prediction quality, while the number of model terms is significantly reduced. The fully quadratic model has an average error of 4.8%, the fully

**(a)** Flow coefficient $c_f$                         **(b)** Tumble number $TU_{VOL}$
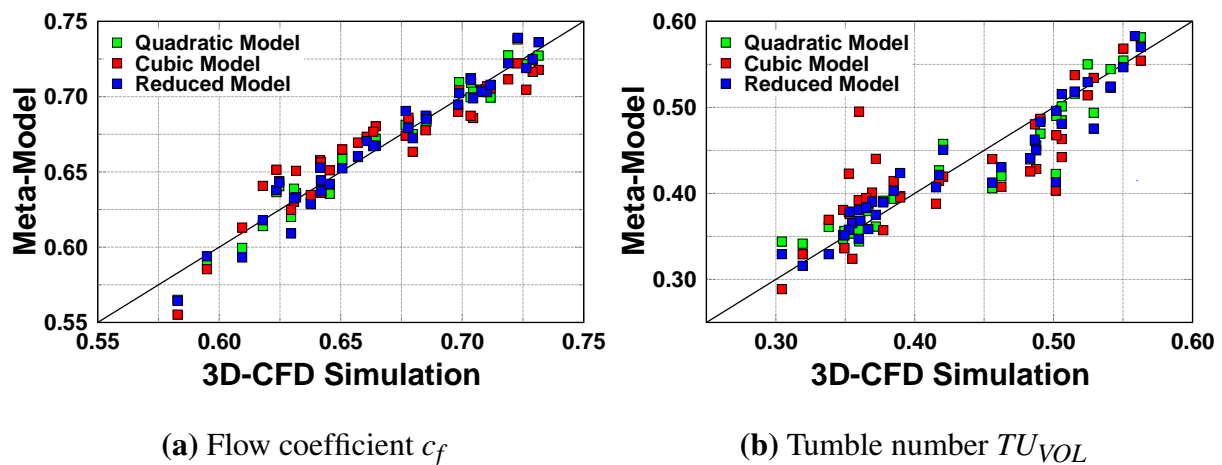
**Fig. 6.11:** Comparison of reduced quadratic, fully quadratic and fully cubic RS-approaches.

cubic 7.8%. The worse performance of the cubic model is mainly caused by too less sampling points for model fitting, as significantly more samplings are required compared to a quadratic model. Futhermore, the Pareto-front shown in **Fig. 6.10** seems to be of quadratic character and is hence most suitably represented by quadratic based approaches. As a conclusion, applying the optimized RS-model the quality is clearly improved with an equal number of samplings. Alternatively, the same quality as for fully models could be achieved with a reduced number of samplings.

## 6.2.2 Evolutionary Algorithms

Response Surface Methods can be very suitable for optimization problems with a limited number of input parameters like the example mentioned above. For increasing numbers of input parameters arising from more detailed optimization problems, the calculation of the RS-model becomes more and more expensive. Evolutionary Algorithms in contrast are intended to handle a multitude of parameters (Bäck (2006)). Hence, by means of EAs a more detailed CAD model of the intake port geometry can be applied promising better results. In the following, a model with 21 parameters is investigated. The particular design parameters are given in **Table B.2 (p.140)**. As analyzed by the sensitivity analysis the flange parameters have no influence and are therefore neglected. For the milling cutter in contrast, as it is an essential part of the production process, all parameters are regarded, even though their influence is less significant. Finally, the cross section along the main construction line is defined significantly more detailed by a total of 15 CAD-parameters.

Another advantage of EAs is their ability to deal with multi-objective problems, which obviously occur when optimizing an intake port as revealed in Section 6.1.1. Therefore, two different EA-approaches are applied, a Genetic Algorithm (GA) and an Evolutionary Strategy (ES). Similar to the RSM-approach before, the aim of this global optimization is to widely cover

the whole range of applicable intake port concepts by means of the more detailed model and assess its potential compared to the simplified model.

### 6.2.2.1 Global Optimization using a Genetic Algorithm

The SPEA2 algorithm, introduced in Section 3.2, is used as GA for this global optimization. The settings for the algorithm, which is based on $(\mu+\lambda)$-selection, are listed in **Table 6.3**. The initial population and the archive size respectively are set to 20 individuals. For the specific start population, which can be defined manually, the particular designs are selected from the Pareto-optimal solutions of the RSM optimization before (Section 6.2.1). By this, a proper spread among the solutions is already preserved at the beginning. The number of parents is set to 10, the number of generations to 30. Altogether, a total of 310 designs is thus defined. In order to increase the selection pressure on good solutions, the *tournament size* is increased to a value of 4 (Dynardo (2008)). For *k-th neighbor* the next neighbor is selected (value 1), as thus a greater diversity among the individuals is supported. For the remaining settings the default values are chosen.

| Parameter | Value |
|---|---|
| Population / archive size | 20 |
| Number of parents | 10 |
| Number of generations | 30 |
| Tournament size | 4 |
| k-th neighbor | 1 |
| Crossover probability | 0.50 |
| Mutation rate | 0.10 |
| Standard deviation | 0.10 (start) – 0.010 (end) |

**Table 6.3:** Settings for the Pareto-algorithm in optiSLang applied for the global intake port optimization.

The results in terms of $c_f$ and $TU_{VOL}$ are shown in **Fig. 6.12**. In contrast to the DoE/RSM approach, where many 'inapplicable' designs due to non-optimal quality are generated by the DoE in order to gain the input for the RS calculation, the GA in general only spreads in a narrow band from the Pareto-front. Thus, almost all delivered designs are of practical interest. Furthermore, a very good diversity is achieved due to the pre-defined start population. A selection of different port types is illustrated in **Fig. B.1 (p.141)**. Diversity is further supported by the recombination mechanism. Compared to mutation, where only small changes are permitted, this operator enables the algorithm to spread quite fast. Due to the population approach of Evolutionary Algorithms, the Pareto-front itself is obtained within a single optimization run. Obviously, for intake ports this front can be approximated well by a quadratic term as already observed for the results of the RSM (**Fig. 6.10**), while the quality of the new found Pareto-front is superior. Particularly for high tumble numbers the performance is
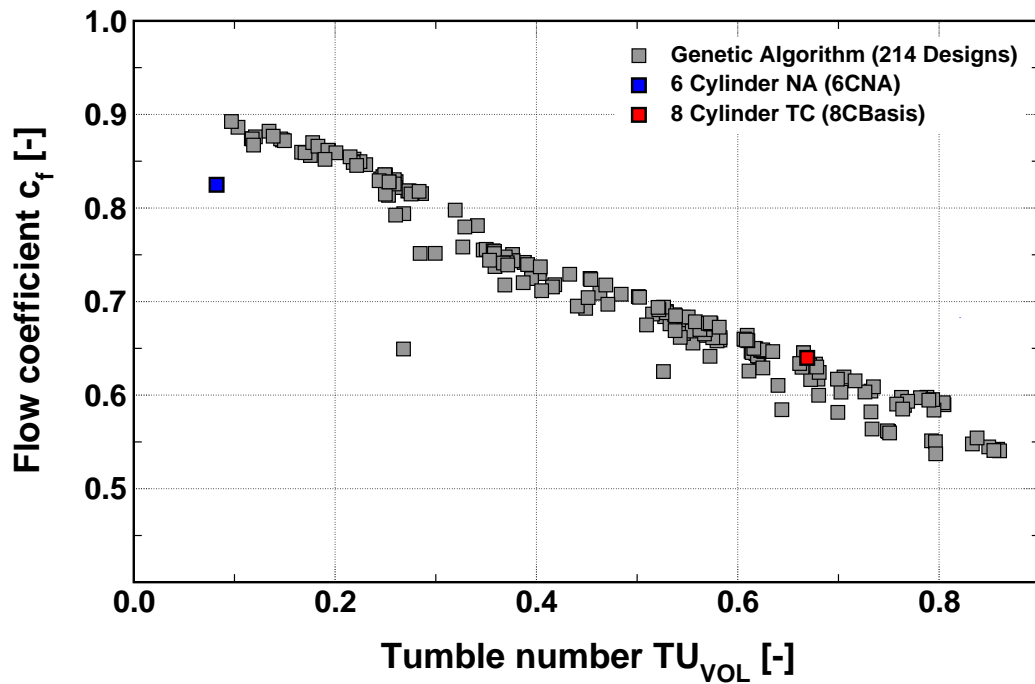
**Fig. 6.12:** Flow coefficient $c_f$ vs. tumble number $TU_{VOL}$ for the intake port optimization using a GA.

significantly improved and the range clearly extended. The reason for this is rather the detailed intake port model, which contains more degrees of freedom, than the optimization method itself. However, the global optimization cannot find improved designs for the intake '8CBasis'.

The range extension concerning $TU_{VOL}$ beyond the reference port '8CBasis' can be explained by means of the intake port shown in **Fig. 6.13**, which reaches the maximum $TU_{VOL}$ value. According to the sensitivity analysis in Section 6.1.1, high $TU_{VOL}$ values are gained by a flat port
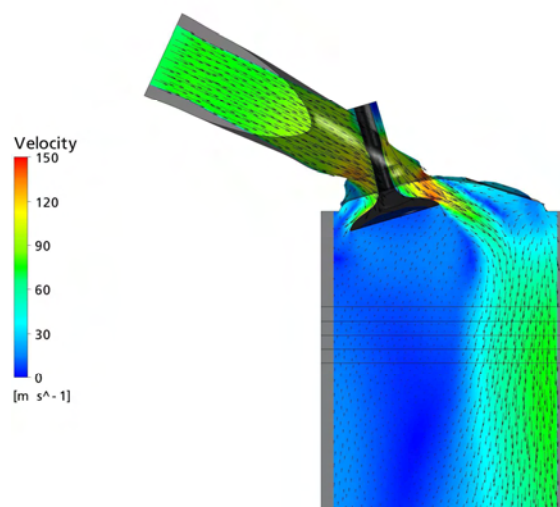


**Fig. 6.13:** Intake port design and flow pattern of the high tumble port with max. $TU_{VOL}$.

geometry with decreasing cross section area and a milling cutter with small depth and radius. For the reference port all these parameters are already set for reaching maximum $TU_{VOL}$, a further increase is not attainable with the simplified model. However, higher $TU_{VOL}$ can be realized by further reducing the cross section area at the backside of the port, which is enabled by the more detailed model where radius and width can be varied independently. Thus, the flow of the air jet through the front part of the valve gap is further enforced leading to increased tumble formation. **Fig. 6.14** clarifies this effect in comparison to the reference tumble port by means of the asymmetrical air flow distribution over the valve gap. Altogether, applying the GA significant quality improvements are realized with respect to the DoE- and RSM-results above. In addition, the number of infeasible and failed designs is clearly reduced. Thus, 214 (69%) designs are analysed to be feasible, while 49 (16%) are infeasible and 47 (15%) failed. This also affirms, that EAs can deal with infeasible and failed designs, which is required for a robust optimization process. Using e.g. gradient-based approaches in contrast the process would be stoped, as the gradient informations demanded for deriving a new search direction are missing.
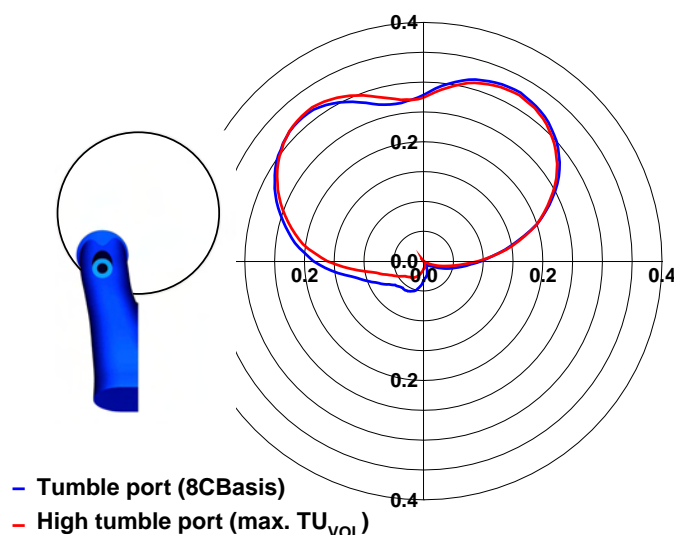


**Fig. 6.14:** Radial mass flow distribution through the intake valve gap for the high tumble port with max. $TU_{VOL}$ and the tumble port '8CBasis'.

#### 6.2.2.2   Global Optimization using an Evolutionary Strategy

In addition to the GA, the ClearVu Global Optimizer in Optimus is applied for the global intake port optimization, while the same CAD-parameters are defined as given in **Table 6.3**. This algorithm is an Evolutionary Strategy (ES), described in Section 3.2. The settings for the algorithm are listed in **Table 6.4**. In order to support a high diversity among the solutions and increase the probability of global convergence (NuTech (2005)), a large number of parents $\mu$ is recommended. Consequently, the number of offspring $\lambda$ increases according to the proposed ratio of $\mu/\lambda \approx 1/7$ (Bäck (1996)), which reduces the number of generations for a given number of total evaluations. As a compromise, the number of parents is set to 3, the number of offspring to 20. Altogether, 300 evaluations, corresponding to 15 generations, are intended

| Parameter | Value |
|-----------|-------|
| Number of parents $\mu$ | 3 |
| Number of offspring $\lambda$ | 20 |
| Number of evaluations | 300 |
| Initial search distribution | 2 |
| Problem initialization | 1 |
| Include reference point | 1 |
| Selection mechanism | $(\mu + \lambda)$ |

**Table 6.4:** Settings for the NuTech CVE-algorithm in Optimus applied for the intake port optimization.

for this optimization similar to the GA optimization. Concerning the selection operator the $(\mu + \lambda)$-selection is chosen for preserving good solutions. For the problem initialization a single starting point is selected, as the alternative method of using a uniform sampling solely delivers infeasible designs. As starting point the basic port '8CBasis' is selected. Based on this design, a medium value for the initial search distribution is found to be suitable. Thus, all derived offspring individuals are feasible, while still a large distribution of the offspring is gained.

**Fig. 6.15** shows the results of the intake port optimization in terms of $c_f$ and $TU_{VOL}$ by using an ES. From the intended 300 designs, 194 (65%) are feasible, while the remaining designs can be divided into 63 (21%) infeasible and 43 (14%) failed designs. Hence, in terms of feasible, infeasible and failed designs the performance is very comparable to the GA. The optimization
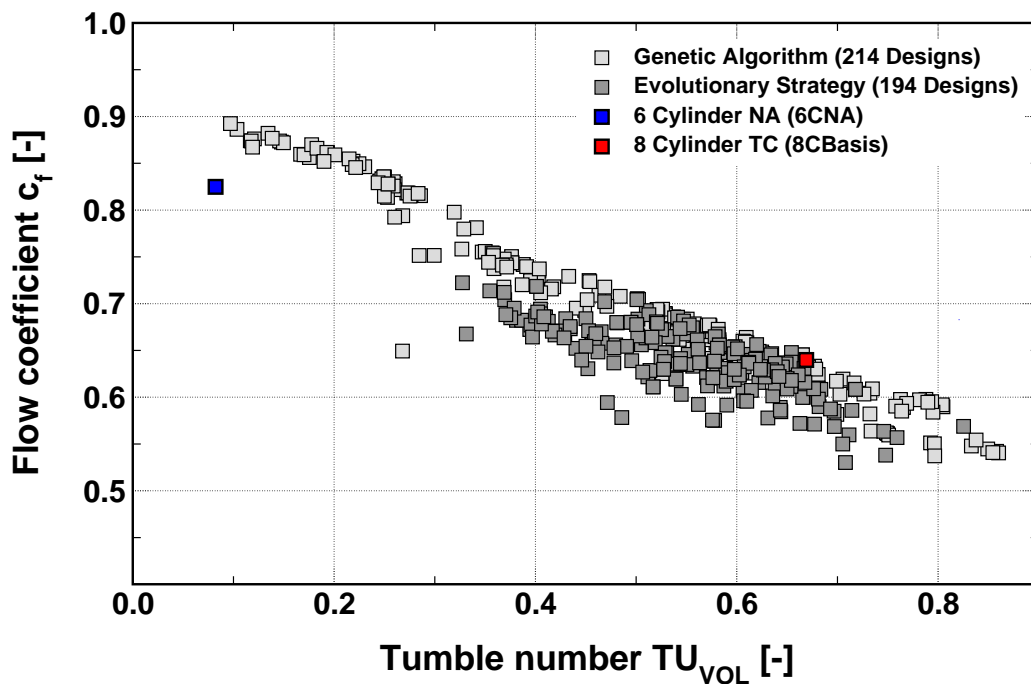


**Fig. 6.15:** Comparison of the optimization results of the GA and the ES algorithm.

results in contrast differ significantly. It is noticeable that, based on the reference port, the focus of the search progress is directed towards intake ports with increased flow rate characteristics. However, the region of standard filling ports, represented by the port '6CNA', is not reached. Towards tumble numbers above the reference tumble port '8CBasis' the optimization obviously stagnates as the density of evaluated designs significantly decreases. This behavior can be explained by the higher probability of infeasible and failed designs for tumble ports as already observed in the context of the DoE in Section 6.1.1. As a result, again a Pareto-front is gained, while its spread is clearly smaller compared to the GA results (**Fig. 6.15**). This is mainly due to the initialization of the optimization process by means of a single design, which leads to a very local initial population. Based on this population the design space is explored by rather small steps, as mutation is the only search operator for the ES. This means that a high resolution of the search space is gained. As a consequence, the diversity of the Pareto-front clearly stays behind and the evaluated designs spread more widely from this front. The quality of the determined Pareto-optimal designs however comes up to the one of the GA. Hence, by increasing the number of evaluations the same extension and quality concerning the Pareto-front as for the GA can be expected. The possibilty of defining an initial population manually e.g. based on the results of a previous investigation could improve the results significantly. By applying a single starting point the ES results in a rather local approach, while in spite of this local search the reference port '8CBasis' is not improved. Hence, a multi-objective ES strategy where diversification is more emphasized would be appropriate.

## 6.2.3 Validation of the Optimization Strategy

The optimization strategy for intake ports as introduced in the present work is based on the design evaluation by means of the steady flow analysis at one particular valve lift. Therefore, the maximum lift is regarded to be representative for the entire valve lift spectrum and finally for the in-cylinder flow of the SI-engine. In order to confirm this hypothesis several intake port designs are evaluated in a first step for the entire lift range by means of the steady flow analysis. In a second step the evaluation by means of the dynamic analysis is performed at a realistic engine operating point. For this purpose, particular ports are selected from the Pareto-front of the GA optimization described in Section 6.2.2.1. Thus, very different intake port designs are regarded, from pure filling ports up to designs for high tumble. The selected 23 intake ports are marked in **Fig. 6.16**.

The results of the steady flow analysis concerning the flow coefficient $c_f$ over the valve lift range from 1 to 10 mm are illustrated in **Fig. 6.17**. For a better illustration the designs are classified into three different port types, namely filling ports, medium tumble and high tumble ports, according to their $c_f$ and $TU_{VOL}$ characteristics. In the case of filling ports, $c_f$ is continuously increasing with rising valve lift, while for high tumble ports a saturation from medium lifts on is observed. This phenomenon is based on the effective flow section. For filling ports it is continuously limited by the valve gap area, which increases with rising valve lift. For tumble ports in contrast it is restricted by the valve gap only at small lifts, while later on it is restricted by the ports cross section. As revealed by means of the sensitivity analysis in Section 6.1.1
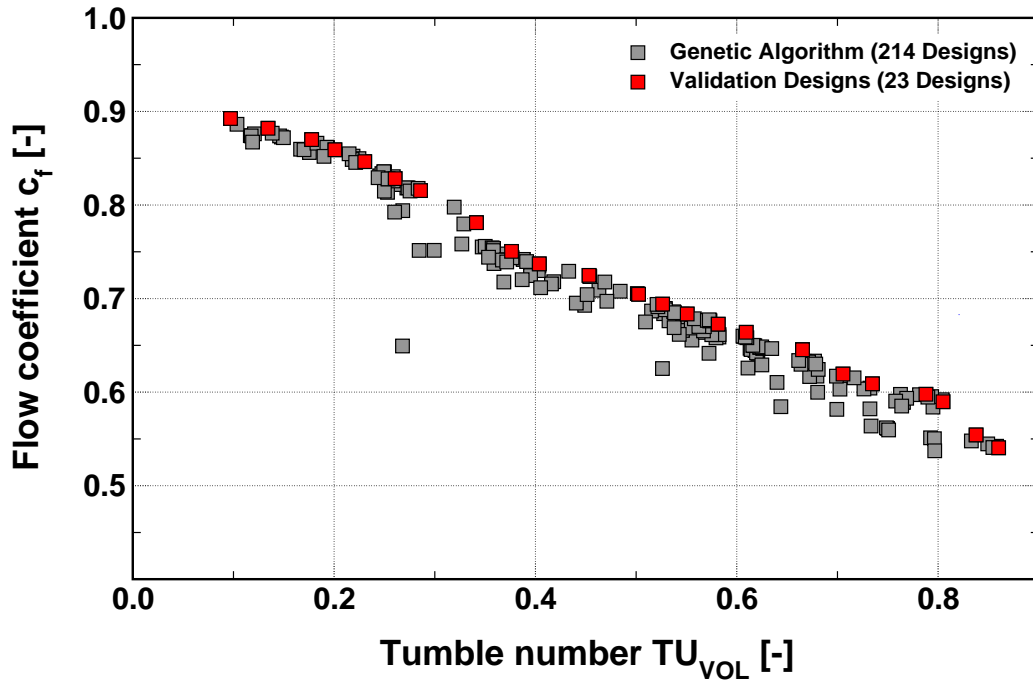
**Fig. 6.16:** Selected designs for the validation of the intake port optimization strategy.

for tumble ports the cross section area decreases from the inlet flange to the valve seat. Thus, the cross section area becomes the limiting factor and $c_f$ stagnates even though the valve lift is further increasing. For medium tumble ports this saturation occurs later near maximum valve lift. In general, as assumed for the optimization strategy the particular curves do not cross each other and the sequence of the ports in terms of $c_f$ coincides with the one from the steady flow
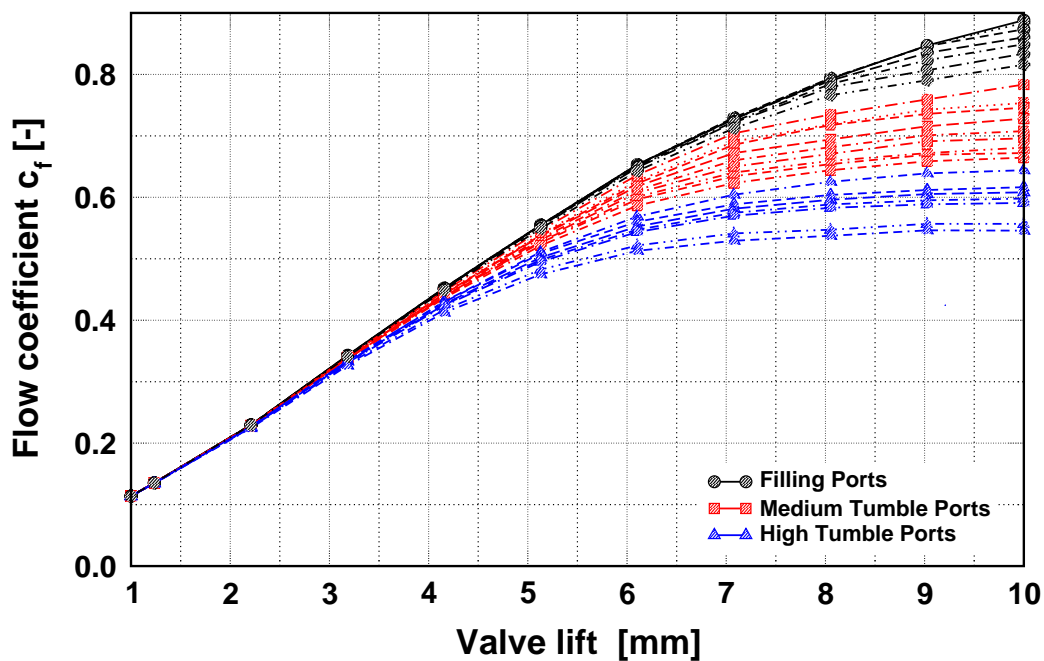


**Fig. 6.17:** Flow coefficient $c_f$ vs. valve lift for the selected validation designs.

analysis at maximum lift. Accordingly, all port designs can be characterized by a single valve lift only. It is also obvious, that for low valve lifts up to 3 or 4 mm the flow rate characteristics are equal for all designs, as the influence of the combustion chamber, which is not varied during the investigation, clearly dominates the influence of the intake port. Hence, for the assessment of intake ports the maximum valve lift appears to be suitable.

However, concerning the real engine performance the specific cylinder filling during the intake process or the volumetric efficiency respectively are crucial. For the evaluation of the intake process, the dynamic analysis is applicable as described in Section 4.4.2. **Fig. 6.18** depicts the curves of the cylinder mass over CA deg for the 23 port designs calculated by means of the dynamic analysis. In the case of direct injection, the decisive fact is the trapped air mass within the cylinder after inlet valve closing (IVC), which is located at 590 deg for the dynamic analysis. Obviously, the order of the port designs according to the remaining cylinder mass is analogous to the order based on the steady flow $c_f$. Hence, the cylinder filling resulting from different port designs can adequately be estimated by means of the $c_f$-results of the steady flow analysis at maximum valve lift.
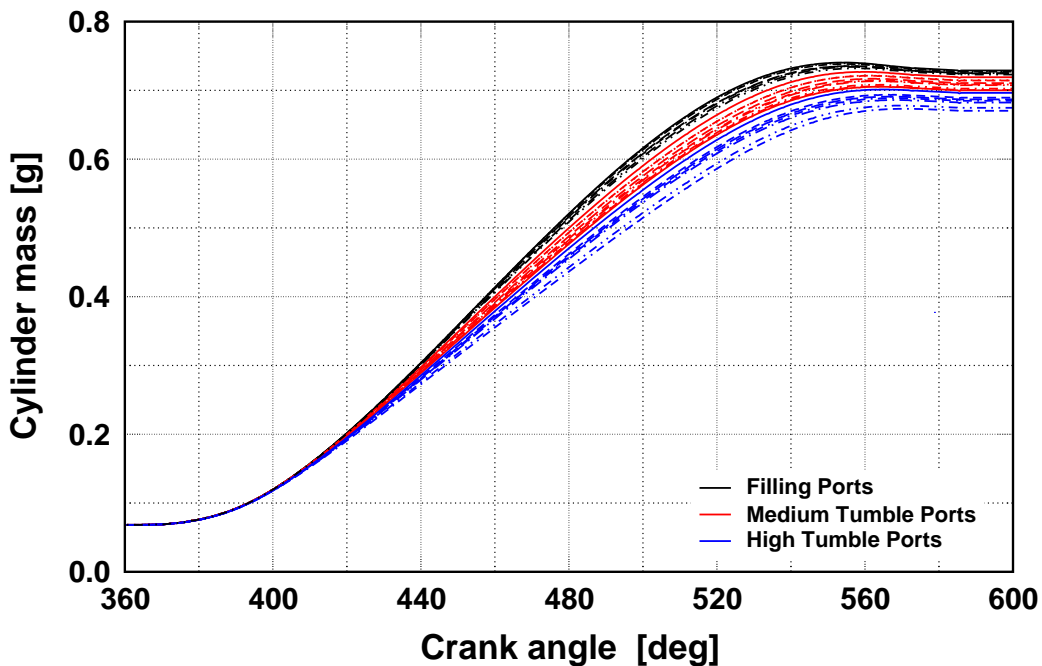


**Fig. 6.18:** Cylinder mass vs. crank angle for the selected validation designs.

**Fig. 6.19** is intended to further clarify the correlations between the particular analysis methods. Therefore, the $c_f$ values derived at 10 mm valve lift from the steady flow analysis are compared with the corresponding results for the volumetric efficiency $\eta_V$ delivered by the dynamic analysis. In this case $\eta_V$, which is equivalent to the cylinder mass when regarding equivalent conditions at the inlet, is taken in order to compare non-dimensional values. Steady flow and dynamic analysis show an almost perfect correlation represented by a correlation coefficient of almost one ($r_{c_f - \eta_V} = 0.999$). Thus, with rising $c_f$ the volumetric efficiency $\eta_V$ is increasing as well. This correlation is of quadratic behavior, while for filling ports with accordingly high $c_f$ values a stagnation in terms of $\eta_V$ is observed. This relation, given in **Fig. 6.19** as an analytical
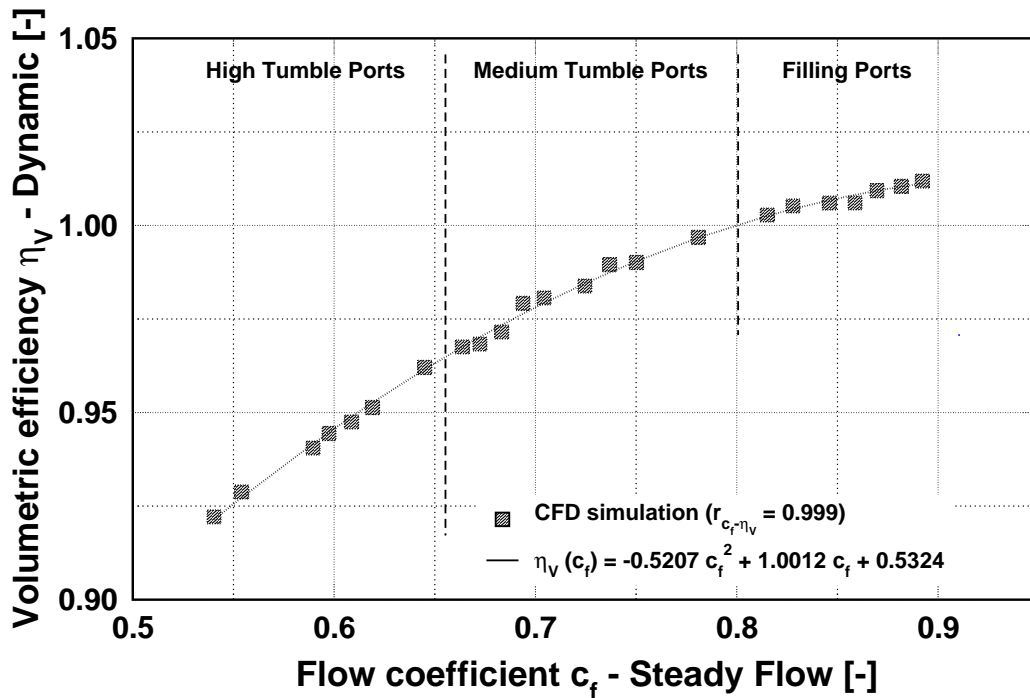
**Fig. 6.19:** Correlation between flow coefficient $c_f$ and volumetric efficiency.

term, has to be considered when assessing $\eta_V$ or the cylinder filling on the basis of steady flow results for $c_f$. Regarding the level of $\eta_V$ it is noticeable, that values above one are reached for the dynamic analysis. For real engine conditions $\eta_V$ is commonly clearly below one due to several effects like heating of the inducted air, fuel vaporization or flow losses (Heywood (1988)). As for the dynamic analysis all these losses are neglected or are very small respectively and dynamic effects lead to an additional cylinder filling, $\eta_V$ may increase slightly above one.

**Fig. 6.20** shows the appropriate results concerning the tumble number $TU_{VOL}$ gained from the steady flow analysis. Likewise $c_f$, the value of $TU_{VOL}$ at maximum valve lift is adequate to characterize the examined intake ports. Even the corresponding classification of the intake port types by means of $TU_{VOL}$ leads to equivalent results. High tumble ports can be characterized by continuously increasing values of $TU_{VOL}$, while for filling ports $TU_{VOL}$ stagnates at a low level. For medium tumble ports $TU_{VOL}$ stagnates at medium lifts, while it rises again towards the maximum lift. Concerning $TU_{VOL}$ at small valve lifts, the influence of the intake port is negligible again as already observed for $c_f$.

For the combustion process, finally charge motion and turbulence level are important indices as described in Section 4.1.2. **Fig. 6.21** shows the tumble curves resulting from the dynamic analysis for the selected intake ports. As mentioned in Section 4.1 for the dynamic analysis commonly two tumble peaks occur, one near maximum valve lift ($\sim$ 500 deg CA) and the other during compression ($\sim$ 645 deg CA). The first peak is primarily impacted by the intake port design, which defines the specific air flow distribution through the intake valve gap and thus the initial tumble formation. The later tumble development in contrast is determined by the interaction of the present in-cylinder flow with the combustion chamber and the piston only. The intake port has no influence, as the intake valves are closed. In the case of filling
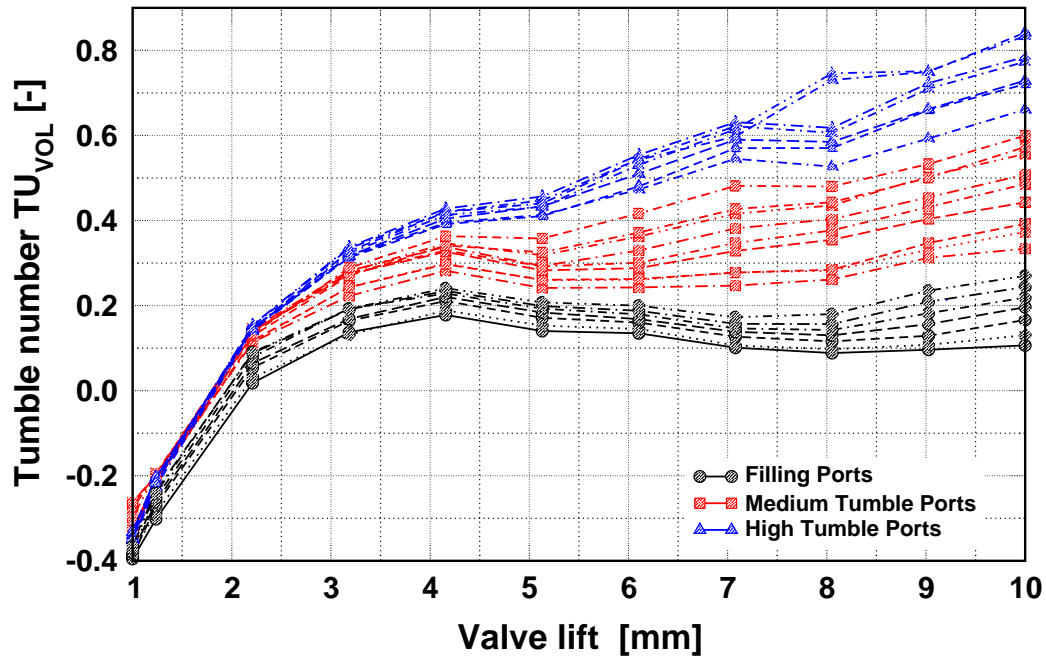
**Fig. 6.20:** Tumble number $TU_{VOL}$ vs. valve lift for the selected validation designs.

ports this second peak is missing, as no tumble motion arises at all. Accordingly, a continuous correlation for the whole spectrum of port types between steady flow and dynamic analysis can only be expected for the first tumble peak during the intake stroke. Here, in fact a well-defined correlation between both analysis methods exists (**Fig. 6.22**). Nevertheless, for the combustion mainly the second peak observed during compression is of interest as it determines
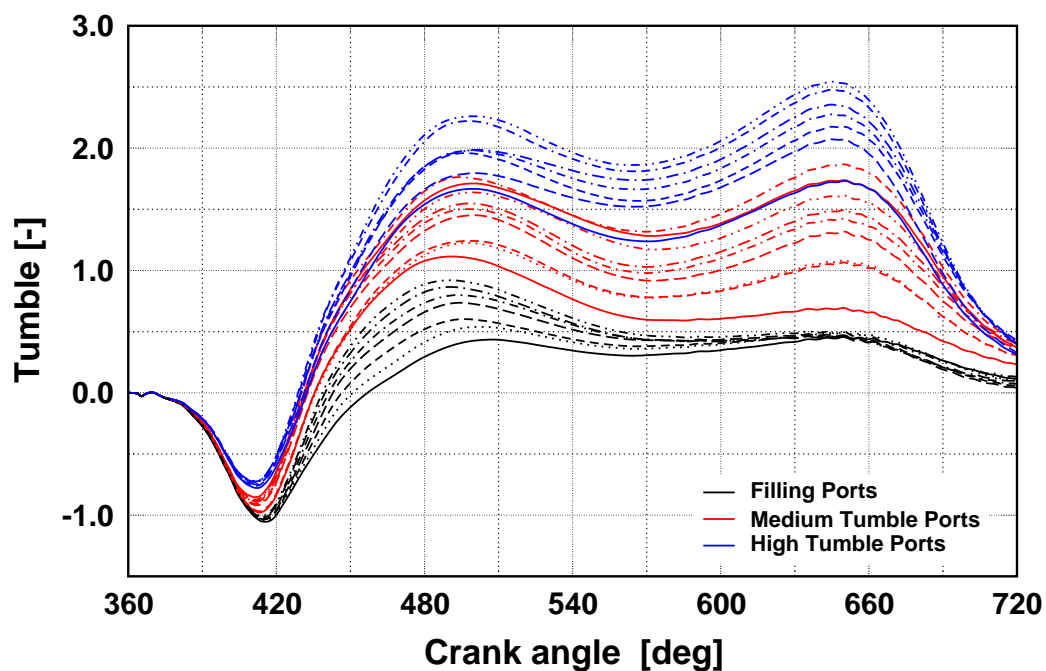


**Fig. 6.21:** Tumble vs. crank angle for the selected validation designs.
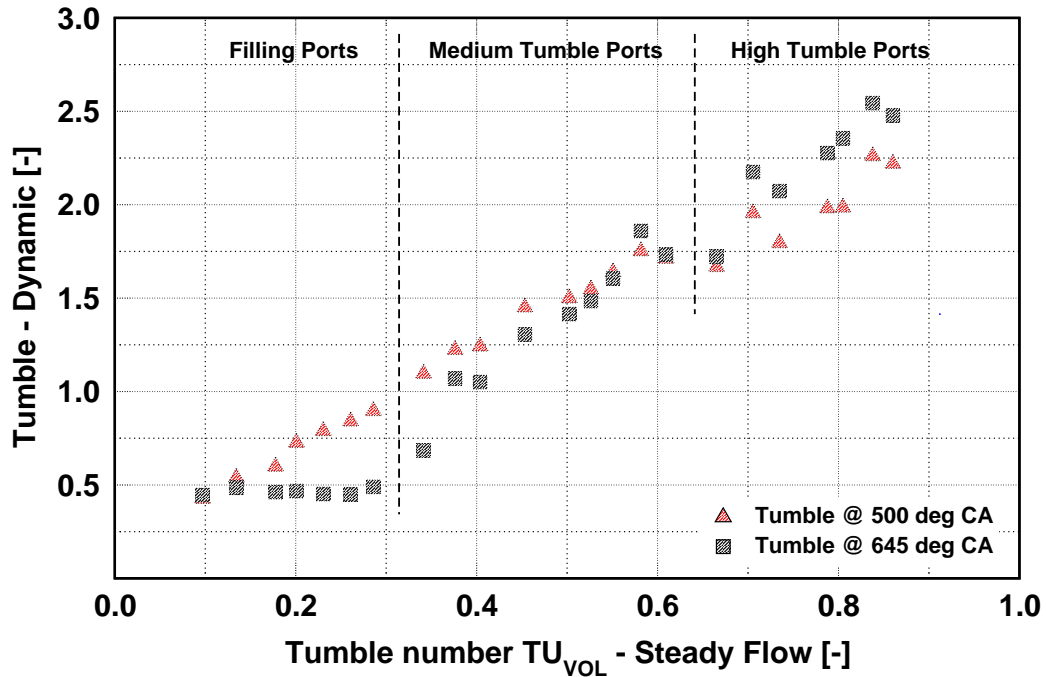
**Fig. 6.22:** Correlation between tumble number $TU_{VOL}$ and tumble peaks at 500 / 645 deg CA.

the achievable degree of turbulence intensity, which results from dissipating the large tumble vortex into even smaller vortices. Hence, involving medium and high tumble ports exclusively, as intended for a turbocharged combustion system, a correlation between tumble and $TU_{VOL}$ is observed as well (**Fig. 6.22**).
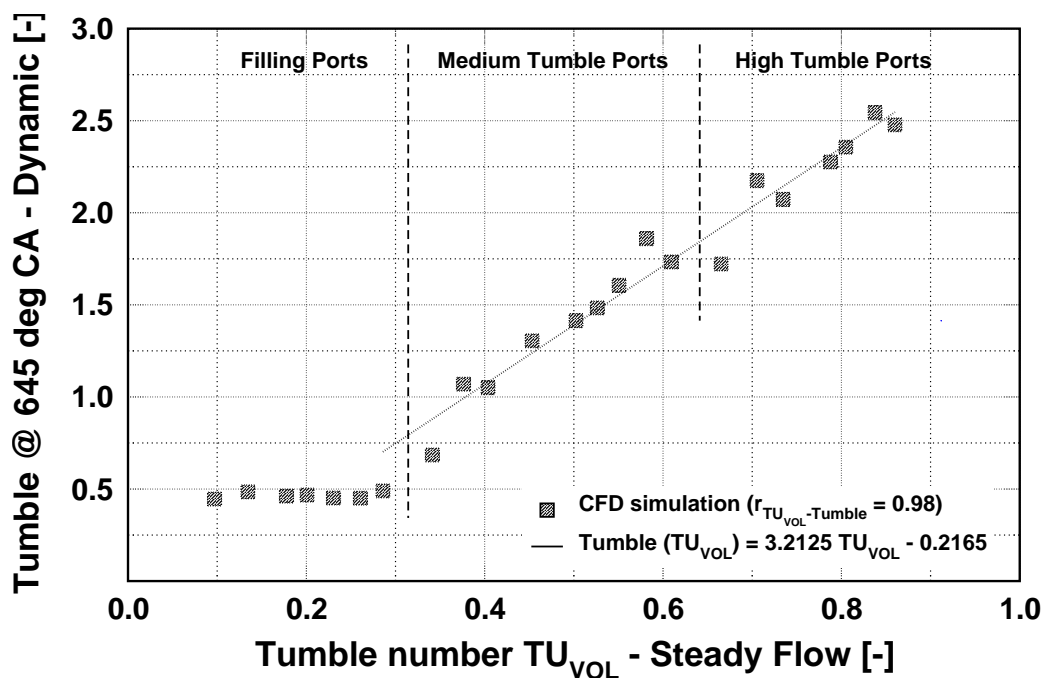


**Fig. 6.23:** Correlation between tumble number $TU_{VOL}$ and second tumble peak at 645 deg CA.

**Fig. 6.23** depicts the correlations between the different analysis methods in the context of charge motion in more detail. Therefore, the values for $TU_{VOL}$ at 10 mm valve lift from the steady flow analysis are plotted against the corresponding second tumble peak at 645 deg CA gained by the dynamic analysis. Likewise $c_f$, for the tumble results a clear correlation between both analysis methods is revealed as well. The relation is however of strong linear character indicated by a high linear correlation coefficient ($r_{TU_{VOL}-Tumble}$ = 0.98). Hence, the tumble motion induced by different port designs can properly be predicted by means of the steady flow tumble number $TU_{VOL}$ at maximum valve lift.

For TKE a similar characteristic as for the second tumble peak is observed (**Fig. 6.24**). Regarding filling ports, TKE remains on a low static level, which is almost equal for all designs. For medium and high tumble ports in contrast TKE clearly rises towards the end of compression according to the tumble level at 645 deg CA. Hence, a correlation between the second tumble peak and TKE exists. As a result, for tumble inducing ports a suitable estimation of tumble and thus TKE near TDC can be gained from the corresponding value of $TU_{VOL}$.
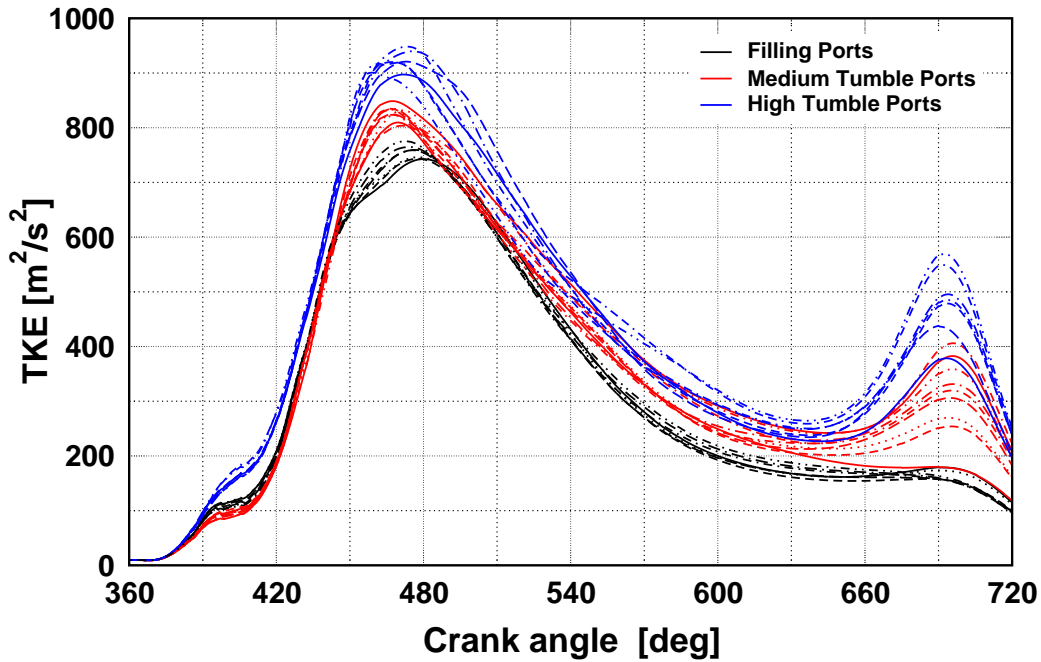


**Fig. 6.24:** TKE vs. crank angle for the selected validation designs.

Altogether, concerning the flow characteristics a very good correlation between the specific analysis methods exists and the resulting cylinder filling can properly be estimated by means of the intake port's $c_f$ value. For charge motion such a correlation is observed as well, while it is not continuous for the entire spectrum of port types. For filling ports e.g. only for the tumble initialization during the intake stroke a distinct correlation exists, while it is missing for the subsequent tumble progress. Nevertheless, when regarding tumble inducing ports exclusively like in the context of turbocharged SI-engines, a well-defined correlation exists as well and $TU_{VOL}$ is a suitable measure for estimating the corresponding charge motion and turbulence level. The reason for this clear relation is based on the in-cylinder flow pattern. In the case of tumble ports a well-defined vortex within the cylinder is generated. By varying only the

intake port parameters without changing the combustion chamber or the piston, the general flow pattern remains. This can be illustrated by analyzing the position of the real tumble center gained by the dynamic analysis. By default, a fixed tumble center is assumed, which is located at the cylinder axis in a height of half the actual stroke plus half the squish gap. Of course, the real tumble center may differ as depicted in **Fig. 6.25**, which contains the coordinates of the particular tumble centers resulting from the different medium and high tumble port designs. The real center is determined by varying the coordinates of the fixed center until the maximum tumble value is gained. As these values only vary in a small range, similar vortex patterns can be expected. Increasing or decreasing tumble values then result from a higher or lower angular velocity of the vortex. An adequate estimation of this angular velocity can be derived from the tumble number $TU_{VOL}$, as this measure is based on the unequal velocity distribution of the air flow, which finally determines the tumble formation (Section 4.1). Accordingly, concerning tumble inducing ports the port layout controls the tumble intensity, while tumble position and shape are hardly influenced. By applying a filling port this typical tumble motion during compression is not present at all and accordingly a correlation between the second tumble peak and $TU_{VOL}$ cannot be expected.
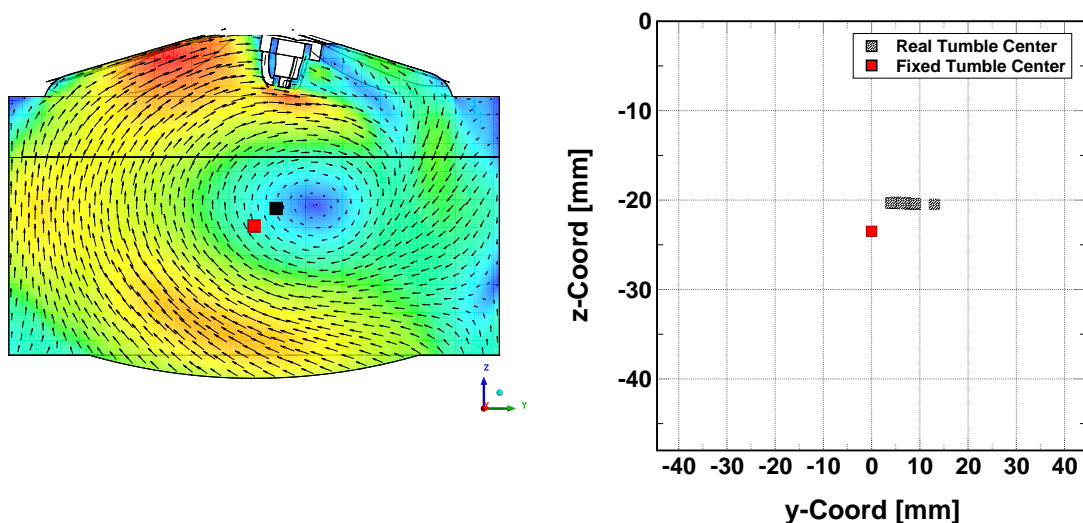


**Fig. 6.25:**   Real vs. fixed tumble center of the regarded medium and high tumble port designs at 645 deg CA (left: tumble pattern for the intake port with max. tumble).

The distribution of $\eta_V$ and tumble analog to **Fig. 6.16** is illustrated in **Fig. 6.26**, where the strict conflict of objectives is confirmed. In terms of $\eta_V$ a difference of approx. 10% between the best performing filling port and the highest tumble inducing port appears. Nevertheless, decreasing flow rates not only result in lower $\eta_V$ and thus cylinder filling but also lead to an increase in pumping losses. This has to be considered for an overall assessment of the flow characteristics of intake ports as it directly influences the engines's potential concerning performance and efficiency. For this purpose the pumping mean effective pressure (PMEP) for the selected port designs is investigated in addition (**Fig. 6.26**). As the exhaust stroke is not regarded by the dynamic analysis a generic value for the PMEP is determined, which is however representative for the particular intake port designs. Therefore, the pressure during exhausting is defined to
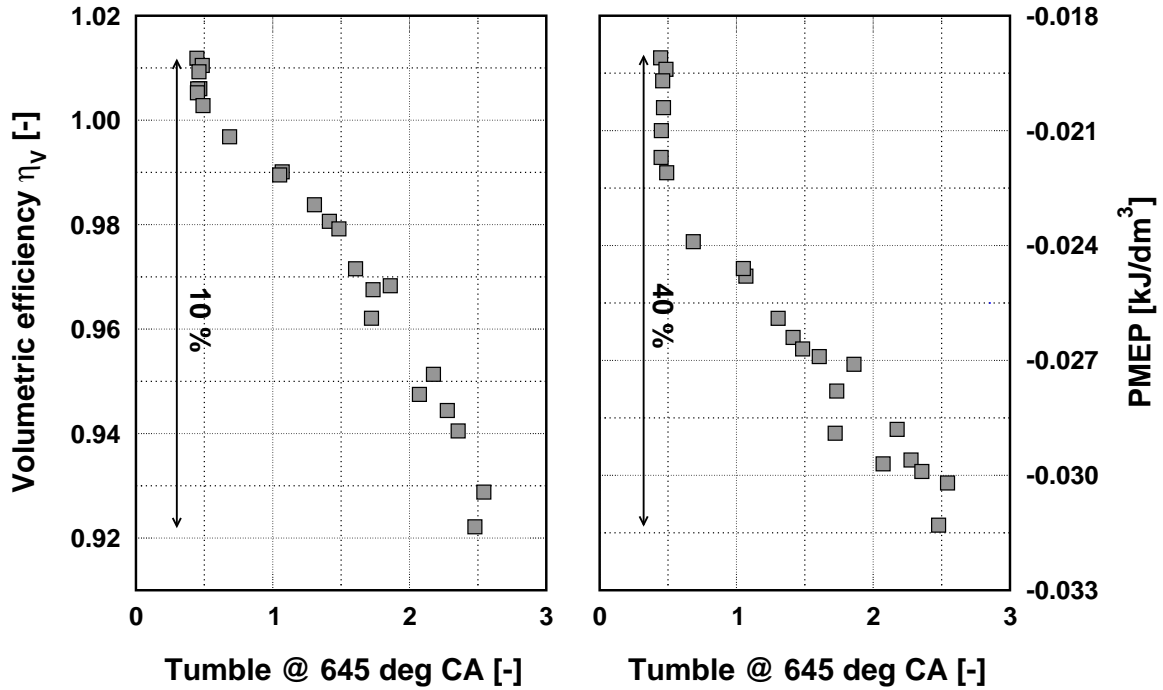
**Fig. 6.26:** Tumble vs. pumping losses for the validation designs.

be static and equal to the reference pressure (1 bar). The resulting gas-exchange cycle is shown in **Fig. 6.27** on the example of both extreme port designs. Thus, apart from a deficit in $\eta_V$ of about 10% a significant increase in PMEP of approx. 40% is calculated between both extreme designs.
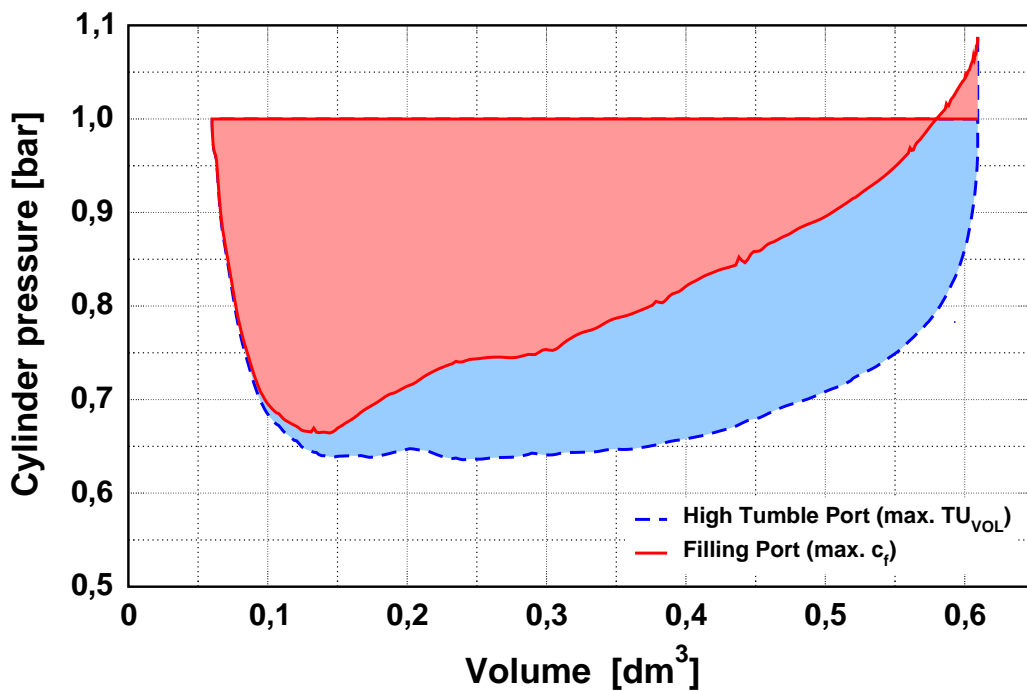


**Fig. 6.27:** Generic gas-exchange cycle for the filling and the high tumble port design.

**Fig. 6.27** also explains the relations found between $c_f$ and cylinder filling or $\eta_V$ respectively. According to **Fig. 6.17** the flow coefficient at small valve lifts is equal for all port designs, as the valve gap area defines the effective area of flow restriction. Due to this the cylinder pressure decreases evenly for both port types at the beginning of the intake stroke. Later on with rising valve lifts the cylinder pressure graphs diverge as for tumble ports the port area itself becomes the restricting factor. The cylinder pressure is therefore below that of the filling port, for which the valve gap area is the dominating flow restriction. As a result, the pumping losses are clearly higher for the tumble port. However, this behavior also leads to a greater pressure difference between the inlet flange and the cylinder. As this difference significantly influences the mass flow rate over the intake valve gap according to Equation 4.5, the final difference in cylinder filling between filling ports and tumble ports is smaller than expected based on $c_f$. Due to this effect a non-linear relation between $c_f$ and $\eta_V$ appears as revealed in **Fig. 6.19**.

### 6.2.4 Optimization of a Series Tumble Port Geometry

For the optimization problems described so far, the aim was to investigate the broad spectrum of feasible intake port designs in general. The following optimization in contrast is performed in order to improve a single intake port design in particular. For this purpose, the existing tumble port of the turbocharged eight-cylinder '8CBasis' is considered. By this, the feasibility of the single lift based optimization strategy concerning a local optimization is investigated.

According to Section 4.2 an apparent conflict between flow rate characteristics, which influence cylinder filling and pumping losses, and charge motion, which significantly impacts the combustion process, exists. The focus of this optimization however is primarily on the flow rate characteristics, as the engine's charge motion level is assumed to be adequate. Accordingly, the aim is to increase the engine's performance at wide open throttle (WOT) conditions due to better cylinder filling and its efficiency at part load conditions as a result of reduced pumping losses. The general combustion characteristics in contrast should be retained almost unchanged. Therefore, similar charge motion is intended. For the optimization, the subsequent task is to maximize the flow coefficient $c_f$ of the intake port, without decreasing its tumble number $TU_{VOL}$. As a consequence, the actual multi-objective problem is reduced to a single-objective one, as only $c_f$ has to be optimized. For retaining the $TU_{VOL}$ value on the level of the basic port '8CBasis', a constraint is introduced. The optimization problem can be described as:

$$\textit{Maximize } c_f(\vec{x}),$$
$$TU_{VOL}(\vec{x}) - TU_{VOL}(8CBasis) \;\geq\; 0. \tag{6.1}$$

Due to this problem definition, the region of possible designs is clearly limited requiring an algorithm with a rather local search process. As discussed in Section 6.2.2.2 the NuTech ClearVu Optimizer in combination with a single starting point is a suitable algorithm for this purpose. Due to its ES approach with mutation as main search operator only small design variations occur, thus restricting the focus of the search process locally. As a result, the objective

space around the reference port is expected to be resolved very detailed. The specific settings of the algorithm for this optimization are listed in **Table 6.5**. Compared to the optimization problem in Section 6.2.2.2, where global convergence is desired, the number of parents $\mu$ is reduced to a value of 2 for the single-objective optimization (SOO) in order to achieve enhanced local progress (NuTech (2005)). The number of offspring $\lambda$ is, according to the recommended ratio of $\mu/\lambda \approx 1/7$ (Bäck (1996)), set to 14. As selection mechanism the $(\mu+\lambda)$-selection is applied. For the problem initialization the option of a specific starting point is selected, while consciously a point of lower quality compared to the reference tumble port is selected. Thus, the performance of the algorithm can be assessed by monitoring the search progress towards the reference design. Furthermore, when choosing a very good starting point it becomes more difficult to find better solutions. Typically, a temporary worsening of the results appears before the optimizer discovers designs with improved characteristics (NuTech (2005)). The remaining settings for the algorithm are defined analogously to the global problem.

| Parameter | Value |
|---|---|
| Number of parents $\mu$ | 2 |
| Number of offspring $\lambda$ | 14 |
| Number of evaluations | 420 |
| Initial search distribution | 2 |
| Problem initialization | 1 |
| Include reference point | 1 |
| Selection mechanism | $(\mu+\lambda)$ |

**Table 6.5:** Settings for the NuTech CVE-algorithm in Optimus applied for the tumble port optimization.

Concerning the particular CAD design parameters, the same as for the global optimization in Section 6.2.2 are selected. The variation range for this local optimization is further restricted by means of lower and upper limits (**Table B.3 (p.142)**). By this, faster convergence towards optimal port designs is expected, as the design space is significantly reduced. Concerning the *y*-coordinate and the milling cutter the restrictions are derived from the results of the sensitivity analysis in Section 6.1.1. The parameters *y-coord*, *milling cutter radius* and *milling cutter depth* are limited to small values in order to keep the basic port's high tumble level as recommended by the sensitivity analysis. For the cross section area in contrast no information concerning suitable restrictions are available, as the cross section area is driven by a single factor and width respectively for the sensitivity analysis, while it is defined by the radius and width at the particular planes here. Therefore, the values for radius and width are varied in a narrow band around the corresponding values of the basic port in order to focus the optimization to this region.

Based on the starting point a total of 420 designs, which corresponds to 30 generations, is defined for this optimization. From these 363 (86%) designs are evaluated by means of 3D-CFD simulations. Due to the constraint in Equation 6.1, only designs which at least equal the $TU_{VOL}$

value of the reference port are feasible. Port designs with a lower tumble number are infeasible, as the optimization target is to increase $TU_{VOL}$. Thus, from these 363 evaluated designs 231 (55%) designs are analysed to be feasible. The remaining 174 (41%) designs are found to be infeasible, 132 (31%) because the constraint concerning $TU_{VOL}$ is violated and 42 (10%) as the valve seat area is exceeded (port not producible). The number of failed designs amounts to 15 (4%). Thus, in contrast to the global multi-objective optimization the number of failed design is significantly reduced for this local optimization. This is mainly due to the limited variation range of the design parameters. In addition, the design variations during the optimization run are rather small as intended for the mutation-based algorithm.

**Fig. 6.28** shows the optimization results concerning $c_f$ and $TU_{VOL}$ in comparison to the results of the global optimization using the GA. Altogether, the calculation duration for the evaluated 363 designs is in the range of about 14 days. In spite of the single-objective optimization again a Pareto-front can be observed, which is characterized by a parallel offset to the one of the global optimization. Hence, the quality of the new found Pareto-designs is superior. **Fig. 6.29** shows the results of this local optimization more detailed. Due to the constraint concerning $TU_{VOL}$ the search direction obviously tends towards higher $c_f$ values and mainly intake port designs with enhanced $c_f$ are gained as intended by the problem definition in Equation 6.1.
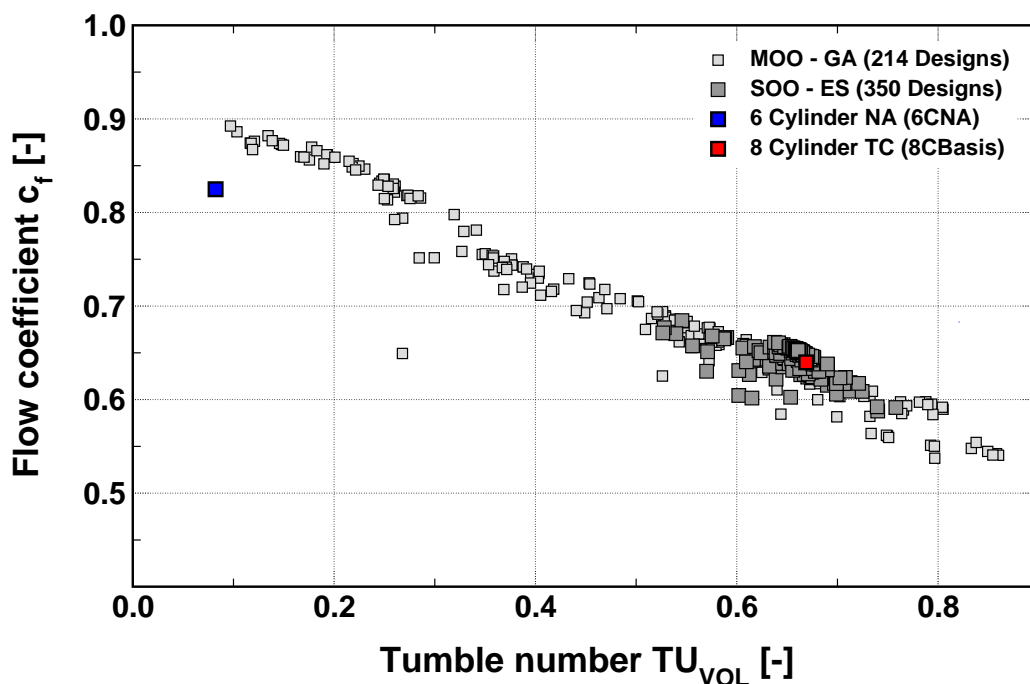


**Fig. 6.28:** Flow coefficient $c_f$ vs. tumble number $TU_{VOL}$ for the tumble port optimization.

The optimization progress is shown in **Fig. 6.30**. While the $c_f$ values oscillate relatively strong at the beginning, a stagnation of the optimization towards a static value is observed at the end. The quality of the reference port '8CBasis' is reached after only 160 iterations, the optimal design is found after 260 iterations. Applying this optimal design an improvement in $c_f$ of about 2% compared to '8CBasis' is achieved, while $TU_{VOL}$ is equal. Besides this design, several other designs are discovered with a similar quality, which could be regarded as well. However, as
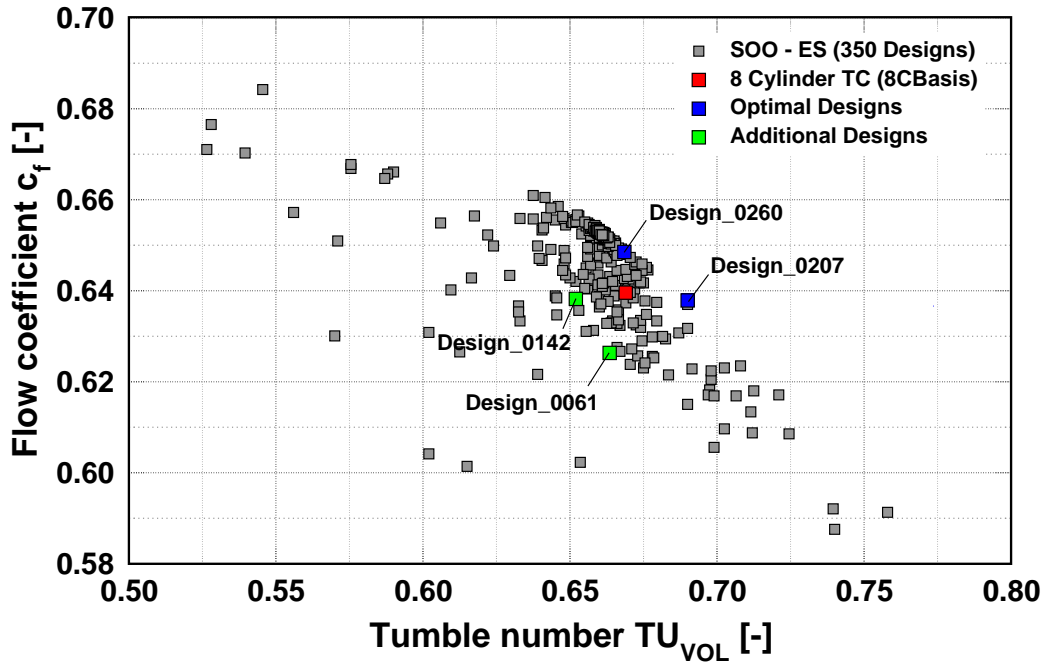
**Fig. 6.29:** Optimal port designs resulting from the tumble port optimization.

the optimization is based on an Evolutionary Strategy, these designs are almost identical, as the mutation-operator varies the design parameters only very little. Accordingly, all these designs can be expected to show similar performance.

In order to explain the improvement by means of 'Design_0260', for both the optimized design and the reference port the CAD-parameters are compared in **Table B.4 (p.143)**. It becomes
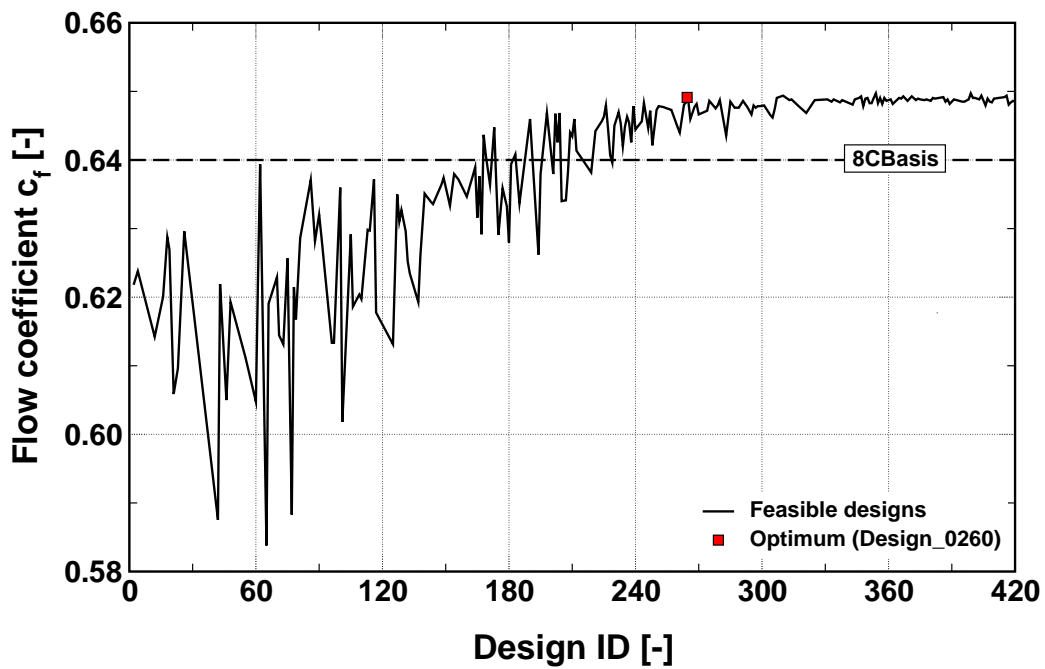


**Fig. 6.30:** Progress of the flow coefficient $c_f$ during the optimization process.

obvious that the increased $c_f$ mainly results from an enlarged cross section area. In particular the top side of the optimized port is enlarged. In addition, the *milling cutter radius* is higher leading to further increased flow rate as explained by **Fig. 6.2**. However, these parameter variations not only influence $c_f$ and would lead to an decrease of $TU_{VOL}$. This is prevented by means of a bulge at the lower part of the intake port shown in **Fig. 6.31**. As a result, the air flow is well-defined guided through the front part of the valve gap, which supports the tumble formation. Furthermore, *y-coord* is slightly lower compared to the basic design thus intensifying this effect. Altogether, the basic tumble level is preserved, while the flow rate is increased. Applying this optimal design, enhanced cylinder filling can be expected, while the influence on the combustion process should be similar to the basic engine design.
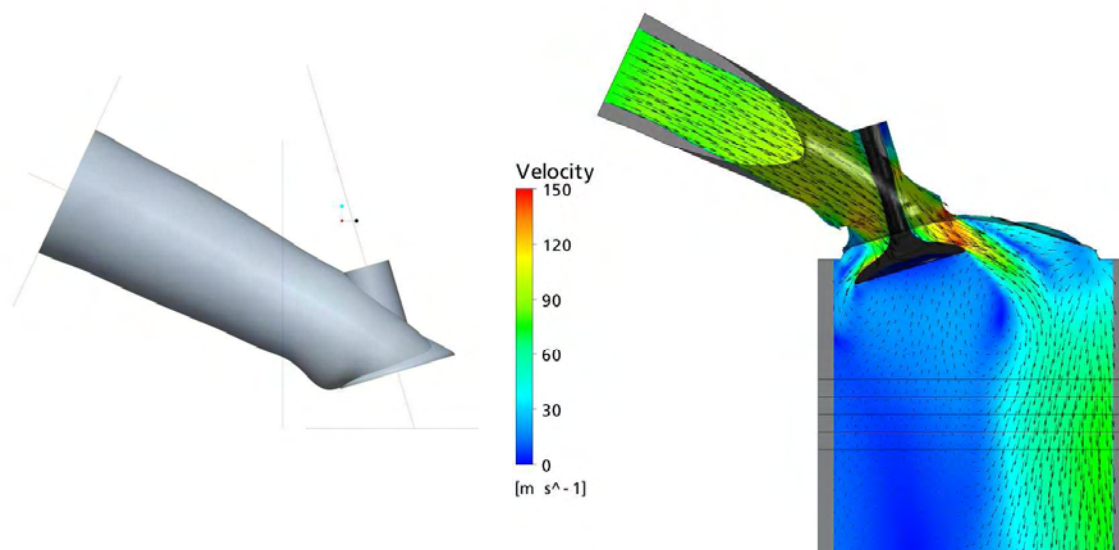


**Fig. 6.31:** Intake port shape and flow pattern of the optimal $c_f$-design.

Apart from increased $c_f$, designs with higher $TU_{VOL}$ are found during the optimization run. Compared to the reference port improvements for $TU_{VOL}$ of about 3% are gained by 'Design_0207', while $c_f$ is equal. **Fig. 6.32** shows the design of this port. Similar to the $c_f$-optimized 'Design_0260', it contains a bulge at the port's underside, which is however even more distinctive thus leading to increased $TU_{VOL}$. Accordingly, the flow characteristics would become worse. In order to equal the basic $c_f$ value, both the cross section area and the *milling cutter radius* are slightly higher in comparison to the basic port '8CBasis'. As a result, the quality of 'Design_0207' exceeds the basic port's quality as $TU_{VOL}$ is enhanced and $c_f$ is on the same level. Applying this optimized tumble port design a clear acceleration of the combustion process compared to the basic engine can be expected. As observed for the intake port comparison in Section 4.2 the efficiency particularly at LET should be increased thus leading to reduced fuel consumption at WOT conditions. Pumping losses and cylinder filling in contrast are supposed to be comparable to the basic port due to an equal $c_f$ value.

In addition to both optimized ports two further designs are regarded in **Fig. 6.29**, 'Design_0061' and 'Design_0142'. 'Design_0061' is characterized by a similar value of $TU_{VOL}$ compared to
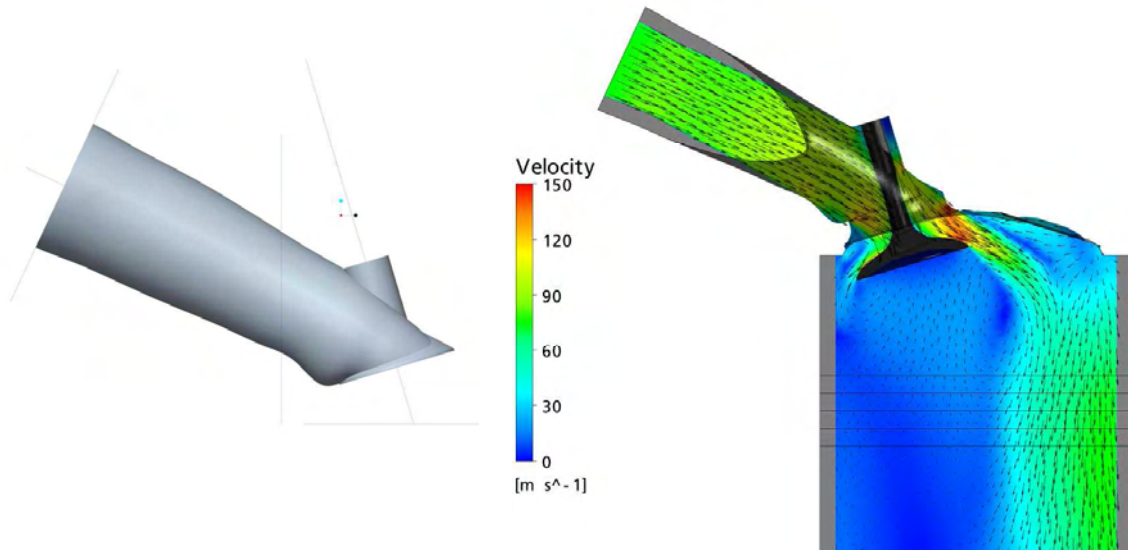
**Fig. 6.32:** Intake port shape and flow pattern of the optimal $TU_{VOL}$-design.

the reference port, while $c_f$ is worsening by approx. 2.0%. 'Design_0142' in contrast has an almost equal $c_f$ value, however $TU_{VOL}$ is decreased by approx. 3.5%. These designs are considered in order to investigate the feasibility of the single lift based optimization approach for a local optimization in more detail. Therefore, $c_f$ and $TU_{VOL}$ are evaluated for these designs as well as for the reference design over the entire valve lift range shown in **Fig. 6.33**. Comparing these results to the results of the single lift analysis a clear correlation between both methods
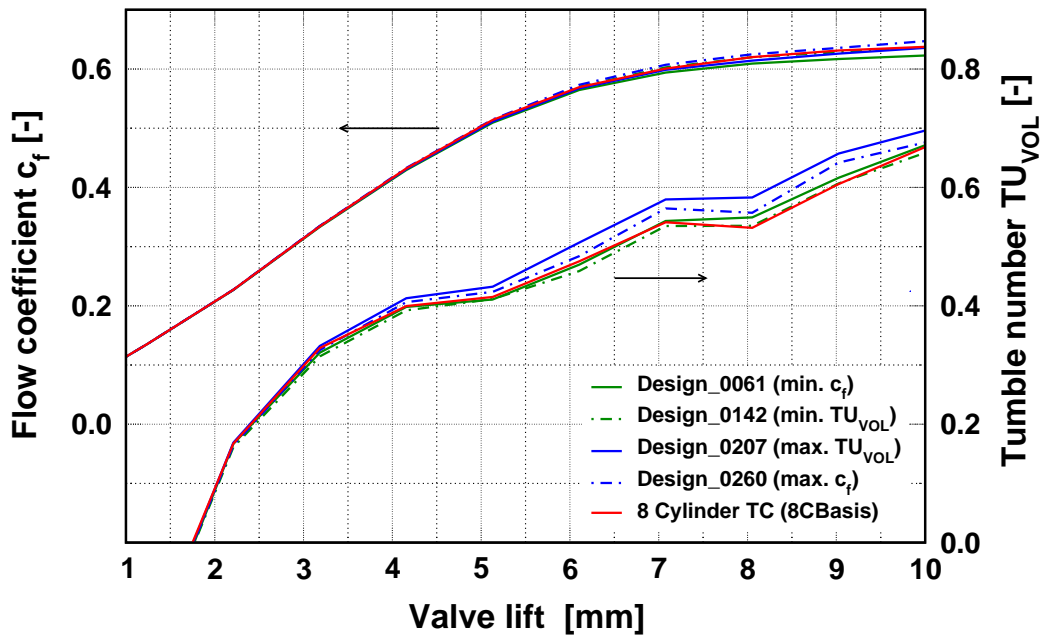


**Fig. 6.33:** Flow coefficient $c_f$ vs. valve lift for the basic and the optimized tumble port designs.

is revealed, as already observed for the global optimization in Section 6.2.3. Accordingly, the same assessment in terms of $c_f$ and $TU_{VOL}$ is delivered.

However, in order to estimate the effects of the particular intake port designs on the performance of the real engine advanced analysis methods are required, which directly assess cylinder filling and charge motion. Therefore, the dynamic analysis is an appropriate method. In **Table 6.6** the corresponding results of both the single lift analysis and the dynamic analysis are compared. **Fig. 6.34(a)** shows the cylinder mass for the basic port, the optimized and additional designs.

| Intake Port Design | $c_f$ [-] | Cylinder Mass [g] | $TU_{VOL}$ [-] | Tumble@645 CA [-] |
|---|---|---|---|---|
| 8CBasis | 0.640 | 0.6899 | 0.669 | 2.144 |
| Design_0061 | 0.626 | 0.6889 | 0.664 | 2.202 |
| Design_0142 | 0.638 | 0.6910 | 0.652 | 2.235 |
| Design_0207 | 0.637 | 0.6900 | 0.690 | 2.384 |
| Design_0260 | 0.649 | 0.6923 | 0.669 | 2.333 |

**Table 6.6:** Comparison of cylinder mass and tumble for the basic and the optimized tumble port designs.



**(a)** Cylinder mass
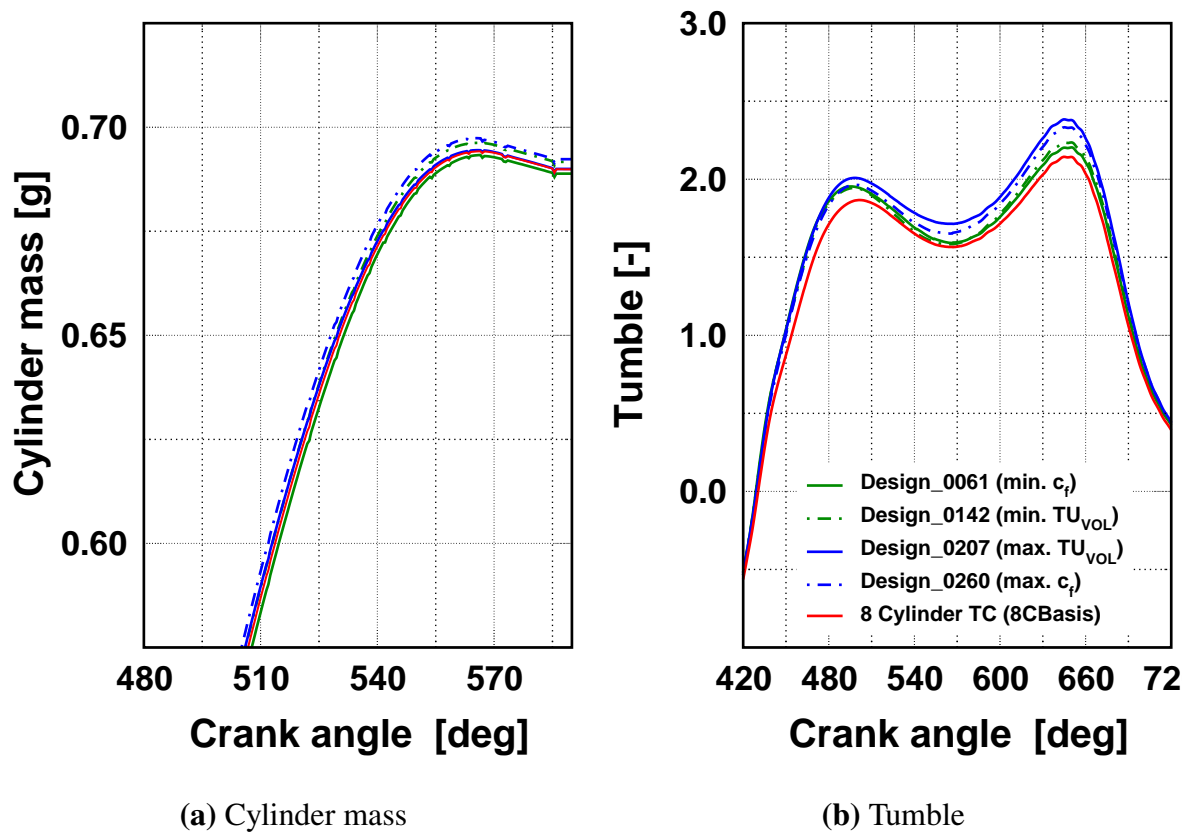
**(b)** Tumble

**Fig. 6.34:** Cylinder mass and tumble vs. crank angle for the basic and the optimized tumble port designs.

As identified by the $c_f$ results above, by applying 'Design_0260' the highest cylinder filling is achieved. Compared to the basic port an improvement of about 0.5% is gained. 'Design_0061' delivers the lowest cylinder filling as assumed, while the remaining port designs perform similar to the basic port. Hence, the flow coefficient evaluated at maximum valve lift is suitable to predict the resulting trapped cylinder mass as an obviuos correlation between both parameters exists.

The results concerning tumble are illustrated in **Fig. 6.34(b)**. It is noticeable that for all designs of the optimization the tumble curves are above the reference port's curve. Nevertheless, within these intake ports the relations are represented according to the single lift evaluation. As expected, 'Design_0207' induces the strongest tumble motion. For the tumble value at 645 deg CA an improvement of more than 10% is observed compared to the design '8CBasis'. The lowest tumble values are gained by 'Design_0061' and Design_0142', which almost perform identical. As determined in Section 6.2.3, the results for the TKE peak near TDC follow the corresponding tumble results at 645 deg CA (**Fig. 6.35**). Thus, by using port 'Design_0207' the highest turbulence level is achived, while for the basic port the lowest is observed. Accordingly, for both tumble and TKE gained by the dynamic analysis a suitable forecast by means of the $TU_{VOL}$ value at maximum lift can be derived, although the correlation fits not as perfect as for the flow characteristics.
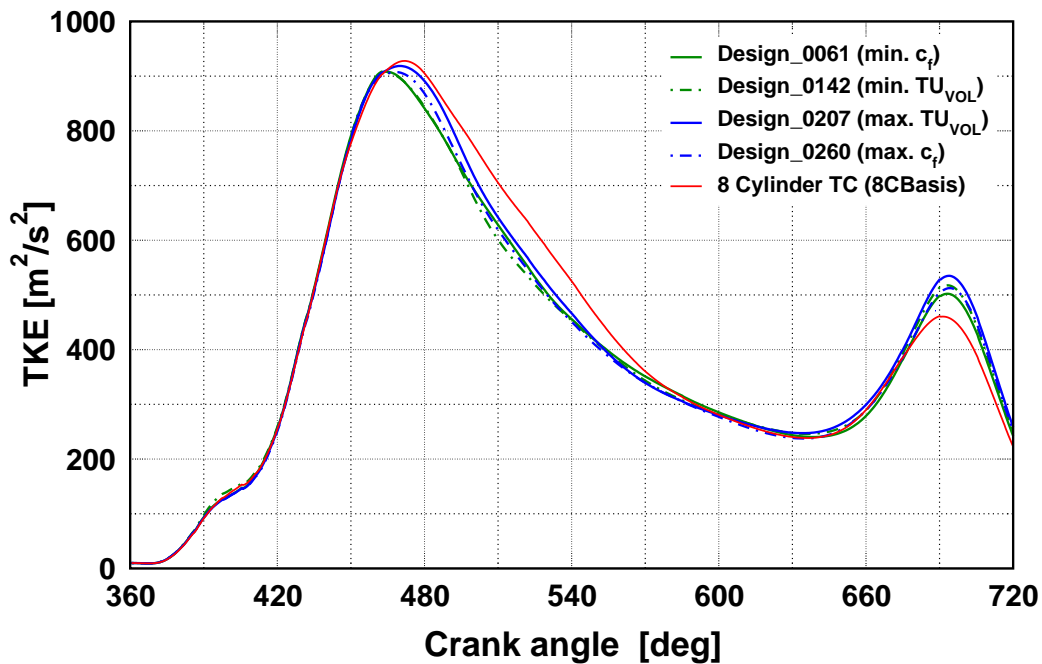


**Fig. 6.35:** TKE vs. crank angle for the basic and the optimized tumble port designs.

### 6.2.5   Conclusions

The present optimization strategy, which is based on a single valve lift for intake ports is found to be suitable. A clear correlation between the steady flow and the dynamic results is observed

for both a global and a local optimization. By means of $c_f$ the resulting cylinder filling can be estimated very well, while the quadratic relation is to be regarded (**Fig. 6.19**). In terms of charge motion and TKE the tumble number $TU_{VOL}$ is an adequate measure for a forecast. Particularly for tumble ports a well-defined correlation exists.

Applying a Response Surface approach as optimization method, the fitness of the basic DoE designs can be improved significantly, while the additional computational effort for the final optimization, which is performed on the basis of the meta-model, is negligible. However, in order to gain reliable quality concerning the forecast of the objective values a sufficient number of samplings is required depending on the number of parameters. Therefore, Response Surface Methods are only interesting for less complex optimization problems. Regarding the powertrain development process this method can be applied for a general preliminary study in an early development stage. Later on, when rather detailed optimization problems arise and reliable results are required, these methods are not suitable, as the model's approximation error is on the same level as the expected optimization potential revealed by the tumble port optimization. Nevertheless, the Pareto-optimal designs derived by meta-models can be applied as starting designs for a subsequent detailed optimization by means of EAs.

Very promising results are obtained by means of EAs. The GA performs best for the global optimization, where a Pareto-front is revealed for the entire range of feasible port designs and the strict conflict between both objectives $c_f$ and $TU_{VOL}$ becomes obvious within a single optimization run. Due to the stepwise variation of the CAD-parameters and the explicitly defined start population the number of failed and infeasible designs is significantly reduced compared to the DoE/RSM-approach. In addition, a more detailed CAD-model can be applied. As a consequence, the GA delivers significantly better results, while the computational effort is on the same level. Within the design process, this algorithm is suitable for a general study of port concepts at the beginning of a series development, where already reliable simulation results are required while the level of detail is still low.

However, in order to improve a particular design a local optimization is required, while the ES is found to be an effective algorithm for this task due to the single starting point approach and the mutation-based search strategy. Compared to the tumble port of the series eight-cylinder SI-engine for both objectives improved designs are delivered. Accordingly, this algorithm is an appropriate method for a detailed optimization later in the engine developing process, when the general port concept is defined and first design proposals exist.

## 6.3    Optimization Strategy for a Combustion Chamber Geometry

Apart from the intake port design the in-cylinder flow is clearly influenced by the layout of the combustion chamber as revealed in Section 6.1.2. In order to improve an intake port geometry the present optimization approach is found to be suitable as demonstrated by means of the global intake port investigation in Section 6.2.3 and the specific tumble port optimization in Section 6.2.4. In order to evaluate the feasibility of the optimization approach for a combustion chamber geometry, two different optimization problems are considered in the current section: a global optimization based on a simplified combustion chamber model and a detailed optimization of the corresponding real combustion chamber design.

### 6.3.1    Global Optimization of a Combustion Chamber Geometry

The global combustion chamber optimization is performed using the simplified, generic CAD-model introduced in Section 5.2.1, while for the intake port the associated tumble port '4CTC' is applied. During the optimization process the port's geometry is not varied. Only its position is adapted according to the variations of the chamber parameters (e.g. the intake valve angle). With respect to the objectives, both $c_f$ and $TU_{VOL}$ are considered like for the intake port investigation in Section 6.2.2.1. As revealed by the DoE-samplings in **Fig. 6.7**, an obvious conflict between these objectives similar to the intake port problem exists, resulting in a multi-objective problem. For this purpose the Genetic Algorithm SPEA2 implemented in the optimization tool optiSLang is an adequate method as illustrated on the example of the intake port problem in Section 6.2.2.1. The specific settings for the algorithm are defined according to this optimization problem (**Table 6.7**). The design parameters (CAD-parameters) and the corresponding upper and lower limits are adopted from the sensitivity analysis (**Table 6.2**).

| *Parameter* | *Value* |
|---|---|
| Population / archive size | 20 |
| Number of parents | 10 |
| Number of generations | 20 |
| Tournament size | 4 |
| k-th neighbor | 1 |
| Crossover probability | 0.50 |
| Mutation rate | 0.10 |
| Standard deviation | 0.10 (start) – 0.010 (end) |

**Table 6.7:** Settings for the optiSLang Pareto-algorithm applied for the global combustion chamber optimization

As depicted by the sensitivity analysis in Section 6.1.2, the influence of CAD-parameters variations on flow rate and charge motion depends on the particular valve lift. Unlike the

intake port, a combustion chamber design thus cannot be characterized by means of a single lift only. Instead, several valve lifts have to be regarded when assessing the overall influence of a combustion chamber on the in-cylinder flow. Therefore, the entire valve lift range is divided into three characteristical sub-ranges, which are then represented by a single lift respectively (Elwan (2008)):

- 3 mm for the low lift range (0 - 4 mm),

- 6 mm for the medium lift range (4 - 7 mm),

- 9 mm for the high lift range (7 - 10 mm).

Of course, the computational effort significantly rises according to the number of valve lift variations. Hence, compared to the intake port optimizing a combustion chamber is much more time-consuming.

For the optimization process the results of the different lift ranges have to be combined to a single value for each objective as required by the algorithm in order to calculate a specific fitness value, which represents the performance of each design. Therefore, weighting factors for the particular lifts according to their influence on the objectives are introduced, by means of which overall values are calculated. Concerning the flow coefficient $c_f$, the influence on the resulting cylinder filling is of interest. For this, the weighting factor is gained by means of 1D gas exchange simulations, where the calculation of the cylinder filling is based on the $c_f$ values over the valve lift. Accordingly, by varying exclusively the $c_f$ values for the corresponding lifts (3 mm, 6 mm and 9 mm) respectively, the influence on the cylinder filling can be evaluated separately for each lift. **Table 6.8** shows the average change in cylinder mass with regard to the basic engine by varying $c_f$ by +10% and -10% respectively. Increasing $c_f$ e.g. at 9 mm valve lift by 10%, while the remaining $c_f$ values are not changed, leads to an increase of approx. 0.387% of the cylinder mass. Obviously, a direct correlation between $c_f$ and the cylinder mass exists, where the influence of large valve lifts is significantly more important compared to smaller ones. The weighting factors $w_{c_f,i}$ are calculated by scaling the particular changes to their sum.

| Valve Lift | $c_{f,i}$ (*Basis*) | Change Cyl. Mass [%] | $w_{c_f,i}$ [-] |
|---|---|---|---|
| 3 mm (i=1) | 0.415 | 0.045 | 0.08 |
| 6 mm (i=2) | 0.638 | 0.100 | 0.19 |
| 9 mm (i=3) | 0.665 | 0.387 | 0.73 |
| $\Sigma$ | - | 0.532 | 1.00 |

**Table 6.8:** Weighting factors for the calculation of $\overline{c}_f$.

The standardized, average $\overline{c}_f$ value for the final evaluation is calculated by:

$$\overline{c}_f = \sum \frac{c_{f,i}}{c_{f,i} \ (Basis)} w_{c_f,i}, \qquad (6.2)$$

where $c_{f,i}$ denotes the flow coefficient of the particular valve lift $i$. Accordingly, the basic combustion chamber design of the four-cylinder SI-engine ('4CTC') has a $\bar{c}_f$ value of 1. For designs with improved overall flow characteristics this value is greater than 1, while it is below 1 for worse designs.

Concerning the tumble number $TU_{VOL}$, its influence on the in-cylinder charge motion is important. In contrast to $c_f$, the calculation of a corresponding $\overline{TU}_{VOL}$ value is definitely more complex, as the $TU_{VOL}$ values for the particular lifts cannot be varied directly as in the case of $c_f$ by means of the 1D gas exchange simulation. Thus, the influence of $TU_{VOL}$ on the resulting overall tumble motion cannot be investigated separately and the correlation between both parameters cannot be evaluated directly. Due to this reason, an average tumble number $TU_{AVG}$ is derived from the $TU_{VOL,i}$ values of the particular valve lifts $i$, where the flow coefficient $c_{f,i}$ and the relative valve opening duration $t_i$ are included similar to the average tumble number used for intake ports in Linse (2006):

$$TU_{AVG} = \frac{\sum TU_{VOL,i} \cdot c_{f,i} \cdot t_i}{\sum c_{f,i} \cdot t_i}. \tag{6.3}$$

The values for $t_i$ and $TU_{VOL,i}$ (*Basis*) are listed in **Table 6.9**, where $t_i$ is determined by the ratio of the opening duration of the particular valve lift range to the entire valve opening duration. It can be observed that the medium valve lift has the greatest fraction concerning the opening duration, while small and high lifts have an equal fraction. For the optimization $TU_{AVG}$ is standardized by the average tumble value of the basic design $TU_{AVG}$ (*Basis*):

$$\overline{TU}_{VOL} = \frac{TU_{AVG}}{TU_{AVG} \ (Basis)}. \tag{6.4}$$

Hence, the basic tumble number $\overline{TU}_{VOL}$ (*Basis*) amounts to 1, while improved designs have values greater than 1 and vice versa.

| Valve Lift | $t_i$ [-] | $TU_{VOL,i}$ (*Basis*) |
|---|---|---|
| 3 mm (i=1) | 0.32 | 0.198 |
| 6 mm (i=2) | 0.36 | 0.464 |
| 9 mm (i=3) | 0.32 | 0.682 |
| $\Sigma$ | 1.00 | - |

**Table 6.9:** Weighting factors for specific lifts and $\overline{TU}_{VOL,i}$ of the basic design.

Applying these weighted values for $c_f$ and $TU_{VOL}$, a multi-objective combustion chamber optimization can be performed. Based on a start population containing 20 designs, which are stochastically derived by means of a Latin-Hypercube sampling, further 19 generations with 10 designs each are defined resulting in a total of 210 designs. From these, 99 (47%) designs are feasible. The remaining 111 (53%) designs are infeasible (25%) or failed (28%), as the parameter combinations do not fulfill the constraints or cannot be regenerated by the

CAD program. For the combustion chamber optimization problem the constraints are defined within the generic CAD-model in order to ensure proper positioning of the particular valves (Section 5.2.1). Compared to the intake port investigations before, the number of infeasible and failed designs is significantly higher, which results from the complexity of the CAD-model and the wide variation range of the parameters. In particular the variation of the intake and exhaust valve angles is critical, as high values significantly reduce the available space within the combustion chamber roof, where the valves have to be arranged in. Thus, the probability of infeasible parameter combinations clearly rises. Nevertheless, for this global optimization a wide variation range is intended in order to investigate a broad spectrum of combustion chamber designs.

**Fig. 6.36** shows the results of the combustion chamber optimization, where the conflict between both objectives $\overline{c}_f$ and $\overline{TU}_{VOL}$ becomes obvious and a Pareto-front (blue squares) is revealed. It is noticeable, that the combustion chamber design of the basic four-cylinder engine '4CTC' is not included within this front. The optimization algorithm obviously delivers designs, which show better performance concerning both objectives. Particularly for the weighted tumble number $\overline{TU}_{VOL}$ a significant improvement of almost 40% is gained compared to the basic engine, while $\overline{c}_f$ is on the same level. The highest $\overline{TU}_{VOL}$ overall is observed for 'Design_0155' (+45%). The improvements for $\overline{c}_f$ in contrast are rather small (approx. 1.5%). The highest value is delivered by 'Design_0178'. The detailed results for 'Design_0178' and 'Design_0155' are listed in **Table 6.10**.
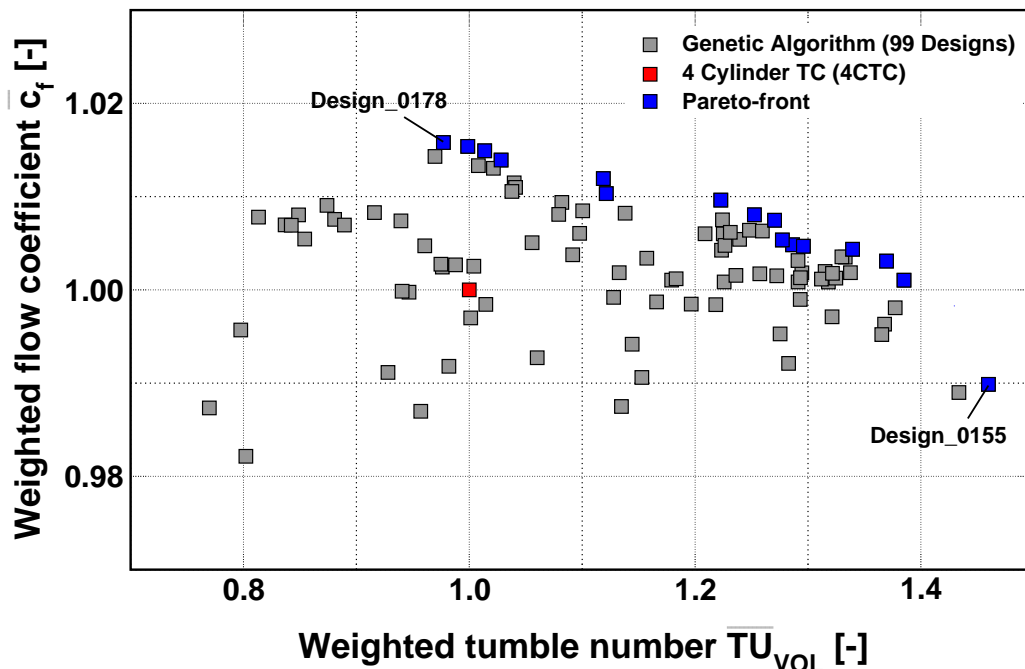


**Fig. 6.36:** Flow coefficient $\overline{c}_f$ vs. tumble number $\overline{TU}_{VOL}$ and resulting Pareto-front for the global combustion chamber optimization.

In order to investigate the reasons for the increase in $\overline{c}_f$ and $\overline{TU}_{VOL}$, the particular design parameters are compared to the basic configuration in **Table B.5 (p.144)**. As the influences

| Valve Lift | 4CTC | | Design_0178 | | Design_0155 | |
|---|---|---|---|---|---|---|
| | $c_{f,i}$ | $TU_{VOL,i}$ | $c_{f,i}$ | $TU_{VOL,i}$ | $c_{f,i}$ | $TU_{VOL,i}$ |
| 3 mm | 0.415 | 0.198 | 0.429 | 0.202 | 0.340 | 0.963 |
| 6 mm | 0.638 | 0.464 | 0.639 | 0.499 | 0.589 | 0.699 |
| 9 mm | 0.665 | 0.682 | 0.676 | 0.624 | 0.681 | 0.610 |

**Table 6.10:** Results for 'Design_0178' and 'Design_0155' in terms of $c_f$ and $TU_{VOL}$.

of the CAD-parameters on flow rate and charge motion vary according to the considered valve lift and the specific weighting factors have to be regarded, it is difficult to explain the resulting non-dimensional numbers in detail. The main relations however can be evaluated by comparing the CAD-parameters.

Regarding 'Design_0155', a tumble progress is predicted, which is typical for a cylinder head with a masking edge as very high tumble numbers appear specifically at low valve lifts. This masking effect is gained, as the distance of the intake valve axis to the cylinder axis (*IV-distance*) as well as the squish area (*IV-SA-depth*) are simultaneously increased (**Fig. 6.37**). As a result, for small valve lifts the back part of the valve head is enclosed and the air flow is forced through the front part of the valve gap thus enhancing tumble formation. For higher lifts, this parameter combination leads to a decrease of the tumble number, while the flow coefficient is increased as revealed by the sensitivity analysis in **Fig. 6.9**. Altogether, by applying the present approach for calculating $\overline{TU}_{VOL}$, the highest overall value is achieved, while it is remarkable that the tumble values at small and medium lifts are clearly dominating.
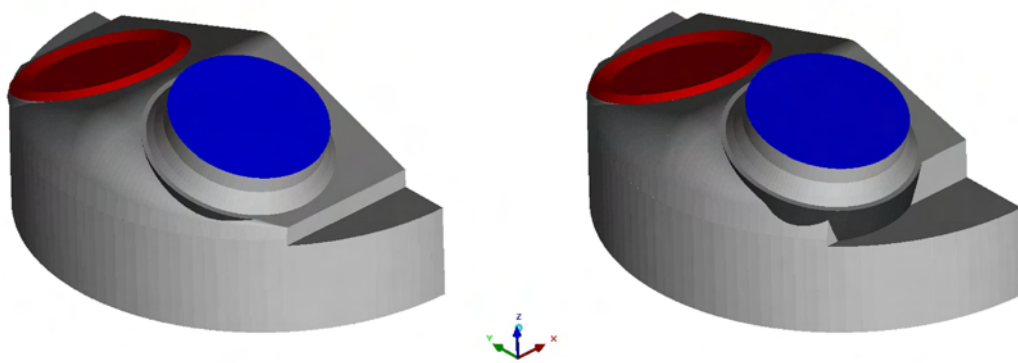


**Fig. 6.37:** Combustion chamber geometry of the basic design (left hand side) and Design_0155 with max. $\overline{TU}_{VOL}$ (right hand side).

Concerning 'Design_0178', which is characterized by maximum $\bar{c}_f$, improvements at small and high lifts are gained due to different reasons. At small lifts the decrease of the parameter *IV-distance* moves the intake valves away from the cylinder wall, which hinders the air-flow into

the cylinder. Thus, the distribution of the mass flow over the valve head is more evenly and the resulting $c_f$ increased (**Fig. 6.38**). At large valve lifts the intake valve shape is responsible for the increase. The enlarged *Valve-stem-radius* leads to an improved flow along the intake valve as flow separation is reduced. In addition, the smaller *Valve-stem-diameter* increases the effective flow section.
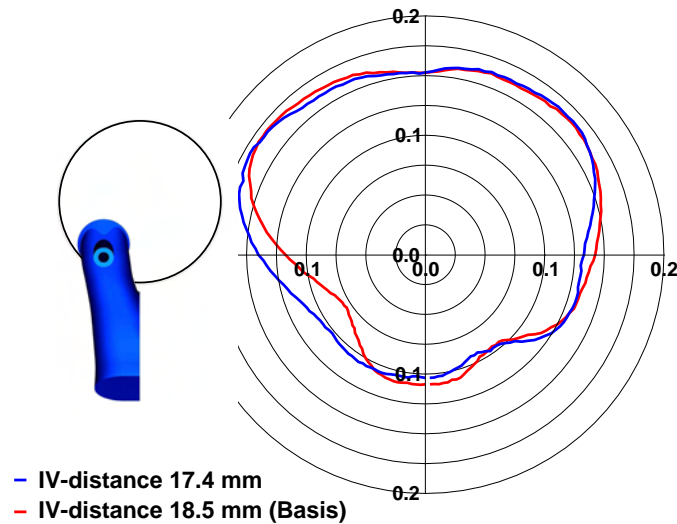


**Fig. 6.38:** Radial mass flow distribution through the intake valve gap for a variation of *IV-distance* (distance of intake valve to symmetry plane) (Elwan (2008)).

However, these investigations are based on weighted values derived by steady flow simulations at three different valve lifts. The final influence on the engine parameters cylinder filling and charge motion has to be evaluated by means of more realistic simulations like the dynamic analysis. For this purpose, both extreme designs of the Pareto-front, 'Design_0178' (max. $\overline{c}_f$) and 'Design_0155' (max. $\overline{TU}_{VOL}$), as well as the basic design '4CTC' are analyzed further. **Fig. 6.39(a)** shows the cylinder mass versus crank angle calculated by means of the dynamic analysis. By applying combustion chamber 'Design_0178' the highest cylinder filling after IVC (590 deg CA) is achieved as predicted by its maximum $\overline{c}_f$ value. Compared to the basic configuration an increase of 1% is gained. 'Design_0155' accordingly leads to a decrease of the cylinder mass of about 0.5% relative to the basis. Hence, concerning cylinder filling the weighted $\overline{c}_f$ value is a suitable non-dimensional number when optimizing a combustion chamber design.

The corresponding tumble curves are illustrated in **Fig. 6.39(b)**. Unlike predicted by $\overline{TU}_{VOL}$, the basic combustion chamber shape leads to the highest in-cylinder tumble motion during intake and compression stroke. 'Design_0155', which is characterized by maximum $\overline{TU}_{VOL}$, performs worse compared to the basic chamber. The lowest tumble value however is, as expected due to the optimization results, achieved by 'Design_0178'. As a result, the in-cylinder tumble motion is not always represented adequately by the proposed $\overline{TU}_{VOL}$ definition and is therefore not suitable for this optimization. As observed above, the high $TU_{VOL}$ values at 3 and 6mm valve lift have a dominating influence according to the $\overline{TU}_{VOL}$ definition (Equations 6.3 and 6.4). Nevertheless, the influence of the tumble number at small lifts is obviously not that important.

**(a)** Cylinder mass
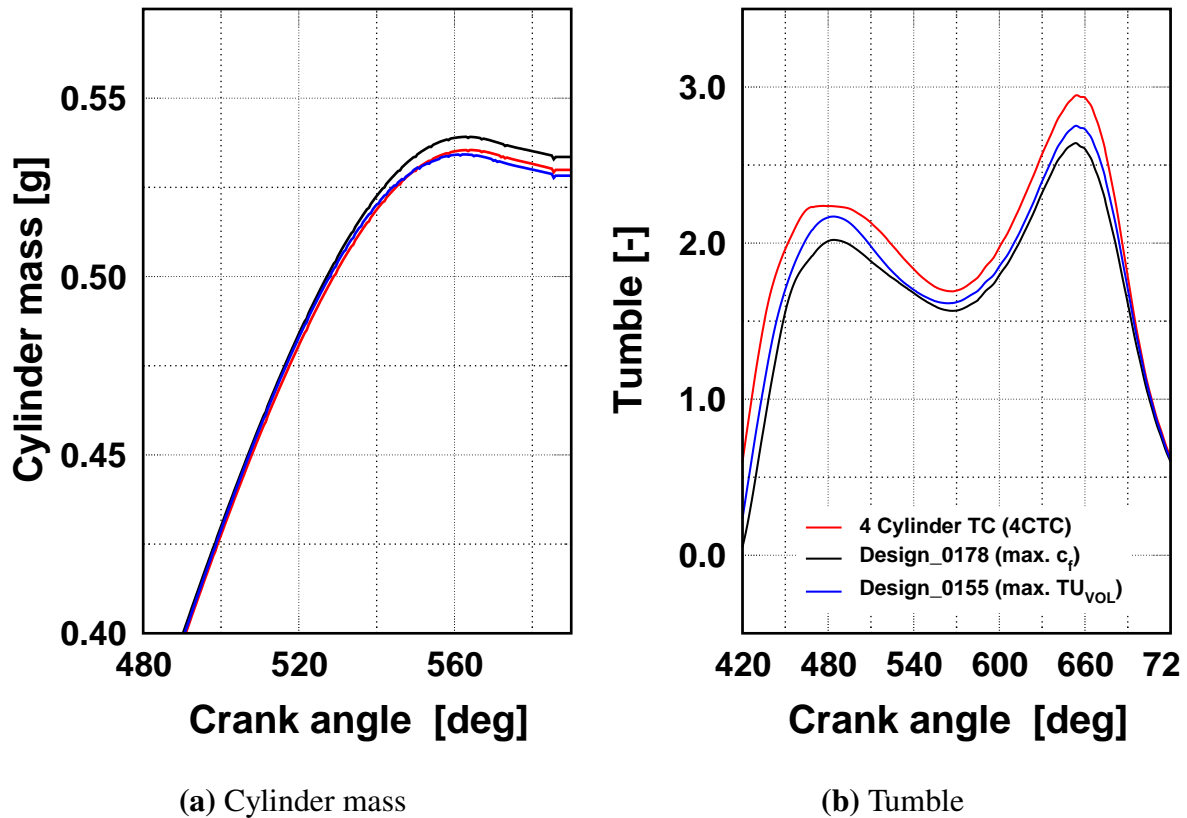
**(b)** Tumble

**Fig. 6.39:** Cylinder mass and tumble vs. crank angle simulated by the dynamic analysis

Hence, an improvement could be expected by reducing the weighting for small and medium lifts in favor of high lifts.

The optimization algorithm in general performs very well as significant improvements concerning the pre-defined objectives are realized. Concerning the flow coefficient, the results in fact correlate well with the corresponding cylinder filling analog to the intake port optimization. Concerning charge motion in contrast, the transfer of the $\overline{TU}_{VOL}$ results to the final tumble motion is not satisfying yet, which can be addressed to the definition of $\overline{TU}_{VOL}$. Modifying this definition a better correlation can be expected.

### 6.3.2   Optimization of a Production Cylinder Head with Masking

In the previous section an optimization strategy for a global investigation of general combustion chamber concepts is described. Apart from this, a strategy for a detailed optimization problem of a cylinder head geometry of a future four-cylinder SI-engine is discussed in the following.

This next generation engine (4CTC) is based on a naturally aspirated four-cylinder SI-engine (4CNA) with a fully variable valve drive and multi-point injection (MPI) introduced in Kessler et al. (2007). The main technical data of both engines are given in **Table A.1**. In order to increase the charge motion level, masking as well as phasing are applied. As described in

Section 4.1, masking is applied to elevate the tumble level at small valve lifts. Additionally, swirl motion is induced by phasing, where both intake valves follow different opening curves. As a result, the charge motion level and subsequently the turbulence level near TDC is increased leading to short combustion delay and fast burning rates. Furthermore, by means of the fully variable valve drive extremely small lifts and as a consequence very small valve gaps are realized at part load. High flow velocities then lead to excellent mixture preparation. Altogether, this combustion system enables very good combustion stability even for high valve overlapping with an accordingly large amount of internal residual gas resulting in reduced pumping losses and thus improved efficiency.

In a next development step of this engine, direct fuel injection combined with turbocharging is applied to further increase the engine's efficiency by downsizing. However, at part load conditions a worsening of 2-4% compared to the reference MPI-engine is observed. As a reason, reduced tolerance to residual gas is identified leading to higher pumping losses. 3D-CFD simulations reveal, that this loss in residual gas tolerance is mainly caused by poor homogenisation of the air-fuel mixture. This assumption is confirmed by laser induced fluorescence (LIF) measurements using an optical engine (Loeffler et al. (2009)). Furthermore, engine testings show a significant increase of CO emissions indicating poor homogenisation. As illustrated in **Fig. 6.40**, rich mixture remains at the piston, while rather lean mixture is observed in the spark plug region. Consequently, an increase in combustion delay and duration results leading to a loss in stability and efficiency. According to the optical measurements poor mixture preparation results from the present in-cylinder charge motion, which is dominated by the swirl component resulting from intake valve phasing. As a consequence, the air-fuel mixture is swirled around the spark plug and the mixing process is thus worsened. With the piston moving upwards the rich mixture remains on its top until ignition.



**(a)** Experiment (Grasreiner (2008))    **(b)** CFD-simulation
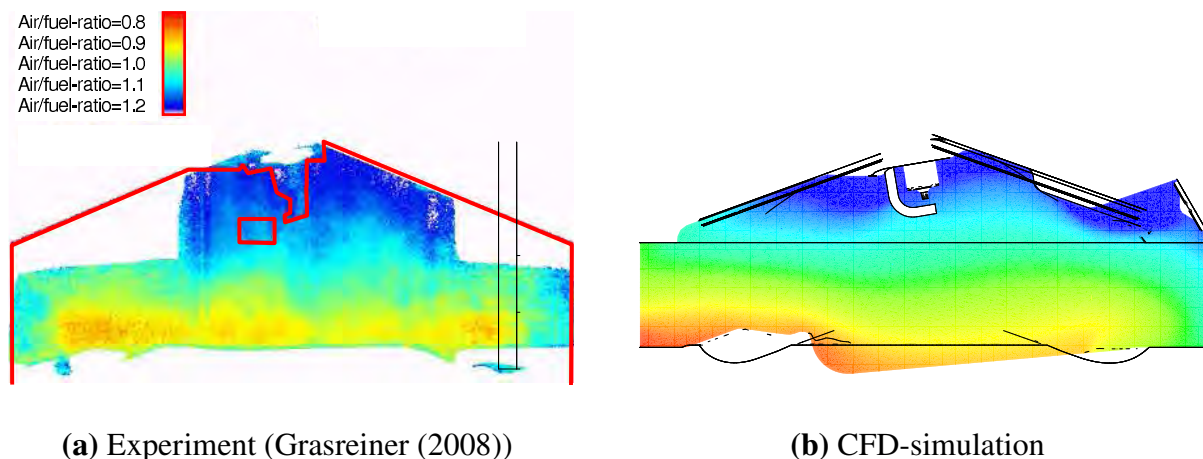
**Fig. 6.40:** Measured and simulated air/fuel-ratio at point of ignition.

According to these investigations, the target is to adopt the in-cylinder flow in order to improve the mixture preparation and further accelerate the combustion. Therefore, reducing the swirl component while increasing the tumble motion is expected to be a suitable measure. Thus, the charge motion axis will be further inclined with respect to the cylinder axis and the injected fuel

no longer be swirled around the spark plug. Due to the small valve lifts at part load operation, the focus is on the combustion chamber shape and particularly on the masking edge, as it mainly influences the in-cylinder flow. Modifying the intake port in contrast is not reasonable, as its influence is restricted to larger valve lifts only (Section 4.2). Accordingly, an optimization of the masking edge is performed, where three objectives are included: tumble number $TU_{VOL}$, swirl number $SW_{VOL}$ and flow coefficient $c_f$, which is influenced by the masking shape as well.

For this optimization the representative part load operating point 1500 rpm and 2 bar IMEP is considered. This point corresponds to a maximum average valve lift of approx. 1.0 mm, where intake valve IV1 opens 1.75 mm at maximum and IV2 0.25 mm. Thus, in contrast to the global optimization in the previous section, a single valve lift position is expected to be adequate for the assessment of the different masking designs as only the small lift region is regarded. Therefore, the maximum lift position 1.75 mm/0.25 mm (IV1/IV2) is evaluated. As a consequence of this phasing position, a full model of the combustion chamber has to be applied, which significantly increases the computational effort. Mesh generation for these small valve gaps, particularly for the intake valve IV2 with 0.25 mm lift, is another challenging task. Applying the standard tetrahedral mesh, the number of nodes vastly rises. By means of hexahedral elements within the narrow valve gaps, better mesh quality is achieved while the number of nodes is reduced by a factor of ten. **Fig. 6.41** shows a cut through the valve gap of intake valve IV1. For the optimization, the hexahedral mesh is remained unchanged, only the combustion chamber mesh is regenerated. Concerning these extreme small valve gaps, the SST turbulence model shows significant better convergence and is therefore applied for this investigation.
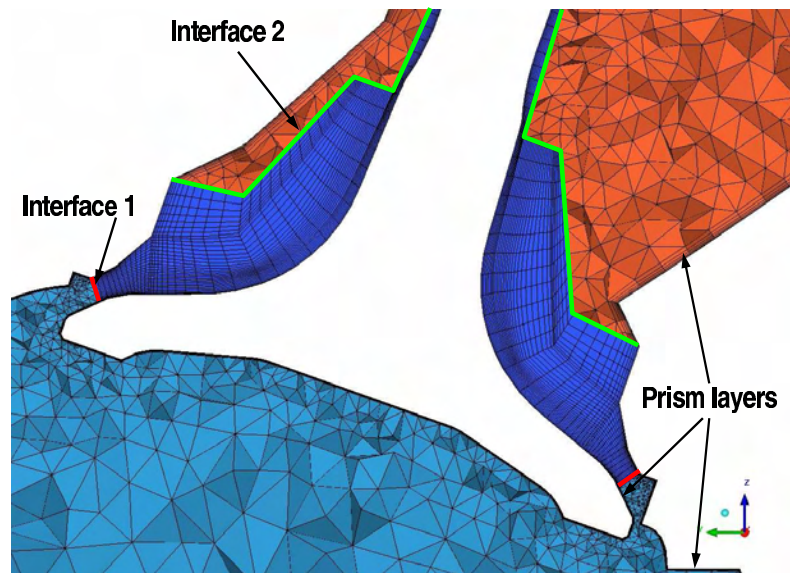


**Fig. 6.41:** Computational mesh in the area of the intake valve IV1 (Full (2007)).

**Fig. 6.42** shows the CAD-parameters, which describe the masking edge. These are the masking height $h$, the masking gap $s$ and the masking angles for both intake valves, $\alpha_{IV1}$ and $\alpha_{IV2}$. The basic masking angle is set to 180 deg, which denotes that half the valve is enclosed. By increasing or decreasing the angle, the valve is more or less enclosed. In total, a range from -15 deg to +15 deg is regarded (**Table 6.11**). A further decrease is not useful, as the masking edge
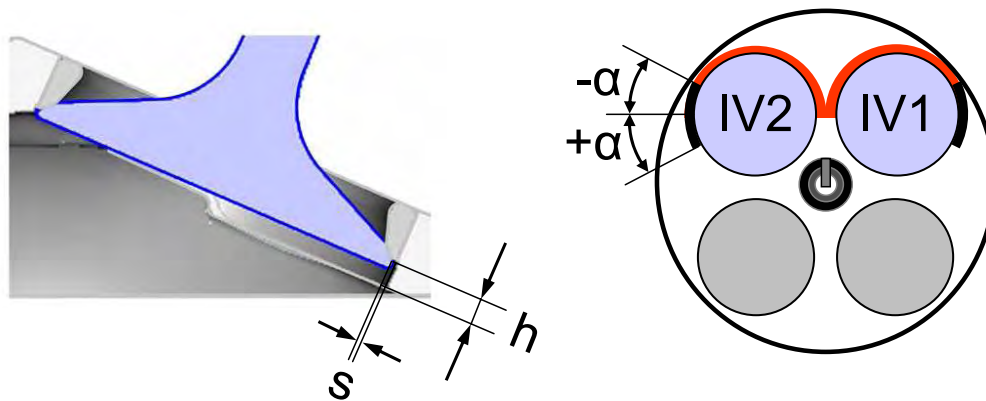
**Fig. 6.42:** Masking CAD-parameters: masking height $h$, masking gap $s$ and masking angles $\alpha_{IV1}$ and $\alpha_{IV2}$ (Full (2007)).

disappears within the combustion chamber shape, while an increase may be critical in terms of knocking, as the edge becomes a possible hot-spot. The masking height $h$ is varied from 1.8 mm to 2.7 mm, which was found to be sufficient within a preliminary study (Full (2007)). The masking gap $s$ is not included for the automatic optimization, as its tumble-enhancing influence is well-known from previous studies. Apart from this, for a series production the masking gap is already at its limit due to manufacturing tolerances.

| Parameter | Name | Basic Value | Lower Limit | Upper Limit | Resolution |
|-----------|------|-------------|-------------|-------------|------------|
| Masking height | $h$ | 2.1 mm | 1.8 mm | 2.7 mm | 0.1 mm |
| Masking angle IV1 | $\alpha_{IV1}$ | 0 deg | -15 deg | +15 deg | 1 deg |
| Masking angle IV2 | $\alpha_{IV2}$ | 0 deg | -15 deg | +15 deg | 1 deg |

**Table 6.11:** Variation range of the optimization parameters.

As for this optimization problem only three design parameters are regarded, a RSM-approach based on a DoE-sampling is applied. In order to calculate a quadratic RS-model with reasonable quality, 69 designs are evaluated derived by means of Latin-Hypercube sampling. The DoE-results for $c_f$, $TU_{VOL}$ and $SW_{VOL}$ are illustrated in **Fig. 6.43**. Concerning $c_f$ and $TU_{VOL}$ again a clear correlation is observed indicating a strict conflict between both objectives. Thus, a well-defined Pareto-front is already derived by the DoE-sampling. Concerning $SW_{VOL}$ a Pareto-front is determined as well, which is however less obvious. Based on the DoE-results a RS-model is calculated, by means of which the actual multi-objective optimization is performed using the SPEA2 GA in optiSLang. However, compared to the DoE-results no improvements are achieved, as a proper resolution of the objective space is already gained by means of the Latin-Hypercube sampling due to the low number of design parameters.

As optimal solution 'Design_0018' is selected, as it delivers maximum $TU_{VOL}$, while $SW_{VOL}$ is clearly reduced, which is intended for the adaption of the in-cylinder flow. This design is found by observing the Pareto-front delivered for $TU_{VOL}$ and $SW_{VOL}$ (**Fig. 6.43**). The CAD-
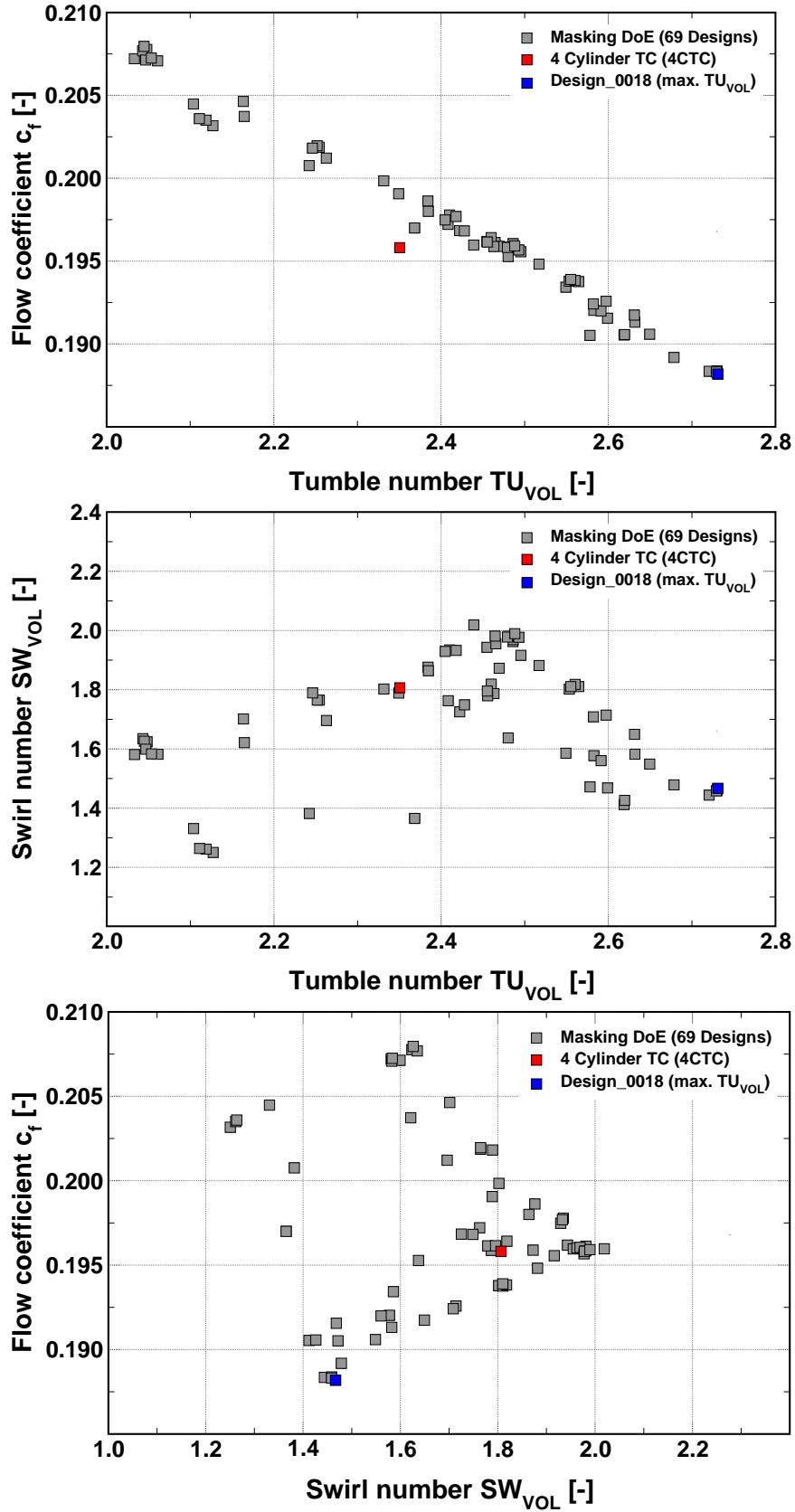
**Fig. 6.43:** Results of the DoE for the masking design in terms of $c_f$, $TU_{VOL}$ and $SW_{VOL}$.

parameters of this masking design are listed in **Table 6.12**. In order to increase $TU_{VOL}$ the masking height is set to the maximum value of 2.7 mm. Thus, the intake valves are fully covered for the regarded maximum lift of 1.75 mm, whereas they are not for the basic height. The swirl reduction is achieved by increasing the masking angle $\alpha_{IV1}$ to 15 deg. Concerning phasing, swirl strength is related to the unequal distribution of the mass flow rates over the particular intake valves. Accordingly, by increasing the amount of enclosing for intake valve IV1 its flow rate is reduced and the inequality diminished. Thus, swirl reduction is gained. On intake valve IV2 in contrast the masking edge has no influence, as the valve lift is extremely small (0.25 mm) resulting in negligible mass flow. As an addition to the optimized parameters, the masking gap is further reduced to 0.35 mm, which is realizable for the test engine. By this a further tumble increase is achieved which is desired for better mixture preparation.

| Parameter | Name | Basic Design | Design_0018 |
|-----------|------|--------------|-------------|
| Masking height | $h$ | 2.1 mm | 2.7 mm |
| Masking angle IV1 | $\alpha_{IV1}$ | 0 deg | +15 deg |
| Masking angle IV2 | $\alpha_{IV2}$ | 0 deg | 0 deg |
| Masking gap | $s$ | 0.45 mm | 0.35 mm |

**Table 6.12:** Parameters of the optimized masking design.

In order to assess the influence of this optimized masking design on the resulting in-cylinder flow, measurements on a steady flow test rig are performed. The results for both the basic and the optimized cylinder head design are illustrated in (**Fig. 6.44**), where a Tippelmann honeycomb is applied for analyzing tumble and swirl. As revealed by the steady flow simulations the tumble ratio significantly rises with respect to the basic design, while the swirl is slightly reduced, however for small lifts only.
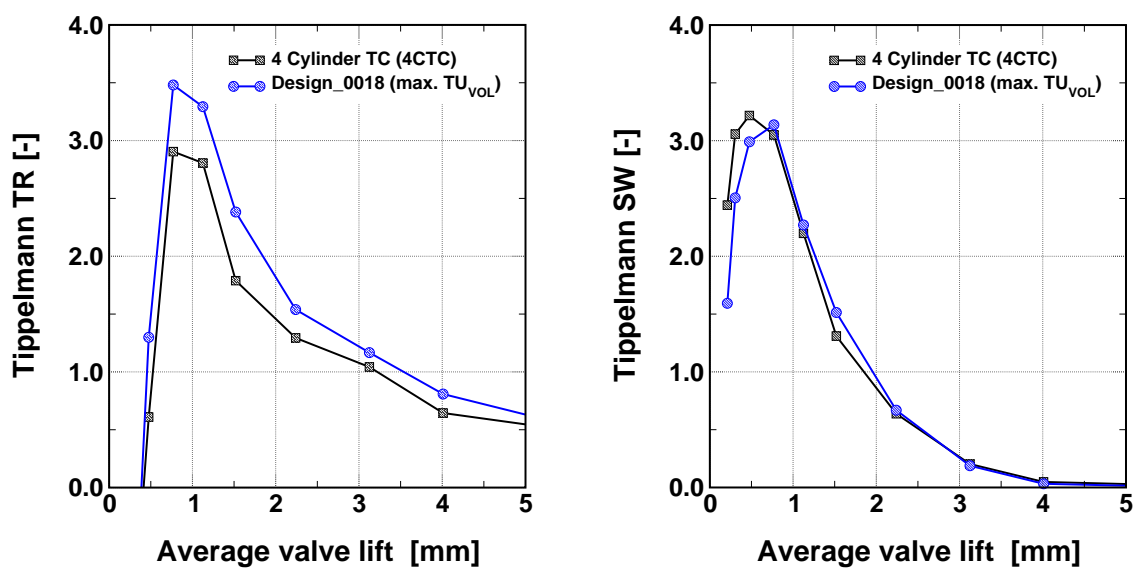


**Fig. 6.44:** Tumble ratios (left) and swirl ratios (right) measured by means of a Tippelmann honeycomb.

The results of the engine testing in terms of ISFC, emissions, combustion stability (CoV) and duration at 1500 rpm and 2 bar IMEP are depicted in **Fig. 6.45**, where both engine designs are investigated. In addition, the series naturally aspirated four-cylinder engine (4 Cylinder NA) is listed as reference. Applying the optimized masking design, homogenization and combustion stability can be improved significantly compared to the basic masking shape. Accordingly, the CO-emissions (ISCO) are on the same level as for the MPI-engine, while the CoV is even better. Apart from this, combustion duration (CD) is reduced by 4 deg CA. As a result, the ISFC is decreased by 2% with respect to the basic engine design. However, in spite of improved mixture preparation, the residual gas tolerance is not enhanced and still a gap to the MPI-engine in terms of fuel consumption remains.
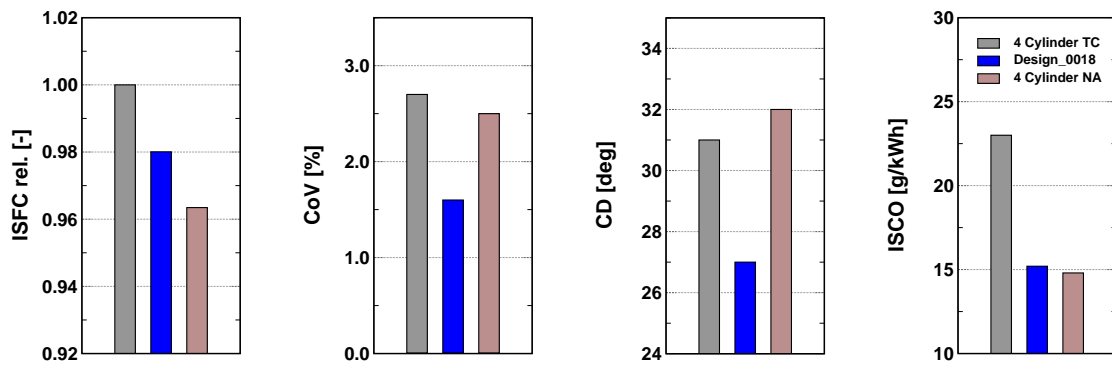


**Fig. 6.45:** Test bench results at 1500 rpm and 2 bar IMEP.

The resulting in-cylinder flow is further analyzed by means of a detailed 3D-simulation of the exhaust, intake and compression stroke. As shown in **Fig. 6.46**, for the optimized masking
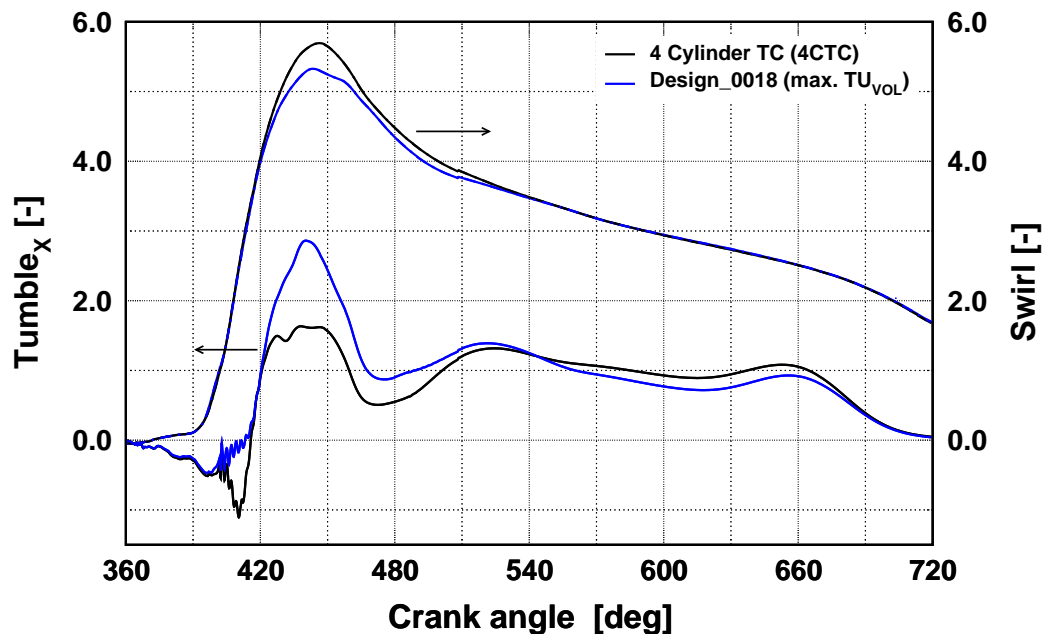


**Fig. 6.46:** Tumble and Swirl vs. crank angle for the basic and the optimized combustion chamber designs.

edge of 'Design_0018' the tumble motion is increased, while the swirl is slightly reduced from the point of injection on (SOI = 406 deg CA). Furthermore, the turbulence level is increased (**Fig. 6.47**). Altogether, improved mixture preparation is achieved indicated by the engine results. In addition, this improvement is confirmed by means of CFD-simulations. **Fig. 6.48** illustrates the air/fuel-ratio at ignition point for both designs. By means of the optimized masking design a more even mixture distribution is gained, particularly in the spark plug region. Nevertheless, still slight charge stratification is remaining, with rich mixture at the piston surface and lean mixture near the chamber roof, which is a serious problem in the context of fuel direct injection. Thus, apart from measures concerning the in-cylinder flow further approaches like multiple injection or combined DI-PFI concepts have to be investigated.
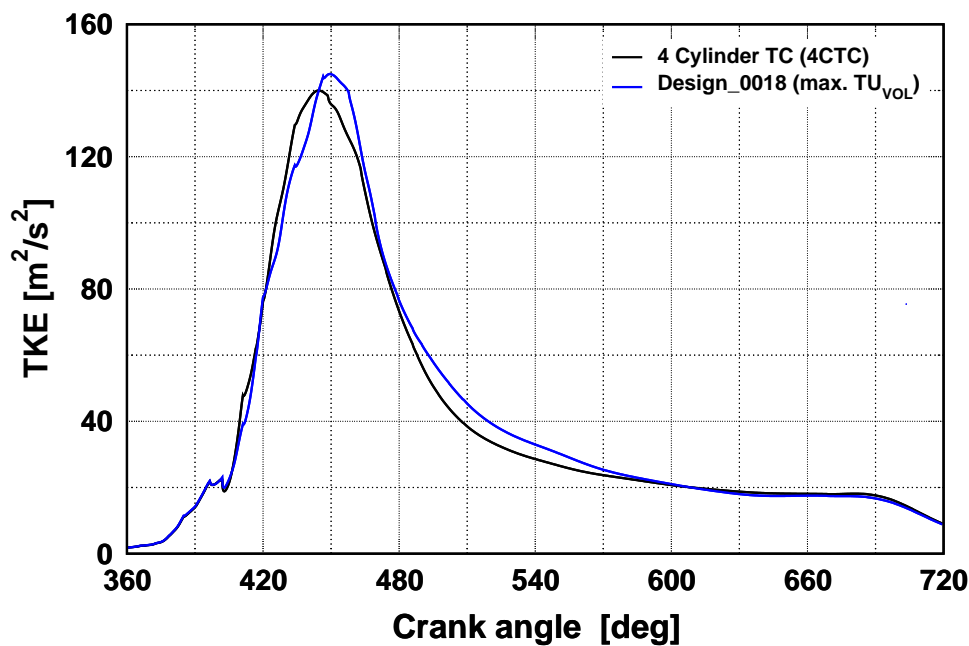


**Fig. 6.47:** TKE vs. crank angle for the basic and the optimized combustion chamber designs.



**(a)** Basis
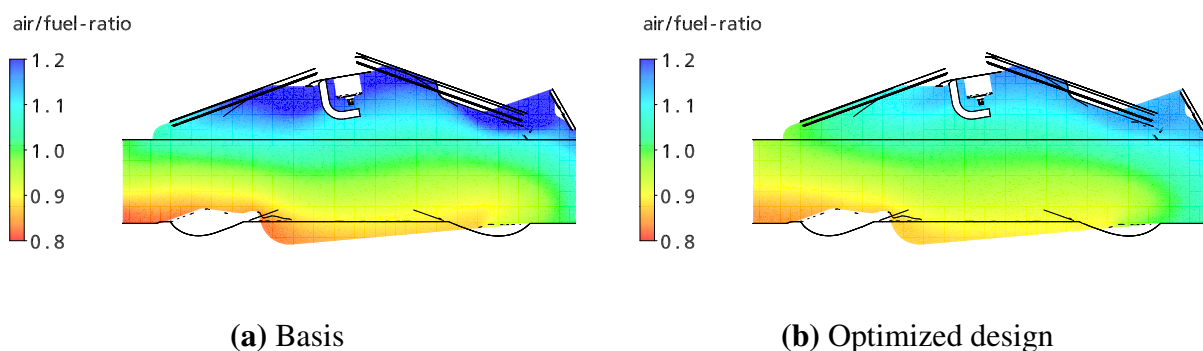
**(b)** Optimized design

**Fig. 6.48:** Simulated air/fuel-ratio at point of ignition for the basic and the optimized masking design.

By means of the proposed optimization strategy using a single lift for evaluation, promising results can be gained for optimizing the specific masking geometry of a cylinder head. A well-defined correlation between both tumble and swirl is observed for the simple steady flow analysis and the detailed simulation of the engine cycle. Altogether, by means of the optimized masking the efficiency of the turbocharged DISI-engine can be improved significantly due to better homogenization. However, further measures concerning mixture preparation are required in order to reach the level of the naturally aspirated SI-engine with port injection.

### 6.3.3 Conclusions

For the intake port optimization a single valve lift position (e.g. maximum lift) is found to be sufficient for assessment. For a global optimization of the combustion chamber in contrast the entire lift range has to be regarded, as the influence varies according to the lift position. As a result, the computational effort clearly rises. For simplification, the division into different lift ranges (e.g. low/medium/large), represented by a particular lift respectively, is a suitable approach. Then, for the actual optimization weighted numbers are required for each objective. In the case of flow rate an adequate characterization can be defined by means of 1D gas exchange simulations. Concerning tumble, the characterization is much more demanding. The present approach, which is based on weighted tumble numbers including valve opening duration and flow coefficient, is not suitable. A modified characterization should deliver more promising results. Nevertheless, by means of the combustion chamber optimization the general extent of its influence on both objectives $c_f$ and $TU_{VOL}$ can be assessed, while it is obviously less compared to the influence of the intake port.

Regarding small lifts however the influence of the combustion chamber design clearly dominates, which is investigated on the example of a optimization of a cylinder head with masking. In order to improve the mixture preparation of a turbocharged SI-engine with VVT a detailed optimization of the in-cylinder flow is performed. As the masking influence is limited to small lifts only, the design evaluation by a single lift position is an adequate approach. In fact, by means of the optimized masking shape the air-fuel homogenization is clearly improved leading to reduced fuel consumption. The results of the simplified single lift approach are validated by means of experimental data from a steady flow test rig and a detailed simulation of the in-cylinder charge motion, where a well-defined correlation between simplified and detailed methods is revealed.

# 7   Robustness Analysis

Intake port and combustion chamber design significantly influence cylinder filling and charge motion and thus the combustion process. As the cylinder head where both devices are integrated is produced in a casting process, tolerances within this process lead to variations from the basic geometry. Optimal designs in particular tend to be sensitive to these small fluctuations of parameters (Dynardo (2008)). In order to guarantee a robust combustion system, the variations of the engine parameters cylinder filling and charge motion resulting from geometry variations have to be investigated carefully (Eichlseder et al. (1998)). For this purpose a robustness analysis is performed. Therefore, the most relevant tolerances and their distribution concerning the intake port are analyzed in the first part of this chapter. Subsequently, the influence on the in-cylinder flow is presented.

## 7.1   Influence of Generic Geometry Tolerances

The intake port manufacturing process is divided into a casting process and a machining operation. Within the casting process the raw part is produced based on a casting core. In the case of the eight-cylinder SI-engine a sand core is applied as illustrated in **Fig. 7.1**. The machining operation is performed by means of a milling cutter, which ensures the correct arrangement of the valve seat ring and the final intake port design. Concerning filling port designs often the entire port is machined, thus reducing the variations resulting from the casting process and improving the port's surface quality. In the case of tumble ports, the machining is commonly limited to the seat ring region only. Here, the proper generation of a flow separating edge is intended. Accordingly, concerning the production process of the intake port a variety of sources for variations exists:

- design parameters of casting core and milling cutter,

- positioning of the casting core,

- positioning of the milling cutter,

- wall roughness (casting quality).

For the present work only variations of the casting core positioning are considered, as for the variations of the casting core design and the wall roughness reliable data are missing and the possible translations of the milling cutter are assumed to be negligible. Apart from tolerances within the production process, further geometry variations appear during engine operation like coking of the intake ports and valves in the context of fuel direct injection. However, the numerical treatment of these problems is very complex and is not part of the present framework.

The regarded translations of the sand core in $x$-, $y$- and $z$-direction are shown in **Fig. 7.2**. Due to these, the raw part is slightly translated relative to the milling cutter, which leads to a deviation

**Fig. 7.1:** Sand core for the tumble port of the eight-cylinder SI-engine.

from the basic port design. A deviation in $x$-direction leads to a lateral translation of the raw part. As a result, the cylinder head design is not symmetric anymore and the full model has to be simulated, which significantly increases the computational effort. Due to this reason, a different method for mesh generation is applied, where the unstructured tetrahedral mesh of the cylinder is replaced by a structured mesh gained by extrusion as explained in Section 5.2.2. Thus, calculation times are reduced almost by half as introduced in **Table 5.2** and accordingly comparable to those of the initial half model.
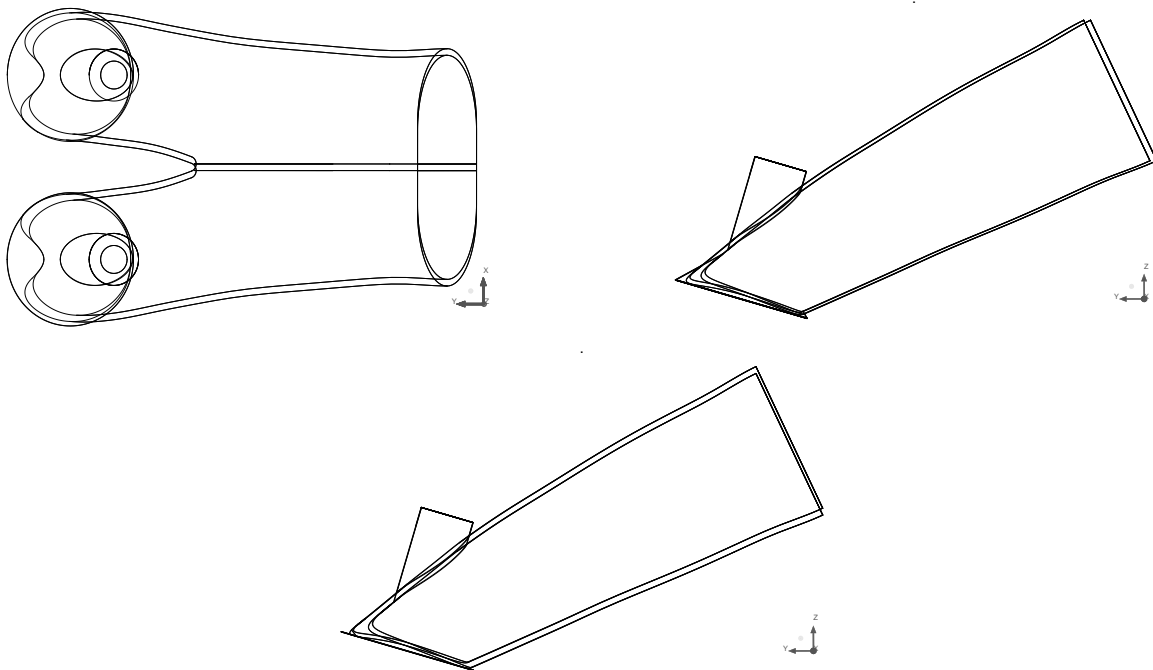


**Fig. 7.2:** Translations of the raw part in $x$-, $y$-, $z$-direction (clockwise from above)

A deviation in $y$-direction denotes a forward or backward translation respectively, while a deviation in $z$-direction signifies, that the core is floating up or down respectively. Concerning the real manufacturing process, all these variations are superposed. In order to investigate their influence on the particular objectives flow rate and charge motion in general, a sensitivity

analysis using Latin-Hypercube sampling is performed as proposed by Will et al. (2003). This analysis is based on the series tumble port '8CBasis' as it has been well investigated and found to enable a robust combustion concept. Using this intake port the particular translations are varied within a range of +/- 0.7 mm, which is defined as a rough interval for a stable production process. Of course, for the real production process a different range of variations will appear. The design evaluation is examined by means of the steady flow analysis at maximum valve lift analog to the optimization process before.

The DoE-results are shown in **Fig. 7.3**. First of all it is noticeable, that the geometry variations caused by the translations of the raw part have a significant influence on both objectives $c_f$ and $TU_{VOL}$. Once more, the strict conflict between both objectives is apparent and the resulting designs spread along the Pareto-front found in **Fig. 6.12**. The investigated designs resulting from the considered translations are part of this Pareto-front or very close to it. Accordingly, in the view of a multi-objective optimization the design variations do not lead to a significant worsening of quality. Apart from this it is remarkable, that in spite of normally distributed translations, generated by LH sampling, the resulting objective variations are distributed unequal. Obviously, the generic translations lead to designs, which tend more likely towards increased $c_f$ and lower $TU_{VOL}$. This can be explained by the specific intake port layout of '8CBasis', which is already designed for high tumble numbers. A further increase of $TU_{VOL}$ is accordingly less probable. As a consequence for the real engine, the cylinder filling will tend to increase, while the charge motion tends to decrease. In fact, increased LET and slightly reduced fuel consumption at part load could be expected with respect to the basic geometry as observed for the cylinder head variation in Section 4.2. The engines efficiency at WOT conditions in contrast would tend to decrease due to a slower combustion.
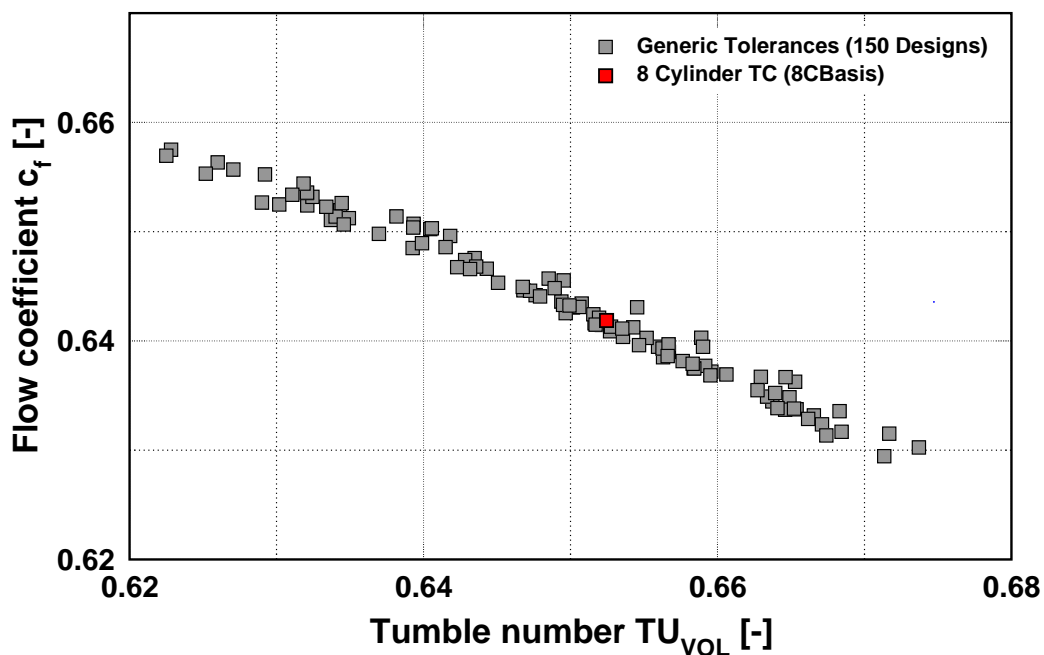


**Fig. 7.3:** Flow coefficient $c_f$ vs. tumble number $TU_{VOL}$ for generic translations of the raw part.

By means of correlations resulting from the sensitivity analysis the most important translations and their influence on the particular objectives can be analyzed. For the considered translations the following conclusions are revealed:

- **$x$-translations** have no influence on flow coefficient $c_f$ and tumble number $TU_{VOL}$, as there is no correlation at all. As the design of the cylinder head is no longer symmetric, a swirl component is induced in addition, where a strong correlation is observed. Nevertheless, this swirl is very weak and can be neglected. As a result, the influence of translations in $x$-direction can be neglected in general.

- **$y$-translations** show a weak correlation to both $c_f$ and $TU_{VOL}$. A positive translation increases $TU_{VOL}$ as the flow separating edge is more distinctive. Furthermore, by shifting the raw part ahead the flow of the air over the front part of the valve is supported. A negative translation in contrast decreases $TU_{VOL}$ and accordingly increases $c_f$. Altogether, these influences should be regarded, even though they are not dominating.

- **$z$-translations** definitely have the largest influence. A strong correlation to both $c_f$ and $TU_{VOL}$ is observed. Analog to the $y$-translation, a positive translation increases $TU_{VOL}$ and decreases $c_f$ and vice versa, due to the same reasons. However, compared to the translations in $y$-direction, the geometry variations and thus the effects are definitely more intensive. Altogether, the $z$-translation is the most influencing parameter and clearly dominates the other translations.

Comparing the results for design '8CBasis' shown in **Fig. 7.3** to the results listed in **Table 6.6** different $c_f$ and $TU_{VOL}$ values appear, which are caused by applying a full instead of a half model and different mesh topology. For the sensitivity analysis, where relative fluctuations with respect to the basic geometry are of interest, this can be excepted. Concerning the optimization process, this behavior is not satisfying. As a consequence, a full model in combination with equal mesh topology should be used in general.

## 7.2 Influence of Realistic Tolerances on the In-Cylinder Flow

For the sensitivity analysis normally distributed variations are required, which are gained by means of Latin Hypercube sampling. From these results general influences can be derived. For the real production process however different distributions will appear. Thus, for the first time a robustness analysis based on actual or realistic translations respectively is performed. By this analysis the most important variation parameters and their impact on the variation behavior of the responses can be evaluated (Will et al. (2003)). For this purpose, the actual translations in $x$- and $z$-direction are measured for 89 cylinder heads of the eight-cylinder engine, which is a sufficient number to obtain reliable statistics (Will et al. (2003)). As an example, the results for the translations in $z$-direction as well as the mean value (red line) are depicted in **Fig. 7.4**. It is noticeable, that the mean $z$-value is elevated from the actual basic value of 0.0 to 0.2. This

**(a)** Measured z-translation

**(b)** Distribution of z-translation
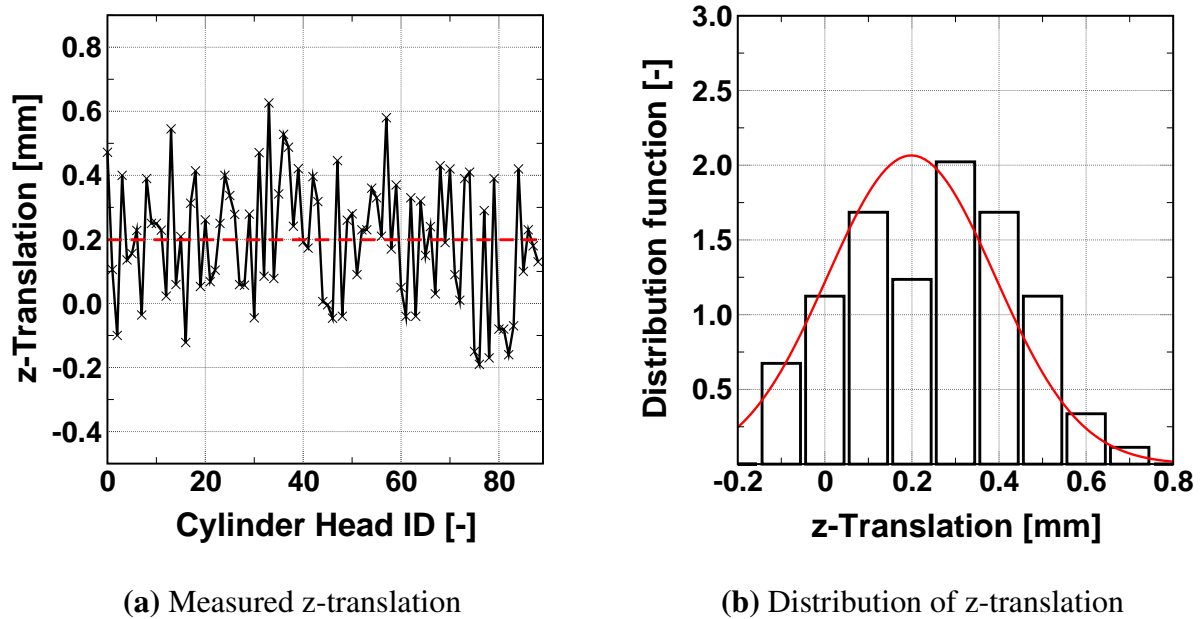
**Fig. 7.4:** Variation of *z*-translations of the intake port raw part during the manufacturing process.

translation of the core in positive *z*-direction is introduced consciously in order to ensure a well-defined edge for flow separation and thus a high tumble level. For the *y*-direction in contrast corresponding data is missing. Due to the steep port design the reasonable measurement of the translations is not possible. Alternatively, a stochastic analysis method as described by Bucher (2007) is applied for the robustness analysis here. It is based on probability distribution functions, which are assumed to properly represent the dispersion of the actual translations about the mean value (Will (2006)). As more precisely informations are missing, an uniform distribution is assumed, while the standard deviation is defined according the measurement data of the *z*-direction. Based on these definitions, the values for the *y*-translation are finally gained by means of a LH sampling.

**Fig. 7.5** shows the results for $c_f$ and $TU_{VOL}$ gained from the robustness analysis of port '8CBasis' based on the above mentioned translations. Analog to the DoE, the designs spread along the Pareto-front, while the range of variation is clearly smaller. As intended by the elevation of the mean *z*-translation, a shifting towards higher tumble numbers is achieved. Hence, the mean tumble number $TU_{VOL}$ is slightly increased (+0.8%) compared to the basic port geometry, while the mean $c_f$ value consequently is decreased (-0.5%) due to the apparent conflict between $c_f$ and $TU_{VOL}$ (**Table 7.1, left side**). As a consequence, compared to the basic engine design a slightly accelerated combustion process can be expected at average. At the same time the maximum torque level will be primarily reached at a slightly higher engine speed analog to revealed relations in Section 4.2. In general, $TU_{VOL}$ varies within an interval of 4.0% and $c_f$ of 2.9%.
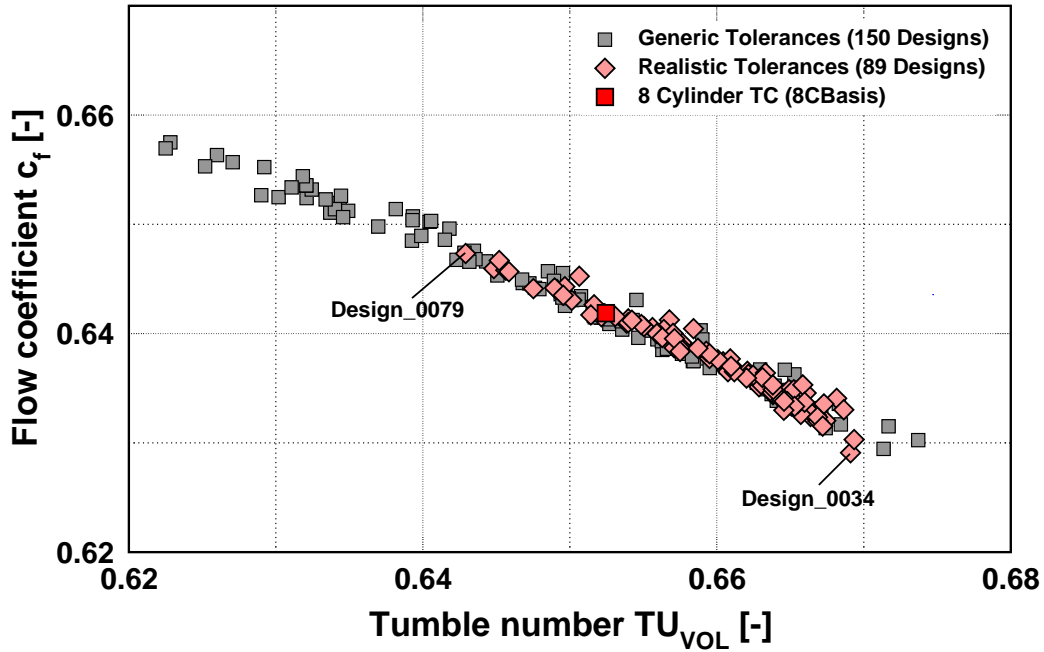
**Fig. 7.5:** Flow coefficient $c_f$ vs. tumble number $TU_{VOL}$ resulting from the robustness analysis of the eight-cylinder tumble port.

As these results are based on the single lift approach analog to the optimization strategy for intake ports before, more detailed simulations are required for the final assessment of the influence on the engine performance. Therefore, the representative designs 'Design_0034' and 'Design_0079', characterized by maximum $TU_{VOL}$ and maximum $c_f$ respectively (**Fig. 7.5**), are evaluated by means of the dynamic analysis. Concerning cylinder filling, the effects identified by means of the robustness analysis are confirmed (**Fig. 7.6**). Compared to the basic geometry, 'Design_0079' (maximum $c_f$) realizes a slightly higher cylinder mass after IVC. However, this effect is negligible. The lowest cylinder mass results from 'Design_0034' (minimum $c_f$), where a decrease of about 0.3% is observed. Compared to the intake port investigation of the six-cylinder TC engine in Section 4.2, where the simulation delivers differences in a range of 1.5% in $c_f$ between both port designs, these variations are rather small. Hence, the influence of variations of the cylinder filling on the performance of real engine can be expected to be small or negligible.

|                | $c_{f(8CBasis)}$ | $TU_{VOL(8CBasis)}$ | $c_{f(Opt.Design)}$ | $TU_{VOL(Opt.Design)}$ |
|----------------|------------------|---------------------|---------------------|------------------------|
| Basic Geometry | 0.642            | 0.655               | 0.645               | 0.673                  |
| Maximum        | 0.647            | 0.669               | 0.654               | 0.697                  |
| Minimum        | 0.629            | 0.643               | 0.630               | 0.648                  |
| Average        | 0.638            | 0.660               | 0.641               | 0.675                  |

**Table 7.1:** Robustness analysis for the basic and the optimized tumble ports.
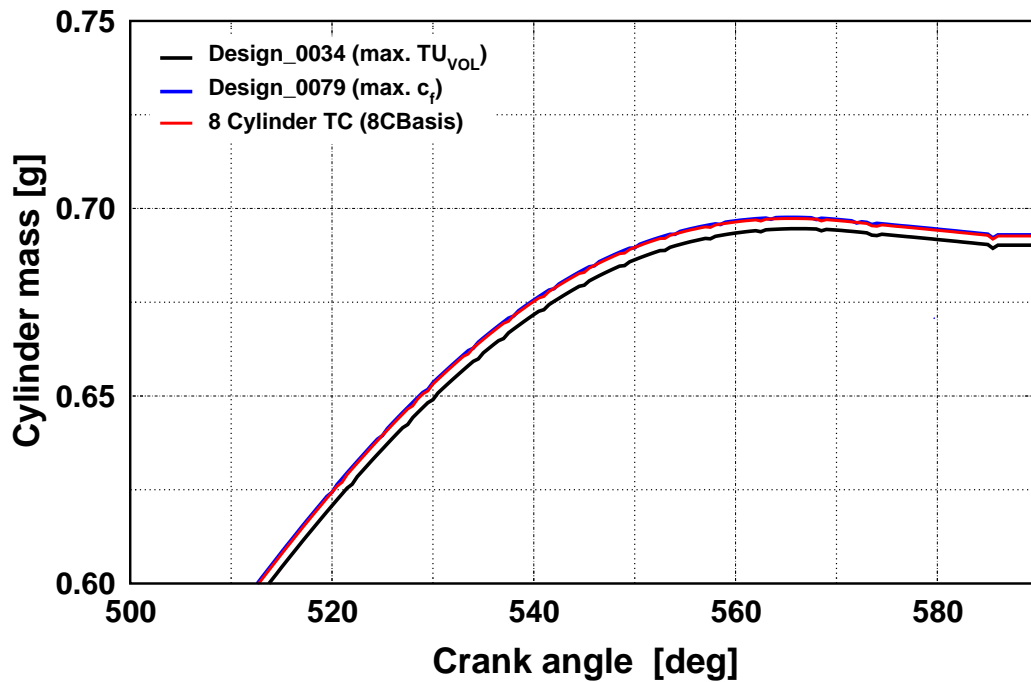
**Fig. 7.6:** Cylinder mass vs. crank angle for the extreme variations of the basic tumble port.

Concerning tumble the relations are depicted well by the steady flow results again (**Fig. 7.7**). As predicted by $TU_{VOL}$, the highest tumble is delivered by 'Design_0034', which is however more or less identical to the tumble value of the basic geometry. The lowest tumble is gained by 'Design_0079', the difference to the basic port at 645 deg CA amounts to 3.5%. As for the intake port comparison (Section 4.2) a difference of almost 30% is predicted, the lack in tumble is not
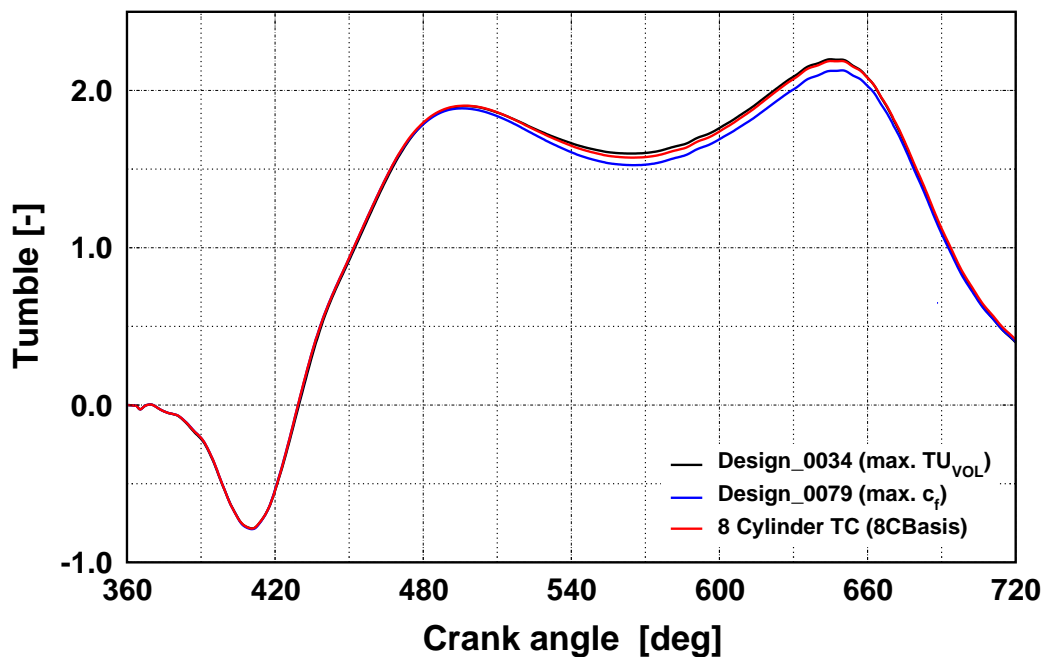


**Fig. 7.7:** Tumble vs. crank angle for the extreme variations of the basic tumble port.

significant. In general, the single lift approach is found to be a suitable method for the robustness analysis as well, due to a well-defined correlation between steady flow and engine-like dynamic analysis. As a result of the robustness analysis the variations of the engine parameters cylinder filling and tumble, caused by varying intake port geometries, can be assessed. After all they are expected to be very limited, which characterizes the tumble port '8CBasis' as a robust intake port design.

As mentioned above, optimal designs tend to lose in robustness. A robustness analysis is therefore performed for the optimized intake port 'Design_0260' (referred to as 'Opt. Design'), found by means of the local optimization in Section 6.2.4, as well. For this analysis the same parameter variations as for the analysis of the series tumble port '8CBasis' before are defined, where the mean $z$-translation is set to value of +0.2. **Fig. 7.8** illustrates the corresponding results for $c_f$ and $TU_{VOL}$. Again, the well-known conflict between both objectives is revealed and a Pareto-front appears. For 'Design_0260' however the considered manufacturing tolerances obviously lead to a wider spread of the responses compared to the series tumble port, particularly in terms of $TU_{VOL}$. In general, this indicates reduced robustness for the optimized design. Apart from this, the designs spread more widely away from the Pareto-front and thus not all designs deliver an optimal solution of the $c_f$-$TU_{VOL}$ conflict. Obviously, concerning intake ports, this phenomenon is another criteria for evaluating robustness of an intake port design. Robust intake port designs spread in a narrow band along a well-defined front, which is part of the corresponding Pareto-front. Less robust designs in contrast spread in an extended band and in addition away from this front.
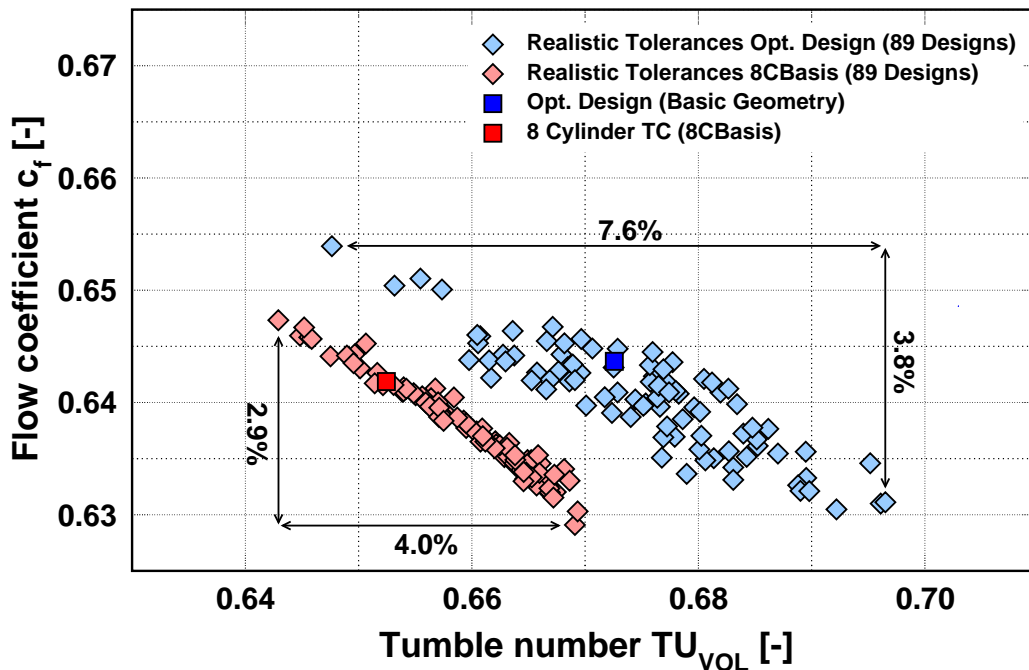


**Fig. 7.8:** Flow coefficient $c_f$ vs. tumble number $TU_{VOL}$ resulting from the robustness analysis of Design_0260.

Concerning the optimized design, the flow coefficient varies by +1.4% and -2.4% with respect to the basic geometry, while the tumble number results vary by +3.5% and -3.7%. For $c_f$ the variations are on the level of the basic eight-cylinder tumble port '8CBasis'. Concerning $TU_{VOL}$, the variations are significantly enlarged. In order to estimate the consequences for the real engine operation, the extreme variations for both objectives are assessed by means of the dynamic analysis. The results for cylinder mass at IVC as well as the tumble value at 645 deg CA are illustrated in **Fig. 7.9** together with the results of the basic tumble port. As predicted by the single lift analysis the variations of flow coefficient and thus cylinder mass are on the same level for both port designs and are acceptable. Concerning tumble the steady flow results are confirmed as well, as the tumble variations at 645 deg CA concerning the optimized designed are significantly increased. The extreme designs with maximum and minimum tumble differ by 7.2%. Compared to the variations of the six-cylinder intake port comparison in Section 4.2, where both ports differ by approx. 30%, an impact on the combustion process can definitely be expected. According to the six-cylinder engine test results e.g. a variation of about 1-2% in fuel consumption for the LET region could result from geometry tolerances. Nevertheless, according to the results of the dynamic analysis the optimized tumble port design can deliver a higher charge motion level compared to the basic port in any case.
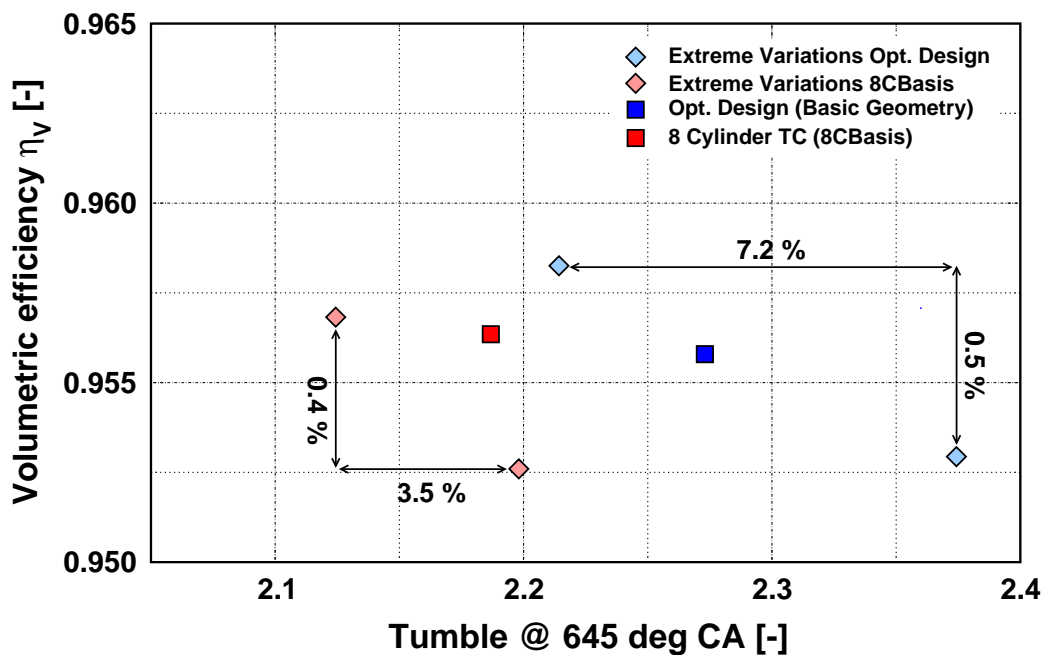


**Fig. 7.9:** Variations of volumetric efficiency and tumble resulting from the dynamic analysis.

## 7.3   Conclusions

In order to analyze the influence of tolerances resulting from the production process on the relevant objectives cylinder filling and charge motion, a robustness analysis is performed. By means of a sensitivity analysis, which is based on uniform distributed geometry variations, a clear impact is determined. In particular, the *z*-translation of the raw part relative to the final

machining operation is identified as main influence parameter, whereas *x*- and *y*-translation have no influence and are of secondary significance respectively. The real variations occurring during production are evidently different, which are considered by a robustness analysis. As a result, mean values as well as maximum and minimum values for flow coefficient and tumble number are obtained for the basic tumble port '8CBasis' and the optimized tumble port. For the basic tumble port the scatter band between minimum and maximum is significantly smaller, which characterizes this port as more robust compared to the optimized design. In addition, all design variations scatter along a well-defined front, which is part of the Pareto-front revealed by the global optimization in Section 6.2.2.1. For the optimized design in contrast the design variations also spread away from the corresponding Pareto-front. Hence, the type of scattering, exclusively along the Pareto-front or also away from it, is another measure for assessing robustness when dealing with intake ports. Altogether, the optimized design is found to be less robust, especially in terms of tumble motion, which will influence engine performance and combustion. Nevertheless, based on the results of the dynamic analysis its tumble level continuously exceeds the basic port. Hence, in order to assess the intake port characteristic adequately optimization and robustness have to be regarded simultaneously, which of course further rises the computational effort.

# 8    Summary and Conclusions

In the present work an automatic CFD-based optimization process is introduced, which has been applied to different problems involving intake port and combustion chamber geometries of turbocharged SI-engines with direct injection. For this combustion concept in particular a very challenging optimization problem arises as a strong conflict of objectives between flow rate and charge motion exists.

In order to analyze the requirements concerning the in-cylinder flow of a turbocharged DISI-engine with VVT, two different tumble inducing ports have been investigated. As a result it has been revealed, that the above mentioned conflict is particularly strict for the low end torque region. High tumble motion with accordingly high turbulence intensity significantly accelerates the combustion process and reduces knocking tendency. Thus, a significant increase in engine efficiency is achieved. Nevertheless, faster burning rates also lead to a decrease in exhaust gas enthalpy. Therefore, the torque output at low engine speeds is limited and the targeted torque plateau is reached later. Reduced mass flow rates due to a worse flow coefficient further intensify this effect. These relations are also observed for rated power. There however, the conflict of objectives is less strict as high turbulence intensities in general are realized due to high engine speeds. Accordingly the optimization can be focused on the flow coefficient in order to reduce boost pressures demands. At part load operation with VVT different phenomena are observed depending on the valve lift curve. For small valve lifts at low loads and engine speeds the intake port geometry hardly impacts the in-cylinder flow, as combustion chamber and valve seat design are clearly dominating. With rising valve lifts however the intake port design gains in significance. Worse flow rate characteristics lead to increased charge exchange losses and accordingly slightly increased fuel consumption. Higher tumble intensities in contrast hardly influence the combustion process at upper part load conditions (valve lift below five to six millimeters) and therefore cannot compensate this disadvantage.

Altogether, concerning the layout of the in-cylinder flow both flow rate and charge motion have to be regarded simultaneously, which leads to a multi-objective optimization problem. In addition it has been observed, that for a turbocharged engine with VVT intake port and combustion chamber respectively have to be analyzed and adapted according to the specific engine operating ranges. For this purpose, a CFD-based process using parametric CAD-models has been established in order to optimize the intake port and combustion chamber geometry automatically. The intake port CAD-model has been developed such that the entire range between filling and high tumble ports can be represented by a single model only. This has been proved by means of a global intake port optimization. In order to guarantee this flexibility, approx. 20 CAD-parameters are required. Concerning the combustion chamber, the generic model has been designed on the basis of a series production engine, where in addition a flexible masking edge and intake valve device is included. Like the intake port model it enables the investigation of a wide range of different chamber designs. Nevertheless, this high flexibility also leads to an enlarged number of failed designs for both parametric models, as not all

parameter combinations can be regenerated. Improving the models' robustness while keeping their flexibility is an important task for future development.

Concerning design evaluation, non-dimensional numbers derived from steady flow CFD-analysis have been found to be suitable for an efficient optimization process. The assessment of the flow rate characteristics is based on the flow coefficient, while the charge motion level is analyzed by means of swirl and tumble numbers. The required calculations are performed at particular valve lifts respectively. Concerning intake ports, evaluating a single valve lift - preferably the maximum lift - appeared to be sufficient. In contrast, the investigation of combustion chamber designs demands that several valve lifts are considered, as the chamber's influence varies with the valve lift position. Only for detailed optimization problems, where exclusively small lifts appear, a single valve lift is sufficient. Due to these relations different optimization strategies have been developed in the framework of the present work according to the particular optimization problem.

For the intake port a global optimization based on the steady flow characteristics at maximum valve lift has been performed, where three different optimization approaches, a DoE-strategy combined with RSM, an ES and a GA, have been applied. For all approaches a continuous Pareto-front of almost linear character has been revealed. While the DoE/RSM and the GA covered the whole spectrum of intake port types, the ES only delivered a section of the Pareto-front. However, the worse performance of the ES is rather due to the single starting point strategy, which results in a rather local optimization, than due to the algorithm. The GA in contrast benefits from a wide-spread starting population, which can be defined at the beginning. In order to validate the applied steady state method and to estimate the impact on the real engine behavior, a representative set of intake ports has been selected from the global Pareto-front and assessed by means of dynamic analysis. For this transient analysis the intake and compression stroke has been simulated, which allowed for analyzing the engine's volumetric efficiency and charge motion level. As a result, a well-defined correlation between volumetric efficiency and flow coefficient has been revealed. Concerning tumble and turbulent kinetic energy (TKE), a clear correlation between steady flow and transient results was observed as well, which is a crucial issue within this work. This correlation is based on the effect, that parameter variations of the intake port impact only the angular velocity of the tumble vortex but not the general flow pattern and position. The angular velocity can be satisfyingly estimated by using steady flow tumble numbers.

Regarding the engine development process in particular detailed investigations are required. A convenient approach for this is to start from a suitable Pareto-optimal design of the global optimization. Therefore, a local optimization has been performed for a series production tumble port of an eight-cylinder turbocharged SI-engine using the ES-algorithm based on a single starting point. The focus has been put on increasing the flow coefficient, as the engine's charge motion level has been defined adequately yet. As a result of the single objective optimization, designs with improved flow coefficient and equal tumble number have been found. For these designs correlation between steady flow and transient results could be approved through the application of the dynamic analysis.

Apart from optimization design robustness is another crucial part within the development process. On the basis of the series production tumble port an approach for a robustness analysis analogously to the optimization process has been established, where measured tolerances resulting from the manufacturing process have been taken into account. Commonly, limited variations of the objectives characterize a robust design. In the present work the type of variation has been identified as another measure for robustness in the context of intake port optimization. For robust designs the objective values are distributed along the Pareto-front, while for less robust designs they spread away from this front. Based on these definitions, the series production port has been found to be more robust in comparison the improved design of the local optimization.

For the combustion chamber a general optimization analog to the intake port and a detailed optimization of a masking edge has been performed. As revealed in the present work, several valve lifts must be considered for assessing the overall influence of a combustion chamber design. In order to run an automatic optimization the particular results are combined to weighted non-dimensional numbers. For the flow coefficient suitable weighting factors have been derived by means of 1D-gas exchange simulations, where the influence of the flow rate characteristics on cylinder filling has been analyzed. In the case of tumble an average tumble number including valve opening duration, flow coefficient and tumble number was applied, which however delivered a non-satisfying prediction of the transient tumble progress. As a consequence, further investigations for adapting the weighting factors or another approach for a global tumble number are required.

A very detailed optimization was performed for a masking edge of a turbocharged DISI-engine with a fully variable valve drive, where small valve lifts lead to special requirements for the in-cylinder flow. In a first engine concept the in-cylinder flow has been identified to be unsuitable for mixture preparation in part load operation. Hence, the aim was to adapt the charge motion by optimizing the masking layout. For the evaluation of the particular masking designs a single lift position has been sufficient due to the limited valve lift heights. Accordingly, good correlations between steady flow and transient analysis results have been delivered for both flow coefficient and charge motion. Applying the optimized layout, reduced fuel consumption and exhaust emissions have been measured resulting from improved air/fuel mixing as analyzed by means of 3D-CFD simulations of the mixing process.

Altogether, the present optimization process has delivered very promising results for both intake port and combustion chamber problems by using steady flow simulations. However, with rising computational capacities a larger number of designs or more detailed CFD-simulations will be enabled even for extensive optimizations. By including spray and combustion simulations the interaction and influence of charge motion can be analyzed directly instead of estimating its influence by means of characteristic numbers.

Concerning the optimization methods, different strategies should be applied according to the development stage. In an early stage fast results can be delivered by DoE-methods combined with meta-models (e.g. RSM), in order to define first concepts for the in-cylinder flow. For an reliable optimization in contrast these methods are not adequate, as the deviations resulting from using meta-models are greater than the improvements expected from the optimization.

However, more accurate meta-models with appropriate prediction quality could diminish the computational effort further by reducing the number of required design evaluations. Later on during the development process, when first concepts for the evaluation have to be selected, a global optimization should be performed in order to improve the design quality. For this purpose Evolutionary Algorithms have been found to be suitable, in particular when the concept designs (delivered by e.g. DoE/RSM) are used as starting points for the optimization like in the case of the investigated GA. As a consequence, this feature should be included to the applied ES as well in order to prevent the algorithm to get stuck in a rather local optimization. For the GA in contrast a self-adaption mechanism would be desirable as it is very difficult to define the parameters of the algorithm appropriately. The final design at the end of the development stage should be determined by applying a local optimization. In this context, using the ES with its self-adaption mechanism and starting from a single design delivered quite promising results.

The problems investigated within the present work focus on intake port and combustion chamber geometries, as these mainly influence the in-cylinder flow in IC-engines. Both parts however were optimized separately. By optimizing intake port and combustion chamber simultaneously, further improvements concerning the strong conflict between flow rate and charge motion could be realized. Additionally, the exhaust port should be included for a cylinder head optimization, in order to investigate the entire charge-exchange process. Apart from the cylinder head, the flexible optimization process can be applied to other flow-guiding engine components, as it already has been for the optimization of a guide blade concept of a compressor (Hach (2009)).

# Appendix

## A  Engine Data

|  |  | 4CTC | 4CNA | 6CNA | 8CTC |
|---|---|---|---|---|---|
| Number of cylinders | - | 4 | 4 | 6 | 8 |
| Displacement | ccm | 1598 | 1598 | 2996 | 4395 |
| Bore | mm | 77 | 77 | 85 | 89 |
| Stroke | mm | 85.8 | 85.8 | 88 | 88.3 |
| Number of valves | - | 4 | 4 | 4 | 4 |
| Compression ratio $\varepsilon$ | - | 10.5 | 11.0 | 10.7 | 10.0 |
| Valve lift intake / outlet | mm | 0.2-9.0 / 9.0 | 0.2-9.5 / 9.0 | 0.2-9.7 / 9.7 | 8.8 / 8.8 |
| Camshaft spread intake | deg | 70 | 70 | 70 | 50 |
| Camshaft spread outlet | deg | 60 | 60 | 55 | 50 |

**Table A.1:** Technical data of the four-cylinder (4CTC) test engine, the serious production four-cylinder (4CNA) and six-cylinder (6CNA), and the eight-cylinder (8CTC) engine.

# B   Problem Specific Definitions for the Optimization

| Parameter | Name | Lower limit | Upper limit |
|---|---|---|---|
| y-coord | $Y - CL$ | 15.00 mm | 17.95 mm |
| Width CS7 | $W - CS7$ | 0.60 mm | 4.25 mm |
| Width CS8 | $W - CS8$ | 0.50 mm | 5.50 mm |
| Width CS9 | $W - CS9$ | 0.35 mm | 7.20 mm |
| Width CS10 | $W - CS10$ | 0.20 mm | 7.20 mm |
| Width CSE | $W - CSE$ | 0.10 mm | 7.20 mm |
| Radius Lower CS7 | $R_l - CS7$ | 8.0 mm | 14.0 mm |
| Radius Lower CS8 | $R_l - CS8$ | 8.0 mm | 14.0 mm |
| Radius Lower CS9 | $R_l - CS9$ | 8.0 mm | 13.5 mm |
| Radius Lower CS10 | $R_l - CS10$ | 8.0 mm | 13.5 mm |
| Radius Lower CSE | $R_l - CSE$ | 8.0 mm | 13.5 mm |
| Radius Upper CS7 | $R_u - CS7$ | 8.0 mm | 14.0 mm |
| Radius Upper CS8 | $R_u - CS8$ | 8.0 mm | 14.0 mm |
| Radius Upper CS9 | $R_u - CS9$ | 8.0 mm | 13.5 mm |
| Radius Upper CS10 | $R_u - CS10$ | 8.0 mm | 13.5 mm |
| Radius Upper CSE | $R_u - CSE$ | 8.0 mm | 13.5 mm |
| Milling cutter angle | $MCA$ | 15 deg | 45 deg |
| Milling cutter depth | $MCD$ | 0.0 mm | 7.0 mm |
| Milling cutter radius | $MCR$ | 0.1 mm | 25.0 mm |

**Table B.2:** CAD-parameters of the intake port model used for the multi-objective optimization.
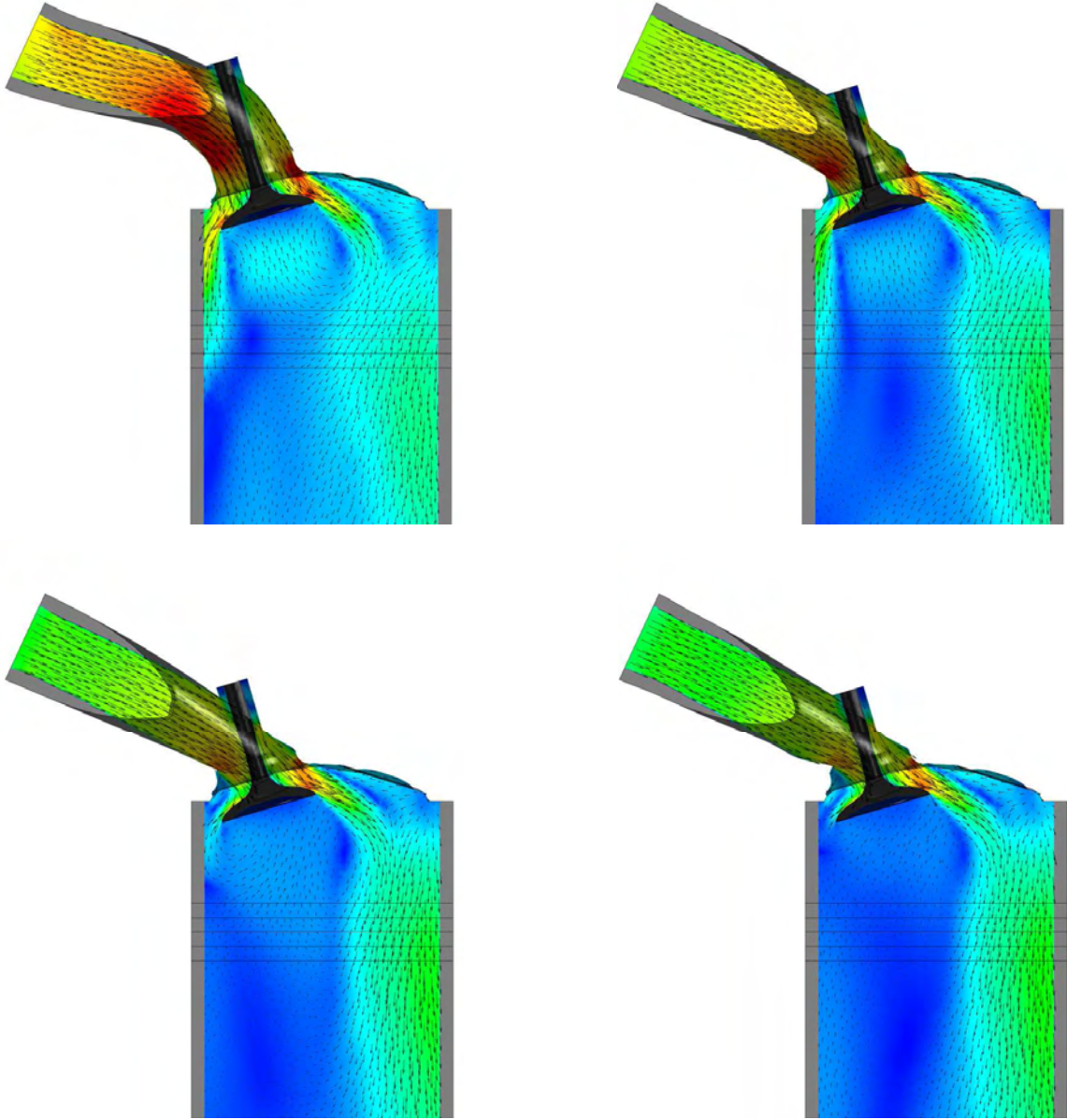
**Fig. B.1:** Flow pattern of a filling and different tumble port designs with rising tumble ratios (clockwise from above).

| Parameter | Name | Lower limit | Upper limit |
|---|---|---|---|
| y-coord | $Y - CL$ | 15.0 mm | 16.50 mm |
| Width CS7 | $W - CS7$ | 1.0 mm | 4.250 mm |
| Width CS8 | $W - CS8$ | 4.0 mm | 5.750 mm |
| Width CS9 | $W - CS9$ | 4.50 mm | 7.50 mm |
| Width CS10 | $W - CS10$ | 5.0 mm | 7.50 mm |
| Width CSE | $W - CSE$ | 5.0 mm | 7.50 mm |
| Radius Lower CS7 | $R_l - CS7$ | 8.0 mm | 14.50 mm |
| Radius Lower CS8 | $R_l - CS8$ | 8.0 mm | 13.50 mm |
| Radius Lower CS9 | $R_l - CS9$ | 7.50 mm | 12.50 mm |
| Radius Lower CS10 | $R_l - CS10$ | 7.50 mm | 12.5 mm |
| Radius Lower CSE | $R_l - CSE$ | 7.50 mm | 11.0 mm |
| Radius Upper CS7 | $R_u - CS7$ | 8.0 mm | 14.50 mm |
| Radius Upper CS8 | $R_u - CS8$ | 8.0 mm | 13.50 mm |
| Radius Upper CS9 | $R_u - CS9$ | 7.50 mm | 12.50 mm |
| Radius Upper CS10 | $R_u - CS10$ | 7.50 mm | 12.50 mm |
| Radius Upper CSE | $R_u - CSE$ | 7.50 mm | 11.0 mm |
| Milling cutter angle | $MCA$ | 35 deg | 45 deg |
| Milling cutter depth | $MCD$ | 0.0 mm | 7.0 mm |
| Milling cutter radius | $MCR$ | 0.1 mm | 10.0 mm |

**Table B.3:** CAD-parameters of the intake port model used for the tumble port optimization.

| Parameter | 8CBasis | Design_0207 | Design_0260 |
|---|---|---|---|
| y-coord | 15.16 mm | 15.0 mm | 15.0 mm |
| Width CS7 | 2.5 mm | 3.0 mm | 2.8 mm |
| Width CS8 | 5.25 mm | 4.95 mm | 4.99 mm |
| Width CS9 | 6.55 mm | 6.41 mm | 6.56 mm |
| Width CS10 | 7.19 mm | 7.45 mm | 7.5 mm |
| Width CSE | 7.13 mm | 7.2 mm | 7.29 mm |
| Radius Lower CS7 | 11.73 mm | 12.0 mm | 11.94 mm |
| Radius Lower CS8 | 10.5 mm | 13.1 mm | 12.98 mm |
| Radius Lower CS9 | 9.8 mm | 8.78 mm | 8.88 mm |
| Radius Lower CS10 | 9.325 mm | 8.82 mm | 8.96 mm |
| Radius Lower CSE | 8.75 mm | 9.04 mm | 8.96 mm |
| Radius Upper CS7 | 11.73 mm | 12.4 mm | 12.50 mm |
| Radius Upper CS8 | 10.5 mm | 11.26 mm | 11.18 mm |
| Radius Upper CS9 | 9.8 mm | 10.23 mm | 10.26 mm |
| Radius Upper CS10 | 9.325 mm | 9.66 mm | 9.76 mm |
| Radius Upper CSE | 8.75 mm | 8.47 mm | 8.52 mm |
| Milling cutter angle | 45 deg | 43.5 deg | 44 deg |
| Milling cutter depth | 0.0 mm | 0.0 mm | 0.1 mm |
| Milling cutter radius | 0.1 mm | 1.3 mm | 1.6 mm |

**Table B.4:** CAD-parameters of the basic and the optimal tumble port designs.

| Parameter | 4CTC | Design_0178 | Design_0155 |
|---|---|---|---|
| IV-distance | 18.50 mm | 17.21 mm | 18.50 mm |
| IV-depth | 12.0 mm | 12.0 mm | 13.0 mm |
| IV-angle | 19.5 deg | 15.0 deg | 15.0 deg |
| IV-dome-height | 7.97 mm | 8.5 mm | 8.5 mm |
| IV-SA-depth | 8.2 mm | 10.0 mm | 12.0 mm |
| EV-angle | 19.5 deg | 19.5 deg | 17.0 deg |
| EV-dome-height | 6.57 mm | 7.0 mm | 7.0 mm |
| IV-VSR-angle | 47.0 deg | 52.5 deg | 50.0 deg |
| IV-VSR-height | 5.9 mm | 5.6 mm | 5.9 mm |
| Valve-stem-radius | 8.0 mm | 10.0 mm | 4.0 mm |
| Valve-stem-diameter | 3.150 mm | 2.485 mm | 2.485 mm |
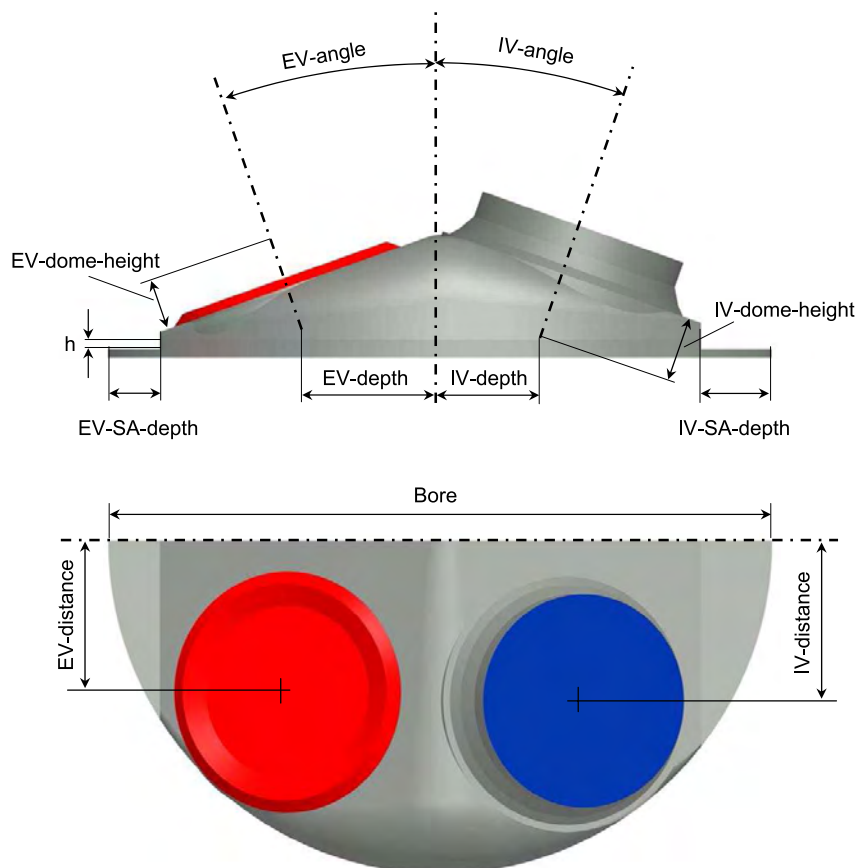


**Table B.5:** CAD-parameters for the basic and the extreme designs of the combustion chamber optimization.

# References

Abad Lozano, M. T., Knipping, S., Winkler, A. and Willand, J. (2007): *Automatische Motorkomponentenoptimierung mittels 3D-Strömungssimulationsmethoden und genetischen Algorithmen*. 2. Internationales Symposium für Entwicklungsmethodik, Wiesbaden.

Adomeit, Ph., Lang, O., Schmidt, A. and Hopp, M. (2006): *CAE-gestützte Kanalentwicklung für moderne Ottomotoren*. MTZ – Motortechnische Zeitschrift, vol. 67.

Affes, H., Trigui, N., Smith, D. and Griaznov, V. (1998): *Shape Optimization of IC Engine Ports and Chambers*. SAE Paper 980127.

ANSYS (2006): *ANSYS CFX-Solver Theory Guide, CFX Release 11.0*.

Arcoumanis, C. (1988): *Internal Combustion Engines (Combustion Treatise)*. Academic Press Inc.

Bartsch, H.-J. (1999): *Taschenbuch Mathematischer Formeln*. Fachbuchverlag Leipzig im Carl Hanser Verlag.

Bäck, Th. (1996): *Evolutionary Algorithms in Theory and Practice*. Oxford University Press.

Bäck, Th. (2006): *Neue Varianten der Evolutionsstrategie für die globale Optimierung*. Technologietag iSight, Garching bei München.

Bensler, H., Kapitza, J., Raposo, J. and Reisch, U. (2002): *A New Experimental Method for Determining Port Generated Swirl Flows*. SAE Paper 2002-01-2846.

Blaxill, H., Hancock, D., Fraser, N. and Sykes, R. G. (2008): *A New 3 Cylinder 1.2l Advanced Downsizing Technology Demonstrator Engine*. SAE Paper 2008-01-0611.

Blumhardt, R. (2001): *Numerische Optimierung des Crashverhaltens von Fahrzeugstrukturen und -komponenten*. Ph.D. thesis, Technische Universität München.

Boussinesq, J. (1877): *Essai sur la théorie des eaux courantes*. Mémoire présentées par divers savants à l'Académie des Sciences de l'Institute de France.

Bucher, Ch. (2005): *Stochastic Analysis in Structural Optimization*. Weimarer Optimierungs- und Stochastiktage 2.0, Weimar.

Bucher, Ch. (2007): *Basic concepts for robustness evaluation using stochastic analysis*. EUROMECH Colloquium 482 - Efficient Methods for Robust Design and Optimization, London.

Bucher, Ch. (2009): *Computational Analysis of Randomness in Structural Mechanics*. Taylor & Francis Group, London.

Bunsen., E., Grote, A. and Willand, J. (2007): *Vom vollvariablen Ventiltrieb zum hocheffizienten Brennverfahren*. Ladungswechsel im Verbrennungsmotor, Stuttgart.

Clement, S., Jordan, A., Sartiono, R., Vajna, S. and Kellner, P. (2004): *Prototypeinsatz evolutionärer Algorithmen in der Motorentwicklung bei Volkswagen*. MTZ – Motortechnische Zeitschrift, vol. 65.

Das, S. and Dent, J.D. (1995): *Simulation of the Mean Flow in the Cylinder of a Motored 4-Valved Spark Ignition Engine*. SAE Paper 952384.

Deb, K. (1995): *Optimization for Engineering Design: Algorithms and Examples*. Prentice-Hall, New Delhi.

Deb, K. (2001): *Multi-Objective Optimization using Evolutionary Algorithms*. John Wiley & Sons.

Deb, K. and Agrawal, R. B. (1994): *Simulated Binary Crossover for Continuous Search Space*. Technical report, Department of Mechanical Enginering, Indian Institute of Technology, Kanpur, India.

Deb, K., Agrawal, S., Pratap, A. and Meyarivan, T. (2000): *A Fast Elitist Non-dominated Sorting Genetic Algorithm for Multi-objective Optimisation: NSGA-II*. Proceedings of the 6th International Conference on Parallel Problem Solving from Nature, pp. 849–858, Springer-Verlag.

Dingel, O., Kahrstedt, J., Seidel, Th. and Zülch, S. (2003): *Three-Dimensional Measurement of Charge Moting Using Doppler Global Velocimetry*. MTZ – Motortechnische Zeitschrift, vol. 64.

Dingel, O., Seidel, Th., Schodl, R. and Willert, C. (2002): *Messung der Zylinderinnenströmung mit Doppler Global Velocimetry*. Optisches Indizieren - Verbrennungsentwicklung für Otto- und Dieselmotoren, Haus der Technik e.V., Essen.

Duddeck, F. (2008): *Multi-disciplinary optimisation of car bodies*. Structural and Multidisciplinary Optimization, vol. 35(4), pp. 375–389.

Dynardo (2008): *optiSLang Manual Version 3.0*.

Ehrgott, M. (2005): *Multicriteria Optimization*. Springer, Berlin.

Eichlseder, H., Hübner, W., Rubbert, S., Schmitz, K. and Stanski, U. (1998): *Aspekte zur Auswahl eines Otto-Direkteinspritzkonzeptes*. 7. Aachener Kolloquium Fahrzeug- und Motorentechnik 1998, Aachen.

Eichlseder, H., Klüting, M. and Piock, W. F. (2007): *Grundlagen und Technologien des Ottomotors*. Springer-Verlag, Wien.

Elwan, K. (2008): *Investigations of the Influence of Charge Motion and Multi-Objective Optimization of a Combustion Chamber Geometry.* Master thesis, Technische Universität München.

FEV (2000): *FEV-Spektrum, Ausgabe 15 / Sept. 2000.*

Fischer, J. (2004): *Einfluss variabler Einlassströmung auf zyklische Schwankungen bei Benzin-Direkteinspritzung.* Ph.D. thesis, Universität Karlsruhe.

FlowHead (2009): *http://flowhead.sems.qmul.ac.uk/.*

Fogel, L.J., Owens, A.J. and Walsh, M.J. (1966): *Artificial Intelligence through Simulated Evolution.* John Wiley & Sons.

Frank, W. (1985): *Beschreibung von Einlasskanaldrallströmungen für 4-Takt-Hubkolbenmotoren auf Grundlage stationärer Durchströmversuche.* Ph.D. thesis, RWTH Aachen.

Full, M. (2007): *Method for an Automated Combustion Chamber Optimisation.* Master thesis, FH Augsburg.

Ganser, M., Grossenbacher, K., Willmes, L. and Schütz, M. (2007): *Simulation meta-models in the early phase of the product development process.* EUROMECH Colloquium 482 - Efficient Methods for Robust Design and Optimization, London.

Glanz, R. (2000): *Differentielle Erfassung von Tumbleströmungsfeldern.* MTZ – Motortechnische Zeitschrift, vol. 61, pp. 40 – 45.

Gold, M., Stokes, J., Morgan, R., Heikal, M. and Sercey, G. Begg, S. (2001): *Air-Fuel Mixing in a Homogeneous Charge DI Gasoline Engine.* SAE Paper 2001-01-0968.

Goldberg, D.E. (1989): *Genetic Algorithms in Search, Optimization and Machine Learning.* Addison Wesley.

Golloch, R. (2005): *Downsizing bei Verbrennungsmotoren: Ein wirkungsvolles Konzept zur Kraftstoffverbrauchssenkung.* Springer-Verlag, Berlin.

Grasreiner, S. (2008): *Analyse eines direkteinspritzenden Turbo-Ottomotors mit variabler Ventilsteuerung am optischen Motor.* Master thesis, Technische Universität Ilmenau.

Göttgens, J., Mauss, F. and Peters, N. (1992): *Analytical Approximations of Burning Velocities and Flame Thicknesses of Lean Hydrogen, Methane, Ethylene, Ethane, Acetylene and Propane Flames.* 24th Symposium (Int.) on Combustion, Sydney.

Hach, A. (2009): *Strömungstechnische Optimierung der Diffusorbeschaufelung eines Radialverdichters.* Master thesis, Fachhochschule München.

Hammel, U. and Bäck, Th. (1998): *Optimierung in der Simulation: Evolutionäre Algorithmen.* Technical report, Universität Dortmund, Informatik XI, Dortmund.

Hascher, H., Jaffri, K., Novak, M., Lee, K., Schock, H., Bonne, M. and Keller, Ph. (1997): *An Evaluation of Turbulent Kinetic Energy for the In-Cylinder Flow of a Four-Valve 3.5l SI Engine Using 3-D LDV Measurements*. SAE Paper 970793.

Hascher, H., Novak, M., Stuecken, T., Schock, H. and Novak, J. (2000): *The 3-D In-Cylinder Charge Motion of a Four-Valve SI Engine Under Stroke, Speed, and Load Variation*. SAE Paper 2000-01-2798.

Haslinger, W. and Steinhagen, U. (2005): *Formoptimierung eines Einlasskanals zur Maximierung des Massenstroms unter Anwendung von CFD und Optimierungsstrategien*. Technical report, ANSYS Germany GmbH.

Haworth, D., El Tahry, S. and Huebler, M. (1990): *Multidimensional Port-And-Cylinder Flow Calculations for Two-And Four-Valve-Per-Cylinder Engines–Influence of Intake Configuration on Flow Structure*. SAE Paper 900257.

Helmetsberger, P. (2009): *Experimentelle Gemischbildungsuntersuchungen an einem Ottomotor mit vollvariablem Ventiltrieb, Direkteinspritzung und Aufladung*. Ph.D. thesis, Technische Universität Graz.

Heywood, J.B. (1988): *Internal Combustion Engine Fundamentals*. McGraw-Hill Book Company.

Holland, J.H. (1975): *Adaption in Natural and Artificial Systems*. University of Michigan Press.

Hongming, X. (2001): *Some Critical Technical Issues on the Steady Flow Testing of Cylinder Heads*. SAE Paper 2001-01-1308.

Kaminski, Th., Giering, R. and Othmer, C. (2005): *Topological design based on highly efficient adjoints generated by automatic differentiation*. Design Optimization International Conference, Las Palmas.

Kessler, F., Kiesgen, G., Schopp, J. and Bollig, M. (2007): *The New Four-Cylinder Engine Series from the Cooperation between BMW and PSA*. MTZ – Motortechnische Zeitschrift, vol. 68.

Kiefer, W., Klauer, N., Krauss, M., Mährle, W. and Schünemann, E. (2004): *Reihensechszylinder-Ottomotor von BMW - Teil2: Thermodynamik und funktionale Eigenschaften*. MTZ – Motortechnische Zeitschrift, vol. 65, pp. 1008 – 1017.

Klimetzek, F., Paterson, J. and Moos, O. (2006): *AutoDuct: Topologieoptimierung von Strömungen*. Konferenz für angewandte Optimierung, Karlsruhe.

Koenigstein, A., Grebe, U., Wu, K.-J. and Larsson, P.-I. (2008): *Differenzierte Analyse von Downsizing-Konzepten*. MTZ – Motortechnische Zeitschrift, vol. 69.

Kolmogorov, A.N. (1941): *Dissipation of energy in the locally isotropic turbulence*. Dokl. Adad. Nauk SSSR, vol. 32, pp. 19–21.

Korte, V., Hancock, D. and Blaxill, H. (2008): *Downsizing-Motor von Mahle als Technologiedemonstrator*. MTZ – Motortechnische Zeitschrift, vol. 69.

Lauer, Th. (2007): *Einfluss der Ladungsbewegung auf Gemischbildung und Entzündung bei Otto-Motoren mit homogenen Brennverfahren*. Ph.D. thesis, Technische Universität Wien.

Launder, B. E. and Spalding, D. B. (1974): *The Numerical Computation of Turbulent Flows*. Comput. Methods Appl. Mech. Eng., vol. 3.

Lecointe, B. and Monnier, G. (2003): *Downsizing a Gasoline Engine Using Turbocharging With Direct Injection*. SAE Paper 2003-01-0542.

Lee, S., Tong, K., Quay, D. Zello, J. and Santavicca, D. (2000): *Effects of Swirl and Tumble on Mixture Preparation During Cold Start of a Gasoline Direct-Injection Engine*. SAE Paper 2001-01-1900.

Lenz, H. P. (1990): *Gemischbildung bei Ottomotoren*. Springer Verlag.

Linse, D. (2006): *Einfluss der Einlasskanal-induzierten Ladungsbewegung auf die Brenngeschwindigkeit in einem direkteinspritzenden Ottomotor*. Master thesis, RWTH Aachen.

Linse, D., Hasse, Ch. and Durst, B. (2009): *An Experimental and Numerical Investigation of Turbulent Flame Propagation and Flame Structure in a Turbo-Charged Direct Injection Gasoline Engine*. Combustion Theory and Modelling, vol. 13(1), pp. 167 – 188.

Loeffler, M.G., Kroeckel, K., Koch, P., Beyrau, F., Leipertz, A., Grasreiner, S. and Heinisch, A. (2009): *Simultaneous Quantitative Measurements of Temperature and Residual Gas Fields Inside a Fired SI-Engine Using Acetone Laser-Induced Fluorescence*. SAE Paper 2009-01-0656.

Lowry, Richard (2010): *Concepts and Applications of Inferential Statistics*. http://faculty.vassar.edu/lowry/webtext.html.

Loy, M. (2005): *Analyse des Einflusses von Einlasskanal-Formparametern auf die Ladungsbewegung mit Hilfe software-gestützter multi-objektiver Optimierungsverfahren*. Master thesis, Technische Universität München.

Makk, P. (1998): *Rechnerunterstützte Optimierung von Einlaßkanälen eines Zylinderkopfes mit Hilfe von Evolutionären Algorithmen*. Master thesis, Technische Universität Budapest.

Makk, P., Wegner, B., Bercsey, T., Vajna, S., Kickermann, H. and Kellner, P. (1999): *Computer Aided Optimization of Cylinder Head Inlet Ports Using Genetic Algorithms*. ICED 99, München.

Menter, F. R. (1994): *Two-equation eddy-viscosity turbulence models for engineering applications*. AIAA Journal, vol. 32(8), pp. 1598 – 1605.

Mollenhauer, K. and Tschöke, H. (2007): *Handbuch Dieselmotoren*. Springer-Verlag, Berlin.

Moos, O., Klimetzek, F. and Rossmann, R. (2004): *Bionic Optimization of Air-Guiding Systems.* SAE Paper 2004-01-1377.

Myers, R.H. and Montgomery, D.C. (2002): *Response Surface Methodology.* John Wiley & Sons.

Noesis (2006): *OPTIMUS Theory manual, Rev. 5.2.*

NuTech (2005): *ClearVu Global Optimizer for Optimus, User Manual Version 1.0.7.1.*

Othmer, C. (2006): *CFD Topology and Shape Optimization with Adjoint Methods.* 13. Internationaler Kongress Berechnung und Simulation im Fahrzeugbau, VDI Fahrzeug- und Verkehrstechnik, Würzburg.

Othmer, C., de Villiers, E. and Weller, H. (2007): *Implementation of a continuous adjoint for topology optimization of ducted flows.* 18th AIAA Computational Fluid Dynamics Conference, Miami.

Othmer, C. and Grahs, Th. (2005): *Approaches to Fluid Dynamic Optimization in the Car Development Process.* EUROGEN 2005, Munich.

Patankar, S.V. (1980): *Numerical Heat Transfer and Fluid Flow.* Hemisphere Publishing Corporation, New York.

Peters, N. (2000): *Turbulent Combustion.* Cambridge University Press, Cambridge.

Pischinger, R., Klell, M. and Sams, Th. (2002): *Thermodynamik der Verbrennungskraftmaschine.* Springer Verlag, Wien.

Pope, S. B. (2000): *Turbulent Flows.* Cambridge University Press, Cambridge, UK.

Quissek, F. (1984): *Über den Einfluss außen erzeugter Ladungsbewegung auf das Betriebsverhalten eines hochverdichteten Ottomotors.* Ph.D. thesis, Technische Universität Wien.

Rechenberg, I. (1973): *Evolutionsstrategie.* Friedrich Frommann Verlag.

Roettger, G., Abad Lozano, M. T., Kiel, M. and Willand, J. (2004): *Automated Intake Port Geometry Optimisation by means of Genetic Algorithms and 3D-CFD.* 22nd CADFEM User Meeting, Dresden.

Roettger, G., Abad Lozano, M. T., Kiel, M. and Willand, J. (2005): *Einsatz von Simulationsmethoden zur automatischen Optimierung von FSI-Einlasskanälen.* 1. Internationales Symposium für Entwicklungsmethodik, Wiesbaden.

Schaffer, J. D. (1984): *Some Experiments in Machine Learning Using Vector Evaluated Genetic Algorithms.* Ph.D. thesis, Vanderbilt University, Nashville.

Schwefel, H.P. (1981): *Numerical Optimization of Computer Models.* John Wiley & Sons.

Seidel, Th. and Steuker, H. (2008): *Doppler Global Velocimetry - Measurement of Flow Inside Cylinders of DI SI Engines*. MTZ – Motortechnische Zeitschrift, vol. 69.

Sorger, H., Zieher, F., Sauerwein, U. and Schöffmann, W. (2008): *Hochbelastete Zylinderköpfe für Otto- und Dieselmotoren*. MTZ – Motortechnische Zeitschrift, vol. 69.

Taylor, Ch. F. (1985a): *The Internal Combustion Engine in Theory and Practice - Vol. 1: Thermodynamics, Fluid Flow, Performance*. The MIT Press.

Taylor, Ch. F. (1985b): *The Internal Combustion Engine in Theory and Practice - Vol. 2: Combustion, Fuels, Materials, Design*. The MIT Press.

Thien, G. (1965): *Entwicklungsarbeiten an Ventilkanälen von Viertakt-Dieselmotoren*. Österreichische Ingenieurzeitschrift, Heft 9.

Thum, S. (2007): *Numerische Optimierung strömungstechnischer Systeme*, Lecture notes, Technische Universität München.

Tippelmann, G. (1997): *Räumlicher Drallmesser für Drall- und Tumblemessung*. MTZ – Motortechnische Zeitschrift, vol. 58, pp. 362 – 363.

Tremel, P. (1997): *Methoden zur Einlaßkanalentwicklung - Möglichkeiten und Grenzen der Verfahren*. 6. Tagung Der Arbeitsprozess des Verbrennungsmotors, Graz.

Tuertscher, A. (1991): *Rechnergestützte Entwicklung und Fertigung von Ventilkanälen*. Ph.D. thesis, Technische Universität Graz.

Unger, H., Schwarz, Ch., Schneider, J. and Koch, K.-F. (2008): *Die Valvetronic - Erfahrungen aus sieben Jahren Großserie und Ausblick in die Zukunft*. MTZ – Motortechnische Zeitschrift, vol. 69, pp. 598 – 605.

Vajna, S., Clement, S., Jordan, A. and Bercsey, T. (2005): *The Autogenetic Design Theory: an evolutionary view of the design process*. Journal of Engineering Design, vol. 16, pp. 423–440.

Van Basshuysen, R. (2002): *Handbuch Verbrennungsmotor*. Vieweg-Verlag.

Versteeg, H. K. and Malalasekera, W. (1995): *An introduction to Computational Fluid Dynamics*. Prentice-Hall, Essex, UK.

Vieser, W., Esch, Th. and Menter, F. (2002): *Heat Transfer Predictions using Advanced Two-Equation Turbulence Models*. Technical report, ANSYS Germany GmbH.

Wieser, K., Ennemoser, A. and Plimon, A. (1998): *Prozessorientierter Einsatz von CFD in der Entwicklung von Motorkomponenten durch die Verfügbarkeit automatischer Netzgeneratoren*. MTZ – Motortechnische Zeitschrift, vol. 59.

Wilcox, D. C. (1988): *Multiscale model for turbulent flows*. AIAA Journal, vol. 26(11), pp. 1311 – 1320.

Wilcox, D. C. (2006): *Turbulence Modeling for CFD*. DCW Industries, Inc., California, USA.

Will, J. (2006): *Optimierung und Robustheitsbwertung in der virtuellen Produktentwicklung*. 11rd Schweizer CADFEM Users' Meeting 2006, Zürich.

Will, J., Roos, D., Riedel, J. and Bucher, Ch. (2003): *Robustheitsbewertung in der stochastischen Strukturmechanik*. NAFEMS Seminar: Use of Stochastics in FEM Analyses, Wiesbaden.

Wurms, R. (1994): *Einfluß einlaßseitig erzeugter Ladungsbewegung auf das Betriebsverhalten von Vierventil-Ottomotoren*. Ph.D. thesis, RWTH Aachen.

Zitzler, E., Laumanns, M. and Thiele, L. (2001): *SPEA2: Improving the Strength Pareto Evolutionary Algorithm*. Computer Engineering and Networks Laboratory (TIK), ETH Zürich – Techn. Rep., vol. 103.

# Lebenslauf

Name              Matthias Karch

Geburtsdatum      29. Juni 1979

Geburtsort        Eichstätt

Familienstand     verheiratet, ein Kind


1985 – 1989       Besuch der Grundschule in Beilngries

1989 – 1998       Besuch des Willibald-Gymnasiums in Eichstätt

1999 – 2006       Studium Maschinenbau an der Technischen Universität Graz

2000              Vordiplom

17.1.2006         Diplomprüfung

3/2006 – 2/2009   Doktorand bei der Firma BMW AG in München

seit 3/2009       Mitarbeiter der Firma AUDI AG in Ingolstadt